Karlsruher Institut für Technologie

# Polyelectrolyte hydrogels with various network architectures: Synthesis, characterization and use in membrane-free desalination

Zur Erlangung des akademischen Grades eines
DOKTORS DER NATURWISSENSCHAFTEN
(Dr. rer. nat.)
der KIT-Fakultät für Chemie und Biowissenschaften
des Karlsruher Instituts für Technologie (KIT)

genehmigte
DISSERTATION
von

Dipl.-Chem. Lukas B. Arens

aus

Landau in der Pfalz

| | |
|---|---|
| Dekan: | Prof. Dr. Reinhard Fischer |
| Referent: | Prof. Dr. Manfred Wilhelm |
| Korreferent: | Prof. Dr. Patrick Théato |
| Tag der mündlichen Prüfung: | 16. Juli 2018 |

Diese Arbeit wurde in der Zeit vom 1. August 2014 bis zum 29. Mai 2018 am Institut für Technische Chemie und Polymerchemie des Karlsruher Instituts für Technologie unter Anleitung von Prof. Dr. Manfred Wilhelm durchgeführt. Hiermit versichere ich, dass ich die von mir vorgelegte Arbeit selbstständig verfasst habe, dass ich die verwendeten Quellen und Hilfsmittel vollständig angegeben und die Stellen der Arbeit, die anderen Werken im Wortlaut oder dem Sinn nach entnommen sind, entsprechend kenntlich gemacht habe.

**Karlsruhe, den 29. Mai 2018**

. . . . . .

(**Lukas Arens**)

# Nomenclature

## Abbreviations

AA ..... Acrylic acid
AUL ..... Absorbency under load
bcc ..... Body cubic centered (Bravais lattice in the cubic crystal system)
CPMG ..... Carr-Purcell-Meiboom-Gill (NMR pulse sequence)
DI ..... Deionized (water)
DPE ..... 1,1-diphenylethylene
DQ ..... Double quantum (effects in NMR)
DRI ..... Differential refractometer, typical detector for SEC measurements
DSC ..... Differential scanning calorimetry
EGDE ..... Glycol diglycidyl ether (surface crosslinking agent)
EGDMA .... Ethylene glycol dimethacrylate (crosslinking agent)
FID ..... Free induction decay (in NMR)
FO ..... Forward osmosis (desalination technique)
FRP ..... Free radical (co)polymerization
FT-IR ..... Fourier-transform infrared (spectroscopy)
ILT ..... Inverse Laplace transform
IPN ..... Interpenetrating network
LB1110 ..... Commercial superabsorber from the BASF (based on surface crosslinked PSA)
LCST ..... Lower critical solution temperature
LVE ..... Linear viscoelastic (regime)
MAA ..... Methacrylic acid
MBA ..... N,N'-methylenebisacrylamide (crosslinking agent)
MED ..... Multiple-effect distillation (desalination technique)
MF ..... Microfluidic, technique to fabricate monodisperse spherical hydrogel beads
MMA ..... Methyl methacrylate (monomer)
MQ ..... Multiple quantum (effects in NMR)
MSE ..... Magic sandwich echo
MSF ..... Multi-stage flash distillation (desalination technique)

NIPAAm .... N-isopropylacrylamide (monomer)
NMR ..... Nuclear magnetic resonance
P*t*BMA ..... Poly(*tert*-butyl methacrylate)
PAA ..... Poly(acrylic acid)
PBMA ..... Poly(butyl methacrylate)
PEG ..... Poly(ethylene glycol)
PMAA ..... Poly(methacrylic acid)
PMMA ..... Poly(methyl methacrylate)
PNIPAAm .. Poly(N-isopropylacrylamide)
PSA ..... Poly(sodium acrylate) (neutralized form of PAA)
PSMA ..... Poly(sodium methacrylate) (neutralized form of PMAA)
RDC ..... Residual dipolar coupling
RO ..... Reverse osmosis (desalination technique)
SA ..... Sodium acrylate (neutralized form of AA)
SAXS ..... Small angle X-ray scattering
SEC ..... Size exclusion chromatography
SEM ..... Scanning electron microscopy
SMA ..... Sodium methacrylate (neutralized form of MAA)
SN ..... Single network
SPS ..... Sodium persulfate, $Na_2S_2O_8$ (thermal initiator)
TD-NMR ... Time-domain (NMR)
TEGDA ..... Tetra(ethylene glycol) diacrylat (crosslinking agent)
TEMED .... N,N,N',N'-tetramethylethylenediamine (forms a redox initiator with SPS)
THF ..... Tetrahydrofuran (organic solvent)
XY16 ..... Special phase cycling for CPMG pule sequence

## Physical quantities

$\bar{P}$ ..... Mean power output in the osmotic engine (see Equation 7.1)
$\chi$ ..... Flory-Huggins (interaction) parameter
$\Delta\mu_{\mathrm{I,el}}$ ..... Elastic contribution to the chemical potential
$\Delta\mu_{\mathrm{I,ion}}$ ..... Electrostatic contribution to the chemical potential
$\Delta\mu_{\mathrm{I,mix}}$ ..... Mixing contribution to the chemical potential
$\Delta G_{\mathrm{mix}}$ ..... Free energy of mixing
$\Delta H_{\mathrm{mix}}$ ..... Enthalpy of mixing
$\Delta S_{\mathrm{mix}}$ ..... Entropy of mixing
$\mu_{\mathrm{el}}$ ..... Number of crosslinks
$\mu_{\mathrm{I}}$ ..... Chemical potential of the solvent in the gel phase

$\nu_{el}$ ..... Number of elastic chains

$\Pi$ ..... Osmotic pressure

$\tan\delta$ ..... Loss factor, defined by Equation 5.6

$\vec{q}$ ..... Wave vector (in SAXS experiments)

$\xi$ ..... Cycle rank, defined by Equation 3.4

$c_p$ ..... Polymer concentration in the swollen state, $c_p = \frac{1}{Q_{eq}}$

$D_{res}$ ..... Residual dipolar coupling constant

$DC$ ..... Degree of crosslinking, defined by Equation 4.1

$DN$ ..... Degree of neutralization, defined by Equation 4.2

$E$ ..... Young's modulus

$E_{m^3}$ ..... Specific energy, which is the energy to obtain 1 m³ of potable water (estimated by Equation 6.5)

$f$ ..... Crosslinking functionality, which is the number of elastic chains per crosslinking point

$G$ ..... Oscillatory shear modulus

$G'$ ..... Storage modulus, defined by Equation 5.4

$G''$ ..... Loss modulus, defined by Equation 5.5

$G^*$ ..... Complex shear modulus, defined by Equation 5.3

$k$ ..... Crosslinker efficiency

$k_B$ ..... Boltzmann constant

$M_c$ ..... Molecular weight of the polymer chains between crosslink points

$m_h$ ..... Mass of swollen hydrogel

$m_p$ ..... Mass of (dry) polymer

$m_s$ ..... Mass of solvent

$M_w$ ..... Weight averaged molecular weight

$N(A)$ ..... Number of MMA units per endblock A in ABA triblock copolymers

$N(B)$ ..... Number of SMA units per midblock B in ABA triblock copolymers

$N(M)$ ..... (Average) number of monomer units per elastic chain

$N_A$ ..... Avogadro's number

$P$ ..... Penetration during surface crosslinking reaction (see Equation 4.4)

$PDI$ ..... Polydisperisity index

$Q(t)$ ..... Time-dependent degree of swelling, defined by Equation 5.1

$Q_{eq}$ ..... Degree of swelling at equilibrium (see Equation 5.1)

$Q_{rel}$ ..... Relative degree of swelling, defined as the water in the system with respect to $Q_{eq}$

$Q_{syn}$ ..... Degree of swelling during the hydrogel formation, defined by Equation 4.3

$RS$ ..... Reduced salinity (in thermal desalination experiments, see Equation 6.10)

$RW$ ..... Recovered water (in thermal desalination experiments, see Equation 6.9)

$SR$ ..... Salt rejection in the supernatant phase normalized to the initial salt concentration (in desalination experiments), usually at $Q_{\mathrm{rel}} = 2$

$T_1$ ..... Longitudinal relaxation (time) in NMR

$T_2$ ..... Transverse relaxation (time) in NMR

$T_{\mathrm{g}}$ ..... Glass transition temperature

# Zusammenfassung

Hydrogele, die aus dreidimensional verknüpften Polyelektrolyten wie z. B. dem Salz der Polyacrylsäure bestehen, zeichnen sich durch eine hohe Quellfähigkeit in wässrigen Lösungen aus. Solche Polymere werden aufgrund ihrer hohen Wasseraufnahme von bis zum 1.000-fachen ihres Eigengewichts häufig als Superabsorber bezeichnet. Sie werden in verschiedenen Einsatzgebieten verwendet, wobei die Nutzung in Hygieneartikeln wie z. B. Windeln am weitesten verbreitet ist. Neuere Studien haben gezeigt, dass die Polyacrylsäurenetzwerke prinzipiell auch für die Meerwasserentsalzung und zur Energiegewinnung aus Salzgradienten (z. B. an Flussdeltas) verwendet werden können. Der weiteren Erforschung dieser beiden neuartigen Ansätze widmet sich die vorliegende Dissertation.

Der Schwerpunkt der Arbeit liegt dabei in der Verwendung der Polyelektrolyte als Separationsmedium für die Entsalzung: Wird das Hydrogel in Salzwasser gequollen, so werden die mobilen Salzionen durch die gebundenen Ladungsträger entlang der Polymermaschen abgestoßen, sodass das aufgenommene Wasser im Gel eine niedrigere Salzkonzentration hat. Das salzärmere Wasser kann durch eine externe Kraft aus dem Gel gepresst, und so zurückgewonnen werden. In der anderen potentiellen Anwendung wird die salzkonzentrationsabhängige Quellung des Superabsorbers genutzt, um durch zyklisches Auf- und Abquellen in Süß- bzw. Salzwasser einen Kolben in einem osmotischen Motor anzutreiben, um so regenerative Energie zu gewinnen.

In vorangegangen Arbeiten wurden für die zwei potentiellen Anwendungen ausschließlich Hydrogele benutzt die mittels freier radikalischer Polymerisation (FRP) dargestellt wurden. Dies ist zwar eine einfache und günstige Synthesemethode, bietet aber nur wenig Kontrolle über die Netzwerkarchitektur, bei der i. d. R. lediglich die mittlere Maschenweitenverteilung eingestellt werden kann.

In der vorliegenden Arbeit wurden unterschiedlichste Netzwerktopologien der geladenen Hydrogele, basierend auf Polyacrylsäure (PSA) und Polymethacrylsäure (PSMA) synthetisiert, um die Auswirkungen auf verschiedene Geleigenschaften mit einem besonderen Fokus auf den Entsalzungsprozess zu untersuchen. Es wurden zunächst PSA und PSMA Hydrogele mittels FRP mit unterschiedlichem Vernetzungsgrad als Referenzmaterial dargestellt. Als weitere Netzwerkarchitekturen wurden Kern-Schale-Partikel, interpenetrierende PSA-*i*-PSA Netzwerke

(IPNs) und Modelsysteme mit einer engverteilten Maschenweitenverteilung ($PDI = 1.04 - 1.17$) synthetisiert.

Die Modelsysteme wurden durch amphiphile Triblockcopolymere PMMA-*b*-PSMA-*b*-PMMA mittels anionischer Polymerisation dargestellt. Diese Polymere phasenseparieren in wässriger Lösung, wobei die hydrophoben Polymethylmethacrylatblöcke (PMMA) sphärische Aggregate bilden, die als physikalische Vernetzungspunkte dienen. Dieses System wurde mit einem besonderen Fokus analysiert, in dem die verschiedenen Blocklängen variiert, und diese Triblockcopolymere auch mit PMMA-*b*-PSMA Diblockcopolymeren gemischt wurden, um Hydrogele mit einem gezielt höheren Anteil an einfach-gebundenen, elastisch nicht-aktiven Ketten zu erhalten.

Neben den reinen Poly(meth)acrylsäuren wurden auch thermo-responsive Hydrogele dargestellt, indem das Monomer N-isopropylacrylamid (NIPAAm), entweder durch Copolymerisation oder in Form von IPNs, in die Netzwerkstruktur eingebaut wurde. Diese Hydrogele weisen abhängig vom PSA-Anteil einen Phasenübergang bei etwa 35 °C auf, sodass während einem Entsalzungszyklus das salzärmere Wasser im Gel durch Temperatur anstatt Druck zurückgewonnen werden konnte.

Die selbst-synthetisierten Polymere wurden mit einer Vielzahl verschiedenster Methoden charakterisiert. Die Quellfähigkeit und die rheologischen Eigenschaften wurden als wichtigste Kenngrößen gemessen, während Kleinwinkelröntgenstreuung (SAXS) und NMR-Relaxometrie im Niederfeld genutzt wurde, um fundiertere Aussagen über die Netzwerkstruktur zu treffen. Mit SAXS ließen sich die Abstände zwischen den Vernetzungspunkten in den Modelsystemen mit einer engen Maschenverteilung analysieren, wobei die Messung der Polymerdynamik mittels transversaler kernmagnetischer Relaxation ($T_2$) und NMR-Doppelquantenkohärenzen sich als geeignete Methode herausstelle um eine erhöhte Heterogenität in den oberflächenvernetzten Hydrogelen und den IPNs nachzuweisen.

In den Entsalzungsexperimenten mit NaCl-Modellösungen erwiesen sich höher-vernetzte Hydrogele mit den entsprechend höheren Ladungsdichten im gequollenen Zustand als energieeffizienter mit einer besseren Separationsleistung. Erste Abschätzungen für die spezifische Energie beliefen sich auf $6 - 20\,\mathrm{kWh/m^3}$. Die Verteilung der gebundenen Ladungen innerhalb der Netzwerke hatte allerdings keinen signifikanten Einfluss auf die Salzabstoßung. Qualitativ konnte die Ladungsverteilung der mobilen Ionen zwischen Hydrogel und überstehender Lösung mit der Donnan-Theorie beschrieben werden. Quantitativ wurde hingegen nur unter der Annahme einer wesentlich geringeren effektiven Ladung des Hydrogels von 10 – 12 mol% eine gute Übereinstimmung gefunden.

Im osmotischen Motor wurde eine maximale mittlere Energieproduktion von 0.23 W/kg trockenen Polymers erreicht, wobei vor allem die Eigenabdichtung der Hydrogele als Herausfor-

derung für eine weitere Energiemaximierung festgestellt wurde. Dieses sogenannte *Gelblocking* konnte durch die Verwendung von Kern-Schale Hydrogelen oder runder Partikel mit einheitlicher Kugelgröße, welche mittels tröpfchenbasierter Mikrofluidik dargestellt wurden, verringert werden um so die Energieproduktion in Zukunft weiter zu steigern.

# Contents

# 1 Introduction

Polyelectrolyte hydrogels are an interesting class of materials due to several unique properties. These networks have a high affinity to water because of the charges present along the polymer chains, while the crosslinking points prevent dissolution of the material. Therefore, such hydrogels exhibit a high uptake of water or aqueous solutions that can exceed several hundred times their own weight. The material is thus often referred to as a superabsorber and is found in many applications [Buchholz98, Elliott04]. The industrial importance of superabsorbent polymers, which are usually based on charged poly(acrylic acid), can be seen by their high annual production of over 3.1 million tons in 2014 [Yu15]. While the largest amount of hydrogels produced is used in hygiene products, like disposable diapers or sanitary napkins, the range of applications is actually very diverse. Superabsorbers are found in a wide range of products, such as artificial snow, sealings and underwater-cable insulations, as additives for drilling fluids or concrete and in agriculture [Zohuriaan-Mehr10]. While all these established products take advantage of their high absorbency, newer applications are also based on stimuli-responsive hydrogels that are sensitive to environmental changes. These "smart" hydrogels are able to switch their swelling state in response to an external stimulus, like pH, temperature, salinity, magnetic field or light. Hence, these materials are used in medical applications or healthcare products, such as wound dressing, biosensors, actuators (artificial muscles) or drug delivery systems [Ganta08, Ebara14].

More recent studies demonstrated that polyelectrolyte hydrogels can be applied in the desalination of saltwater using a membrane-free process [Höpfner10, Höpfner13a]. When a dry hydrogel swells in saline feedwater, the mobile salt ions from the solution are partially rejected by the fixed charges of the network and remain in the supernatant phase. Hence, the amount of added ions is smaller inside the gel than outside. This effect can be described in terms of the Donnan membrane equilibrium [Donnan32, Katchalsky55]. The water with its reduced salinity inside the network can be recovered by compressing the hydrogel with an externally applied force. This new method for a desalination process based on inexpensive hydrogels as the separation agent, is of great interest due to the rising scarcity of potable water. The shortage of freshwater is already a problem in many parts of the world and will increase further in future due to population growth, increasing standards of living and climate change.

The desalination of brackish- or seawater offers one solution to supply enough water with a suitable quality. Thus, the further development of existing or new desalination methods is of general interest.

In all the described applications, the superabsorbent polymers are usually produced via the simultaneous free radical copolymerization of the monomer and crosslinker due to the simplicity of the synthesis. However, the resulting network exhibits a broad pore size distribution leading to an undefined product as the crosslinks are randomly placed [Lorenzo13]. While the average mesh length in such networks can be adjusted, the control over the topology itself is poor. More sophisticated network architectures are accessible using more elaborated synthetic routes and the right strategy.

The purpose of the present thesis is the synthesis of a broad range of network structures (see Figure 1.1) with the aim to test these hydrogels in the membrane-free desalination process. The following driving questions shall be answered: How can the different topologies be synthesized? How are the macroscopic properties of the hydrogel influenced by the network architecture? Which characterization techniques are able to map the topological structure of the hydrogels? How does the network structure influences the salt separation and the performance in the membrane-free desalination process?

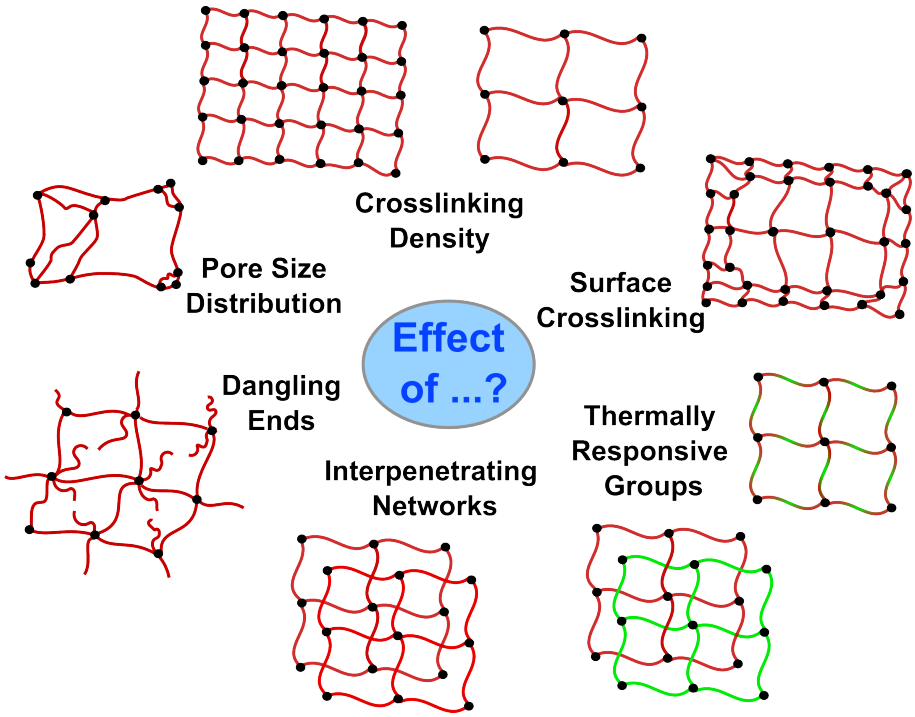


**Figure 1.1:** Several polyelectrolyte network architectures are synthesized in the present thesis. Their influence on the hydrogel properties is investigated with a special focus on the membrane-free desalination.

Several steps are necessary to answer these questions, which include the synthesis, characterization and the testing of the polyelectrolyte hydrogels. This thesis is structured in the following order:

In Chapter 2, the rising scarcity of potable water and the importance of seawater desalination is discussed. An overview of the commercially established methods and the current challenges thereof are provided. Then, the membrane-free desalination via polyelectrolyte hydrogels is introduced and the main results of previous work are summarized to define the starting point of the present thesis.

In Chapter 3, theoretical models for charged polymer networks are described. The challenges that arise are discussed including why it is so difficult to model these systems. Furthermore, it is shown how molecular parameters affect the macroscopic properties.

In Chapter 4, the synthesis of the diverse network topologies is explained, starting from simple randomly crosslinked hydrogels as a reference system to more complex topologies. It is shown how the different architectures can be achieved and which synthetic parameters are varied. While most hydrogels are produced by free radical polymerization, the more sophisticated anionic polymerization method is utilized to obtain networks with a defined mesh size distribution. In addition to the pure polyelectrolyte networks, which are made of either poly(sodium acrylate) (PSA) or poly(sodium methacrylate) (PSMA), thermally responsive N-isopropylacrylamide (NIPAAm) groups are incorporated into the network. The addition of this monomer allows the hydrogels to be compressed by temperature instead of pressure.

The synthesized networks are characterized in Chapter 5. After a short introduction of the theory behind the applied methods, it is discussed how the synthetic parameters influence the macroscopic quantities. The absorbency and mechanical strength of the hydrogels are studied, as these are the most critical performance properties for most applications. Furthermore, techniques like SAXS and NMR-relaxometry are employed to gain information about the network structure itself.

In Chapter 6, the hydrogels are applied in the membrane-free method for saltwater desalination. It is demonstrated how the different networks influence the desalination performance and how the energy demand for this new technique can be estimated. This allows for a coarse comparison with commercially established methods and shows the necessary steps to bring the process closer to a commercial realization.

In Chapter 7, the desalination method is reversed. A cyclic swelling of the hydrogels in salt-free water followed by shrinking in highly concentrated salt solutions is used to recover energy from salt gradients in an osmotic engine.

The concluding Chapter 8 presents a summary of the main findings of this thesis and an outlook to the future, where further possible developments are discussed to improve the desalination process and the energy output in the osmotic engine.

# 2 Seawater desalination

This chapter contains some general remarks about the water stress situation in the world and the rising importance of seawater desalination as part of the solution. The desalination techniques most often used and their commercial relevance are briefly explained. At the end of the chapter, the membrane-free desalination process via polyelectrolyte hydrogels is introduced. The main findings of previous work are summarized and put into context of this thesis.

## 2.1 Numbers and figures

Water covers about 70% of the Earth's surface, but only a small fraction of it has potable quality. More than 97% of the global water is seawater and 80% from the remaining water is bond as snow in permanent glaciers. This means only 0.5% of the total water is available for direct use. As this remaining water is unequally distributed, many regions already suffer of a high water stress nowadays. This situation will become even worse in future since the demand for freshwater will rise due to population growth, increasing standard of living and climate change. Forecasts predict that over 4 billion people could suffer under water stress by 2050 [Kucera14].

To tackle the challenge of the scarcity of potable water, methods like conversation, reuse, desalination and transport of water are already in use and will rise in their importance. The desalination of seawater (besides brackish or wastewater) may play the most important role, as most regions, where water stress is present, are located near the coast.

The phenomenon of desalination was already described more than 2,300 years ago by Aristotle who observed that "saltwater becomes sweet when it turns into vapor and the vapor does not form saltwater when it condenses again" [Aristotle52]. The first practical use of desalination is probably the shipboard distillation in the 16th century [Kucera14]. Since the development of the first semi-permeable membranes for reverse osmosis in the late 1950s by Sidney Loeb [Loeb64], the research and the use of water desalination is constantly rising. The global desalination capacity is continuously growing since 1950, as illustrated in Figure 2.1, left.

In 2015, over 18,000 desalination plants were in operation that produced about 90 million cubic meter fresh water per day to supply over 300 million people in 150 countries [IDA15]. Nowadays, already more than 1% of the total consumed water was prior desalinated, with a

typical growth rate of 7 – 9% per year. Desalination is particularly for dry and warm regions like Middle East, Spain and California of immense importance (see Figure 2.1, right). In future, desalination will be also more present in Asia and Africa due to the growing population and this billion dollar market will increase further [Kucera14].

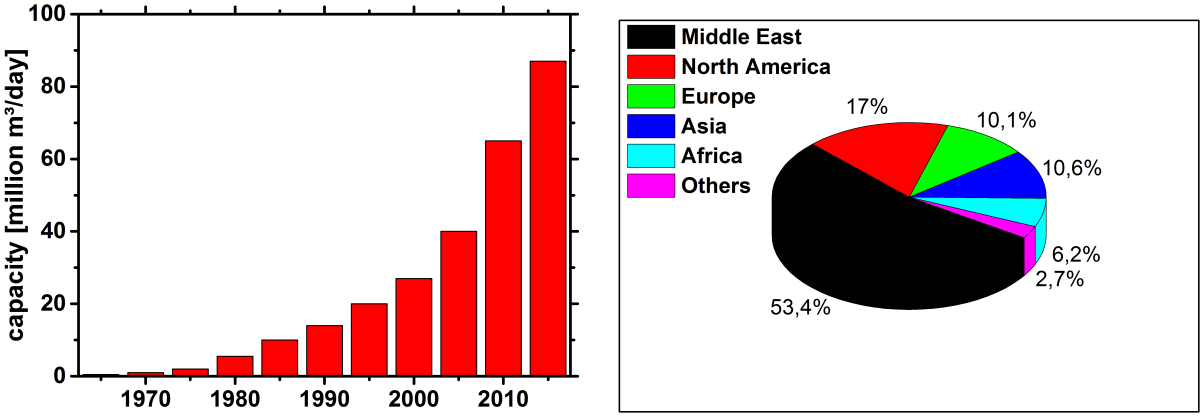


**Figure 2.1:** Left) The worldwide desalination capacity illustrates the increasing importance to produce potable water. Right) Regions with the highest capacity in 2015: Middle East (mainly Saudi Arabia & United Arab Emirates), North America (mainly U.S.) and Europe (mainly Spain) [IDA15].

## 2.2 Methods

A large variety of desalination methods exists and a lot of research is currently focusing on the further development of new or already established techniques. It is not straightforward to generally answer which method is the best, since every method has its advantages and drawbacks. Which technique is suitable depends on investment costs, space constraints, needed water productivity, energy costs, feedwater and produced water quality, which can be very diverse. The market share of the commercialized desalination technologies is summarized in Figure 2.2. Reverse osmosis (RO) is with about 63% the most often applied method. This membrane-based technique leads the market ahead of thermal processes like multiple-effect distillation (MED) and multi-stage flash distillation (MSF), which are still preferably used in the Middle East, where the energy costs are lower [Kucera14].

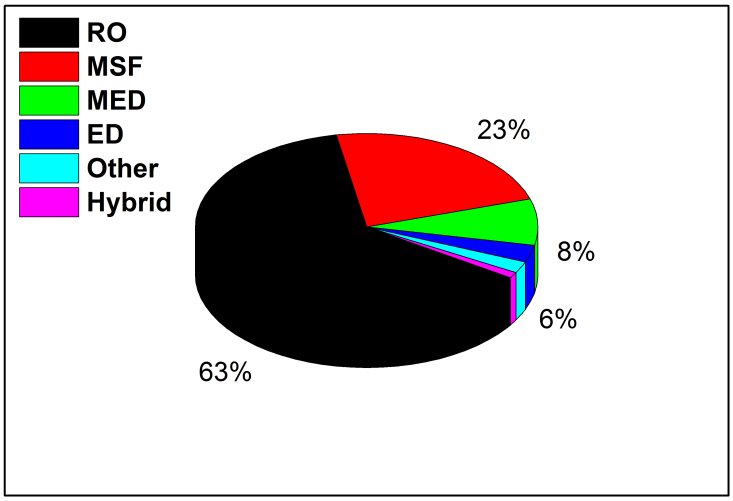


**Figure 2.2:** The global installed desalination capacity by technology in 2011 shows that meanwhile reverse osmosis (RO) is the most important technology and has replaced the two thermal methods, multi-stage flash (MSF) and multiple-effect distillation (MED), as the market leader. Electro-dialysis (ED), hybrid systems and other technologies hold only a small part of the market share [Kucera14].

Nowadays, ongoing research in the desalination sector mainly focuses on the following issues [Kucera14]:

- Reduction of investment and permanent costs
- Increasing of energy efficiency
- Use of renewable energy sources
- Improvement of materials with more resistance and longer durability
- Use of new chemicals as antiscalants
- Reduction of carbon footprint
- Disposal of concentrated brine

The desalination techniques are historically divided in thermal, membrane and other processes. The most important techniques are briefly described in the next sections.

### 2.2.1 Thermal processes

The thermal distillation of saltwater, which boils the water and collects the steam, is the oldest known method for desalination [Aristotle52]. However, a simple evaporation by distillation of saltwater is too expensive on a large scale since the phase transition requires significant amounts of energy (*e. g.* $E_{m^3} \approx 717\,\mathrm{kWh/m^3}$ to boil water with an initial temperature of 20 °C). Therefore,

several techniques exist to reduce the energy demand. An additional preheating of the feedwater by the recovery of condensation heat, vacuum chambers to lower the evaporation temperature and multiple-effects for the evaporation are commonly applied methods [Kucera14].

MSF was historically the most important desalination technique with a market share of 78% in 1999 [Kucera14]. However, in recent years the thermal processes are gradually substituted by RO (see Figure 2.2). Nowadays, MSF and the other major thermal desalination technique MED are only economical in the Middle East, where the energy costs are low and high amounts of desalinated water are needed [Mezher11].

Both methods become more energy efficient with more involved stages. This also increases the investment costs, though. Hence, these techniques are usually only used in very large desalination plants. The largest modules can have a capacity of 75,000 $m^3$/day and 45,000 $m^3$/day for MSF and MED, respectively [Khawaji08]. The market share of MED is smaller than MSF (see Figure 2.2), but the number of MED plants is rising faster [Kucera14]. The MSF process is generally less energy efficient, but has lower investment costs and a lower tendency to scaling (crystallization of solid salts, such as $CaCO_3$ or $CaSO_4$) [Khawaji08, Mezher11].

#### Multi-stage flash distillation (MSF)

The MSF process is based on the evaporation and condensing of saline water, where the effect is used that water instantly boils (flashes) when the pressure is rapidly reduced. A typical plant consists of a series of stages, containing a heat exchanger and a condensate collector. In a first step, the saline feedwater is passed through tubes in the several stages to preheat the water before it reaches its final operating temperature in the brine heater. The heated water flows in a chamber or stage, where the pressure is reduced by a valve. A fraction of the water flashes and the formed vapor condenses on the tubes that carry the input saline water. The distillate is collected and the remaining water is brought to the next stage with an even lower pressure [Mezher11]. This process is typically continued for 19 – 28 stages, since only a small percentage of the heated water is converted into vapor at each stage [Khawaji08].

#### Multiple-effect distillation (MED)

The MED process uses the same principle as the MSF, the evaporation and condensation at reduced pressure. This takes place in a series of closed vessels, which are called effects [Mezher11]. The serial arrangement improves the energy efficiency, but not the water quality since potable water can be produced in one stage [Kucera14]. The saline feedwater undergoes multiple boiling without supplying additional heat after the first effect. The seawater is heated by steam in each stage in tubes, usually by spraying the saline water onto them. Some water

evaporates and the vapor of the first effect is then condensed to freshwater product, while transferring heat to the second effect, which is used to evaporate again a new portion of the saline feedwater. This process of evaporation and condensation is repeated several times (usually 4 to 21 effects), while each stage uses successively a lower pressure and temperature [Khawaji08].

### 2.2.2 Membrane processes

In the late 1950s, Sidney Loeb invented the first semi-permeable membrane for desalination applications [Loeb64]. While RO has become the most important technique to desalinate water in the last decade (see Figure 2.2) [Kucera14], several publications from recent years also focus on other membrane-based desalination processes, like forward osmosis (FO). The big advantages of membrane-based processes are the lower energy consumption, the smaller infrastructure and the simplicity of the process, combined with less corrosion of the material since only ambient temperatures are employed [Khawaji08, Kucera14].

In the next sections, the principle of osmosis is briefly explained, followed by the introduction of RO and presenting some newer research about FO.

#### Osmotic pressure

If two solutions with a different salinity are separated by a semi-permeable membrane, more water molecules will flow from the side with the lower salt concentration to the side with the higher salt concentration as *vice versa*. This phenomenon is well known as osmosis and the driving force is the difference of the chemical potential.

The osmotic pressure $\Pi$ is defined as the pressure difference between both sides of the membrane, as displayed in Figure 2.3. For diluted solutions, the osmotic pressure can be described by the van't Hoff equation [Hoff87]:

$$\Pi = \frac{n}{V_\mathrm{m}} * iRT\,, \tag{2.1}$$

where $n$ are the moles of dissolved molecules (*e. g.* NaCl), $V_\mathrm{m}$ is the volume of solvent, $R$ is the universal gas constant, $T$ is the absolute temperature, and $i$ is the van't Hoff factor (*e. g.* $i = 2$ for NaCl). As a consequence of Equation 2.1, the osmotic pressure $\Pi$ increases linearly with an increasing salt concentration (*e. g.* $\Pi(35\,\mathrm{g/L\ NaCl}) \approx 29\,\mathrm{bar}$).

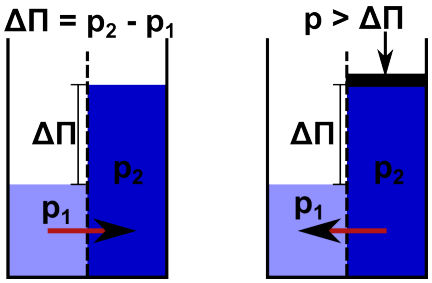


**Figure 2.3:** Principle of osmosis: Left) Forward osmosis. Right) Reverse osmosis.

#### Reverse osmosis (RO)

In the RO process, the saline feedwater is pumped in a closed vessel, where it is pressurized against a semi-permeable membrane (pore size: $< 1$ nm). The osmotic pressure of the saline feedwater is overcome (see Figure 2.3, right) and pure water permeates through the membrane, whereas the brine left behind is discharged [Mezher11].

A modern RO plant usually includes the following systems [Khawaji08]:

- Pretreatment (*e. g.* chlorination) to prevent membrane fouling
- High-pressure pumps (typical range 50 – 80 bar)
- High-performance membranes (*e. g.* a spiral wound polyamide fiber)
- Posttreatment (*e. g.* pH adjusting)
- Energy recovery systems and pressure exchangers

The energy recovery systems have led to a strong improvement of the energy efficiency (3 – 6 kWh/m³), which is already close to the theoretical limit of 0.7 – 1 kWh/m³ [Wade01, Elimelech11]. As a consequence, RO is especially popular in Europe and the U.S. and has replaced MSF as the market leader.

Disadvantages of the process are the high costs of the membrane and the need for their regular replacement due to biofouling and clogging, which is particularly a problem if the feedwater has a high salinity and marine life [Avlonitis03]. These costs contribute up to 15.5% of the total cost per cubic meter freshwater [Avlonitis02].

The life of the membrane is usually extended by pretreatment, which is however related to higher costs and more complex setups. Furthermore, a failure in one point of the membrane makes the module unusable and it has to be replaced immediately.

#### Forward osmosis (FO)

The FO process is a membrane-based desalination method that deploys the principle of direct osmosis (see Figure 2.3). This technique employs a drawing agent with a higher osmotic

potential than the saline feedwater to draw water to the filtrate side of the membrane. After the drawing agent, which usually consists of thermally removable salts (*e. g.* $(NH_4)_2CO_3$), is separated from the water and regenerated, potable water is recovered [Cath06, Cai13].

As an advantage, FO operates at low or no hydraulic pressure, which decreases the tendency to biofouling [Cath06]. In the past, much less research was conducted compared to RO and only a few pilot plants exist. Nevertheless, there is an increasing attention to FO in recent years and the fundamental research is growing. In the perspective of this thesis, it is interesting that an increasing number of publications deal with FO, where hydrogels are used as drawing agent, which are regenerated (deswollen) by pressure or temperature [Li11, Li13a, Li13b, Cai13, Razmjou13, Cai16]. Even though, these examples still use a semi-permeable membrane for the separation instead of the hydrogel itself, the principle is similar to the desalination technique focused in this thesis.

### 2.2.3 Other desalination processes and supporting technologies

Several other techniques exist to desalinate saltwater, which have not achieved the level of commercial success like MSF, MED and RO. However, under special circumstances and with further improvements, these methods could become more important in future [Khawaji08]. For the sake of completeness, the most ambitious techniques are very briefly explained:

**Electro-dialysis** uses electrical energy to selectively move salt ions through an ion-exchange membrane, leaving freshwater behind. This technique is commercially used for brackish water desalination and profits from a reduced tendency to biofouling [Mezher11].

**Vapor compression distillation** is another thermal process, where the heat for the saline water evaporation comes from the compression of vapor. Smaller plants with capacities below 3,000 $m^3$/day already exist [Khawaji08].

**Solar evaporation** mimics part of the natural hydrological cycle, in which seawater is heated by sunbeams to produce potable water. A disadvantage is that very large solar collection areas are needed, which are related with high capital costs [Khawaji08].

**Freezing** uses the effect that dissolved salt is excluded during the formation of ice crystals. Even though, the theoretical energy consumption is very low and a few pilot plants exist for several decades, the process has not been successfully commercialized [Khawaji08].

Other supporting technologies are regularly used in pretreatment systems, especially for membrane-based processes. They include but are not limited to the following methods [Mezher11]:

**Microfiltration** reduces the turbidity and removes suspended solids and bacteria via a sieving mechanism under a low pressure (pore size: $> 0.1\,\mu m$).

**Ultrafiltration** removes contaminates that effect the color, such as dissolved organic compounds, bacteria and some viruses (pore size: $2 - 100\,\text{nm}$).
**Nanofiltration** softens the water and removes organics, sulfates and viruses (pore size: $1 - 2\,\text{nm}$).
**Ion exchangers** remove undesirable ions in water (mainly $Mg^{2+}$ and $Ca^{2+}$).

### 2.2.4 Desalination using polyelectrolyte hydrogels as the separation agent

One aim of the present thesis is the further investigation of the new desalination technique via polyelectrolyte hydrogels, which was introduced by Höpfner *et al.* in 2010 [Höpfner10]. This method can be understood as a membrane-free forward osmosis process, in which the polyelectrolyte hydrogels act as both, the drawing and the separation agent, simultaneously. The principle of the separation process is based on the charges along the polymer chains in the polyelectrolyte network [Höpfner13b]. These charges lead to an extensive osmotic potential of the hydrogels, which causes them to absorb tremendous amounts of water (several hundred times their own weight in case of deionized water) [Buchholz98]. Therefore, these polyelectrolyte hydrogels, which are usually made of crosslinked poly(acrylic acid), are often referred to as superabsorbers [Elliott04].

If a charged but dry polyelectrolyte is placed in a brine solution, the hydrogel will swell and the charges inside the polymer will interact with the dissolved ions. Water molecules enter the polymer first, while the mobile salt ions from the solution are electrically shielded by the fixed charges of the network. The mobile ions are partly rejected by the network and remain mainly in the supernatant phase, as displayed in Figure 2.4, left [Höpfner13a]. This separation effect can be described in terms of the Donnan membrane equilibrium [Donnan32, Flory53, Katchalsky55] and was successfully applied to desalinate saltwater in a three step process [Höpfner10, Höpfner13b].

The basic idea of this three step process, in which the superabsorbent material is used as a reusable salt separation agent, is schematically displayed in Figure 2.4, right. The dry polymer particles are first mixed with the saline feedwater to swell the polyelectrolyte (1). In the second step, the supernatant phase with the enriched salt concentration is removed (2). Next, an external pressure is applied to deswell the gel and to recover water with a decreased salinity as the third step (3). Afterward, the gel particles can be reused in a new cycle by adding again saline feedwater.

In order to see the *status quo* of this new desalination technique and to define the starting point of the present thesis, the main results of Höpfner *et al.* shall be briefly summarized here [Höpfner10, Höpfner13a, Höpfner13b]:

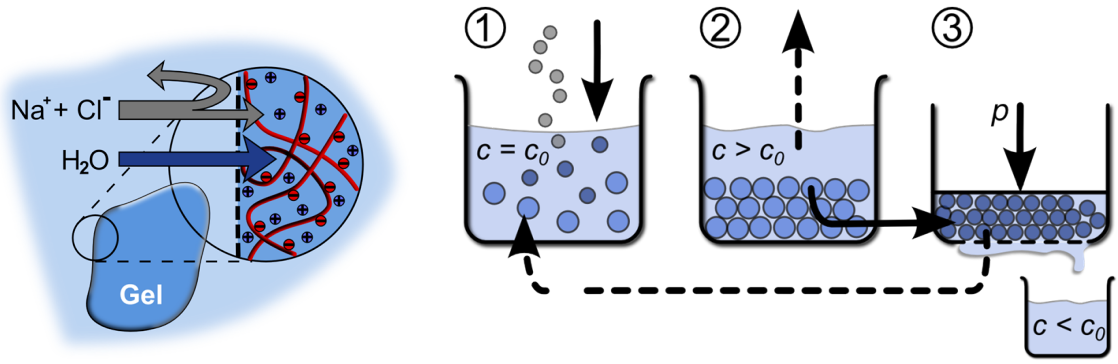


**Figure 2.4:** Left) The principle of the desalination process via charged hydrogels is based on the partial repulsion of mobile ions by the polyelectrolyte network. Right) The implementation of this effect to reduce the salinity in a three step process. Figures are adapted from [Höpfner13b]. See text for a detailed explanation.

In previous work, the proof of principle for the desalination method was demonstrated with chemically crosslinked hydrogels based on partially neutralized poly(acrylic acid). In addition to commercial samples, polyelectrolytes were synthesized by free radical polymerization, in which the degree of crosslinking (*DC*) and the degree of neutralization (*DN*) were systemically varied in the range of $DC = 0.05 - 5\,\text{mol\%}$ and $DN = 0 - 95\,\text{mol\%}$. The main finding was that high values of *DC* and *DN* result in an increased charge density, which favors the salt separation, as qualitatively desrcibed by the Donnan theory [Donnan32, Katchalsky55].

The deswelling of the gel under pressure was investigated in a self-constructed setup to study the desalination process. The press apparatus is also utilized in this thesis and is described in detail in Appendix A.3.1. The deswelling experiments were conducted with various hydrogels and different process parameters, such as applied pressure profile and initial NaCl concentration. The process works in the whole typical range from seawater to freshwater (0.1 – 35 wt% NaCl) and values for the specific energy, which is the energy needed to get one cubic meter freshwater, were estimated to $20 - 80\,\text{kWh/m}^3$. In these estimations, hydrogels with a higher *DC* have an increased energy efficiency.

During the preparation of the present thesis, a few publications outside this group were dealing with similar ideas to desalinate saltwater via polyelectrolyte hydrogels in a membrane-free process.

Fan *et al.* investigated poly(sodium acrylate), poly(2-hydroxyethyl methacrylate) and the respective copolymer hydrogels in 35 g/L NaCl solutions under externally applied pressure. They were able to reduce the salinity with all polymers, but found an enhanced salt rejection when sodium acrylate was incorporated into the hydrogel [Yu16].

In cooperation with the group of Christian Holm, coarse-grained hydrogels were simulated in salt solutions using a modified Katchalsky model to investigate the salt partitioning. Desalination cycles, qualitatively similar to the here applied experiments, were studied and the energy costs were estimated to 1.5 – 3 kWh/m³, which is close to the theoretical limit of 0.7 – 1 kWh/m³. In these idealized simulations, either highly charged hydrogels with a high *DC* and *DN* or very soft hydrogels with a low *DC* and *DN* performed best [Richter17a, Richter17b].

An extension of the proposed technique, where the hydrogels were always investigated under externally applied force, was introduced by Ali *et al.* [Ali15]. They incorporated thermally responsive N-isopropylacrylamide (NIPAAm) groups in a poly(acrylic acid) network. In this way, the partially desalinated water inside the hydrogel could be recovered by applying a temperature of 50 °C instead of pressure as an external stimulus. This approach is an interesting alternative, since most countries, in which desalinated water is needed, are in rather warm regions located (see Figure 2.1, right, in Section 2.1).

## 2.3 Summary

The scarcity of potable water is a rising problem all over the world. By 2050, over 4 billion people could suffer under water stress. The desalination of seawater is part of the solution to tackle this challenge.

Nowadays, reverse osmosis (RO) is the most important desalination technique and leads the market far ahead thermal processes. Even though, RO is a very energy efficient technology, some drawbacks still exist. The high-performance membranes are expensive and need a regular cleaning or replacement due to deterioration, clogging and other blocking phenomena like biofouling and scaling, which cannot be totally avoided, even if effective pretreatment of feedwater is conducted.

A new method to desalinate saltwater is based on inexpensive, polyelectrolyte hydrogels that are used in a membrane-free forward osmosis process, as schematically shown in Figure 2.4. Previous work demonstrated the proof of principle for this concept with commercial and self-synthesized poly(acrylic acid). While in that work, the degree of crosslinking was varied as the main synthetic parameter, no attempts were made to optimize *i. a.* the network topology for the best desalination efficiency.

In the next chapter, the network structure of polyelectrolyte networks is mathematically described. Theoretical models are introduced to depict the structure-property relationship of charged hydrogels.

# 3 Theoretical description of polyelectrolyte hydrogels

Polymer networks consist of crosslinked macromolecules and show fundamentally different behaviors than linear or branched polymer chains. Networks swell rather than dissolve, have a large deformation elasticity (rubberlike material) and exhibit both, solid- and liquidlike behavior [Mark07].

In case of polyelectrolyte hydrogels, the polymer chains carry many charges and the three-dimensional network is swollen either in water or aqueous (salt) solutions. The ionic nature of the polymer network leads to a set of unique properties for this class of materials. Especially the ability to absorb large amounts of water of several hundred times of their own weight makes hydrogels an interesting product for a large variety of applications (see Chapter 1) [Buchholz98].

The swelling behavior depends on the ionic strength of the aqueous solution and on the valency of the low molecular weight counterions. Other crosslinked polymer networks like rubbers were extensively studied in early work and can be quite well modeled by the classical theory of rubber elasticity [Flory53]. In contrast, the modeling of polyelectrolyte hydrogels is much more complicated due to several reasons [Oppermann92]: First, the polyelectrolyte effects (*e. g.* electrostatic repulsion, shielded electric potential) are dominant and hard to model itself. Second, water is a difficult solvent since it has large-range coulombic interactions as well as short-range interactions such as hydrogen bonds. Third, no synthetic methods are established yet to obtain defect-free model-networks (see also Section 4.3).

In this chapter, the basic concepts for a theoretical description of networks are introduced. The most important terms for swollen polyelectrolyte hydrogels are individually discussed and then compared. At the end, the macroscopic water uptake is explained by molecular parameters.

## 3.1 Structural characteristics of polymer networks

The most important structural characteristics of an ideal network are described in this section. A polymer network consists of elastic chains that form the meshes, which are fixed on both sides in junctions or crosslinking points to build a three dimensional structure. In the ideal network, all meshes have the same length and the same crosslinking functionality $f$, which is the number of elastic chains per junction. This leads to a homogeneous structure throughout the whole network with a uniform pore size (Figure 3.1, left).

However, such perfect networks can never be synthetically obtained and any real network will contain defects, such as dangling ends, cyclic loop formations and entanglements (see Figure 3.1, right). Additionally, when the network is formed by free radical polymerization, the statistics of the crosslinking process lead to a length distribution for the elastic network chains, resulting in a broad pore size distribution and regions in which the polymer concentration is permanently higher (see Section 4.3) [Mark07].

For a mathematical description of an ideal network, the extent of crosslinking has to be defined, which can be expressed either by the concentration of elastically active chains $\frac{\nu_{el}}{V_0}$, or by the crosslinking density $\frac{\mu_{el}}{V_0}$. Here, $\nu_{el}$ describes the number of elastic chains, *i. e.* the number of chains connecting two crosslinking points, $\mu_{el}$ is the number of crosslinks and $V_0$ is the volume of the dry network.

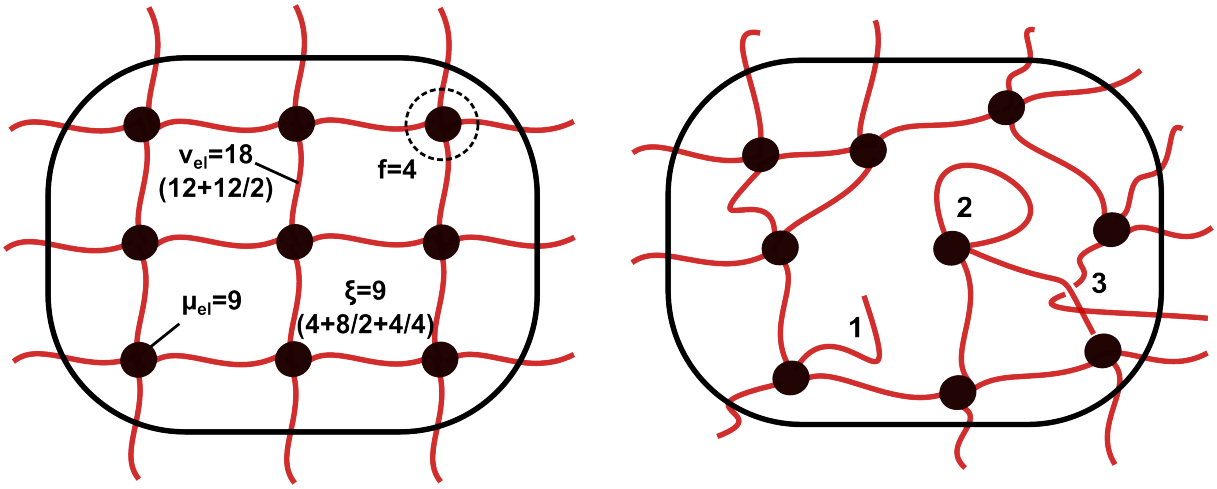


**Figure 3.1:** Left) An ideal network is displayed to clarify the quantities: number of crosslinks $\mu_{el}$, number of elastic chains $\nu_{el}$, cycle rank $\xi$ and crosslinking functionality $f$. Right) A real (model) network with typical defects such as dangling ends (1), cyclic loops (2) and intermolecular (network) entanglements (3).

The number of elastic chains $\nu_{el}$ and the number of crosslinks $\mu_{el}$ define the cycle rank $\xi$, which is the number of independent circuits in a network (see Figure 3.1, left) [Flory76]:

$$\xi = \nu_{el} - \mu_{el}\,, \tag{3.1}$$

where $\nu_{el}$ and $\mu_{el}$ are linked by the crosslinking functionality $f$ [Graessley75]:

$$\mu_{el} = \frac{2}{f}\nu_{el}\,. \tag{3.2}$$

Substitution of the number of elastic chains by the (average) molecular weight of the polymer chains between the crosslinking points,

$$M_c = \rho\frac{V_0 N_A}{\nu_{el}}\,, \tag{3.3}$$

yields in a relationship between crosslinking functionality, elastic chain length and cycle rank [Flory76, Mark07]:

$$\xi = \nu_{el}\left(1 - \frac{2}{f}\right) = \frac{\rho V_0 N_A}{M_c}\left(1 - \frac{2}{f}\right)\,, \tag{3.4}$$

where $N_A$ is the Avogadro number, $\rho$ the gel density and $V_0$ the corresponding gel volume.

## 3.2 Description of polyelectrolyte hydrogels

Hydrogels are usually investigated, when they are swollen in aqueous solutions. At the swelling equilibrium, the Gibbs free energy between gel (phase I) and the surrounding solution (phase II) reaches its minimum.

$$\Delta G = G_I + G_{II} = 0 \tag{3.5}$$

The three factors that contribute to the swelling behavior are the free energy of mixing $\Delta G_{mix}$, which describes the mixing of solvent and network, the elastic free energy $\Delta G_{el}$, which describes the network elasticity, and the electrostatic free energy $\Delta G_{ion}$, which considers the mixing of charges with the solvent. To tackle this three contributions, they can be separated and individually described in a first approximation [Flory43, Hooper90, Yin92]:

$$\Delta G = \Delta G_{mix} + \Delta G_{el} + \Delta G_{ion} = 0\,. \tag{3.6}$$

Instead of the free energy $\Delta G$, the correlated intrinsic quantity in form of the chemical potential $\mu_\mathrm{I}$ of the solvent in the gel phase can be used:

$$\Delta\mu_\mathrm{I} = \Delta\mu_\mathrm{I,mix} + \Delta\mu_\mathrm{I,el} + \Delta\mu_\mathrm{I,ion} = 0\,, \tag{3.7}$$

where the chemical potential $\mu_\mathrm{I}$ is the partial derivative of the free energy with respect to the amount of solvent molecules $n_1$ at a certain temperature $T$ and pressure $p$:

$$\Delta\mu_\mathrm{I} = \left(\frac{\partial\Delta G}{\partial n_1}\right)_{\mathrm{T,\,p}}\,. \tag{3.8}$$

The individual terms of the chemical potential and their calculation from microscopic quantities are successively discussed in the next sections. While the mixing and the electrostatic contributions seek for a maximum dilution of the polyelectrolyte, the elastic term of the network prevents to reach this highly strained state. At equilibrium, the individual potentials are in balance and can be used to predict macroscopic quantities such as mechanical moduli and degrees of swelling.

### 3.2.1 The mixing term, $\Delta\mu_\mathrm{I,mix}$

The mixing of a polymer in a solution is generally described by the Flory-Huggins theory [Flory53, Treloar75]. Even though, this theory was initially developed for non-crosslinked systems, it is also regularly applied to describe crosslinked networks [Schröder96]. The resulting energy of mixing $\Delta G_\mathrm{mix}$ is given by

$$\Delta G_\mathrm{mix} = \Delta H_\mathrm{mix} - T\Delta S_\mathrm{mix} = k_\mathrm{B}T\left(n_1\ln\phi_1 + n_2 ln\phi_2 + \chi n_1\phi_2\right)\,, \tag{3.9}$$

where $H_\mathrm{mix}$ is the enthalpy of mixing, $S_\mathrm{mix}$ is the entropy of mixing, $T$ is the absolute temperature, $k_\mathrm{B}$ is the Boltzmann constant, $n$ is the number of moles, $\chi$ is the Flory-Huggins parameter and $\phi$ is the volume fraction of solvent (index 1) and polymer (index 2), respectively.

The derivation of the formula is based on the liquid-lattice model, where the solvent molecules and the polymer segments are randomly distributed on a lattice. The increase of the entropy $\Delta S_\mathrm{mix} = -k_B[n_1\ln\phi_1 + n_2\ln\phi_2]$ is of statistical nature since the number of possible conformations of a polymer chain increases when the system is diluted. The enthalpic term $\Delta H_\mathrm{mix} = k_\mathrm{B}T\chi n_1\phi_2$ reflects with the interaction parameter $\chi$ (energy normalized to $k_\mathrm{B}T$) the quality of the solvent. In a bad solvent that favors demixing, $\chi$ is larger than 0.5, whereas $\chi$ is smaller in a good solvent. The conversion of Equation 3.9 to the chemical potential by Equation 3.8 results in

$$\Delta\mu_\mathrm{mix} = RT\left(\ln(1-\phi_2) + \phi_2 + \chi\phi_2^2\right)\,. \tag{3.10}$$

The Flory-Huggins theory describes the contribution to the mixing energy in non-polar environments quite well, but does not reflect for example hydrogen-bond interactions which are present in polar systems [Mark07]. Additionally, the assumption that the free energy in the swollen network is the same as in a polymer solution is a strong approximation. Therefore, the applicability of Equation 3.10 for hydrogels is highly questionable.

More realistic models, which also consider hydrogen bonds and orientation dependent interactions have been successfully used [Prange89, Beltran90, Hooper90]. However, these models are mathematically much more complicated and contain three adjustable interaction parameters. As the degree of swelling in polyelectrolyte hydrogels is very large, the contribution of the mixing energy is usually quite small compared to the ionic term $\Delta\mu_{\mathrm{I,ion}}$. Therefore, the use of the less complicated Flory-Huggins equation is still reasonable [Schröder96].

### 3.2.2 The elastic term, $\Delta\mu_{\mathrm{I,el}}$

The basic concepts to describe the elastic contribution of polymer networks are derived from the classical theory of rubber elasticity, which is based on two assumptions [Flory53]:

(i) the elastic free energy of the network is the sum of the elastic free energies of elastic chains

(ii) the distribution of the end-to-end vectors $\vec{r}$ of the network chains is Gaussian,

$$P(\vec{r}) = \left(\frac{3}{2\pi < r^2 >_0}\right)^{3/2} * \exp\left(-\frac{3\vec{r}^2}{2 < r^2 >_0}\right), \tag{3.11}$$

where $< r^2 >_0$ is the mean value of the end-to-end distance.

The two most discussed models with these assumptions are the affine and the phantom model.

In the affine model, the position and the fluctuations of the crosslinking points is completely suppressed by intermolecular entanglements with neighboring elastic chains. A movement of a network junction is only possible when all neighboring chains are moving. The network can only transform affinely and the local deformations are the same as the macroscopically imposed ones [Mark07].

The elastic term of the free Gibbs energy of the affine model is given by [Flory76]:

$$\Delta G_{\mathrm{el}} = \left(\frac{\nu_{\mathrm{el}} k_{\mathrm{B}} T}{2V_0}\right)\left[\lambda_{\mathrm{x}}^2 + \lambda_{\mathrm{y}}^2 + \lambda_{\mathrm{z}}^2 - 3\right] - \left(\frac{\mu_{\mathrm{el}} k_{\mathrm{B}} T}{V_0}\right)\ln\left(\lambda_{\mathrm{x}}\lambda_{\mathrm{y}}\lambda_{\mathrm{z}}\right), \tag{3.12}$$

where $\lambda_i = \frac{l_i}{l_{i,0}}$ is the extension ratio of the deformed length $l_i$ normalized to the undeformed length $l_{i,0}$ in the three spatial directions ($i = x, y, z$).

In the phantom model, the elastic chains are allowed to move freely through their neighboring chains and crosslinking points fluctuate around their mean positions. During a deformation, only the mean position of the network junctions is affinely changing with the macroscopic deformation, while the fluctuations of the mean-position is completely uncorrelated [James47]. This results in the following expression for the elastic term of the free Gibbs energy:

$$\Delta G_{\mathrm{el}} = \left(\frac{\xi k_{\mathrm{B}} T}{2V_0}\right)\left[\lambda_{\mathrm{x}}^2 + \lambda_{\mathrm{y}}^2 + \lambda_{\mathrm{z}}^2 - 3\right] . \tag{3.13}$$

The two models show the limiting cases for the network properties, although they do not perfectly describe the behavior of real networks. In real networks, the fluctuations of junctions is in between those two extremes since the crosslinking points are connected to both, short meshes with a high affinity and longer elastic chains with no constraints. More advanced models, which also consider intermolecular (network) entanglements and other steric constraints, are *e. g.* the constrained junction model [Ronca75, Flory77] or the tube model [Edwards86, Gaylord90].

However, compared to rubber material, the degree of swelling is very large in polyelectrolyte hydrogels. Hence, the elastic chains are highly extended and the Gaussian statistics fail to describe the end-to-end distance of the chains properly [Schröder96]. More realistic equations are necessary which include non-Gaussian statistics. This is usually treated by the use of an inverse Langevin function $\mathcal{L}^{-1}$. The elastic term for the chemical potential is then given by

$$\Delta\mu_{\mathrm{I,el}}(\text{non-Gaussian}) = \frac{1}{3} A \nu^* R T V_1 q_{\mathrm{c}}^{-1} q_{\mathrm{r}}^{-2/3} n^{1/2} \mathcal{L}^{-1}\left(q_{\mathrm{r}}^{1/3} n^{-1/2}\right) . \tag{3.14}$$

In this equation, $q_{\mathrm{c}}$ is the degree of swelling during the crosslinking process and $q_{\mathrm{r}}$ the relative degree of swelling, which are both related by the total degree of swelling

$$q = q_{\mathrm{c}} * q_{\mathrm{r}} = \frac{1}{\phi_2} . \tag{3.15}$$

Furthermore, $A$ is a structure factor, $\nu^*$ is the number of elastic chains per unit dry volume, $V_1$ is the molar volume of the solvent and $n$ is the number of statistical segments per network chain. The structure factor A is equal to $(1 - \frac{2}{f})$ with the assumption of affine displacement of crosslinking points, which should be valid since swelling is isotropic. If the parameter $\nu^*$ is

expressed by $\nu^* = \frac{\nu_{el}}{V_0 * N_A} = \frac{\rho}{M_c}$, combining Equation 3.14 and 3.3 results in

$$\Delta\mu_{I,el}(\text{non-Gaussian}) = \left(1 - \frac{2}{f}\right) \frac{\rho}{3M_c} RTV_1 q_c^{-1} q_r^{-2/3} n^{1/2} \mathcal{L}^{-1}\left(q_r^{1/3} n^{-1/2}\right) . \tag{3.16}$$

While Equation 3.16 was successfully used to describe the elasticity at large deformations, two challenges arise: First, the inverse Langevin function must be solved numerically since it cannot be written in a closed form [Jedynak15]. An often used approximation from Cohen is given by [Cohen91]

$$\mathcal{L}^{-1}(y) = y\frac{3 - y^2}{1 - y^2} . \tag{3.17}$$

Second, the number of statistical segments per network chain $n$, which depends in addition to the elastic chain length also on the stiffness of the polymer backbone, is not straightforward to compute. Especially in polyelectrolytes, besides the Kuhn length, an additional term has to be included to consider the electrostatic persistence [Skolnick77]. While many approaches exist to solve this problem for linear polyelectrolytes in various differently concentrated (salt) solutions [Schmidt04], those approaches are usually only valid in a rather small regime or fail to describe the swelling characteristics in polyelectrolyte networks properly [Mann05].

Qualitatively, the number of segments per network chain increases with larger elastic chains. Quantitatively, $n$ can be experimentally obtained by swelling measurements [Oppermann92] and may be approximated by

$$n = \left(\frac{q}{q_c}\right)^{2/3} . \tag{3.18}$$

If $n$ approaches infinity, Equation 3.14 reduces to the Gaussian description [Oppermann92]:

$$\Delta\mu_{I,el}(\text{Gaussian}) = A\nu_{el} V_1 RT \phi_2^{1/3} q_c^{-2/3} \tag{3.19}$$

### 3.2.3 The electrostatic term, $\Delta\mu_{I,ion}$

The electrostatic term includes all charged species and has to consider that the concentration of mobile salt ions inside the gel $c_s(g)$ and outside the gel $c_s(l)$ is not identical [Donnan32, Katchalsky55]. If concentrations are used instead of activities by applying the approximation of diluted solutions, the chemical potential can be expressed by [Ricka84, Brannon-Peppas90]

$$\Delta\mu_{I,ion} = -RTV_1 \left[\sum c_i(g) - c_i(l)\right] . \tag{3.20}$$

The difference of mobile ion concentrations is caused by the fixed charges on the polymer, which require an equivalent number of counterions in the gel phase to achieve electro-neutrality.

If the sodium salt of poly(acrylic acid) is considered in an aqueous NaCl solution (1-1 electrolyte), the equilibrium conditions read

$$c_{Na^+}(l) * c_{Cl^-}(l) = c_{Na^+}(g) * c_{Cl^-}(g)\,. \tag{3.21}$$

The ion concentration outside the gel is

$$c_{Na^+}(l) = c_{Cl^-}(l) = c_s\,, \tag{3.22}$$

whereas the sodium ion concentration inside the network is given by

$$c_{Na^+}(g) = c_{Cl^-}(g) + \frac{\rho\phi_2}{M_2}\,, \tag{3.23}$$

where $\rho$ is the density of the dry polymer, $M_2$ is the molar mass of polymer per free counterion and $\phi_2$ is the volume fraction of the polymer in the gel.

This equation allows that additional ions diffuse inside the gel. Additionally, the $\frac{\rho\phi_2}{M_2}$ charges on the polymer chain are regarded and electro-neutrality is established. It should be noted that $M_2$ has not to be the molecular weight of a monomer since a complete dissociation of the polyelectrolyte is usually not possible due to a too high charge density. Once the reduced charge density $\zeta$ exceeds a certain threshold value (=1 for monovalent ions), the counterions are bound to the polyelectrolyte by the so-called Manning or counterion condensation [Manning69, Manning78].

$$\zeta = \frac{e_0^2}{4\pi\epsilon_r\epsilon_0 k_B T b}\,, \tag{3.24}$$

where $e$ is the elementary charge, $\epsilon_0$ is the dielectric constant, $\epsilon_r$ is the relative dielectric constant and $b$ is the effective charge density (also called Bjerrum length). As a result of the Manning condensation, counterions are bound to the polyelectrolyte to increase the effective charge spacing to $b = 7$ Å (in case of monovalent ions) resulting in larger values for $M_2$.

The salt concentration in the surrounding solution $c_s$ at equilibrium conditions is obtained by putting Equation 3.22 and 3.23 into Equation 3.21, which yields

$$c_s^2 = \left(c_{Cl^-}(g) + \frac{\rho\phi_2}{M_2}\right) * c_{Cl^-}(g)\,. \tag{3.25}$$

Combined with Equation 3.20, the dependency of the chemical potential from the external salt concentration (under the assumption of an infinite large salt bath) is described by

$$\Delta\mu_{\mathrm{I,ion}} = 2RTV_1 \left[ c_\mathrm{s} - \sqrt{c_\mathrm{s}^2 + (\frac{\rho\phi_2}{2M_2})^2} \right] . \tag{3.26}$$

### 3.2.4 Comparison of the individual terms to the chemical potential

To visualize the contributions of the individual terms to the total chemical potential (see Equation 3.27), they are plotted as a function of the polymer concentration $\phi_2$ in Figure 3.2.

$$\begin{aligned} \Delta\mu_\mathrm{I} = {} & RT \left( \ln(1-\phi_2) + \phi_2 + \chi\phi_2^2 \right) + \\ & + \left( 1 - \frac{2}{f} \right) \frac{\rho}{3M_\mathrm{c}} RTV_1 q_\mathrm{c}^{-1} q_\mathrm{r}^{-2/3} n^{1/2} L^{-1} \left( q_\mathrm{r}^{1/3} n^{-1/2} \right) + \\ & + 2RTV_1 \left[ c_\mathrm{s} - \sqrt{c_\mathrm{s}^2 + (\frac{\rho\phi_2}{2M_2})^2} \right] . \end{aligned} \tag{3.27}$$

The parameters were chosen to be suitable for a typical poly(acrylic acid) hydrogel used in this thesis, which has a $DC$ of 1 mol% and a $DN$ of 75 mol%:

- $\rho = 1.22\,\mathrm{g/cm^3}$, the density of dry poly(acrylic acid) [Mark07].
- $M_2 = 1/0.75 * M(\mathrm{AA}) = 96\,\mathrm{g/mol}$, without consideration of any counterion condensation.
- $M_\mathrm{c} = 100 * M(\mathrm{AA}) = 7,200\,\mathrm{g/mol}$, as the average molecular weight between two crosslinks.
- $f = 4$, since MBA was used as crosslinking agent.
- $q_\mathrm{c} = 4$, as the polymer concentration during polymerization was 25 wt%.
- $\chi = 0.5$, with the assumption that water is a $\theta$-solvent.
- $c_\mathrm{s} = 0$, the gel is swollen in deionized water.
- $V_1 = 18\,\mathrm{cm^3/mol}$, as the molar volume of pure water.
- $n = 9$, as a typical value for the statistical segment length.

The plot of the different chemical potentials in Figure 3.2 reveals several aspects. First, the contribution of $\mu_{\mathrm{I,mix}}$ is indeed negligible for poly(acrylic acid), since $\mu_{\mathrm{I,ion}}$ is much larger at the relevant polymer concentrations ($q > 10$). Second, the Gaussian chain statistics fail to describe the elastic term properly, providing a much higher degree of swelling than experimentally determined. Third, the inverse Langevin function can describe the elastic term quite good to provide absorbencies very close to those measured in the experiment.

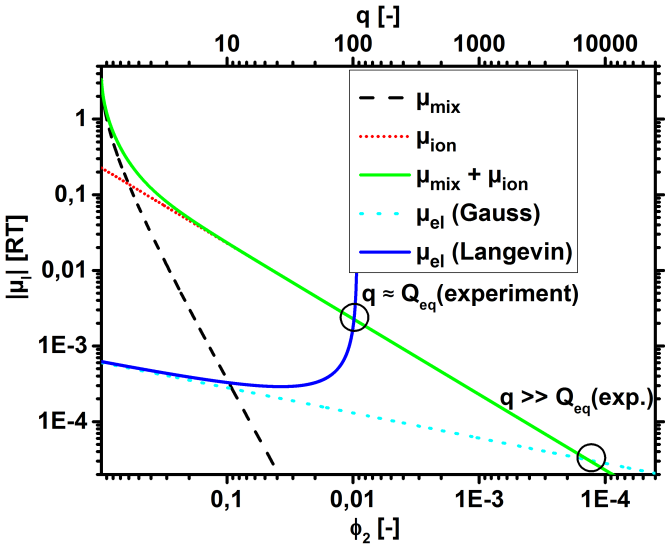


**Figure 3.2:** The individual contributions of the different chemical potentials ($\mu_{\mathrm{I,mix}}$, $\mu_{\mathrm{I,ion}}$, $\mu_{\mathrm{I,el}}$) are shown as a function of the polymer concentration $\phi_2$ (see Equation 3.27). The graph shows the importance to use an inverse Langevin function for the chain distribution to describe the correct degree of swelling at equilibrium $Q_{\mathrm{eq}}$ (see Section 5.1.1), since a Gaussian approach distinctly overestimates the absorbency.

However, the theoretically obtained degree of swelling can be manipulated widely with Equation 3.27 by adjusting the parameters to match the experimental data. While most parameters can be estimated quite good, the statistical segment number $n$ is not straightforward to compute, but has a strong effect on the elastic contribution $\mu_{\mathrm{I,el}}$. Furthermore, the provided theoretical description within this chapter only reflects ideal networks without considering any structural defects (see Figure 3.1), which are always present in real networks. A theory that can satisfyingly describe real, inhomogeneous and more complex network structures is still missing.

## 3.3 Summary

In this chapter, models were introduced to describe polymer networks mathematically. The models, which are based on Flory's rubber theory, were derived from the equilibrium thermodynamics of the gel and surrounding solution phase. While the rather simple phantom model usually predicts the behavior in rubbers or uncharged hydrogels with intermediate absorbencies quite well, it fails to describe polyelectrolyte hydrogels properly with the corresponding large degrees of swelling. In such systems, not only the elastic and mixing term have to be considered, but the ionic interactions between charges and water molecules should also be taken into

account. Additionally, the Gaussian chain statistics fail in the highly expanded networks and thus, more advanced models are necessary to describe the polyelectrolyte hydrogels.

However, these models are more complex and use further parameters, which are not straightforward to predict itself. A satisfying theory to describe *e. .g.* the degree of swelling at equilibrium $Q_{eq}$ in polyelectrolyte networks, which derives only from molecular parameters, is therefore still missing. This is particularly true when structural defects, such as dangling ends, loops or intermolecular entanglements shall be considered, too.

# 4 Synthesis

The main goal of the present thesis is to understand how macroscopic properties of polyelectrolyte hydrogels are influenced by the network architecture, with a special focus on the membrane-free desalination application. Therefore, a large variety of polyelectrolyte networks is synthesized, where both, the network topology and the synthetic parameters of each topology itself, is systematically adjusted.

In this chapter, general considerations are presented, how the different network architectures can be synthetically accomplished and which chemical parameters are varied.

First, the synthesis of poly(sodium acrylate) (PSA) and poly(sodium methacrylate) (PSMA) hydrogels via free radical polymerization is described. These polyelectrolytes serve as a reference system, as they are also widely spread in industrial applications. Strategies are shown that allow producing highly crosslinked networks and hydrogels with a uniform particle bead size.

Second, surface crosslinked hydrogels are synthesized, where the hydrogels have a specifically desired higher crosslinking density at the shell of the particles.

Third, basic strategies are critically discussed, how model polyelectrolyte networks with a uniform mesh size distribution can be produced. In this context, two approaches are employed to synthesize so-called quasi-model systems via anionic polymerization: The chemically end-linking of living precursor chains and the self-assembly of amphiphilic ABA triblock copolymers. Furthermore, these triblock copolymers are mixed with AB diblock copolymers to study the effect of a varying amount of dangling ends.

Fourth, interpenetrating networks are synthesized that consist of two individual PSA polymer networks.

At the end of this chapter, another class of hydrogels is introduced. Thermally responsive networks are synthesized, where poly(N-isopropylacrylamide) (PNIPAAm) segments are incorporated into the polyelectrolyte. These segments are either introduced into the hydrogel by copolymerization of the respective monomers or in form of interpenetrating double networks.

## 4.1 Randomly crosslinked PSA and PSMA networks made by free radical copolymerization

### 4.1.1 Reference PSA and PSMA hydrogels

Crosslinked poly(sodium acrylates) and poly(sodium methacrylates) are synthesized via free radical (co)polymerization (FRP) from the respective acrylic monomers with a difunctional initiator in water. These hydrogels shall serve as a reference system to the other network topologies. The FRP was chosen as synthetic procedure, since it is easy to perform and is also widely used in the industrial production of superabsorbers [Buchholz98, Umendra99].

During the reaction, the polymers are formed by the successive addition of monomers, which carry a free radical. A double bond is transferred into two C-C single bonds and the monomer remains in the growing polymer chain. A suitable initiator, which should be water soluble and work at ambient temperature, has to be chosen to generate a radical in the acrylic monomer. In this work, the redox initiator sodium persulfate (SPS, $Na_2S_2O_8$) with the accelerator N,N,N',N'-tetramethylethylenediamine (TEMED) is used. The polymerization is usually carried out under an inert $N_2$-atmosphere to avoid side reactions with oxygen, which can inhibit the polymerization, leading to undefined samples with an increased content of unbound polymer (sol).

N,N'-methylenebis(acrylamide) (MBA) was chosen as the crosslinking agent for most samples [Buchholz98, Umendra99]. The synthetic procedure is displayed in Figure 4.1 and was adapted from the literature [Oppermann92, Höpfner13a]. The exact quantities and a list of the hydrogels synthesized is given in Appendix A.1.2.

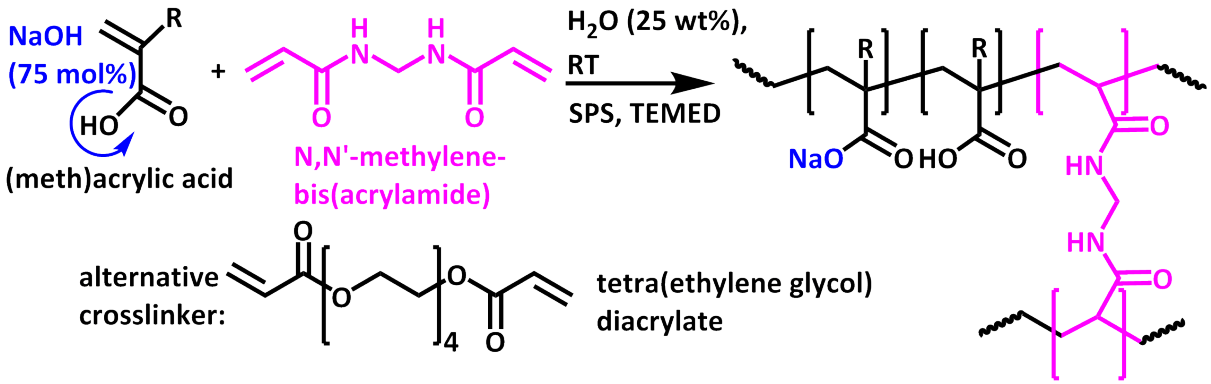


**Figure 4.1:** The free radical polymerization procedure of neutralized (meth)acrylic acid with the crosslinker MBA is shown. As MBA has a limited solubility in water, TEGDA was used for highly crosslinked samples ($DC$ > 5 mol%).

The synthesis offers the possibility to vary several parameters to adjust the hydrogel properties. The degree of crosslinking (*DC*) defines the average elastic chain length between the crosslinking points and hence, influences strongly the absorbency and the mechanical properties. The *DC* is defined as the moles of crosslinker with respect to the moles of monomer and is given by

$$DC = \frac{n(\text{crosslinking agent})}{n(\text{monomer})} * 100\,\text{mol\%}\,. \tag{4.1}$$

The amount of charges on the polymer backbone is described by the degree of neutralization (*DN*), as given in Equation 4.2. It is defined as the ratio of the base to the total moles of ionizable groups.

$$DN = \frac{n(\text{base})}{n(\text{ionizable monomer})} * 100\,\text{mol\%} \tag{4.2}$$

Additionally, the polymer concentration $c_\text{p}$ or expressed as the inverse, the swelling ratio during the synthesis $Q_\text{syn}$ is defined by mass, as the ratio of polymer with respect to water (Equation 4.3).[1] This reference state of the gel defines the relaxed state of the meshes and influences *i. a.* the pore size distribution [Höpfner14].

$$Q_\text{syn} = \frac{m(\text{water})}{m(\text{monomer}) + m(\text{crosslinker})} = \frac{1}{c_\text{p}} * 100\,\text{wt\%} \tag{4.3}$$

During the synthesis in this work, $Q_\text{syn}$ was kept constant at 4 g/g, since higher ratios cause more sol, whereas smaller values lead to solubility problems of the crosslinker.

The acrylic monomers were neutralized to 75 mol% prior the polymerization, since more charges are beneficial for the salt separation, as found in previous work [Höpfner13a]. The addition of even more NaOH resulted in a slightly alkaline solution, where the gelation was inhibited. If counterion condensation (see Section 3.2) is considered, a *DN* of 75 mol% will already result in a maximum charged hydrogel. Hence, no significant differences in the gel properties (*e. g.* mechanical modulus or degree of swelling) were found, when the polymers were subsequently fully neutralized by adding an excess of NaOH.

The degree of crosslinking was varied with respect to the mechanical stability of the formed hydrogels over the range of 0.3 to 5 mol%. Higher values for *DC* were not accessible, when MBA was used as the crosslinker due to its limited solubility in water. An increase of the water content during the synthesis would also involve an undesired increase of sol. Therefore, part of the hydrogels in this work were copolymerized instead with tetra(ethylene glycol) diacrylate

[1] In chapter 3 the degree of swelling during the crosslinking process is described by $q_\text{c}$, which is defined as the volume ratio, though.

(TEGDA) as crosslinker, since previous work demonstrated that a higher *DC* is beneficial for the desalination efficiency [Höpfner13a, Arens17a].

A list of the synthesized reference samples is listed in Appendix A.1.2. The following short nomenclature has been used to describe samples in this thesis: First, the polymer type is defined, which is either poly(sodium acrylate) (PSA) or poly(sodium methacrylate) (PSMA). Second, the degree of crosslinking is given in mol% and, if not MBA but TEGDA was used as the crosslinker, also the supplement TEGDA. A poly(sodium acrylate) with a degree of crosslinking of 30 mol%, using TEGDA as crosslinker, is given in his short form as PSA-DC30-TEGDA. A poly(sodium methacrylate) crosslinked with 1 mol% of MBA is named as PSMA-DC1.

### 4.1.2 Monodisperse particle size using droplet-based microfluidic technique

The hydrogel synthesis via solution polymerization allows no control about the macroscopic size and shape of the polymer particles. During the polymerization, one hydrogel block is formed, which is subsequently cut or ground into smaller fractions. These fractions have, depending on the grinding and sieving process, a rather broad particle size distribution with a poor control of their shape (see Figure 4.2). The advantage of having a uniform hydrogel bead size is the maximization of the void spaces and channels among particles. If hydrogels are used under load, the pressure on the semi-swollen gel will cause a blockage in this area preventing further liquid to enter the gel. The channels are closed due to the deformation of the gel particles [Elliott04]. This phenomenon is well known as gel-blocking and will be discussed further in the next section.

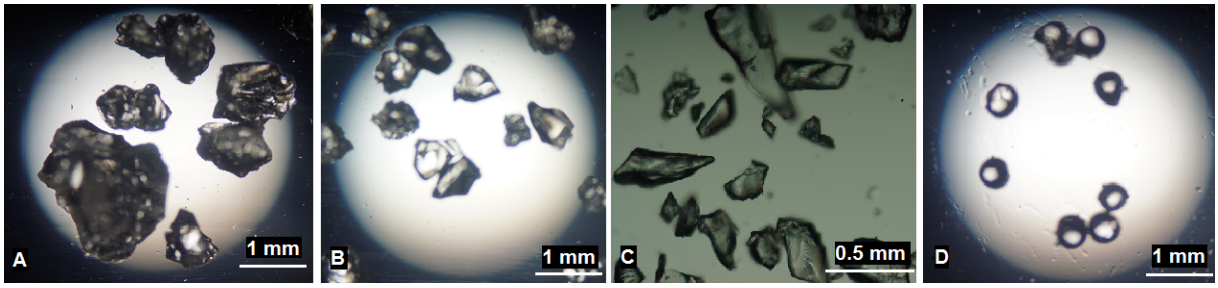


**Figure 4.2:** Light microscope pictures of dried hydrogel particles. A-C: Different fractions (A: >650 µm, B: 350 – 650 µm, C < 350 µm) obtained by grinding and sieving the hydrogel after the polymerization in solution. D: Spherical particles obtained by droplet-based microfluidic templating process.

The droplet-based microfluidic technique has been used to generate monodisperse particles of sub-millimeter-sized spheres [Xu05]. The typical setup for creating the uniform particles is shown in Figure 4.3, where the essential device consists of two micrometer-sized channels. In one channel is a stream of a microgel precursor solution created (dispersed phase, A), which is

periodically interrupted by flow-focusing with a second immiscible carrier fluid (continuous phase, B). When the two fluids meet in point C, droplets are formed in a "drop-by-drop" fashion due to a balance between the interfacial tension and the shear forces [Seiffert11]. The native size of the particles is controlled during the formation by transmission microscopy. The size depends on the dimensions of the capillaries, the viscosities, the polarities and the flow rates of the fluids. The formed droplets, containing the monomer precursor solution with a photo initiator, are eventually irradiated by UV-light. The particles polymerize and retain their uniformity by droplet gelation.

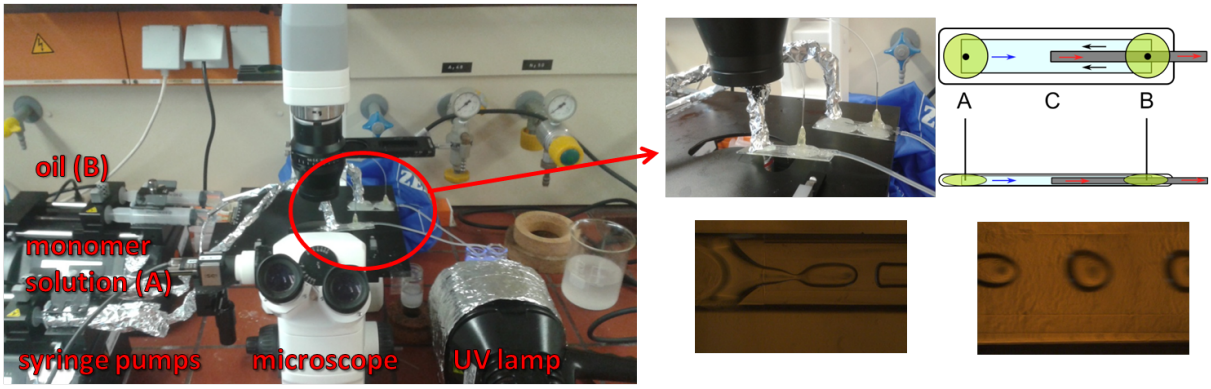


**Figure 4.3:** The microfluidic (MF) setup, to produce uniform microgel spheres with a narrow size distribution, is displayed. It consists of two syringe pumps with the continuous (oil) and dispersed (monomer solution) phase to allow adjustable, but constant flow rates. The essential MF part is shown on the right and is made of two glass capillaries, which provide the channels for the two phases. In point C, both liquids meet, form droplets that are observed online by a transmission microscope and are then gelified via UV-light.

## 4.2 Surface crosslinked PSA hydrogels

The reference hydrogels, which were described in the previous section, have no specifically desired heterogeneity in their network structure. In this section, hydrogels are synthesized that have a purposely higher degree of crosslinking at the outer layer than the rest of the network. These hydrogels can be referred to as core-shell particles and are obtained by an additional surface crosslinking of a first network (see Figure 4.4).[2]

The basic idea, using surface crosslinked hydrogels in the scope of this work, is to combine the advantages of a high *DC* and a low *DC*. It shall be evaluated, whether it is possible to use both, the high water absorbency of a low *DC* and the better salt rejection of a high *DC*.

[2]The surface crosslinked hydrogels were synthesized and partially investigated by Mr. Dennis Barther in form of a Bachelor thesis under the supervision of the author [Barther16].

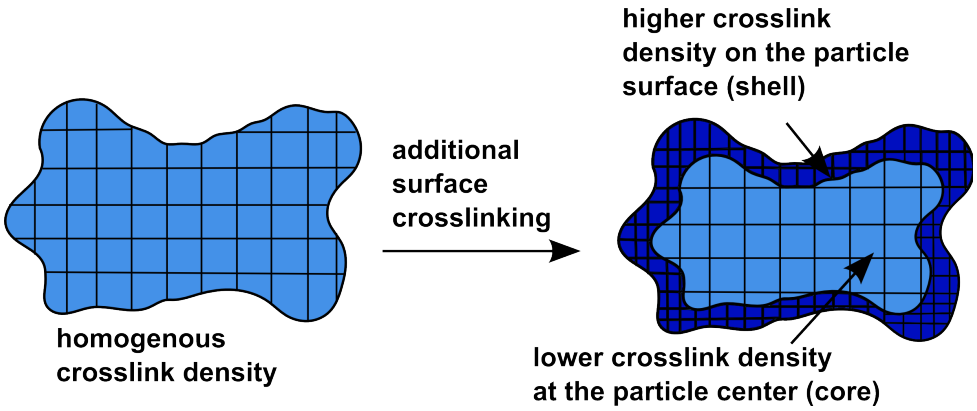


**Figure 4.4:** A homogeneously crosslinked hydrogel is additionally treated to increase the crosslink density on the surface, leading to a core-shell particle.

Surface crosslinked hydrogels are commonly used in hygiene products like diapers. A low *DC* is advantageous for a high swelling in superabsorbent polymers, though the absorbency under load (AUL), *e. g.* when a baby is sitting on its diaper, is rather poor in these hydrogels [Buchholz98]. Additionally, a pressure on the semi-swollen gel can cause a blockage in the voids among the particles, which prevents further liquid entering the gel beads due to a drastically increased flow resistance [Elliott04]. Surface crosslinking is used to avoid this so-called gel-blocking and to improve the AUL without considerably increasing the *DC* throughout the whole network. The higher crosslink density at the shell increases the mechanical stability of the swollen hydrogel beads and makes the particle stiffer without drastically reducing the absorbency. As a result, the particles retain their original shape and thus, also the void spaces to easily transport liquid in between the particles.

In industry, the post-crosslinking is usually performed on the dried, milled and sized polymer particles as the final stage of the process [Elliott04], in which a crosslinking solution is sprayed on the beads followed by a "curing" through heat. The chemical for this additional crosslinking must have at least two functional groups that are capable of reacting with the carboxyl groups on the polymer backbone. Typical examples are polyhydric alcohols such as glycerin or sugars [Ruttscheid04]. The surface crosslinking agent is sprayed on the particles, followed by heating to 150 – 200 °C for about 30 – 60 minutes. However, more recent studies employ instead an irradiation with UV-light to avoid higher temperatures, which can cause degradation of the polymer [Flohr07, Jockusch09].

Ethylene glycol diglycidyl ether (EGDE) is used as the surface crosslinking agent in this thesis and the synthetic procedure is adapted from a patent [Obayashi82]. EGDE offers the advantage that the esterification of the carboxyl group of the poly(acrylic acid) with the epoxide

is more favored compared to the reaction with a alcohol due to the additional ring strain of the diepoxide. This allows to reduce the reaction temperature to 65 °C to avoid polymer degradation.

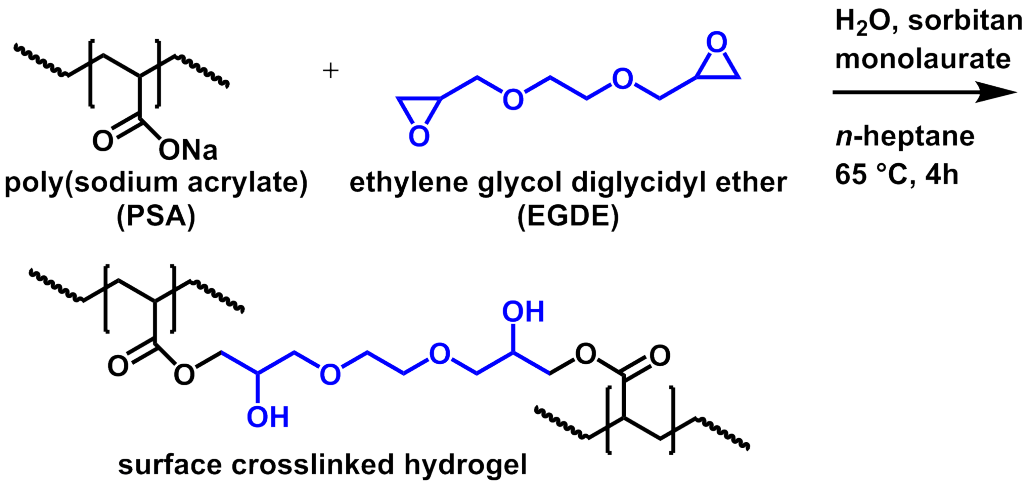


**Figure 4.5:** The poly(sodium acrylate) is crosslinked with EGDE via an esterification, after the polymerization of the crude hydrogel. For the sake of clarity, the PSA is drawn as a linear polymer, although networks are additionally crosslinked at their surface.

In the synthesized particles, the initial *DC* of the precursor hydrogels and the thickness of the additionally crosslinked shell was varied. Therefore, a fraction of dried hydrogel particles with a size between 350 and 650 µm was suspended in *n*-heptane. Next, different amounts of water with a certain EGDE concentration were added. The amount of water was chosen with respect to the degree of swelling $Q_{eq}$ of the first network and was adjusted by Equation 4.4, where $P$ is the volume fraction of the hydrogel that is penetrated by the surface crosslinker.

$$P = \frac{m(\text{water})}{Q_{eq} * m(\text{PSA, dry})} * 100\,\text{vol\%} \tag{4.4}$$

The penetration $P$ was chosen to be either 1 or 10 vol%, which means that 1 or 10 vol% of the shell is additionally crosslinked. The amount of EGDE was calculated by Equation 4.5, which refers to the moles of EGDE, if it would quantitatively react with every carboxyl group in the penetrated area.

$$n(\text{EGDE}) = \frac{n(\text{SA}) * P}{2} \tag{4.5}$$

The surface crosslinking reaction is displayed in Figure 4.5, while the synthesis is described in detail in Appendix A.1.4, where also a table with the synthesized samples is given. The nomenclature from Section A.1.2 was extend by the token Px, where x describes the penetrated

area, which was additionally crosslinked. A PSA hydrogel with $DC = 1\,\text{mol\%}$ and $P = 10\,\text{vol\%}$ is accordingly named as PSA-DC1-P10.

## 4.3 Quasi-model systems for PSMA hydrogels

Synthesized polymer networks can never be perfect and will always have topological defects such as dangling ends, loop formations, intermolecular entanglements and crosslinker-crosslinker shortcuts (see Figure 3.1) [Hild98]. Hydrogels, which are prepared by free radical crosslinking copolymerization, are well studied due to their industrial importance and easiness of the synthesis [Buchholz98, Gulrez11, Laftah11]. However, these systems additionally exhibit a marked degree of nanostructural heterogeneity in form of an inhomogeneous spatial distribution of crosslinks, in addition to the described defects [Lorenzo13]. This heterogeneity leads to a broad distribution of mesh sizes. The inhomogeneity of the crosslinking density in the polymer network is even more pronounced in the swollen state: Upon swelling, areas with a lower crosslinking density will swell more, while higher crosslinked domains will have a lower water uptake [Bastide88].

The origin of the spatial heterogeneity lies in the mechanism of the crosslinking copolymerization and different aspects have to be considered. During the early stage, the chain cyclization and the spatially localized multiple crosslinking is more pronounced, which leads to a suspension of nanogel clusters. At higher conversions, these clusters get rather loosely interconnected to a continuous 3D polymer network — a macroscopic gelation occurs. As a result, the formed hydrogel displays a pronounced heterogeneity on a $10 - 100\,\text{nm}$ length scale [Lorenzo13]. Furthermore, the free radical polymerization itself leads, with its statistical occurring termination and chain transfer reactions, to a certain molecular weight distribution in linear polymers ($PDI = 1.5 - 2$). The $PDI$, combined with the statistical incorporation of the crosslinker molecules, already causes a broad mesh size distribution (see Figure 4.6, A).

In this section, a short literature review is given to discuss how hydrogels with a narrow mesh size distribution can be synthesized. Then, two approaches are presented, which were used in this thesis to synthesize more defined polyelectrolyte hydrogels. The purpose in the context of the present work is to study, if a hydrogel with a narrow mesh size distribution will be advantageous for the salt separation or the desalination efficiency, since a small pore size distribution is also crucial in any 2D-membrane process.

### 4.3.1 Strategies to synthesize hydrogels with a narrow pore size distribution

As already described in Chapter 3, ideal networks can never be synthetically obtained, since defects such as dangling ends, loop formations or intermolecular (network) entanglements are always present [Hild98]. The best producible polymer network is a model network, where the crosslinking functionality and the elastic chain length are well defined (see Figure 4.6, C).

Such systems are more elaborate to synthesize and the combination of a living polymerization technique followed by a click-type coupling, *e. g.* an azide-alkyne Huisgen cycloaddition, is usually necessary. Well established is for example the preparation of PEG-hydrogels [Malkoch06], while less work has been focused on charged systems due to less synthetic control [Shefer93]. Probably the best example for a poly(methacrylic acid) model system so far was introduced by Wegner *et al.* [Mengel01]. They synthesized well defined P*t*BMA star precursor polymers containing an anthryl group at the end of each arm, followed by photodimerization to the network with the subsequent transformation to a PMAA network by hydrolysis.

A compromise between structural perfection of the network and easiness of the synthesis represents a so called quasi-model system, in which the mesh length between the crosslinking points is fixed, but the crosslinking functionality has a certain distribution (see Figure 4.6, B) [Hild98, Triftaridou07].

A common technique to obtain such quasi-model systems is the synthesis of elastic chains via a living polymerization technique, followed by the addition of a multifunctional crosslinker to chemically end-link these meshes. In this way, several organogels, such as poly(styrene), poly(isoprene) and poly(alkyl methacrylate) have been synthesized by anionic polymerization [Weiss71, Beinert75, Rempp79, Hild98]. The group of Patrickios has extensively used group transfer polymerization to produce a large variety of poly(alkyl methacrylate) networks, including hydrogels based on poly(methacrylic acid) [Kali06, Triftaridou07].

Symmetrical amphiphilic triblock copolymers of the structure ABA are another, fundamentally different type of quasi-model networks. In these systems, the endblock A is made of a hydrophobic polymer which forms micelles in water that can act as physical crosslinking points, while the midblock B is a hydrophilic polymer that spans the 3D network among these aggregates [Annable93, Tam98, Kadam11]. While earlier work focused on non-charged systems, in more recent publications sodium (meth-)acrylates were also used as the midblock [Tsitsilianis00, Tsitsilianis02, Ryan05, Howse06, Guvendiren07, Henderson10].

In the present thesis, two different approaches are used to synthesize quasi-model systems based on poly(sodium methacrylates) (see Figure 4.6, B). One attempt is the chemical end-linking of living P*t*BMA precursor molecules by a difunctional crosslinker, followed by hydrolysis (see Section 4.3.4). In the other approach, the amphiphilic triblock copolymer poly(methyl methacrylate)-*b*-poly(sodium methacrylate)-*b*-poly(methyl methacrylate) is synthesized to

obtain physically crosslinked hydrogels (see Section 4.3.3). In both cases, poly(*tert*-butyl methacrylate) is synthesized first via anionic polymerization, followed by hydrolysis to the polyelectrolyte. Therefore, some general remarks on the anionic polymerization technique is given in the next section with some special aspects of the anionic polymerization of methacrylates in particular, before the two synthetic approaches are explained in more detail.

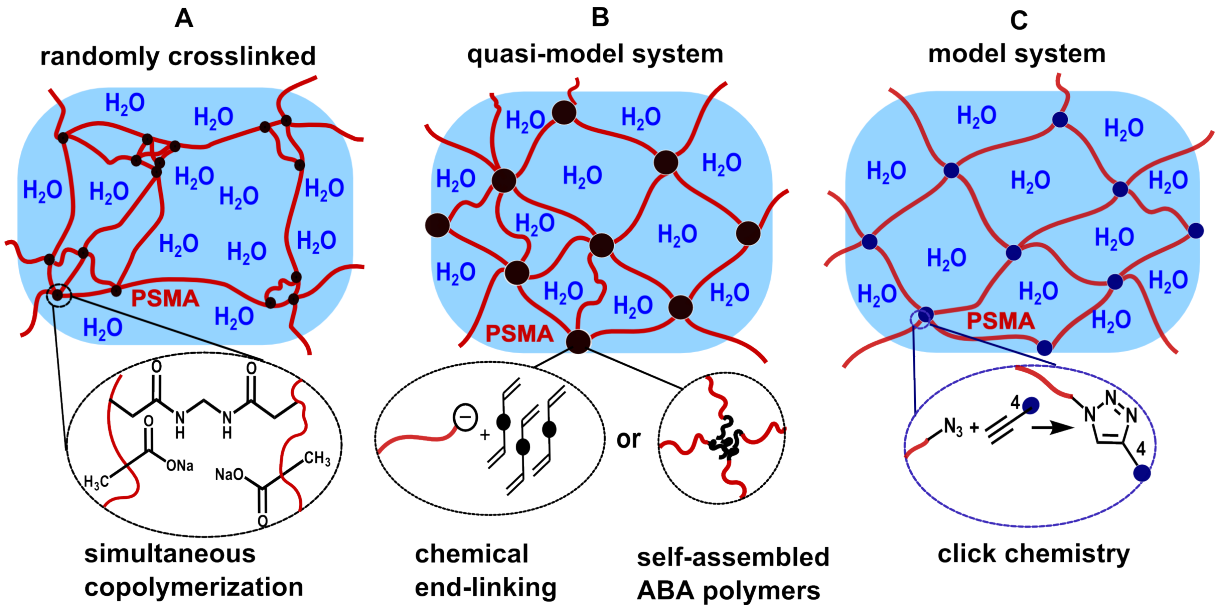


**Figure 4.6:** A) Randomly crosslinked hydrogels made by the simultaneous free radical copolymerization, which leads to the typical clustering of highly crosslinked areas and a broad pore size distribution. B) Quasi-model systems with a defined mesh length, but a certain distribution in the crosslinking functionality. C) Model systems with a fixed mesh length and crosslinking functionality. From left to right, the degree of homogeneity is increasing, but also the synthetic effort. Structural defects such as dangling ends, loop formations and intermolecular entanglements are not shown, although they are present in any network type (see Figure 3.1).

### 4.3.2 General remarks on the anionic polymerization of methacrylates

The anionic polymerization is a powerful technique to synthesize polymers with a low polydispersity ($PDI < 1.1$). It is, like the free radical polymerization, a chain growth reaction including the three steps chain initiation, chain propagation and chain termination, whereby the propagating species is a carbanion.

In contrast to the FRP, there is theoretically no termination reaction present and the propagating chain end remains active, why it is also referred to as a "living" polymerization [Szwarc56]. Hence, this technique can be used to synthesize high molecular weight polymers with a low

*PDI* and is particularly suitable to create block copolymers by the addition of a second type of monomer to the first, still living polymer.

Several precautions have to be complied to ensure the living character of the anionic polymerization. All reagents have to be absolutely free of protic molecules (such as water, alcohols and acids), carbon dioxide and oxygen, since all these components can react with the carbanion, resulting in an undesired termination [Hadjichristidis00]. Therefore, the used monomers and solvents have to be dried and degassed prior to the synthesis. Additionally, high vacuum techniques and the usage of an argon inert gas atmosphere are necessary. As a consequence of the sensitivity toward protic components, acidic monomers like (meth-)acrylic acid cannot be directly polymerized by anionic polymerization, but the acid group has to be protected. A common protecting group for carboxyl groups is *tert*-butyl, which can be easily cleaved from the polymer afterward by hydrolysis with HCl in dioxane [Leon94].

Furthermore, it is more elaborate to keep the living character during the anionic polymerization of methacrylates compared to styrene or dienes due to the carbonyl group, which may cause several side reactions (see Figure 4.7) [Hsieh96, Baskaran07, Cadova08]:

- An 1,2-addition of the initiator onto the carbonyl function can occur.
- The intramolecular backbiting reaction and the intermolecular attack of the carbanion onto the carbonyl group lead to self-termination.

The reaction conditions have to be adjusted to ensure that the polymerization is still living [Mori03, Baskaran07]: The reactivity of the propagating carbanions has to be decreased by lowering the temperature (*e. g.* $< -60\,^{\circ}\mathrm{C}$) and the addition of salts like LiCl that form a $\mu$-ligand type complex at the reactive centers [Varshney90]. The initiator has to contain substituents with a high steric hindrance (*e. g.* DPE-Li) to inhibit kinetically the attack on the carbonyl group, which is especially important for MMA with the small ester group. The polymerization should take place in a polar medium like THF, which helps in controlling the ion-pair aggregation and reduces the backbiting reaction [Baskaran07, Cadova08].

Generally, the anionic polymerization of acrylates like *t*BA is also possible [Kitano77, Fayt87] and was successfully tested by the author of this thesis. Nevertheless, the use of acrylates was avoided and the methacrylates MMA and *t*BMA were used instead. Acrylates miss the steric hindrance as well as the +I-effect of the methyl group, which can lead to an abstraction of the hydrogen atom. This causes a reduced stability during the anionic polymerization (even lower temperatures are necessary) and can lead to a slightly crosslinked material after the hydrolysis.

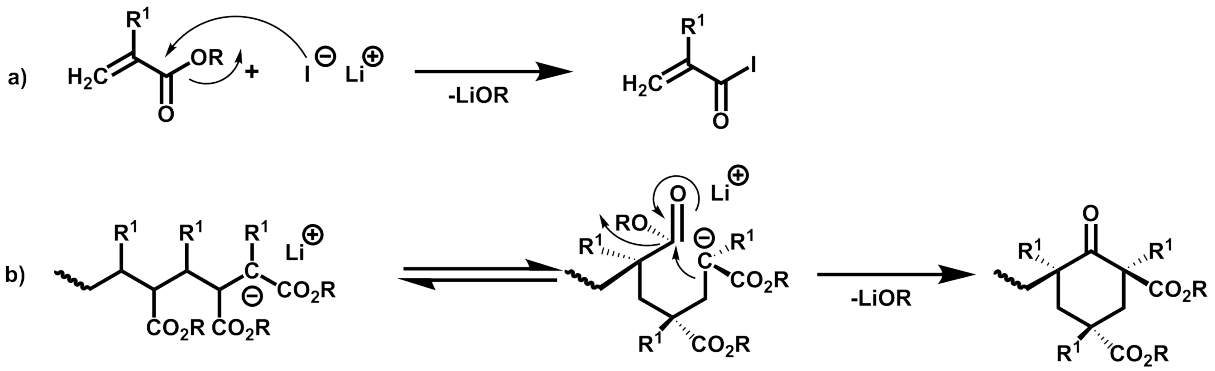


**Figure 4.7:** Typical side reactions in the anionic polymerization of (meth-)acrylates: a) 1,2-addition of the initiator I (*e. g. s*-BuLi) onto the carbonyl function. b) Intramolecular backbiting reaction of the carbanion onto the carbonyl group. The attack can also occur intermolecularly.

### 4.3.3 Physically crosslinked hydrogels made by self-assembled amphiphilic ABA triblock copolymers

One technique to obtain quasi-model systems with a defined mesh length is based on the self-assembly of amphiphilic ABA triblock copolymers, where the endblocks A consist of a hydrophobic polymer (here: PMMA), whereby the midblock B is the hydrophilic PSMA. This triblock copolymer phase separates in water. The endblocks self-assemble into aggregates, *e. g.* in form of spherical micelles, which act as physical crosslinking points, while the midblocks form bridges between these junctions to span the 3D network [Annable93, Tam98, Kadam11].

In order to obtain the physically crosslinked networks, the synthesis of the triblock copolymers is described first, followed by the formation into the hydrogels.

#### Synthetic methods for ABA triblock copolymers

The anionic polymerization of symmetrical ABA triblock copolymers is principally possible with three different synthetic approaches [Hadjichristidis00]:

**i) Sequential monomer addition**

In this synthetic approach, each monomer is polymerized in a block-by-block fashion: Block A is polymerized first, followed by the addition of monomer B to the still living polymer. The addition of monomer A' to the living diblock copolymer AB results in the triblock copolymer ABA' (see Figure 4.8).

The sequential approach is only possible, if the reactivity of the monomers will be similar to enable a mutual initiation. This is one of the main reasons why PMMA was chosen as

the endblock in the triblock copolymers within this work, since meth(-acrylates) are able to initiate each other [Varshney91, Matsuo13]. The three necessary monomer addition steps are one disadvantage of this method, since they increase the probability to introduce impurities. Furthermore, slightly asymmetric triblock copolymers can be obtained if not the exact stoichiometric amount of MMA is added in the first and last step, respectively. On the other hand, an advantage of the sequential approach is its feasibility without the need of a difunctional initiator or a coupling agent. In addition, it is possible to analyze each block by size exclusion chromatography (SEC) and $^{1}$H-NMR spectroscopy separately.

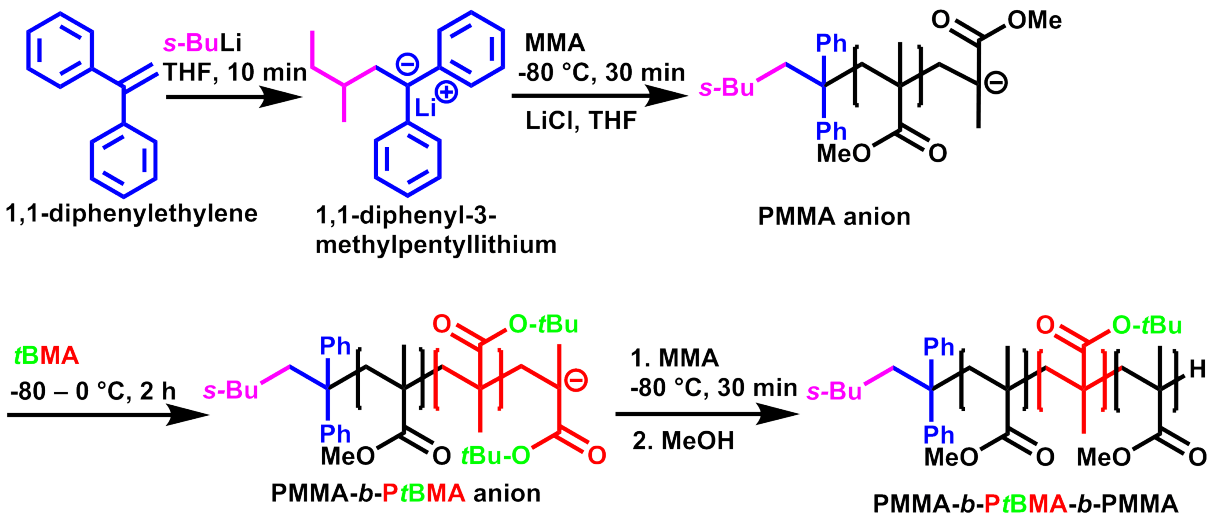


**Figure 4.8:** Anionic polymerization of PMMA-*b*-P*t*BMA-*b*-PMMA via the sequential addition of the respective monomers.

**ii) Use of a difunctional initiator**

In this approach, a difunctional initiator is used to synthesize the midblock B first. Then, the monomer A for the endblocks is added, which reacts with the two living ends on both sides of the midblock polymer (see Figure 4.9).

The resulting triblock copolymer is always symmetrical, if no termination occurs, since the chains are growing with the same probability at both sides. Another advantage is that only two monomer addition steps are necessary, which reduces the risk of introducing impurities. This method is especially suitable for poly(alkyl methacrylate) triblock copolymers, since DPE is able to dimerize in polar solvents in the presence of alkali metals such as Li or Na [Wang78], and increases the steric hindrance of the initiator.

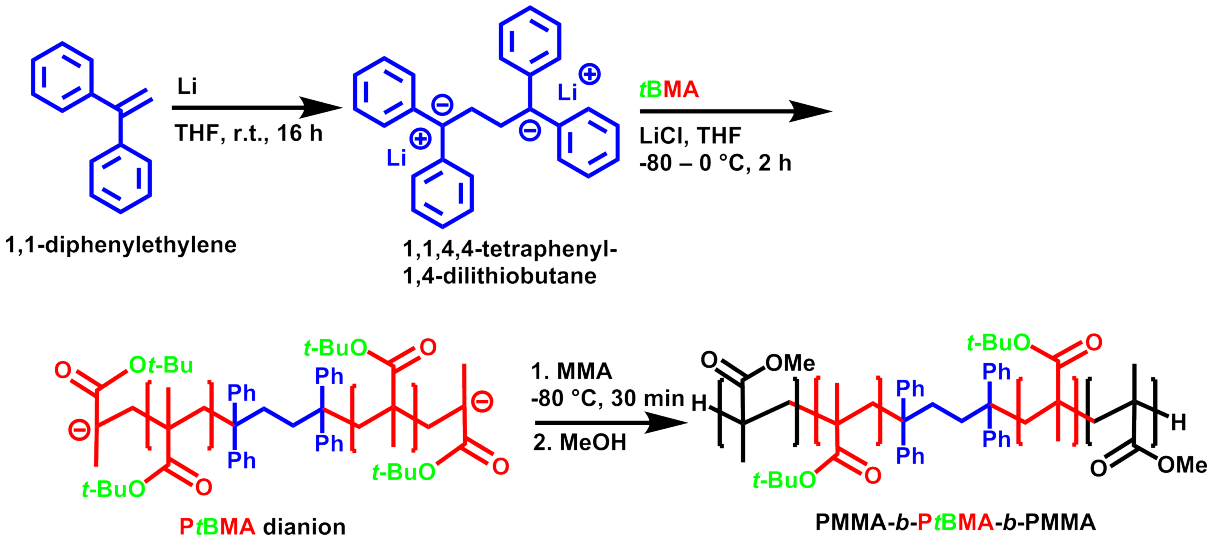


**Figure 4.9:** Anionic polymerization of PMMA-*b*-P*t*BMA-*b*-PMMA using a difunctional initiator.

### iii) Coupling of living AB chains

In this strategy, a diblock copolymer AB is synthesized first by the sequential monomer addition (analogously to the first approach). Then, a coupling agent X (such as terephthaloyl chloride [Varshney98] or 1,4-bis(bromomethyl)benzene [Pitsikalis99]) is added, which can react with two living polymer chains to form a triblock copolymer of the general form AB-X-BA. Although this approach needs only two monomer addition steps and always leads to symmetrical triblock copolymers, it was not used in this thesis. Preliminary tests revealed that usually no more than 60% coupling yield was realized [Arens14], resulting in 40% diblock copolymer fraction as impurity. This might originate from two problems: First, the amount of added coupling agent has to be stoichiometrically exact, since a quantitative coupling is otherwise not possible. Second, the added LiCl, which is necessary to ensure the living polymerization of MMA, not only reduces side reactions but also lowers the reactivity of the coupling reaction. Consequently, long reaction times of several days at low temperatures of -78 °C to -30 °C are necessary [Pitsikalis99], which is less practical.

#### Applied synthesis

In general, both applied synthetic methods, the sequential monomer addition (see Figure 4.8) and the use of a difunctional initiator (see Figure 4.9) led to well defined PMMA-*b*-P*t*BMA-*b*-PMMA triblock copolymers with a low *PDI* in the range of 1.04 to 1.17, as shown in the SEC elugrams in Figure 4.10. The synthetic procedures are described in detail in Appendix

A.1.5, where also a list of the synthesized samples is provided. When the sequential monomer addition was used, a small amount of unreacted homopolymer (typically less than 5 mol%) was present in the slightly asymmetric triblock copolymer with a *PDI* of usually less than 1.10. In contrast, using a difunctional initiator led to symmetric products with no homo- or diblock copolymer impurities, but a slightly higher *PDI* in the range of 1.10 to 1.17.

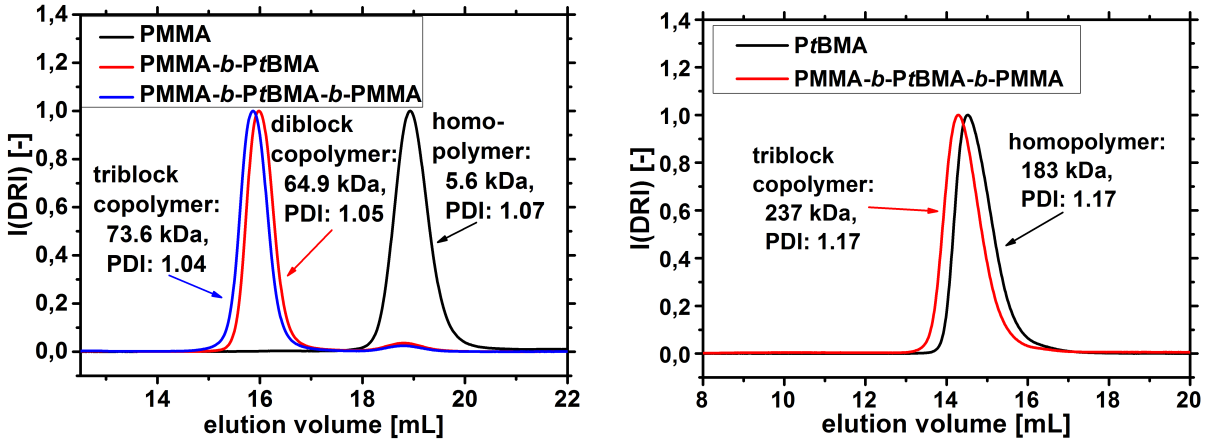


**Figure 4.10:** The SEC elugrams for the intermediates and the final PMMA-*b*-P*t*BMA-*b*-PMMA triblock copolymer are displayed. Left) Synthesis via the sequential monomer addition. Right) Synthesis using a difunctional initiator.

The number of monomers per block was calculated from SEC measurements in THF against PMMA standards.[3] Additionally, $^1$H-NMR spectroscopy was used to calculate the ratio between PMMA and P*t*BMA in the block copolymers by integrating the peaks of the methoxy groups ($\delta$ = 3.59 ppm) and the *tert*-butyl groups ($\delta$ = 1.44 ppm) (see Figure 4.12). The most precise values for the number of monomers in each block were obtained by the combination of both methods: The monomer number in the first block was determined from the measured molecular weight by SEC. Then, $^1$H-NMR spectroscopy was used to calculate from the PMMA to *Pt*BMA ratios the monomer number in the second and third block, respectively.

The conversion of the P*t*BMA midblock to PSMA was accomplished by hydrolysis with HCl in dioxane, followed by the neutralization with NaOH (see Figure 4.11 and Appendix A.1.5). The reaction was found to be quantitative, since the signal of the *tert*-butyl group in the triblock copolymer was completely vanished after the hydrolysis, as seen in the $^1$H-NMR spectra in Figure 4.12.

[3] A small amount of the reaction mixture was always taken out prior the addition of the next monomer, to separately analyze each polymer block by SEC and $^1$H-NMR spectroscopy.

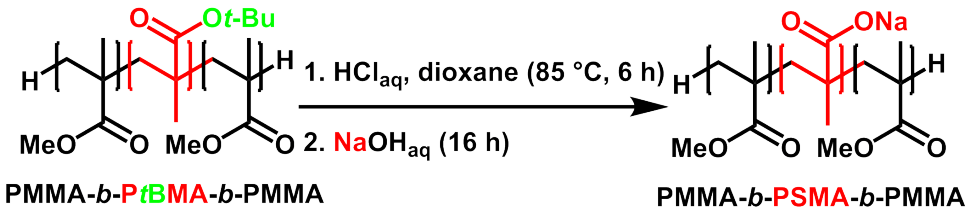


**Figure 4.11:** Conversion of the P*t*BMA midblock to PMAA by hydrolysis with HCl in dioxane. After the neutralization with aqueous NaOH in water, the charged PMMA-*b*-PSMA-*b*-PMMA triblock copolymer is obtained.

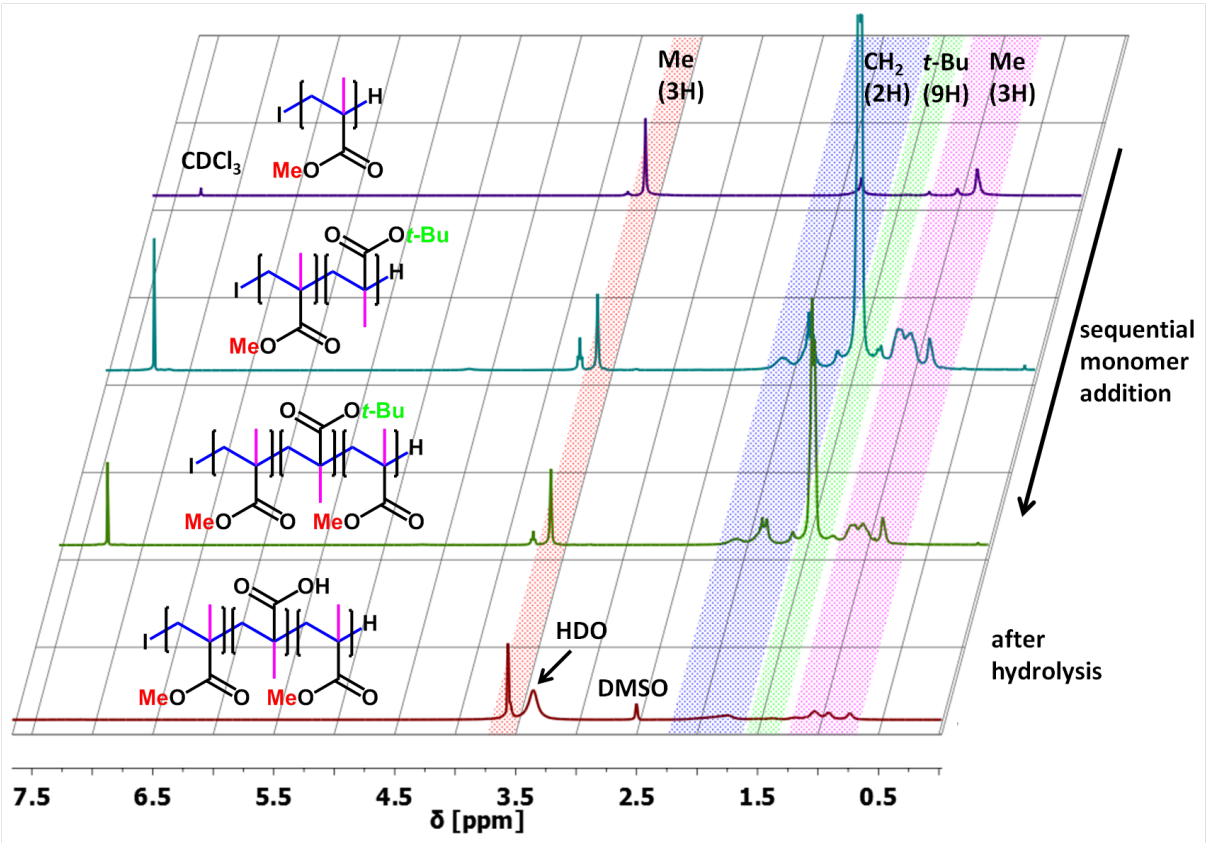


**Figure 4.12:** The $^1$H-NMR spectra are shown for the different steps in the synthesis of an amphiphilic PMMA-*b*-PSMA-*b*-PMMA triblock copolymer (sample 60-340-53), which was prepared by the sequential monomer addition, followed by hydrolysis of the midblock. The spectra are normalized to the three protons of the methoxy group ($\delta$ = 3.59 ppm).

## Nomenclature

In this work a series of different PMMA-*b*-PSMA-*b*-PMMA triblock copolymers was synthesized to systematically vary the length of the endblock A, the length of the midblock B and the overall polymer length ABA to study the effect on different hydrogel properties such as mechanical stability, absorbency and desalination performance. A complete list of the synthesized samples is given in Table A.3 in the appendix. To keep the nomenclature of the polymers simple and consistent, the samples are described by the number of monomer units in each block, as calculated by the combined use of SEC and $^{1}$H-NMR spectroscopy, in the following fashion: A triblock copolymer with 50 MMA units in each endblock and 300 *t*BMA, respectively 300 SMA units in the midblock is abbreviated by 50-300-50.

## Hydrogel formation

When the amphiphilic triblock copolymers PMMA-*b*-PSMA-*b*-PMMA were stirred in aqueous solutions for the first time, they did not necessarily form swollen hydrogels, but turbid viscous solutions were sometimes obtained instead. This phenomenon is related to the formation of so-called frozen micelles. The exchange rate of the PMMA blocks in water is so slow that the chains are kinetically trapped [Nicolai10]. The hydrophobic groups of the triblock copolymer self-assemble in water into rather randomly organized aggregates. If the amount of loop formations (two PMMA endblocks aggregate in the same micelle) is too high, no 3D connected networks, but flower-like micelles will be formed [Tsitsilianis18]. Consequently, it was first necessary to get the PMMA groups reversibly mobile to enable the change from a loop to a bridging conformation and the transition to a well ordered state.

Different techniques can be used to increase temporarily the exchange rates. A common method is the addition of a co-solvent that also dissolves the outer block, followed by a slow solvent exchange to pure water until the system is again kinetically trapped in the new state under equilibrium conditions [Tae05]. The slow solvent exchange can be realized either by dialysis or by a solvent-vapor exchange. The latter case was successfully used to rearrange PMMA-*b*-PMAA-*b*-PMMA triblock copolymers from DMSO/water mixtures by Shull *et al.* [Guvendiren07].

However, those techniques are usually applied for small sample amounts ($\ll 1$ g) and are quite time consuming, which is rather impractical for the larger quantities used in the present work ($10 - 20$ g). Therefore, a temperature change was used instead to transform the system into its equilibrium state without the use of any co-solvent. In this approach, the outer block has to be insoluble at room temperature, but soluble at higher temperatures to "melt" the frozen micelles. This method was previously used for different organogels, *e. g.* PMMA-*b*-

P*t*BA-*b*-PMMA [Drzal03]. For polyelectrolyte hydrogels, Tsitsilianis reported a transition of PS-*b*-PSA-*b*-PS triblock copolymers from turbid solutions into a hydrogel after heating the polymer for 24 hours in aqueous media [Tsitsilianis02].

To induce the hydrogel formation in this thesis, the PMMA-*b*-PSMA-*b*-PMMA triblock copolymers were heated in water for 6 hours at 100 °C (usually as a 2 wt% aqueous solution, if not otherwise noted). This temperature was found to be sufficient to increase the exchange rate of the PMMA block, which was seen on the formation of homogeneous hydrogels, as shown in Figure 4.13. It should be noted that a temperature of 100 °C is sufficient to exceed the glass transition temperature ($T_g$) of PMMA in water, since PMMA is able to absorb a few percent of water, which acts as a plasticizer and decreases $T_g$ considerably [O'Driscoll91, Hancock94]. Extending the heating time from 6 hours to up to one week lead to no further observable structural change (*e. g.* in the SAXS patterns), which indicates that 6 hours were enough time for the system to reach its equilibrium state.

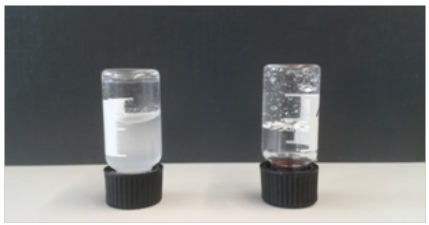

**Figure 4.13:** The PMMA-*b*-PSMA-*b*-PMMA triblock copolymer 60-340-53 as a 2 wt% aqueous solution in its non-equilibrium state (left) and after heating the sample for 6 h at 100 °C (right). The increased PMMA exchange kinetics lead to the formation of a hydrogel.

### Networks with an increasing amount of dangling ends

One type of network defects are dangling ends, which are polymer chains that are only connected with one end to a crosslinking point. Therefore, these chains form no elastic meshes and will contribute not at all or at least less to the mechanical strength of the hydrogel. In the scope of the present thesis, this could be advantageous for the desalination efficiency, since it allows to decouple the charge density and the mechanical strength of the network. It is simple to tune the amount of dangling ends in the physically crosslinked hydrogels by mixing the amphiphilic triblock copolymer PMMA-*b*-PSMA-*b*-PMMA with a varying amount of diblock copolymer PMMA-*b*-PSMA, which has only one hydrophobic endblock. Consequently, each diblock copolymer can only self-assemble into one aggregate resulting in a non-elastic dangling end, as displayed in Figure 4.14.

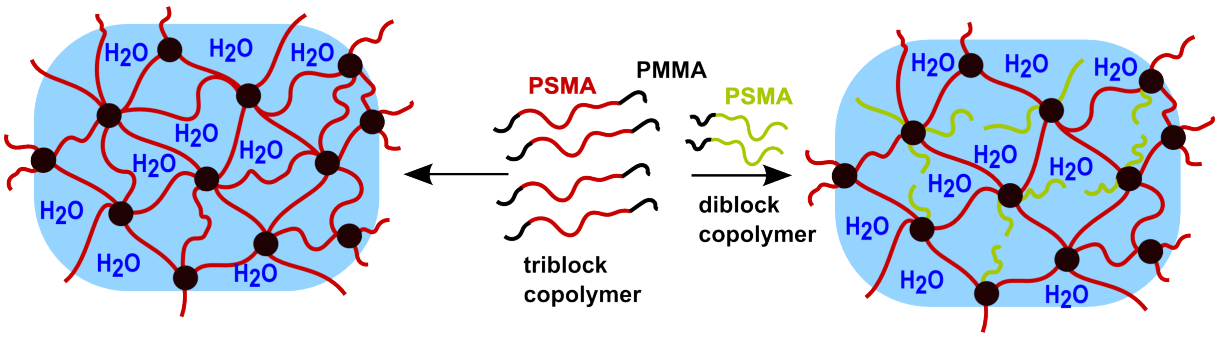


**Figure 4.14:** PMMA-*b*-PSMA-*b*-PMMA triblock copolymers (red-black) can be mixed with PMMA-*b*-PSMA diblock copolymers (green-black) to purposely increase the fraction of dangling ends (right).

### 4.3.4 Chemically crosslinked PSMA-EGDMA hydrogels made by end-linked precursor chains

Chemically crosslinked quasi-model systems are synthesized in this thesis as an alternative to the physically crosslinked hydrogels formed by the self-assembled amphiphilic triblock copolymers. The synthetic strategy was already described in the introduction of this section. As a general idea, the elastic chains are formed first and afterward, a difunctional chemical agent is added to crosslink these chains. In this way, the crosslinking process is temporally separated from the mesh formation and does not take place at the same time, like in the hydrogel formation in the free radical copolymerization.

The anionic polymerization was used to synthesize narrowly distributed P*t*BMA chains, as already described in detail in the previous section, followed by the addition of ethylene glycol dimethacrylate (EGDMA) as the difunctional component. The organogels are subsequently transformed into hydrogels by hydrolysis. This approach can be either used to synthesize polymer stars or networks, depending on the initiator type, as displayed in Figure 4.15. A monofunctional initiator forms star polymers, whereas a difunctional initiator leads to a network formation.

In previous work of other groups, this end-linking process of living polymer chains by EGDMA has been used to synthesize PMMA and PBMA star polymers via anionic polymerization [Efstratiadis94, Held00]. Those results revealed that the number of arms per star polymer depends *i. a.* on the reaction time, the crosslinker to initiator ratio [EGDMA]/[I] and the molecular weight of the linear precursor chains.

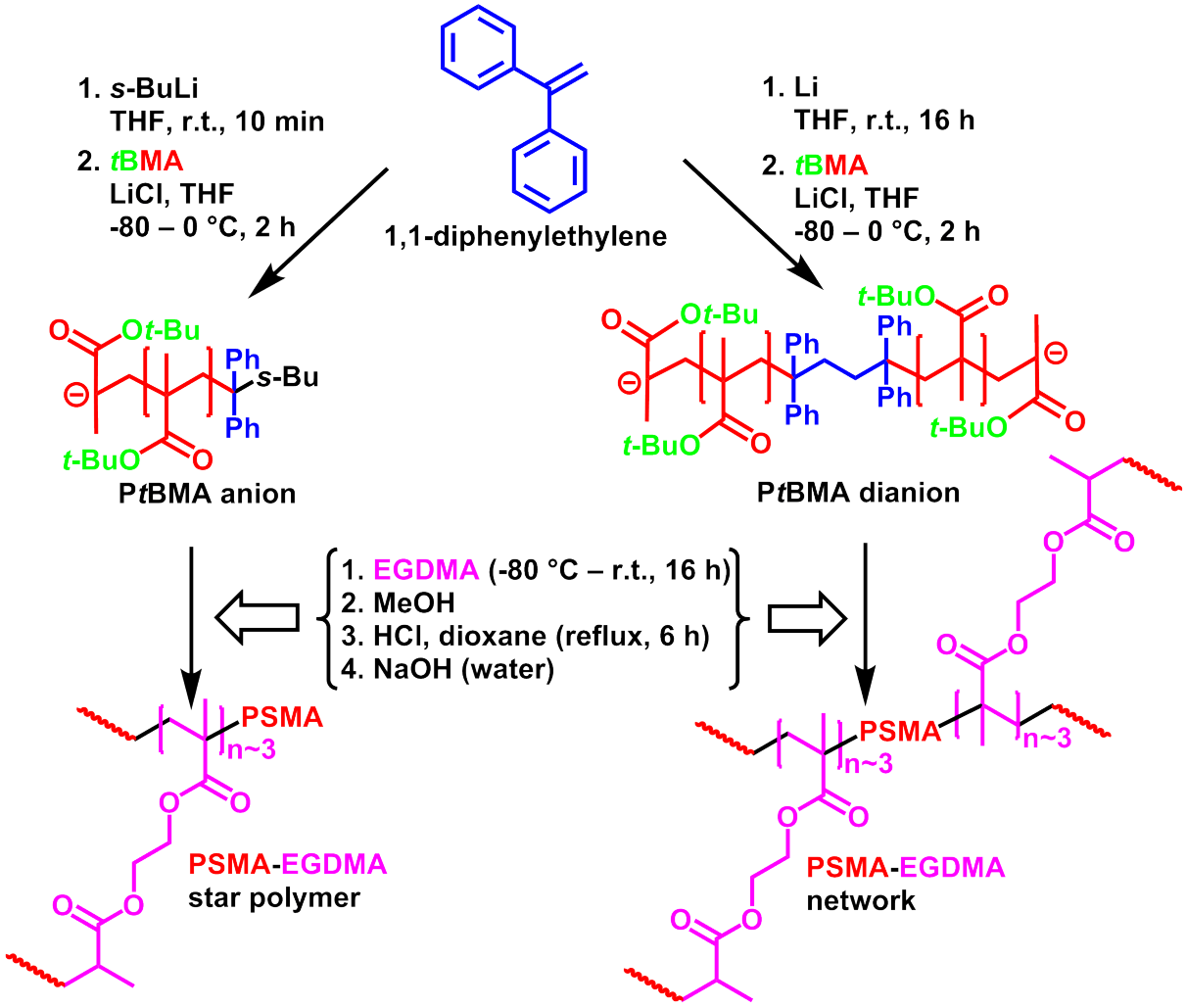


**Figure 4.15:** The synthetic route to produce defined PSMA architectures via the end-linking process of living P*t*BMA polymers. Left) The addition of ethylene glycol dimethacrylate (EGDMA) to the polyanion leads to defined star polymers. Right) If instead a difunctional initiator is used, the end-linking will result in the formation of a network. In both cases, the subsequent hydrolysis and neutralization leads to polyelectrolytes.

In the present thesis, two different star polymers were polymerized first using a monofunctional initiator, in order to find the optimal reaction conditions and to get at least an estimate for the crosslinking functionality in the subsequent network formation. The highest yields of star polymer were obtained, when EGDMA was added at -80 °C to the living P*t*BMA chains and the reaction mixture was then allowed to stir overnight without further cooling, while room temperature was reached. In this manner, mainly one narrow distributed star polymer ($PDI < 1.1$) with five arms was obtained, with less than 20% impurities of linear precursor molecules, as shown in the SEC elugram in Figure 4.16, left. The number of arms $f_w = M_w(\text{star})/M_w(\text{arm})$ was five, independent of the [EGDMA]/[I] ratio, which was only varied in the range of 4 to 7, though. A larger incorporation of arms is probably restricted by steric hindrance without using a much higher amount of EGDMA. The fraction of unreacted precursor chains was with 17% compared to 12% slightly higher for the polymer with the longer arms. These results are also summarized in Table 4.1.

| Sample | [EGDMA]/[I] [mol/mol] | $M_w$ (arm) [kDa] | $PDI$ (arm) [-] | $M_w$ (star) [kDa] | $PDI$ (star) [-] | $f_w$ [-] | $w$ (arm) [mol%] |
|---|---|---|---|---|---|---|---|
| Star-1 | 4 | 17 | 1.05 | 85 | 1.08 | 5.0 | 12 |
| Star-2 | 7 | 52 | 1.04 | 267 | 1.07 | 5.1 | 17 |

**Table 4.1:** The molecular weight $M_w$ and the polydispersity index $PDI$ is shown for two synthesized star polymers and the corresponding precursor chains. The average number of arms per star and the fraction of unreacted precursor molecules is is given by $f_w$ and $w$ (arm), respectively.

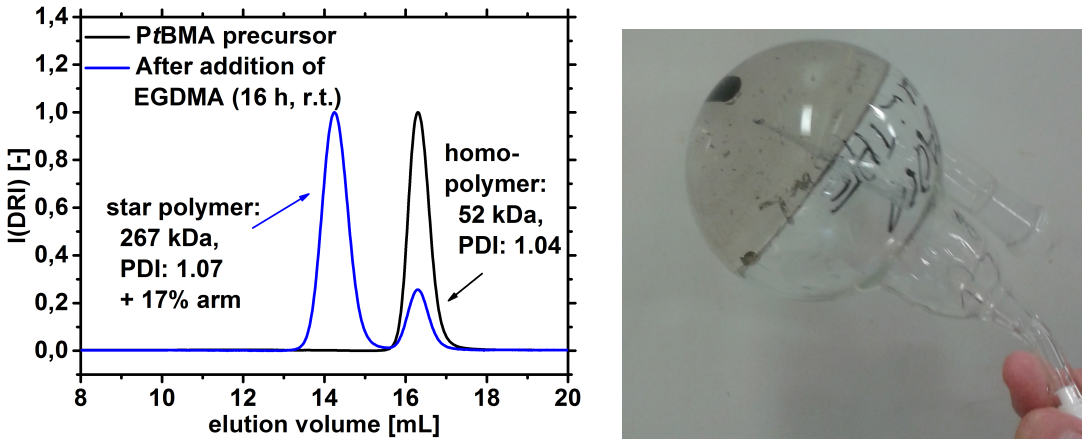


**Figure 4.16:** End-linking of living P*t*BMA polymer chains by the addition of EGDMA in the anionic polymerization. Left) Use of a monofunctional initiator results in the formation of a narrow distributed 5-arm star polymer, as shown in the SEC elugram. Right) Use of a difunctional initiator yields a transparent organogel.

After the successful synthesis of the star polymers, the crosslinked networks were polymerized under the same conditions. The only differences were that a higher polymer concentration was needed to exceed the overlap concentration, and the polymerization was started with a difunctional instead of the monofunctional initiator. This caused a large viscosity increase after the addition of EGDMA and the formation of a homogeneous organogel (see Figure 4.16, right). The sol content was gravimetrically determined by extensive washing of the organogel with THF and was found to be less than 10 wt%. The reaction details and a list with the synthesized hydrogels are shown in Appendix A.1.6.

## 4.4 Interpenetrating PSA-*i*-PSA networks

Various network architectures have been described in the previous sections, which all consist of one single network, where all monomer units are part of the same macromolecule. In recent years, more and more publications have also been focused on so-called interpenetrating networks (IPNs). Interpenetrating double networks contain two individual networks, which cannot be separated unless chemical bonds are broken [Dragan14]. Such double networks were introduced first by Gong *et al.* to improve the mechanical properties of hydrogels, which are often mechanically weak and brittle with low fracture energies or low elastic moduli [Gong03]. Gong *et al.* used rigid and brittle polyelectrolytes as a first network, while a soft and ductile neutral polymer served as the second network [Gong10]. The strong network entanglements lead to extremely high mechanical strength and high mechanical toughness, comparable to rubbers [Gong03, Chen15].

The idea in the scope of this thesis is to use the homo-interpenetrating double network PSA-*i*-PSA due to two different reasons.[4] First, the charge density could be highly increased without lowering the absorbency much. Second, the formed double network should have a more homogeneous charge density compared to the single network, even though the network structure (including polymer mobility) is more heterogeneous: In the single network, the typical clustering of highly crosslinked areas leads to a broad pore size distribution (see Figure 4.6(A)). If a second monomer solution is polymerized within the first network, the second network will have a heterogeneous structure, too. However, the highly crosslinked parts of the second network might be more likely placed in the larger pores of the first network and they could be therefore spatially separated from the clusters of the first network. Hence, the overall charge density throughout the whole network would be more homogeneously distributed.

The method generally used to synthesis interpenetrating double networks is the two-step sequential polymerization [Gong10, Chen15]: A polyelectrolyte hydrogel is polymerized first.

[4] A part of the double networks were synthesized by Mr. Raphael Geissinger under the supervision of the author.

Then, this network is swollen in an excess of a second neutral monomer solution. The reactants of the second network will diffuse into the first gel network, which undergoes a large volume expansion, due to the high swelling nature of the polyelectrolyte [Chen15]. After reaching the absorbency at equilibrium (*e. g.* after 1 – 3 days), the second monomer is polymerized, resulting in a double network, as schematically displayed in Figure 4.17.

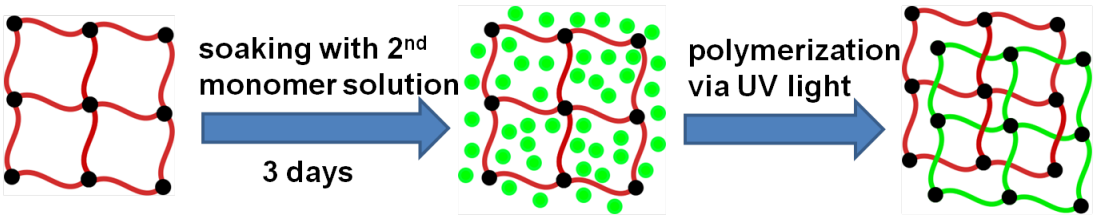


**Figure 4.17:** Scheme to synthesize interpenetrating double networks. The degree of crosslinking can be adjusted in both networks separately and does not have to be the same, as displayed here.

Other methods to synthesize IPNs are for example based on the simultaneous polymerization of both networks. This can be realized, when the precursors of both networks are mixed and synthesized at the same time by two independent, non-interfering routs such as chain- and step-growth polymerization [Dragan14]. However, the monomer choice is usually limited by this method, which was therefore not used in this work.

Many parameters can be adjusted by synthesizing double networks in the two-step sequential polymerization: The *DC*, the *DN* and the polymer concentration of both reactant solutions may be varied. Furthermore, the ratio of second to first monomer solution can also be changed. To keep the number of samples manageable, but still large enough to observe a wide range of different structures, the following parameters were used: The monomer concentration of both precursor solutions was kept constant at 25 wt% ($Q_{syn}$ = 4). The first PAA network was always neutralized by 75 mol% prior to the reaction and polymerized in a mold of usually 4 mL volume to get a disk-shaped hydrogel. This disk was then swollen in an excess of the second precursor solution containing acrylic acid, the crosslinker and a photoinitiator. The photoinitiator was used instead of a thermal redox initiator to allow longer soaking times of 3 days without a premature polymerization. The finally polymerized double networks were fully neutralized and extensively washed to remove all contaminates. A full list with all synthesized interpenetrating networks and a detailed description of the synthetic procedure is given in Appendix A.5. The following nomenclature is used to name the double network samples: PSA-DCx-*i*-PSA-DCy, where x and y describe the *DC* of the first and second network, respectively, which were varied over the range of 0.3 to 5 mol%.

### Semi-Interpenetrating networks

In addition to the double networks, other interpenetrating networks, which are referred to as semi-IPNs, were synthesized in this thesis. Semi-IPNs consist of two polymer components, where one has a network and the other a linear structure [Dragan14]. The idea, to use this kind of architecture for the desalination, is a decoupling of charge density and mechanical strength. Linear or star polymers should be trapped inside the network to add charge density without significantly increasing the mechanical moduli of the hydrogel (see Figure 4.18). However, satisfying results could not be realized with the semi-IPNs, which shall therefore not be discussed any further in this work. The challenge was that the used linear or star polymers, which were tried to be trapped inside the hydrogel by a lot of intermolecular entanglements with the network, were either too small or too large. If the polymers were too small, they were almost completely leaked out, while swelling the hydrogel in an excess of water. In contrast, if the linear polymers were too large, no sufficiently hydrogel formation was realized during the synthesis. Whether it is even possible to fabricate semi-IPNs, where the linear or star polymers will not be leached out, remains still questionable. However, it should be noted that simulations of coarse-grained hydrogels suggest that such semi-interpenetrating networks will not strongly affect the desalination efficiency or might perform even worse [Richter17a].

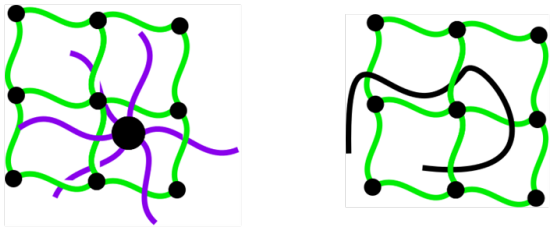

**Figure 4.18:** Two semi-IPN's, where either star or linear polymers are trapped by network entanglements inside a hydrogel.

## 4.5 Thermally responsive hydrogels based on PNIPAAm

As introduced in Chapter 2, Ali *et al.* published a similar approach to desalinate saltwater in a membrane-free process via polyelectrolyte hydrogels. They incorporated thermally responsive groups to deswell the hydrogels by temperature instead of pressure as an external stimulus.

The thermally responsive groups were made of poly(N-isopropylacrylamide) (PNIPAAm), which is a well studied polymer with a lower critical solution temperature (LCST) at around 32 °C [Halperin15]. The reversible volume phase transition of PNIPAAm upon heating is caused by a change in its hydration state. The weakening of hydrogen bonds between polymer and

surrounding water molecules induces a transition from a hydrophilic to a more hydrophobic state, which finally causes a phase transition, as seen in Figure 4.19 [Halperin15].

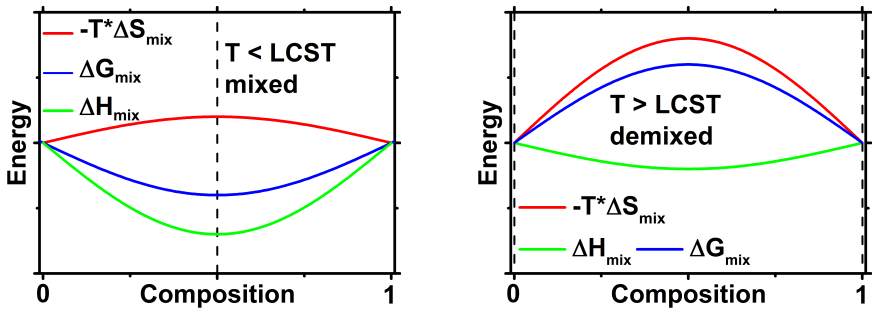


**Figure 4.19:** The phase transition from one mixed phase to two demixed phases ($X_A$ and $X_B$) caused by increasing the temperature above the lower critical solution temperature (LCST) is shown. The H-bonds between water and amide molecules become weaker upon heating. This leads to an increase of both, the mixing enthalpy $\Delta H_{mix}$ and the entropic term $-T * \Delta S_{mix}$. Above the LCST, the mixing energy $\Delta G_{mix}$ becomes positive and the system demixes.

The hydrophobicity of the polymer network is crucial for the phase transition and hence, the LCST of P(NIPAAm-*co*-SA) networks is strongly influenced by parameters such as salinity of the solution, the ratio of NIPAAm to AA and the degree of neutralization of AA [Hirotsu87, Yu93, Brazel95, Liu04, Pei04]. The introduction of too many hydrophilic groups will lead to a disappearance of the LCST due to the weakened hydrophobic aggregation force [Zhang08].

### 4.5.1 P(NIPAAm-*co*-SA) copolymer networks

The P(NIPAAm-*co*-SA) networks were synthesized via the free radical copolymerization of partly neutralized acrylic acid with NIPAAm and MBA in water below the LCST (see Figure 4.20). The synthetic procedure and a list with all produced samples are given in Appendix A.1.8. In the present thesis, the *DC* and the ratio of NIPAAm to SA in the networks were systematically varied over the range of 0.3 – 1 mol% and 0 – 100 mol%, respectively.

Although the synthesis is similar to the polymerization of sodium acrylate described in Section 4.1, the following aspects should be considered:

- NIPAAm is less soluble in water and therefore, the monomer concentration during the polymerization was decreased from 25 to 20 wt% ($Q_{syn}$ = 5).
- The polymerization kinetics of NIPAAm were found to be much faster and thus, a smaller amount of the accelerator TEMED was used.
- The temperature of the reaction mixture was kept below the LCST of NIPAAm during the polymerization, since otherwise, only mechanically weak, white and rather undefined

hydrogel samples were obtained (see Figure A.1 in Appendix A.1.8). In order to control the polymerization heat, the synthesis was only carried out in smaller batches using less than 10 g monomer.

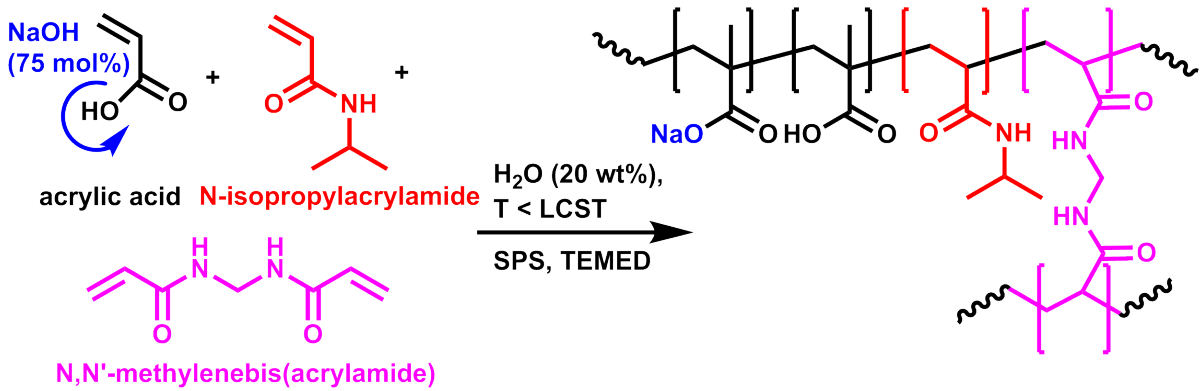


**Figure 4.20:** Free radical polymerization of P(NIPAAm-*co*-SA) hydrogels.

The dried P(NIPAAm-*co*-SA) networks were chemically analyzed by FT-IR spectroscopy. Three peaks can be distinguished, which were found to be specific for the ratio of NIPAAm to SA, as displayed in Figure 4.21:

- Integration boundaries of Peak 1 (CO-stretching): $1475 - 1605\,\mathrm{cm}^{-1}$.
- Integration boundaries of Peak 2 (NH-bending): $1605 - 1750\,\mathrm{cm}^{-1}$.
- Integration boundaries of Peak 3 (mainly water content): $2722 - 3722\,\mathrm{cm}^{-1}$.

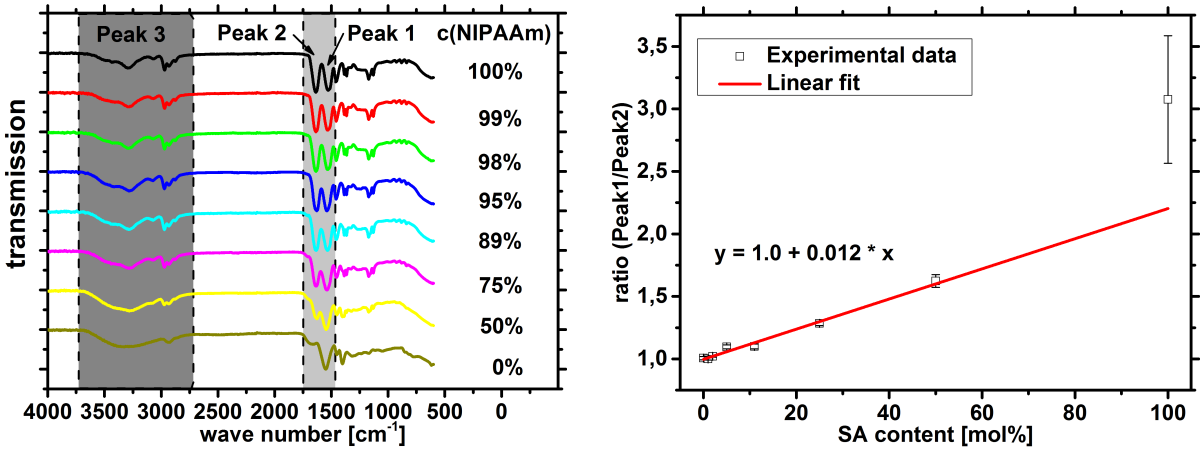


**Figure 4.21:** Left) FT-IR spectra of different P(NIPAAm-*co*-SA)-DC1 copolymers with a varying NIPAAm fraction. The three peaks correspond to CO-strechting (Peak 1), NH-bending (Peak 2) and water (Peak 3). Right) The integral ratio of Peak 1 and Peak 2 is plotted against the SA content.

The following conclusions can be drawn from the FT-IR measurements: The water content (Peak 3) increases with a higher SA content, since the more hydrophilic samples absorb more and faster moisture from the environment. Furthermore, the ratio of the integrals from Peak 1 and Peak 2 are compared after a baseline correction (subtraction of the maximum in between 500 and 2000 $cm^{-1}$ as a constant). The integral ratio is plotted as a function of the SA fraction in Figure 4.21, right. The ratio increases since less amide groups (Peak 2) are present. The data was fitted with a linear function to calculate the NIPAAm content in unknown samples, as shown in the next section.

### 4.5.2 Interpenetrating PSA-*i*-PNIPAAm double networks

The synthesis of the interpenetrating double networks PSA-*i*-PSA has been already described in Section 4.4, where the aim was a maximization and homogenization of the charge density. In case of the PSA-*i*-PNIPAAm double networks, the goal is to enhance the thermal response compared to the single P(NIPAAm-*co*-SA) networks [Zhang08, Dragan14]. The hydrophobic aggregation force of PNIPAAm generally correlates with the PNIPAAm segment length [Zhang08, Ali15]. However, the segment length will be considerably reduced to 50, 33 or 20% of its initial length, even if only small fractions of 1, 2 or 5 mol% SA are statistically incorporated into the elastic chain. Consequently, it was reported that a distinct LCST will vanish with only a small amount of SA units in the range of 1 – 2 mol% [Zhang08], while the thermal response disappears above 10 to 18 mol% SA [Yu93].

Zhang *et al.* summarized different strategies to improve the response rate of thermosensitive PNIPAAm hydrogels [Zhang08]. One main aspect is the use of different network architectures to get longer PNIPAAm segments and a higher SA content without losing the thermal responsiveness. Such network types can include grafted polymer segments [Ali15] or interpenetrating double networks [Chen04].

In this thesis, different PSA-*i*-PNIPAAm double networks are synthesized, where either the *DC* of the first or the second network is varied. The synthesis is very similar to the procedure described in Section 4.4 and can be found in detail in Appendix A.1.8, where also a table with the produced samples is provided. During the synthesis, the PSA hydrogels were polymerized first, which were then fully swollen in an excess of the NIPAAm monomer solution. This order maximizes the absorbency of the second monomer solution due to the higher osmotic forces of the polyelectrolyte [Gong10, Chen15].

The amount of the second network depends on the degree of swelling of the first network and therefore, mainly on the *DC*. The content between SA and NIPAAm in the double networks was gravimetrically measured and also determined by FT-IR, using the calibration from Figure 4.21.

Both measurements are compared in Figure 4.22, where it can be seen that the NIPAAm content decreases with the *DC* of the first PSA network due to the lower absorbency.

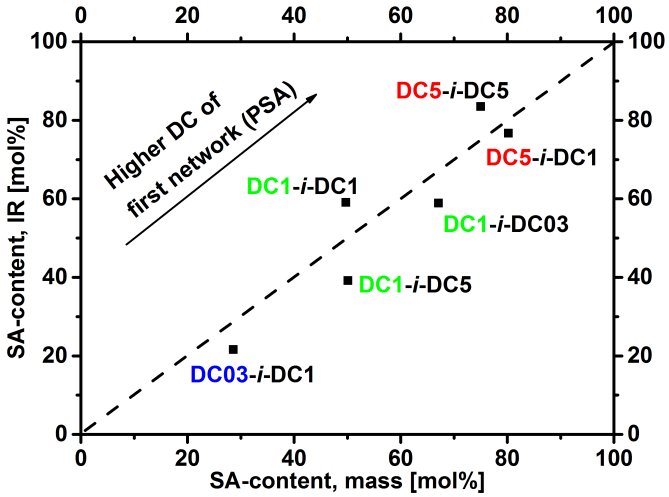


**Figure 4.22:** The amount of PSA in the PSA-*i*-PNIPAAm double networks as measured by FT-IR and mass, respectively. The sample names are given in their short form, where the *DC* of the PSA (first number) and PNIPAAm (second number) network is noted.

## 4.6 Summary

The synthesis of a large variety of polyelectrolyte hydrogels with different topologies was described in this chapter. PSA and PSMA hydrogels with a varying degree of crosslinking were made by free radical polymerization. These randomly crosslinked polymers serve as a reference system for the other network architectures. One part of these reference hydrogels was additionally crosslinked at the particle surface via an esterification with a diepoxide. This leads to core-shell particles with a specifically desired higher crosslinking density at the surface. Interpenetrating PSA-*i*-PSA double networks were produced as another network type. This architecture, which consists of two individual PSA polymer networks, was accomplished by polymerizing a second monomer solution within a first PSA network.

Furthermore, networks with a defined elastic chain length ($PDI = 1.04 - 1.17$) were synthesized via anionic polymerization of P*t*BMA, followed by hydrolysis and neutralization to PSMA. Two different approaches were used to crosslink these meshes: The chemically endlinking of the living polymer chains with EGDMA and the self-assembly of amphiphilic ABA triblock copolymers, as the hydrophobic PMMA endblocks phase separate into aggregates to obtain physically crosslinked hydrogels. These physically crosslinked hydrogels offered

the possibility to easily tune the amount of dangling ends in the networks by mixing the PMMA-*b*-PSMA-*b*-PMMA triblock copolymers with PMMA-*b*-PSMA diblock copolymers.

In addition to the pure polyelectrolyte hydrogels, also thermally responsive PNIPAAm segments were incorporated into the network by the copolymerization of the respective monomers or in form of interpenetrating PSA-*i*-PNIPAAm double networks.

In this chapter, standard characterization methods in polymer chemistry (like SEC, $^{1}$H-NMR spectroscopy and FT-IR) were employed to verify the synthetic procedures, but without gathering information about the macroscopic properties of the produced hydrogels. In the next chapter, the structure of the polyelectrolyte networks is investigated in more detail by different methods. Swelling experiments and rheology study the most important macroscopic quantities in hydrogels. Furthermore, NMR relaxometry and small angle X-ray scattering experiments are used to gain a deeper insight and understanding of the network topology.

# 5 Characterization

The knowledge of the basic properties of the self-synthesized hydrogels is of crucial importance for the desalination process and the osmotic engine. Thus, a fundamental understanding of the hydrogel features is necessary to optimize these applications.

In this chapter, the basic characteristics of the produced gel samples are investigated. The macroscopic properties are probed by swelling and rheological measurements. The water absorbency is the essential feature of a hydrogel. The amount and dynamics of the solution uptake is consequently the first quantity to be studied. The mechanical behavior of the polymers determines the resistance of the material in the desalination process (see Chapter 6), since pressure is needed to squeeze the gel samples. Furthermore, the mechanical properties also limit the energy output in the osmotic engine (see Chapter 7).

In addition to the macroscopic properties, the microscopic picture and the pore size distribution are investigated. Small angle X-ray scattering provides a direct measurement of the distance between crosslinking junctions in the quasi-model hydrogels, which correlates with the mesh length. Furthermore, $^{1}$H-NMR relaxometry is used to measure the polymer mobility in the network. The different flexibility of chain segments is probed and correlated to the hydrogel structure to draw conclusions about the network architecture.

In this chapter, the theories behind the characterization methods are briefly explained first. Details are given how the experiments were conducted and how the raw data was treated to reduce the amount of collected data to a meaningful minimum. This provides a set of parameters to quantify the hydrogels properties, which are subsequently used to compare the different network topologies. The characterization of the different network types is separately described in the respective sections, but the samples are always compared with respect to the reference hydrogels in Section 5.2.

## 5.1 Short description of the applied characterization methods

### 5.1.1 Water absorbency

The ability to absorb and retain large volumes of water or aqueous solution is probably the most important property of polyelectrolyte hydrogels [Elliott04]. This polymeric material is therefore ideal to be used in water absorbing applications, as described in Chapter 1 [Buchholz98]. Upon swelling, the elastic chains of the network get expanded, while the crosslinking points prevent an *infinite* swelling, *i. e.* dissolving. At equilibrium conditions, the tendency of the hydrophilic chains to swell to infinite solution and the elastic retraction force of the network are in balance, as explained in Section 3.2.

The degree of swelling $Q(t)$, which is quantified by the ratio of solvent to polymeric material, is extensively used for the characterization of hydrogels due to its simplicity.[1] This ratio can be either defined by mass or volume. In this thesis, the mass ratio (see Equation 5.1) is used, as it can be simply gravimetrically measured, as explained in detail in Appendix A.2.2.

$$Q(t) = \frac{m_\mathrm{s}(t)}{m_\mathrm{p}}\,, \tag{5.1}$$

where $m_\mathrm{p}$ is the mass of dried polymer and $m_\mathrm{s}$ is the mass of solvent, *e. g.* deionized water or an aqueous NaCl solution.

The degree of swelling at equilibrium $Q_\mathrm{eq} = \lim_{t\to\infty} Q(t)$ depends on solvent quality, temperature, external pressure and several synthetic parameters such as monomer type, degree of crosslinking (*DC*) and degree of neutralization (*DN*) [Buchholz98, Elliott04]. The following trends are characteristic for hydrogels and well known [Brannon-Peppas90, Elliott04, Höpfner13a]: The degree of swelling $Q_\mathrm{eq}$ is monotonically decreasing with an increasing degree of crosslinking [Flory53, Yin92, Schröder96]. A higher *DC* leads to more elastic constraints, *i. e.* the elastic term $\mu_\mathrm{el}$ becomes larger and thus, the water uptake reduces, which will be discussed in more detail in Section 5.2.

As already explained in Section 3.2, ionic hydrogels show a high solvent capacity and the ionic term $\mu_\mathrm{ion}$ is usually much larger than the mixing term $\mu_\mathrm{mix}$, as seen in Figure 3.2. Therefore, the amount of charges along the elastic chains, *i. e.* the degree of neutralization, has a large influence on $Q_\mathrm{eq}$. In Flory's network theory, the water absorbency increases monotonically with a higher *DN*, which is within this theory reflected by a change of the interaction parameter $\chi$ [Flory53, Brannon-Peppas90, Safronov15]. In contrast, in some work a plateau value or even a slight decrease is experimentally observed at a very high *DN*. This behavior can be explained by

[1] In chapter 3 the degree of swelling is described by $q$, which is however defined as the volume ratio.

considering the counterion condensation that limits the number of free ions, which contribute to the osmotic pressure, after a certain value [Hasa75, Konak89, Elliott04]. The dependency of $DN$ on the degree of swelling is shown for a typical poly(acrylic acid) hydrogel used in this work in Figure 5.1, left. The trend can be qualitatively described by considering the counterion condensation.

As the hydrogels in this work are employed in NaCl solutions, it is important to understand how the degree of swelling changes with the salt concentration. A higher salinity decreases the driving force for swelling, since the difference between the osmotic pressure inside and outside the network becomes smaller. Consequently, the absolute value of the electrostatic contribution $\mu_{\text{ion}}$ is smaller in higher concentrated NaCl solutions and $Q_{\text{eq}}$ is decreasing. The experimental data for a 1 mol% crosslinked poly(sodium methacrylate) hydrogel is displayed in Figure 5.1, right. For this sample, it was empirically found that the power fit $Q_{\text{eq}} = 13.5 * c(\text{NaCl})^{-0.41}$ represents the data well.

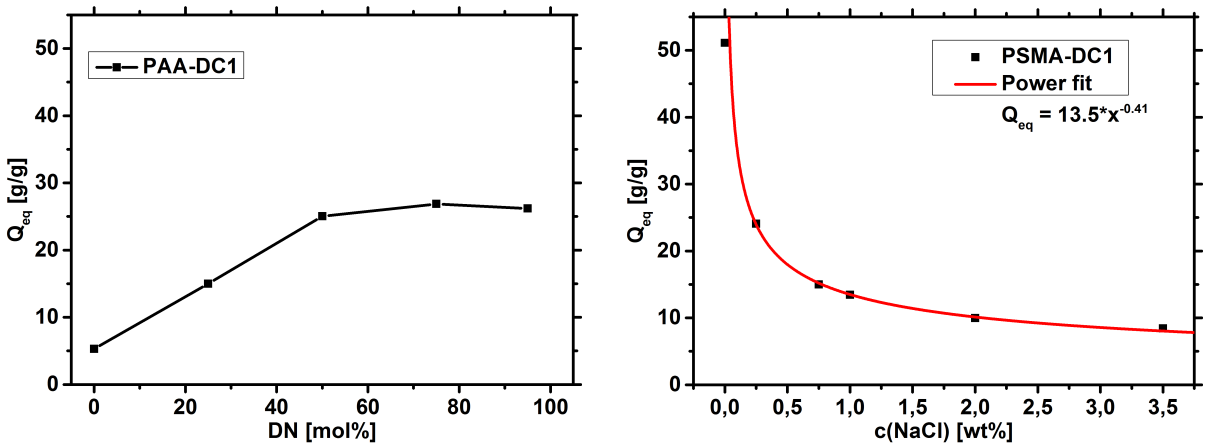


**Figure 5.1:** Left) The dependency of the degree of swelling $Q_{\text{eq}}$ on the degree of neutralization $DN$, measured in a 1 wt% NaCl solution. Right) $Q_{\text{eq}}$ as a function of salinity for PSMA-DC1.

The water absorption $Q(t)$ is a time-dependent process [Tanaka79, Buchholz98], where the velocity of the water uptake is interesting in the scope of this work, as this a limiting factor for the efficiency in the osmotic engine (see Chapter 7). In all the samples in this work, a monotonic increase of the degree of swelling with time was observed. The swelling kinetics depend mainly on the size and shape of the particles, as well as the maximum degree of swelling, since it is a diffusion controlled process. The experimental data was usually fitted well with Equation 5.2.

$$Q(t) = Q_{\text{eq}} * \left[1 - \exp\left(\frac{-t}{\tau}\right)\right], \tag{5.2}$$

where $\tau$ is the characteristic swelling time.

No clear trends were discernible for the various network structures and $\tau$ was found to be within the range from 0.3 to 6.2 min for ground samples with a dried particle size between 350 and 650 µm. The characteristic swelling time $\tau$ increases with the maximum degree of swelling at equilibrium $Q_{eq}$ in a 1 wt% NaCl solution, as these hydrogels need longer times to absorb more water, as displayed in Figure 5.2.

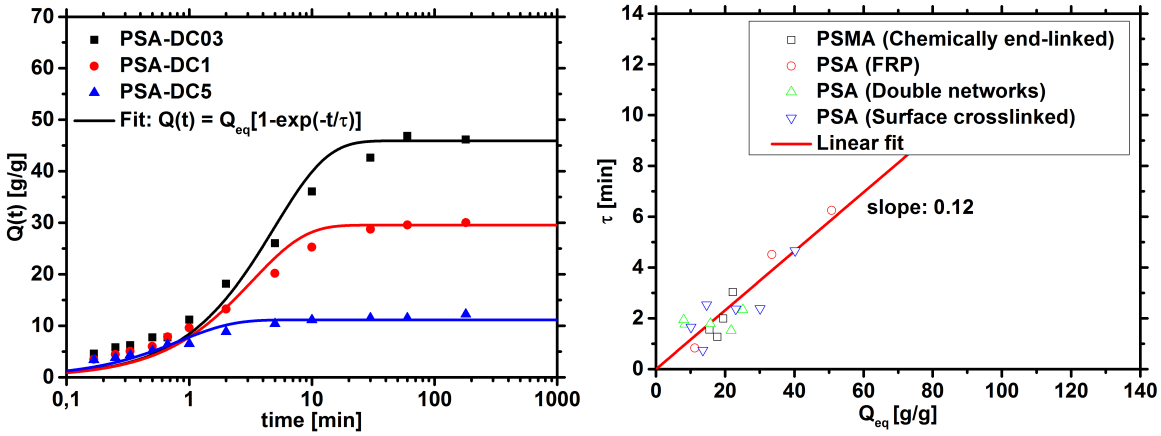


**Figure 5.2:** Left) Swelling kinetics for three PSA reference hydrogels swollen in a 1 wt% NaCl solution. Right) The characteristic swelling time $\tau$ is plotted against the degree of swelling at equilibrium $Q_{eq}$ for various network structures swollen in a 1 wt% NaCl solution. The linear fit (of all data points) indicates that the swelling kinetics depends mainly on the maximum water uptake, but less on the internal network structure.

### 5.1.2 Rheology

Rheological measurements are used to study the mechanical properties of the fully swollen hydrogels in deionized water. Hydrogels can be typically characterized either in the *as prepared* state or swollen to equilibrium in different aqueous solutions. In the *as prepared* state, the monomer solution can be directly polymerized in a cylindrical mold to obtain disk-shaped specimens (see [Höpfner13a], p. 32). However, most of the hydrogels produced in this thesis needed an additional chemical treatment (like hydrolysis, surface crosslinking, etc.) and therefore, the hydrogels could not be prepared in a suitable mold. Additionally, the *as prepared* state does not allow to remove undesired material from the hydrogel networks, like sol or unreacted monomers, which can strongly influence the rheological properties. Another advantage of using fully swollen samples is that the obtained mechanical moduli are comparable to the ones found in the actual application, *e. g.* the osmotic engine.

For hydrogels, the routinely employed methods to measure mechanical moduli are oscillatory shear and compression tests. In oscillatory shear rheology, the suitable experimental parameters

can be found in a relatively fast and easy way. The experiments were conducted on the strain-controlled rheometer Ares G2 and the input parameters are listed in Appendix A.2.3. The following considerations and mathematical deviations are based on the book of Thomas Mezger [Mezger06].

### Oscillatory shear rheology

In oscillatory shear rheology, the hydrogel specimen is excited by a sinusoidal shear strain with the amplitude $\gamma_0$ and the angular frequency $\omega$, while the resulting stress $\sigma$ and the phase angle $\delta$ are measured, as displayed in Figure 5.3. The complex shear modulus $G^*$ is calculated in the linear viscoelastic (LVE) regime by

$$G^* = \frac{\sigma^*(t)}{\gamma^*(t)} . \tag{5.3}$$

The complex shear modulus defines the gel strength and can be separated into the storage modulus $G'$, which describes the elastic part, and the loss modulus $G''$, which reflects the viscous part of the sample (see Figure 5.3 and Equation 5.4 and 5.5).

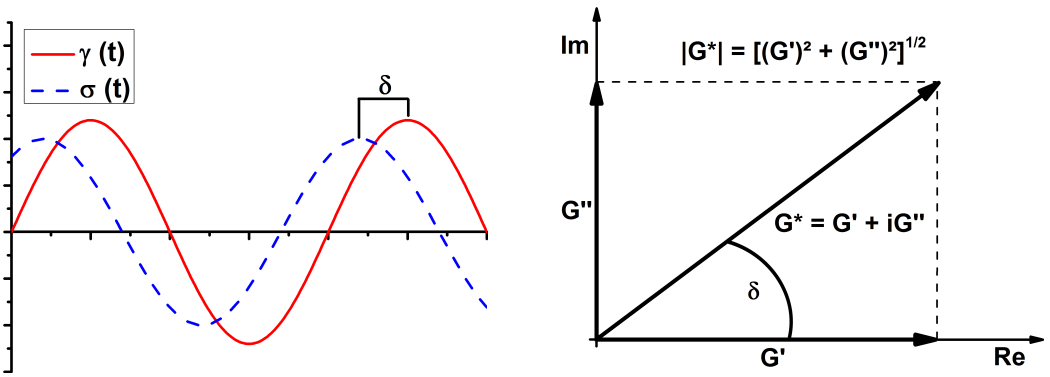


**Figure 5.3:** Fundamentals of oscillatory shear rheology: Left) The sample is excited by a sinusoidal shear strain $\gamma_0$. The resulting stress $\sigma$ and the phase angle $\delta$ are measured. Right) Vector diagram showing the complex shear modulus $G^*$ and its subdivision into the elastic part (storage modulus $G'$) and the viscous part (loss modulus $G''$).

$$G' = \left(\frac{\sigma}{\gamma}\right) * \cos\delta \tag{5.4}$$

$$G'' = \left(\frac{\sigma}{\gamma}\right) * \sin\delta \tag{5.5}$$

The ratio between viscous and elastic part is described by the loss factor $\tan\delta$ (see Equation 5.6) and quantifies the viscous contribution.

$$\tan\delta = \frac{G''}{G'} \tag{5.6}$$

For an ideal viscous material (*e. g.* water) $\tan\delta$ approaches *infinity*, while for an ideal elastic material (like a spring) $\tan\delta = 0$. The rheological behavior for polymer hydrogels is in between these two limiting cases and the mechanical quantities depend on a number of experimental parameters, such as frequency, strain and applied axial force.

To study a new sample, first an oscillatory strain sweep was applied to find the LVE regime. In this test, the polymer sample was sheared with a constant frequency (here: $\omega = 1$ rad/s) and the amplitude was varied over a large range (here: $\gamma_0 = 2 * 10^{-5} - 10$). The resulting complex modulus and the loss factor are plotted for the fully swollen sample PSA-DC1 as an example in Figure 5.4, left. In the LVE regime, both quantities are independent of the applied strain and show a constant plateau. The loss factor $\tan\delta$ was found to be in the range of $0.01 - 0.1$, which is related to the gel character of the material and is very typical for networks [Mezger06].

As a second measurement, frequency sweeps were employed, in which the amplitude was kept constant (here: $\gamma_0 = 0.1\%$, which was always assumed to be in the LVE regime, see Figure 5.4), while the frequency was changed in the range from 0.1 to 100 rad/s. Typical curves for the mechanical modulus $G'$ and $G''$ are displayed in Figure 5.4, right.

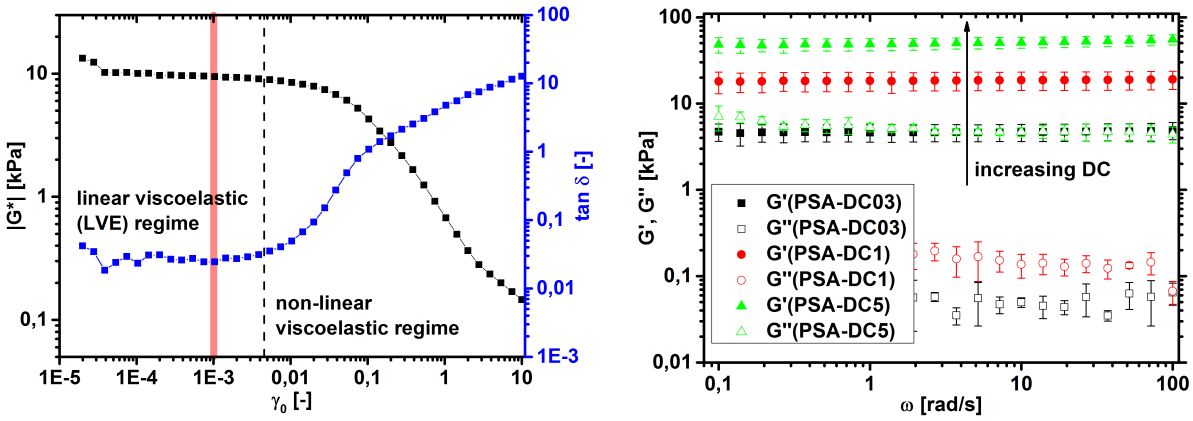


**Figure 5.4:** Left) Oscillatory strain sweep for sample PSA-DC1 at 1 rad/s. Right) Frequency sweeps for three different crosslinked PSA hydrogels at 0.1% amplitude.

The following conclusions can be drawn from this graph and the three samples investigated:

- $G'$ and $G''$ show both an independent behavior of the applied frequency and stay constant over the whole frequency range.
- $G'$ is always about a factor of $10 - 100$ higher than $G''$, which is typical for hydrogel networks.

- Both mechanical moduli ($G'$ and $G''$) are increasing with a higher degree of crosslinking, which will be discussed in more detail in Section 5.2.

It is useful to reduce the amount of collected data points to a minimum in order to compare the different network types in this work. Therefore, the absolute of the complex modulus $|G^*|$ at 0.1% strain and 1 rad/s, which was measured by frequency sweeps, is taken as the characteristic rheological quantity.

#### Oscillatory compression

Mechanical properties can be also determined by oscillatory deformation tests in compression. In these measurements, a small sinusoidal deformation (dynamic strain $\epsilon$) is superimposed on a larger static strain $\lambda_s$. The static prestrain has to be higher than the dynamic strain to ensure that the sample is always in contact with the geometry. This makes the compression tests more complex and more effort is usually needed to find suitable test parameters for measuring new samples. Instead of $G$ moduli, which are measured by oscillatory shear, Young's moduli $E$ are accessible by oscillatory compression. Both quantities are connected by the *Trouton* ratio

$$\frac{|E^*|}{|G^*|} = 2 * (1 + \mu), \tag{5.7}$$

where $\mu$ is the *Poisson* ratio. For rubber-elastic materials, like hydrogels, $\mu$ is 0.5, yielding in $|E^*| = 3 * |G^*|$. This relationship was also confirmed in this work by comparing the frequency sweeps of the sample PSA-DC1 measured with both methods, in oscillatory shear and in compression, as displayed in Figure 5.5.

The compression measurements were carried out with an Eplexor 150, which was additionally equipped with a humidifier to control the humidity (see Appendix A.2.3). The humidifier allows measurements at higher temperatures without drying the hydrogel specimens. However, the drying of the hydrogels was found to be negligible during the rheological measurements in oscillatory shear at room temperature since the measuring time per sample was kept short (below 45 minutes). In the subsequent sections, only the $G$-moduli of the different hydrogel samples are compared, since this quantity is easier accessible and no further information is obtained from the $E$-moduli. The measured temperature sweeps of PNIPAAm hydrogels, where the temperature is gradually increased, while the other parameters are fixed, are one exception. There, a controlled humidity was necessary to avoid drying upon heating and thus, the tests were performed in compression at the Eplexor 150 using the humidifier. The input parameters for the experiments are listed in Appendix A.2.3.

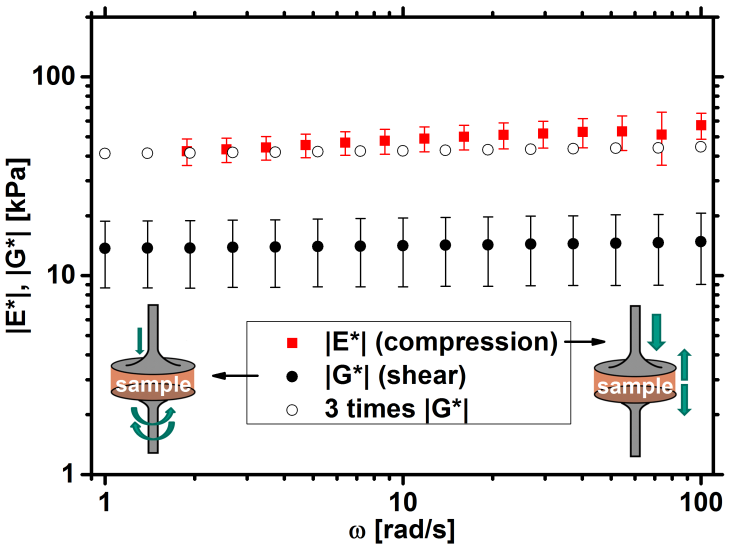


**Figure 5.5:** Comparison of oscillatory shear and compression tests on sample PSA-DC1. $|E^*|$ is three times as high as $|G^*|$, as theoretically predicted by the Trouton ratio having a *Poisson* ratio of $\mu = 0.5$ (see Equation 5.7).

### 5.1.3 Small angle X-ray scattering (SAXS)

SAXS is a powerful method to characterize the structure of condensed matter on the length scale between 1 and 500 nm. It is therefore suitable to analyze the morphology in block copolymers, since they can phase separate in structures, where the microphase domain size is on an appropriate length scale [Glatter82].

In general, the interference between electromagnetic radiation and matter may be desrcibed by two different processes — absorption and scattering. Absorption is a dissipative phenomenon that is quantified by Lambert-Beer's law:

$$I_t = I_0 * \exp\left(-\epsilon_i(\lambda) c_i L\right) , \tag{5.8}$$

where $\epsilon_i(\lambda)$ is the extinction coefficient, $c_i$ is the concentration of the absorbing species i, $L$ is the length of the irradiated sample, $I_0$ is the initial intensity and $I_t$ is the intensity of the transmitted radiation.

Scattering occurs, when electromagnetic waves interfere with the electrons of an atom or molecule. The observed scattering intensities are interferences of all scattered electromagnetic waves. It can be distinguished between elastic scattering, where the frequency of the scattered waves is unchanged (Thomson scattering) and inelastic scattering, where the frequency is altered (Compton scattering).

In most SAXS experiments, the inelastically scattering processes can be neglected, while the absorption can be experimentally determined and depends on the initial intensity of the

primary beam. In the following, only the elastic scattering should be considered. In this case, the radiation frequency remains unchanged and the wave vectors are described by [Schnablegger13]:

$$|\vec{k_0}| = |\vec{k}| = \frac{2\pi}{\lambda}\,, \tag{5.9}$$

where, $\vec{k_0}$ and $\vec{k}$ are the wave vectors of the primary beam and the scattered beam, respectively, and $\lambda$ is the wave length of the X-rays (here: $\lambda = 1.54$ Å).

In order to become independent from the wave length $\lambda$, the scattering patterns are usually presented as a function of the wave vector

$$\vec{q} = \vec{k} - \vec{k_0} = \frac{4\pi}{\lambda} * \sin(\theta)\,, \tag{5.10}$$

where $\theta$ is the scattering angle, as shown in Figure 5.6.

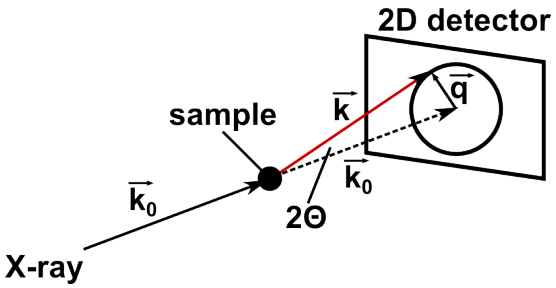


**Figure 5.6:** Schematically illustration of a SAXS experiment, adapted from [Langela01].

In a SAXS experiment, the X-rays penetrate the sample and the resulting scattering intensity, originating from areas with different electron densities, is recorded by the detector, as schematically shown in Figure 5.6. As a result, a 2D interference pattern is obtained, which is characteristic for the sample morphology. Whether constructive or destructive interference is observed, is described by Bragg's law:

$$n\lambda = 2d * \sin(\theta)\,, \tag{5.11}$$

where $n$ is a positive integer and $d$ is the distance of identical crystal layers.

If block copolymers phase separate into a highly ordered and periodical arrangement, a pronounced peak in the $q$-space will be observed. Its maximum indicates the distance between the aligned phases for lamellar structures. In case of spherical microdomains, the distance between the centers of next neighboring spheres is observed:

$$d = \frac{2\pi}{q_0}\,. \tag{5.12}$$

As an important requirement, the analyzed networks need regular ordered microdomains with different electron densities. Only if the polymer segments in the block copolymer have a different electron density, their periodic microphase separation will result in a periodical electron density distribution in the material.

In this thesis, only the anionicially synthesized hydrogels had a homogeneous network, where the crosslinking junctions are periodically distributed. Hence, only the amphiphilic triblock copolymers PMMA-*b*-PMSA-*b*-PMMA and the chemically end-linked PSMA-EGDMA networks have been analyzed by SAXS. The difference of the electron density between PMMA and PSMA was found to give enough contrast, and changing the counterion from sodium to cesium did not improve the scattering patterns (not shown).

A typical 2D scattering pattern and its radial averaging into a 1D plot is shown for the PMMA-*b*-PSMA-*b*-PMMA triblock copolymer 90-80-105 in Figure 5.7, left.

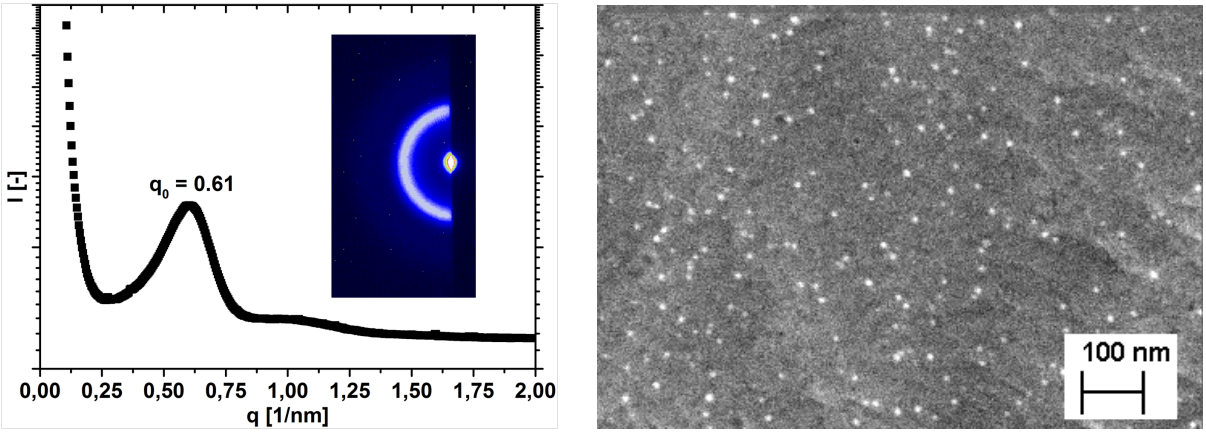


**Figure 5.7:** Left) Small angle X-ray scattering pattern for the dried PMMA-*b*-PSMA-*b*-PMMA triblock copolymer 90-80-105. Right) The SEM image of the ground powder shows the spherical PMMA aggregates which act as crosslinking points.

The appearance of higher-order reflections can give information about the morphology of the microdomains to distinguish *e. g.* spherical, hexagonal or lamellar structures (see Table 5.1). However, the determination of the unit cell by SAXS was not possible in the measured samples in this work. Scanning electron microscopy (SEM) was used as a second method. A typical picture is displayed in Figure 5.7, right, where it is shown that the PMMA aggregates can be considered as spherical micelles.

In the following, the spherical microdomain structure of the PMMA micelles is assumed to be a body-centered cubic (*bcc*) lattice (see Figure 5.8). This morphology is the most stable, spherical structure and thus, it is usually found in neat block copolymers [Semenov85, Matsen96, Kim10].

| Type of microdomains | Relative peak position of the higher-order reflections |
|---|---|
| Lamellae | $q_0$, $2q_0$, $3q_0$, $4q_0$, $5q_0$ |
| Hexagonally packed cylinders | $q_0$, $\sqrt{3}q_0$, $\sqrt{4}q_0$, $\sqrt{7}q_0$, $\sqrt{9}q_0$ |
| Spheres (simple cubic) | $q_0$, $\sqrt{2}q_0$, $\sqrt{3}q_0$, $\sqrt{4}q_0$, $\sqrt{5}q_0$ |
| Spheres (body-centered cubic) | $q_0$, $\sqrt{2}q_0$, $\sqrt{3}q_0$, $\sqrt{4}q_0$, $\sqrt{5}q_0$ |
| Spheres (face-centered cubic) | $q_0$, $\sqrt{3}q_0$, $\sqrt{4}q_0$, $\sqrt{8}q_0$, $\sqrt{11}q_0$ |
| Gyroids | $q_0$, $\sqrt{3}q_0$, $\sqrt{4}q_0$, $\sqrt{7}q_0$, $\sqrt{8}q_0$ |

**Table 5.1:** Characteristic reflections for morphologies with different microdomains [Langela01].

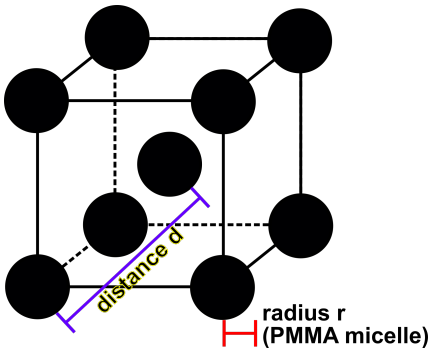


**Figure 5.8:** Body-centered cubic lattice.

Under the assumption of a *bcc* lattice, the radius $r$ of the PMMA micelles is given by Equation 5.13, where $\phi_{\mathrm{PMMA}}$ is the volume fraction of PMMA.[2]

$$r = \frac{d}{\sqrt{3}} \left( \frac{3\phi_{\mathrm{PMMA}}}{\pi} \right)^{\frac{1}{3}} \tag{5.13}$$

Furthermore, the number of PMMA blocks per aggregate can be estimated from the micelle volume ($V_{\mathrm{micelle}} = \frac{4}{3} * r^3\pi$) and the density of PMMA ($\rho_{\mathrm{PMMA}} = 1.185\,\mathrm{g/cm^3}$ ) [Billmeyer84] to get information about the crosslinking functionality:

$$n\left(\frac{\mathrm{chains}}{\mathrm{micelle}}\right) = \frac{N_{\mathrm{A}} * V_{\mathrm{micelle}} * \rho_{\mathrm{PMMA}}}{M(\mathrm{MMA}) * N(\mathrm{A})}\,, \tag{5.14}$$

where $N_{\mathrm{A}}$ is Avogadro's number, $M(\mathrm{MMA}) = 100\,\mathrm{g/mol}$ is the molecular weight of MMA and $N(\mathrm{A})$ is the number of MMA units per endblock.

[2] The discrepancy of $r$ is less than 20% compared to structures, in which the lattice is considered to be simple cubic or face-centered cubic.

### 5.1.4 Nuclear magnetic resonance (NMR)

NMR spectroscopy is a powerful, routinely used technique to investigate the electronic environment of individual nuclei and was established by E. Purcell and F. Bloch in 1946 [Bloch46, Purcell46]. In this thesis, NMR was used by two different means. On the one hand, $^1$H-NMR spectroscopy was applied at high-field (400 MHz) to obtain information about the chemical structure of self-synthesized polymers. The ratio of the different blocks in the PMMA-*b*-P*t*BMA-*b*-PMMA block copolymers could be quantified in this manner as well as the subsequent hydrolysis in these systems (see Section 4.3.3 and Figure 4.12).

On the other hand, $^1$H-NMR relaxometry was used at low-field (20 MHz) to study the polymer mobility. The hydrogel networks consist of rigid parts like the crosslinking points and very flexible chains in between. These parts relax with different time constants and valuable information about the network topology are accessible via NMR in the time-domain.

In order to understand the basic principles of NMR and get an overview on the differences of the applied methods, a short introduction of the technique shall be provided in this section. For more details, the reader is referred to the extensive literature [Abragam61, Derome87, Bovey88, Schmidt-Rohr94].

#### Basics of pulse NMR

Most isotopes possess a spin or angular momentum $I$, which is quantized into $2I + 1$ discrete energy states. Hydrogen ($^1$H) has a spin of $I = 1/2$ and the two energy levels have Eigenvalues of $m_\mathrm{I} = +1/2$ or $m_\mathrm{I} = -1/2$.

In an external, static magnetic field $B_0$ along the z-axis, an ensemble of similar spins do not align their magnetic moments in the field direction but the spins undergo precession along the field direction. This precession is described by a characteristic frequency, the Lamor frequency

$$\omega_\mathrm{L} = \gamma B_0 \,, \tag{5.15}$$

where $\omega_\mathrm{L}$ depends on the strength of the magnet field $B_0$ as well as the gyromagnetic ratio $\gamma$, which specifies the magnitude of nuclear magnetic moments of a certain type of nuclei.

In the $B_0$-field, the energy levels of the spins are no longer degenerate and the two states ($m_\mathrm{I} = +1/2$ and $m_\mathrm{I} = -1/2$) will differ by the energy $\Delta E$, as displayed in Figure 5.9, left. The population difference of these two states is governed by the energy difference $\Delta E$ and is given by the Boltzmann relationship:

$$\frac{N_{+1/2}}{N_{-1/2}} = \exp\left(\frac{-\Delta E}{k_\mathrm{B} T}\right) \approx 1 - \frac{\hbar \omega_\mathrm{L}}{k_\mathrm{B} T} \,. \tag{5.16}$$

Compared to the thermal energy, the energy difference $\Delta E$ is small and therefore, the population difference is only in the range of 100 ppm for protons.

The population difference results in a macroscopic net magnetization $M$ in the direction of the magnetic field $B_0$, since more spins are in the ground state, as shown in Figure 5.9, left. To trigger a transition between the ground state ($m_I = -1/2$) and the excited state ($m_I = +1/2$), energy is needed. A second, non-stationary magnetic field $B_1$ perpendicular to the static $B_0$-field is emitted from the probe coil (usually in the form of a 90° pulse). If the frequency $\nu$ of the second field fits the Lamor frequency $\omega_L/2\pi$, there is resonance and a transition (Rabi oscillation) between the two energy levels is possible by absorbing or emitting the energy difference

$$\Delta E = h\nu = \hbar\omega_L = \hbar\gamma B_0 \,. \tag{5.17}$$

After the 90° pulse, both energy levels are saturated and the net magnetization $M$ rotates in the xy-plane. It is common to visualize the energy exchange in a coordinate system (x'y'z) that rotates with $\omega_L$, where $B_1$ and $M$ appear static, as displayed in Figure 5.9.

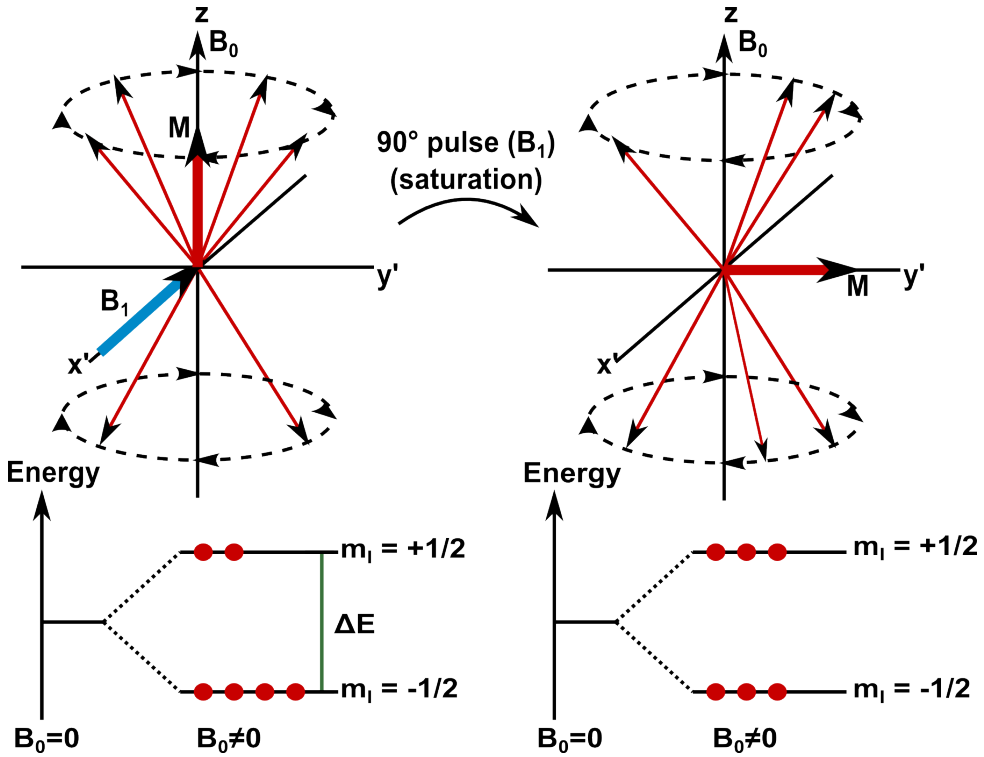


**Figure 5.9:** The principle of nuclear magnetic resonance (NMR): Right) Spins precess about an external magnetic field $B_0$ along the z-axis. The population difference between the two separate energy states results in a net magnetization $M$. A second magnetic field $B_1$ perpendicular to the static field $B_0$ gives the energy $\Delta E$ in the form of a pulse to the system to allow the spins to flip. This results in saturation of the energy levels and the net magnetization is in the x'y'-plane (right).

After a certain time, different relaxation mechanisms (see Figure 5.10), triggered by local inhomogeneities in the magnetic field, bring the population back to the initial Boltzmann distribution. Then, a new pulse or scan can be applied to the sample.

To analyze the chemical structure of molecules, the energy difference in form of the corresponding resonance frequency between the two states is measured. If all nuclei have the same resonance frequency, only one signal will be detected in a NMR spectrum. However, the protons are surrounded by electrons, which shield the external magnetic field $B_0$. The different chemical environment results in a distinct effective $B$-field at the nuclei. Therefore, $\Delta E$ and the resonance frequency are slightly different for hydrogen atoms with a different chemical environment. Consequently, a spectrum is obtained in NMR-spectroscopy with several peaks depending on the chemical structure of the investigated molecule. As the population difference depends on $B_0$, higher magnetic fields result in a better sensitivity of the spectrometer. Hence, the $^1$H-NMR measurements are conducted at high-field at a 400 MHz spectrometer (see Appendix A.2) to get good resolution.

NMR can be also used in the time-domain (TD-NMR). Here, not the specific resonance frequency but the relaxation processes, which lead to the energy dissipation after the saturation, are evaluated. The decay of the NMR signal is analyzed in terms of two relaxation mechanisms, as illustrated in Figure 5.10, each with their own time constant: The longitudinal relaxation, also termed as spin-lattice relaxation $T_1$ and the transverse relaxation, also referred to spin-spin relaxation $T_2$.

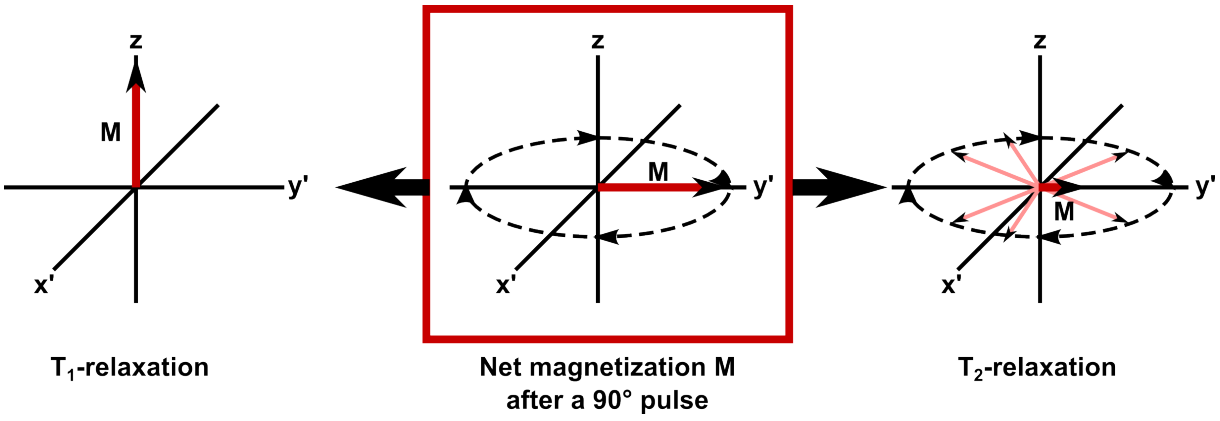


**Figure 5.10:** The net magnetization $M$ is rotating in the x'y'-plane after a 90° pulse (middle). Two relaxation mechanisms lead $M$ back to its initial state at equilibrium: The longitudinal $T_1$-relaxation (left), where the energy is transfered to the surroundings (lattice) and the transversal $T_2$-relaxation (right), where an ensemble of spins is dephasing over time.

By analyzing the relaxation mechanism (particularly $T_2$), valuable information about the dynamics of the polymer chains in the network is accessible, which can be used to draw con-

clusions about the network topology. As this method cannot provide spectral resolution, the measurements can be conducted on a simpler spectrometer at lower field (here 20 MHz, see Appendix A.2.8). Such instruments are inexpensive, they offer easier access and were successfully used to analyze dynamics in polyelectrolyte hydrogels in previous work [Höpfner14].

### $T_1$-relaxation

During the longitudinal or spin-lattice relaxation, the magnetization $M$ returns to its full equilibrium value along the z-axis. The dissipation of energy is accomplished by interactions (*e. g.* dipole-dipole interactions) with the surroundings (the *lattice*). The necessary field with the suitable Lamor frequency $\omega_L/2\pi$, to change the state of a spin, is generated by other nuclei's motions. This relaxation mechanism is quantified by the time constant $T_1$, which is the time it takes for the longitudinal magnetization to recover approximately 63% $(1-(1/e))$ of its initial value, after being flipped into the magnetic transverse plane.

The commonly used *saturation recovery* pulse sequence, which is described in detail in Appendix A.2.8 is applied in this thesis to measure the $T_1$-relaxation time [Freeman71, Anderson72]. Two distinctly separated contributions to the relaxation are observed in the analyzed hydrogel samples. The data is fitted by a double exponential function with the two assigned time constants $T_{1,p}$ and $T_{1,water}$, as displayed in Figure 5.11, left. The shorter time constant $T_{1,p}$ describes the relaxation of the polymer component with its restricted mobility, while the longer constant $T_{1,water}$ originates from the highly mobile residual HDO.

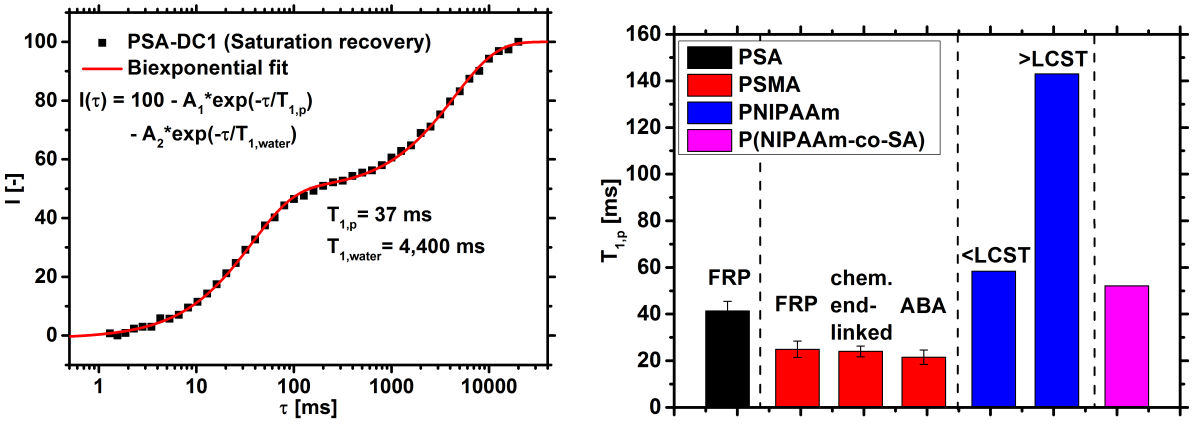


**Figure 5.11:** Left) The $T_1$ relaxation of sample PSA-DC1, measured by the saturation recovery pulse sequence, shows biexponential relaxation behavior. Right) The shorter time constant $T_{1,p}$ is related to the type of monomer but it is independent of the network structure or polymerization technique. The error bars indicate the standard deviation of samples with different synthetic parameters (*e. g. DC*).

The measured time constant $T_{1,\mathrm{water}}$ is always in the range of 1 – 5 s, with no systematic change between the samples. The shorter time constant $T_{1,\mathrm{p}}$ for the same monomer type shows only a small dependency on synthetic parameters within the margin of error. In contrast, when the monomer is changed, a significant shift in the time constant is observed.

In Figure 5.11, right, the $T_{1,\mathrm{p}}$ values of the different monomers used in this thesis are summarized. The error bars indicate the standard deviation over all measured samples of the same monomer type but with different synthetic parameters (*e. g. DC*). Neither the network topology nor the polymerization technique influences $T_{1,\mathrm{p}}$, but the monomer type does. This is in good agreement with previous published data, where the author also concluded that the $T_1$-relaxation time depends on the local unit structure rather than the overall network structure [Höpfner13a].

The relaxation time $T_{1,\mathrm{p}}$ of PSA (about 41 ms) is considerably higher than $T_{1,\mathrm{p}}$ of PSMA (about 24 ms), but smaller than $T_{1,\mathrm{p}}$ of PNIPAAm hydrogels (ca. 58 ms). The copolymer P(NIPAAm-*co*-SA50) has with $T_{1,\mathrm{p}} = 52$ ms a value in between both homopolymers. The thermally responsive PNIPAAm hydrogel additionally showed a strong temperature dependency in contrast to the other polymers. Heating sample PNIPAAm-DC1 above the LCST resulted in a large increase of $T_{1,p}$, as shown in Figure 5.11, right. This is probably related to the change of its hydration state, as discussed in Section 4.5, which causes a different chemical surrounding and the collapse of the network.

### $T_2$-relaxation

The transverse or spin-spin relaxation is associated with an exponential decay of the macroscopic magnetization $M$ in the x'y'-plane. The decay, characterized by the time constant $T_2$, is observed due to the interactions of an ensemble of spins dephasing from each other (see Figure 5.10, right). After a 90° pulse, all spins have the same phase, since they were excited by the same pulse. The spins rotate as well as the resulting net magnetization $M$ with the Lamor frequency $\omega_{\mathrm{L}}$ around the z-axis. During the rotation in the x'y'-plane, the spins interact with each other, mainly via magnetic dipolar interactions, by sampling local field inhomogeneities: Some spins precess slightly faster, other slower than the average. This causes a loss of phase coherence and a fanning out in the rotating frame. The overall magnetization $M$ in the x'y'-plane is exponentially decaying, and after the time $T_2$, only 37% ($1/e$) of its initial value is left.

The $T_2$-relaxation is quite sensitive to the mobility of protons. While fluids have long $T_2$ times of seconds, solid materials like polymers have much shorter time constants (µs – ms) depending on their chain flexibility. Therefore, measuring the spin-spin relaxation is a good way to investigate indirectly the topology of networks such as hydrogels, since crosslinking junctions and elastic chains strongly differ in their mobility [Shapiro11].

The measurement of the transverse relaxation process is usually done by echo techniques, since a direct recording of the free induction decay (FID) is not possible due to field inhomogeneities, which would result in a shortened, apparent time $T_2^*$. The basic concept of such spin or Hahn-echoes is the refocusing of the spin magnetization by combining a 90° and a 180° pulse. During a Hahn-echo, a 90° pulse is applied first that rotates the magnetization in the x'y'-plane, followed by a 180° pulse after an evolution time $\tau$ to flip all spins in the plane. After the same time delay $\tau$, the spins rephase to form a $T_2$-echo, where the $T_2^*$ effects are removed [Hahn50].

In previous work, it was demonstrated that the advanced CPMG/XY16 pulse train combined with a magic sandwich echo (MSE) is necessary to cover the whole $T_2$-relaxation behavior in hydrogels [Höpfner13a, Höpfner14]. While the Hahn-echo creates only one echo, the CPMG pulse sequence uses a train of echoes to capture larger parts of the relaxation curve at once [Carr54]. To avoid spin-lock effects in the CPMG experiments, the pulse phases are cycled within the echo train by advanced pulse trains such as XY16 [Gullion90, Guthausen98]. The fast initial decay is probed by the MSE to overcome the dead-time of the instrument (here about 10 µs) [Powles63]. The whole relaxation decay can then be measured by the combination of a MSE and the CPMG/XY16 pulse train [Maus06].

However, the relaxation spectrum in hydrogels is very broad and stretches over more than five decades. In order to obtain the whole relaxation curve, the CPMG/XY16 pulse sequence has to be applied with different echo delays $\tau$. The used parameters and pulse sequences were adapted from previous work [Höpfner14] and are summarized in Appendix A.2.8. The whole relaxation curve was measured by four individual experiments, as displayed in Figure 5.12, left. The MSE and the CPMG/XY16 experiments with three different delay times $\tau$ can be also combined in one experiment to reduce effort and halve the measuring time. This results in a lower density of data points, though. However, the reduced data density did not significantly affect the further data treatment, such as exponential fitting or use of the inverse Laplace transform (ILT), and was therefore preferably used.

The $T_2$-relaxation curve for a typical sample (PSA-DC1) is displayed in Figure 5.12, left. Two distinctive features for hydrogels are observed in this graph: First, the relaxation behavior is quite complex and the full decay needs more than five decades. Second, every sample has a long, characteristic relaxation time in the range of 2 – 5 seconds. This is related to the highly mobile species of residual HDO. In order to eliminate the effect of a varying amount of solvent, the data was consistently treated in the following manner: The long relaxation time of HDO was fitted by a single exponential function for $\tau > 20$ ms. This fit was then subtracted from the raw data and the resulting curve was renormalized to 100% (see green squares in Figure 5.12, left).

The normalized relaxation behavior can be analyzed by two methods. On the one hand, the data may be fitted with an empirical function for a quantitative analysis. On the other hand, the data can be treated with an ILT to deconvolve the exponential decay in a distribution of relaxation times.

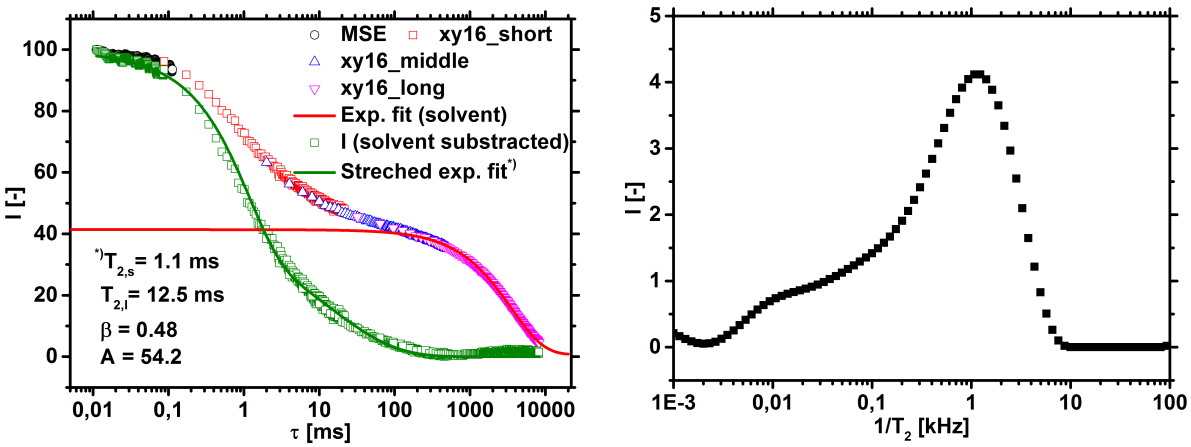


**Figure 5.12:** Left) Displaying the whole $T_2$-relaxation curve for a typical sample (PSA-DC1) by combining the CPMG/XY16 experiments with three different evolution times with the early points measured by MSE. In green squares: The solvent subtracted data fitted with a combined stretched exponential function as described in the text. Right) The distribution of relaxation rates $T_2^{-1}$ obtained by the ILT.

A previously used empirical fit function consists of the combination of an exponential and a stretched exponential function [Höpfner14], which is given by Equation 5.18 and visualized in Figure 5.12, left.

$$I(\tau) = A * \exp\left[-\frac{\tau}{T_{2,s}}\right] + (100 - A) * \exp\left[-\left(\frac{\tau}{T_{2,l}}\right)^{\beta}\right] \tag{5.18}$$

This empirical function fits the relaxation behavior of randomly crosslinked hydrogels quite well. However, in systems with very immobile parts, such as PMMA in the physically crosslinked hydrogels, this is not the case. Furthermore, hydrogels can be quite inhomogeneous in their structure (see Section 4.3), resulting in the presence of many different relaxation processes with different relaxation rates. Hence, it is more reasonable to assume a distribution in $T_2$-times rather than describing the data with only two distinctive relaxation times. Consequently, the second method, where the data is analyzed by an ILT (see below) was preferably used by the author of this thesis.

The ILT, as given by Equation 5.19, allows to deconvolve a set of overlaying exponential functions in a signal. The result is a distribution in relaxation times, as shown in Figure 5.12,

right. This is quite useful to compare the data by eye.

$$\mathcal{L}^{-1}\{F(t)\} = \frac{1}{2\pi i} * \int_{\gamma-i\infty}^{\gamma+i\infty} F(s) * \exp(st)\, ds\,. \tag{5.19}$$

Unfortunately, the ILT is an ill-posed problem, which can only be solved numerically and with prior assumptions. A commonly used regularization method to invert data is known as the *CONTIN* algorithm and was first written by S. Provencher in Fortran [Provencher79, Provencher82a, Provencher82b]. In the present thesis, the implementation of *CONTIN* in the *Matlab* software by I.-G. Marino was used, which is freely accessible on the *Matlab* homepage as the *rilt.m* script [Marino07]. The main control parameters in the *rilt.m* script are the regularization or smoothing factor $\alpha$ and the point density. These parameters have to be chosen beforehand and depend *i. a.* on the noise of the data. For the characterized hydrogels in this thesis, $\alpha = 10$ and 100 points, logarithmically spaced in the range from 0.001 − 1000 ms, were found to be reasonable values to obtain stable and physically meaningful results.

#### Residual dipolar coupling (RDC)

A fundamentally different approach to probe the molecular dynamics of polymer chains in a network is based on double quantum (DQ) coherences. Proton DQ or multiple quantum (MQ) NMR experiments allow a more direct measurement of the residual dipolar coupling (RDC) of neighboring spins along the chain. The RDC between two spins occurs due to an incomplete averaging of spatially anisotropic dipolar couplings and its extend can be described in the secular approximation by the Hamiltonian [Bovey88]

$$\hat{H}_\mathrm{D} = d(3\hat{I}_\mathrm{z}\hat{S}_\mathrm{z} - \hat{\vec{I}}\hat{\vec{S}})\,, \tag{5.20}$$

with the coupling constant

$$d = -\frac{\hbar\mu_0\gamma_\mathrm{I}\gamma_\mathrm{S}}{4\pi r_\mathrm{IS}^3}(3\cos^2\theta_\mathrm{IS} - 1)\,, \tag{5.21}$$

where $r_\mathrm{IS}$ is the distance between the spins I and S, and $\theta_\mathrm{IS}$ is the angle between $B_0$ and the vector of these two spins (see Figure 5.13). The RDC is orientation-dependent and its extent is directly related to the topology [Saalwächter07a]: In solution, the fast motion of linear polymer segments averages the dipolar coupling interactions, since all the different accessible conformations are isotropic. However, in polymer networks, constraints like crosslinking points and network entanglements lead to non-isotropic segmental fluctuations and therefore to the persistence of a weak RDC, which is quantified in the residual dipolar coupling constant $D_\mathrm{res}$

[Valentín09]. The advantage of DQ-NMR experiments is that two sets of data are simultaneously gathered, which can be directly related to either isotropic or non-isotropic relaxation.

In previous work, DQ-NMR experiments were successfully applied to study elastomers [Saalwächter04, Saalwächter07b, Saalwächter12] and polymer hydrogels [Valentín09, Lange11, Höpfner14]. For more information about DQ-NMR, the reader is referred to the mentioned publications and the review article by Kay Saalwächter, which gives a more detailed overview on this topic [Saalwächter07a].

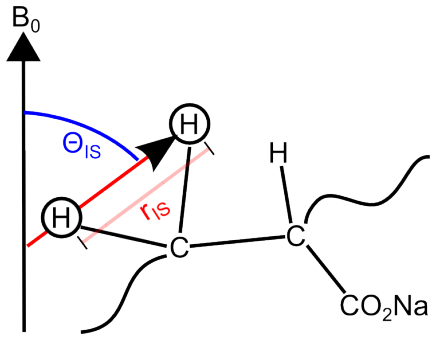


**Figure 5.13:** The dipolar coupling of two spins depends on their distance $r_{IS}$ and the angle $\theta_{IS}$.

The measurement of DQ coherences is accomplished by the complex Baum-Pines pulse sequence, which was improved further and implemented for the minispec by Saalwächter *et al.* [Baum86, Saalwächter07a]. The pulse train is displayed in Appendix A.2.8 and consists of two parts. A first sequence excites the coupling between two spins and the second sequence reconverts the magnetization back to an observable signal. At the end, a 90° pulse is applied, which discriminates with its relative phase between the actual DQ intensity $I_{DQ}$ (blue triangles in Figure 5.14, left) and all the other intensities $I_{ref}$ (red circles in the same graph).

Before the DQ data can be evaluated, a thoughtfully applied data treatment is necessary, which is described in more detail in Appendix A.2.8. First, the DQ data $I_{DQ}$ is renormalized to recover the true build-up curve undistorted by relaxation effects: The long-time tail of the build-up curve, which is related to the slow relaxing of solvent and other non-elastic components (such as sol, loops and dangling ends), is stepwise fitted with simple exponential functions. The two components are then subtracted from the initial signal, leading to the normalized build-up curve $I_{nDQ}$ (see green diamonds in Figure 5.14, left) [Lange11].

Different approaches can be applied to extract the RDC constants from the DQ build-up curves. This includes for example fitting the curves with semi-analytical build-up functions. These functions use specific statistic models such as Gaussian or Gamma distributions [Saalwächter07b]. The RDCs can be extracted from this fits as the distribution average $D_{avg}$. However, hydrogels are usually composed of different elastic chain lengths and are rather inhomogeneous (see

Section 4.3). This results in different mobilities in the network and consequently a rather broad distribution in $D_{res}$ is expected [Höpfner14].

The distribution in the $D_{res}$ constants is estimated using the numerical Tikhonov regularization procedure, which is described in more detail in Appendix A.2.8 and in previous publications [Lange11, Chassé11]. The regularization was implemented by Weese in the *FTIKREG* program, which was modified by Chassé for the use with DQ data [Weese92, Chassé11].[3]

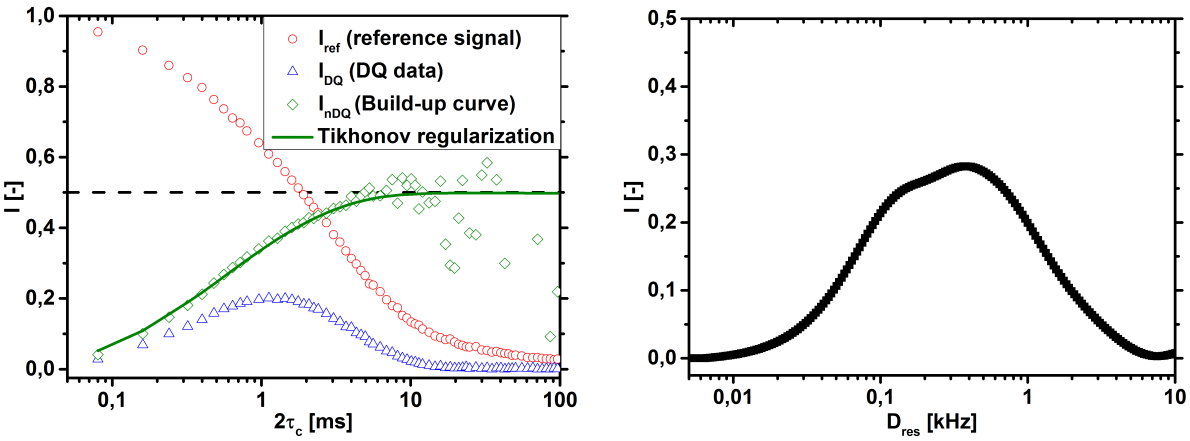


**Figure 5.14:** Left) Typical results of DQ-NMR experiments for sample PSA-DC1. The renormalized build-up curve $I_{nDQ}$ is analyzed by the Tikhonov regularization (green line). The corresponding distribution in $D_{res}$ is shown in the right graph.

The main advantage of the Tikhonov regularization is that the resulting $D_{res}$ distribution is calculated for different error parameters $\epsilon$ together with a $\chi^2$-error. The latter parameter gives the deviation between the experimental build-up curve and the build-up curve from the regularization procedure [Chassé11]. Hence, a criterion for the most reliable distribution is defined, while this is not the case for the $T_2$ analysis with the inverse Laplace transform. The best fit for the DQ build-up curve from the Tikhonov regularization is displayed in Figure 5.14, left, as a green line, and the corresponding $D_{res}$-distribution is given in the same figure in the right graph. Both distributions ($D_{res}$ and $T_2^{-1}$) are broad and have a similar range of rates in between 0.01 – 10 kHz for sample PSA-DC1 (compare Figure 5.12 and 5.14).

[3]The *FTIKREG* program is freely available in the supporting information of [Chassé11], including a short instruction.

## 5.2 Reference PSA and PSMA hydrogels

The water absorbency and mechanical response of randomly crosslinked poly(sodium acrylate) hydrogels synthesized via FRP have been extensively studied in the literature [Yin92, Schröder96, Buchholz98]. In this thesis, such hydrogels serve as a reference system for all the other network topologies, since they were also used in the proof of principle for the proposed desalination process [Höpfner10]. Therefore, the influence of *DC* on the observed quantities form the different characterization methods shall be discussed first.

In general, a lower *DC* results in longer elastic chains and the average number of monomers per elastic chain $N(\mathrm{M})$ increases. Thus, a lower *DC* causes the formation of a looser network with larger pores that can incorporate more solution by extension: The water absorbency increases with the average number of monomers per elastic chain $N(\mathrm{M})$, whereas the mechanical modulus is decreasing, which is displayed in Figure 5.15.

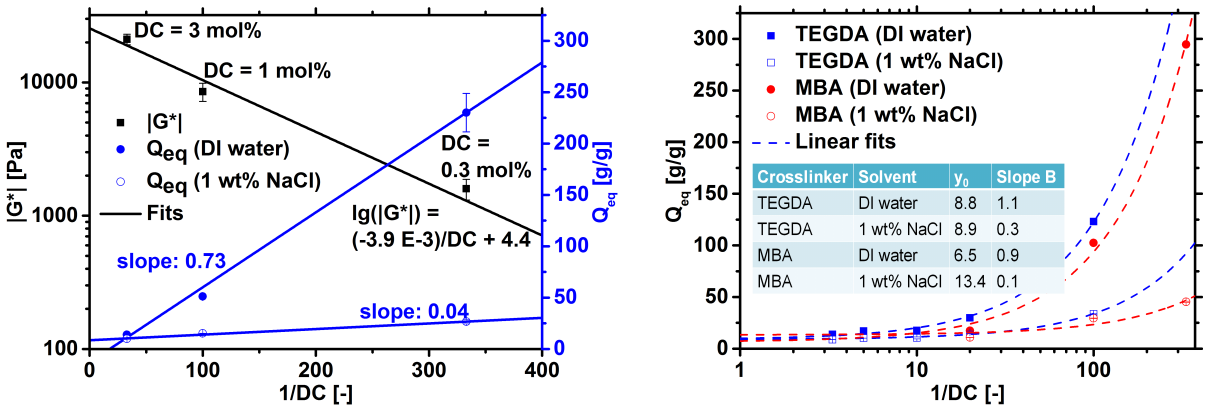


**Figure 5.15:** Left) The complex modulus $|G^*|$ and the degree of swelling $Q_{\mathrm{eq}}$ in deionized (DI) water, respectively in a 1 wt% NaCl solution, are plotted against the inverse *DC* for three PSMA samples. Right) The water absorbency for different PSA hydrogels, which were crosslinked with either TEGDA or MBA.

The swelling data was fitted with the function $Q_{\mathrm{eq}} = y_0 + B/DC$, which was found to represent the data quite well. The fits with the respective parameters are displayed in Figure 5.15 for differently crosslinked PSMA (left) and PSA polyelectrolytes (right). The slope B is for all samples considerably smaller in a 1 wt% NaCl solution compared to deionized water, which is a previously reported phenomenon and in good agreement with the theoretical prediction [Yin92, Höpfner13a]. Furthermore, the slope for the PSMA samples is smaller than for the PSA samples, where the latter monomer type is more hydrophilic and has higher absorbencies.

In Figure 5.15, left, the complex moduli $|G^*|$ for fully swollen PSMA hydrogels are plotted as a function of the inverse *DC*. The strong increase of the mechanical strength with an increasing *DC* has two reasons: First, more crosslinking junctions introduce more, but shorter

elastic chains, which exert higher elastic forces during deformation. Second, the hydrogels are measured in their fully swollen state. This means that lower crosslinked samples also have a lower polymer concentration. The effective concentration of elastic meshes per unit volume is reduced and the samples become softer.

For a quantitative comparison of the experimental data with the theory (see Section 3.1), the average number of monomer units between two crosslinking points $N(\mathrm{M})$ has to be calculated from the *DC* by Equation 5.22, which is derived from Equation 3.4.

$$N(\mathrm{M}) = \left(1 - \frac{2}{f}\right) * \frac{1}{DC * k}\,, \tag{5.22}$$

where $f$ is the crosslinker functionality (here:$f = 4$) and $k$ is the crosslinker efficiency. Typical values for $k$ in case of MBA and PS(M)A are in the range of 15 − 78% [Wack06]. If $k$ is assumed to be 50%, Equation 5.22 simplifies to $N(\mathrm{M}) = 1/DC$.

However, the crosslinker efficiency is not a constant for a certain monomer/crosslinker system, but also depends on the ratio of monomer to crosslinker and thus, on the *DC* itself [Baselga87, Schröder96]. This is related to the formation of inelastic network defects, such as loops and crosslinker-crosslinker shortcuts [Baselga89, Hild98, Lorenzo13], which was already discussed in Section 4.3. Furthermore, $k$ is usually estimated from swelling or rheological data on the basis of different theoretical models, *e. g.* the phantom model. This is questionable, since these models cannot properly describe fully swollen polyelectrolyte hydrogels, as explained in Section 3.1. This basic problem will be discussed further in Section 5.4.3, where the hydrogels made by FRP are compared with the quasi-model systems.

Figure 5.15, right, reveals another issue that should be considered, too. In reality, the crosslinking junctions consist not of one single point, but the crosslinker itself has a certain length. In case of a low *DC* and using MBA as crosslinker, this can be neglected. However, in the highly crosslinked samples ($5\,mol\% < DC < 30\,mol\%$), which were synthesized with the more soluble crosslinker TEGDA (see Figure 4.1), the situation is different. The length of TEGDA is equal to the length of eight SA monomer units. This means that above a *DC* of 12.5 mol% and assuming the relationship $N(\mathrm{M}) = 1/DC$ is valid, the crosslinker itself is longer than the actual elastic PSA mesh. Hence, for a $DC > 12.5\,mol\%$, the network becomes indeed less hydrophilic, but not looser, resulting in basically no change in the absorbency or mechanical moduli (not shown).

Rheology and water absorbency quantify the macroscopic properties of hydrogels, but lack to describe their mesh size distribution. NMR-relaxometry experiments measure the distribution in $T_2$-relaxation rates and residual dipolar constants $D_{\mathrm{res}}$, respectively, as introduced in Section 5.1.4, to gain insights into the network dynamic heterogeneity. In Figure 5.16, the

$T_2$-relaxation curves (left) and the Laplace inversion results (right) are displayed for three PSA samples with a varying *DC* of 0.3, 1 and 5 mol%. The higher crosslinked samples have more constraints in the network, which lead to a reduced mobility of the chain segments. The relaxation process becomes faster with a higher *DC* and in particular the highly crosslinked sample PSA-DC5 shows a pronounced initial decay in the MSE part of the curve. In the Laplace inversion results, the distributions are accordingly shifted to higher relaxation rates for samples with an increasing *DC*. In sample PSA-DC5, highly restricted motions are discernible at 10 kHz, which are related to very rigid parts of the network.

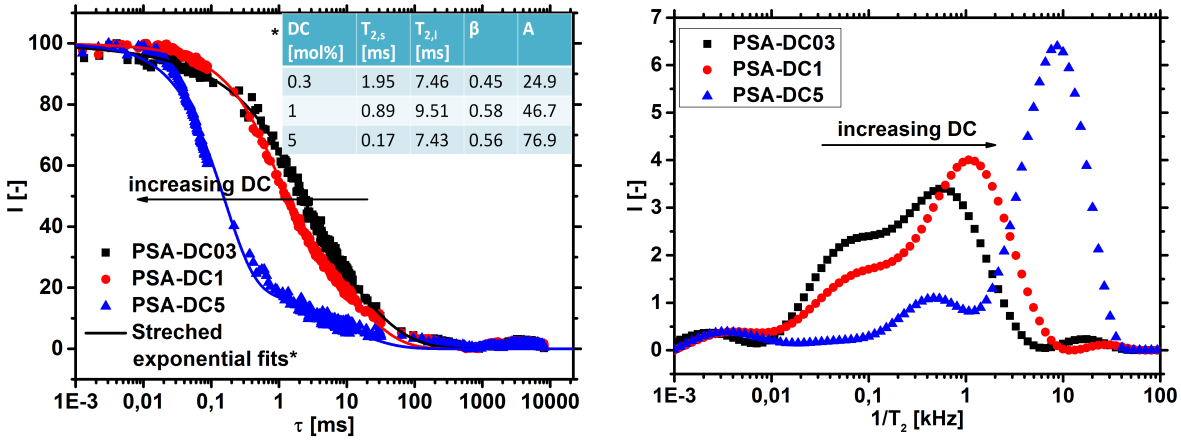


**Figure 5.16:** The $T_2$-relaxation curves for three different PSA samples with a varying *DC* (left) and the corresponding distribution in the relaxation rates obtained by the inverse Laplace transform (right).

The results of the DQ-measurements are displayed in Figure 5.17 and are in good agreement with the $T_2$-relaxation data. An increasing *DC* causes a faster build-up curve, since more constrained network chains lead to a higher dipolar coupling strength. The first data point of sample PSA-DC5 already shows a DQ intensity of more than 50% of the final signal. Therefore, the resulting distribution in $D_{\mathrm{res}}$ has a quite high value at the highest measurable $D_{\mathrm{res}}$ of approximately 10 kHz. Shorter times of $2\tau_{\mathrm{c}} < 80\,\mu\mathrm{s}$ could not be investigated due to the quite long Baum-Pines pulse sequence (see Appendix A.2.8).

The NMR results confirm previously published data on similar PSA samples [Höpfner14] and demonstrate that the heterogeneity of swollen hydrogels is much higher than in other polymer networks, like rubbers [Chassé11]. This is to be expected, since the heterogeneity in networks increases with the absorbency [Bastide88]: Higher crosslinked domains swell less, while lower crosslinked parts can swell more. Hence, the higher the solvent uptake, the more pronounced is the difference among differently crosslinked regions.

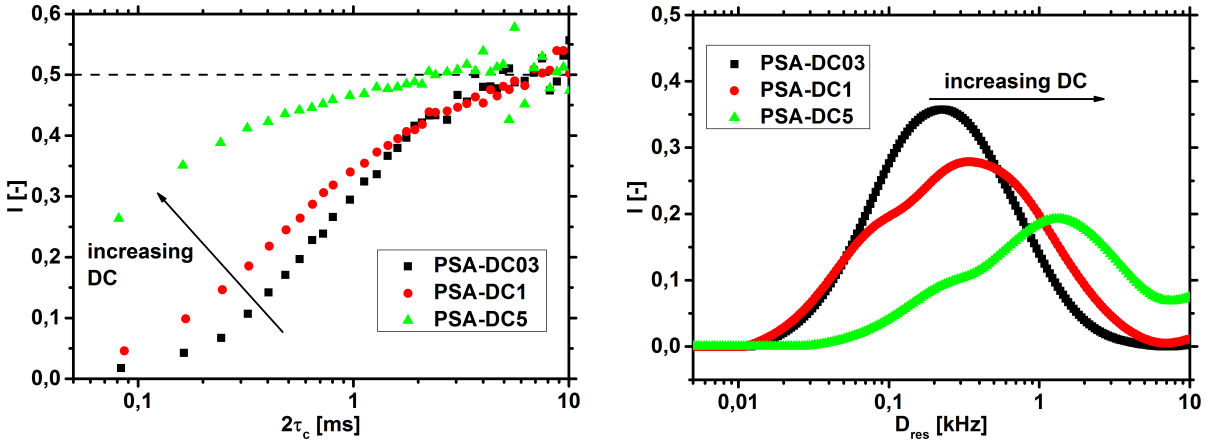


**Figure 5.17:** Left) The DQ build-up curves for three different PSA samples with a varying *DC*. Right) The corresponding distribution in the residual dipolar coupling constants $D_{res}$ obtained by the Tikhonov regularization.

## 5.3 Surface crosslinked PSA hydrogels

The hydrogels in this section were synthesized from the PSA reference hydrogels by additionally crosslinking the particle surface via an esterification with EGDE (see Section 4.2). The absorbency of deionized water is shown for the different networks in Figure 5.18. Increasing the penetration *P* of the treated surface yields a thicker, higher crosslinked shell and reduces the water uptake. This can be expected since more constraints were introduced into the network and only the absorbency under load (compare Chapter 7) should be increased [Jockusch09].

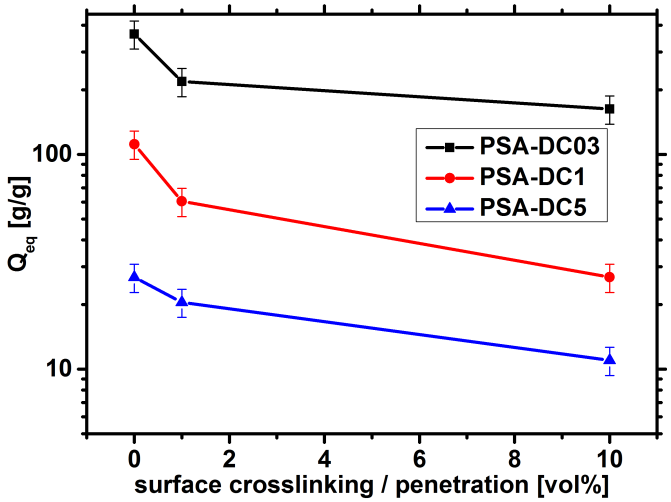


**Figure 5.18:** The degree of swelling $Q_{eq}$ in deionized water as function of the surface crosslinked area for three different *DC*.

TD-NMR was used to probe the surface crosslinking by measuring the local polymer mobility. The commercial surface treated sample LB1110 from BASF shows a distinctive heterogeneity in the $T_2^{-1}$ and $D_{res}$ distributions, as shown in Figure 5.19 and previous work [Höpfner14]. More detailed information is obtainable by analyzing the self-synthesized samples before and after the surface crosslinking procedure (same Figure). The reference hydrogel reveals one broad distribution with no distinguished peaks, whereas the 1 vol% surface crosslinked sample PSA-DC1-P1 shows two specific peaks. One at smaller relaxations rates ($T_2^{-1} \approx 0.1 - 10$ kHz), which corresponds to the core and one at higher relaxations rates of 1 to 10 kHz corresponding to the shell. Increasing the penetration (sample PSA-DC1-P10) leads to a further reduction of the intensity at smaller rates and a shift of the second peak to even higher rates, which indicates a larger and stiffer shell with a lower mobility. These results could be found in both distributions, obtained from the $T_2$-measurements (left) and the DQ-measurements (right) in Figure 5.19.

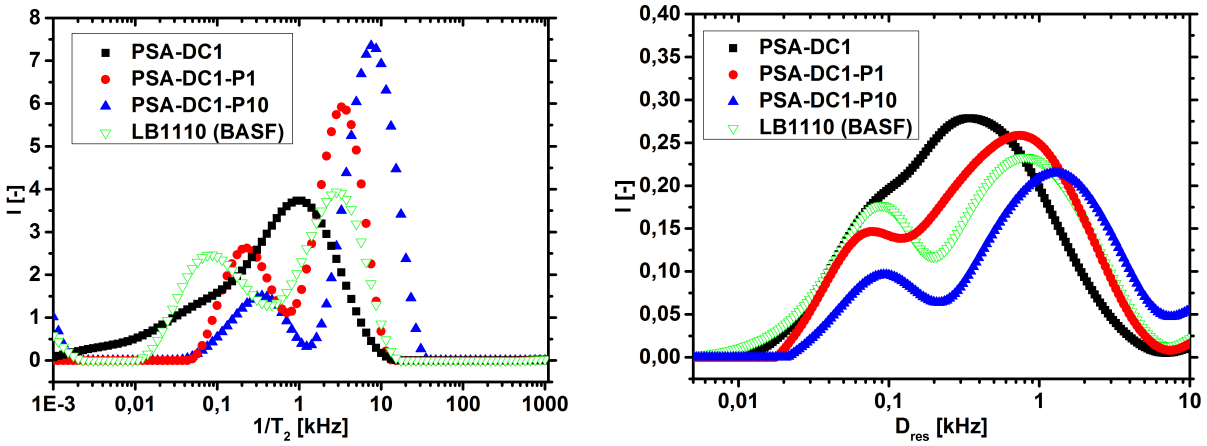


**Figure 5.19:** The $T_2$ relaxation rate distributions (left) and the corresponding distributions of the residual dipolar coupling constants $D_{res}$ (right) are shown for different surface crosslinked samples and the untreated reference hydrogel PSA-DC1.

## 5.4 Quasi-model systems for PSMA hydrogels

### 5.4.1 Self-assembled amphiphilic ABA triblock copolymers

The well-defined amphiphilic triblock copolymers PMMA-*b*-PSMA-*b*-PMMA formed homogeneous hydrogels after heating them in an aqueous solution, as already described in Section 4.3.3. The morphology of the physically crosslinked hydrogels was determined by SAXS and SEM (see Figure 5.7), suggesting three dimensional networks, where the crosslinking points are made of spherical PMMA aggregates. The SAXS patterns were usually measured in the dried

state and typical distances between the crosslinking points were found to be in the range of 10 – 40 nm. From these distances, the micelle radii of the different samples were calculated by Equation 5.13 to 4 – 16 nm, resulting in approximately 45 – 330 PMMA chains per aggregate (see Equation 5.14), depending on the length of the polymer blocks and their ratio. Thus, the crosslinking functionality is much larger than in the free radical polymerized hydrogels. However, the number of chains per micelle is not identical to the functionality of the network, since it is not known how many chains are really bridging and how many only form loops (both PMMA endblocks assemble in the same micelle). Furthermore, it is also likely that several chains will bridge between the same two aggregates. As the micelle radius was calculated under the assumption of a *bcc* lattice, every PMMA aggregate should have eight next neighbors and thus, the effective crosslinker functionality shall also be considered to be eight.

The sample 90-80-105 was, in addition to the dried state, also studied swollen in different NaCl solutions by SAXS. This sample shall show the typical trends for the increasing distance of the PMMA aggregates upon swelling, as not all samples were measurable in their swollen state, due to the limited $q$-space of the SAXS instrument. The obtained SAXS patterns are displayed in Figure 5.20, left, and the calculated micelle distance $d$ is plotted as a function of the polymer concentration $c_p$ on the right.

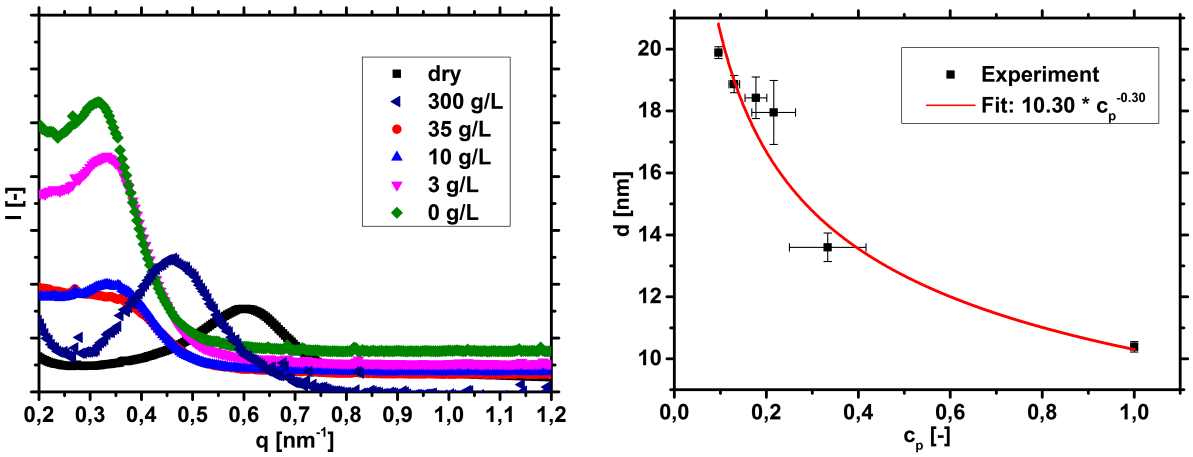


**Figure 5.20:** Left) SAXS patterns for sample 90-80-105 swollen to equilibrium in different aqueous NaCl solutions and in the dried state. Right) Calculated crosslink spacing $d$ from the peak maximum as a function of polymer concentration $c_p$, which was gravimetrically determined by separate swelling experiments. The error bars indicate the standard deviation of three individual experiments.

The peak in the $q$-space is shifted to higher $q$-values in the more concentrated salt solutions, which corresponds to a decreasing distance between the crosslinking points. The higher salinity of the aqueous solution causes a lower water absorbency and thus, a higher polymer concentration in the swollen networks, as already discussed in Section 5.1.1. Hence, the

distance $d$ is decreasing in the higher concentrated salt solutions, since the elastic chains of the networks are less expanded. A power fit revealed that $d \propto c_p^{-0.30}$. The scaling exponent is close to the theoretical value of -0.33 for a three-dimensional expansion [Waters10]. Comparable results could also be realized, when the polymer was swollen in deionized water to different concentrations. However, in these experiments, no regular ordering could be observed at higher polymer concentrations (*e. g.* 50 wt%), presumably due to a macroscopically inhomogeneous swelling.

In the following subsections, several synthetic parameters are systematically varied, such as the length of the endblock A, the length of the midblock B, the overall polymer length ABA and the polymer concentration during the hydrogel formation, to study in detail the effect on network structure, absorbency and mechanical properties.

#### Variation of the polymer concentration during the hydrogel formation

First, the polymer concentration during the hydrogel formation was varied in the range of 0.1 – 10 wt%, by heating the sample 72-408-71 in water to 100 °C for 6 hours. This parameter determines the reference state for the polymer chains in the relaxed state. In triblock copolymers, it additionally influences the ratio between non-elastic loops (two endblocks A in one micelle) and bridging elastic chains [Charbonneau11, Zhang11, Tsitsilianis18].

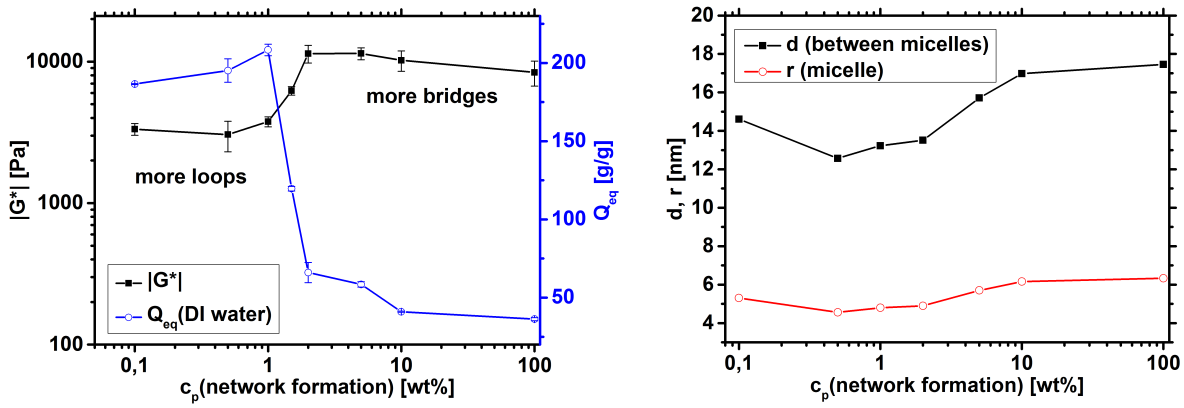


**Figure 5.21:** Left) The degree of swelling $Q_{eq}$ in deionized water and the complex modulus $|G^*|$ of the fully swollen hydrogels are plotted as a function of the polymer concentration during the hydrogel formation for sample 72-408-71. Right) The corresponding distance $d$ between the PMMA aggregates measured by SAXS and the resulting micelle radius $r$.

By lowering the polymer concentration during the hydrogel formation (see Figure 5.21), the aggregate radius decreases by up to 30% and thus, fewer PMMA chains A per micelle are present. The amphiphilic block copolymer has more space to form a larger 3D-network and the

elastic chains can expand further. Hence, the water absorbency increases, while the mechanical moduli of the fully swollen hydrogels decrease with a lower polymer concentration during the hydrogel formation, as displayed in Figure 5.21. The changes in the degree of swelling $Q_{eq}$ were found to be the largest between 1 and 2 wt% (factor of 4 in deionized water). As the aggregation size and distance is constant in this range, a transition from a bridge to a loop formation is likely. The chains are not long enough to always reach the next micelle and two ends of the same polymer might aggregate in the same micelle. This transition can also explain that below 1 wt%, $Q_{eq}$ is slightly decreasing, while the PMMA aggregation size is increasing. The PMMA aggregates become larger, without having more effective elastic chains or forming mechanically stronger hydrogels.

#### Variation of the number of MMA units in the endblock A

In this section, the number of monomer units $N$(A) in the PMMA endblock is varied in the range from 15 to 169, while the PSMA midblock length B is kept constant at ca. 410 units. The length of the hydrophobic endblock plays an important role for the stability of the formed hydrogels. When the number of MMA units becomes less than 50, a large decrease in the $G$-moduli and a large increase in the water absorbency was measured, as displayed in Figure 5.22. A further reduction of the endblock length below 35 MMA units resulted in non-stable hydrogels and rather viscous solutions were obtained. This behavior is related to the faster exchange kinetics of smaller PMMA chains [Halperin89, Nicolai10].

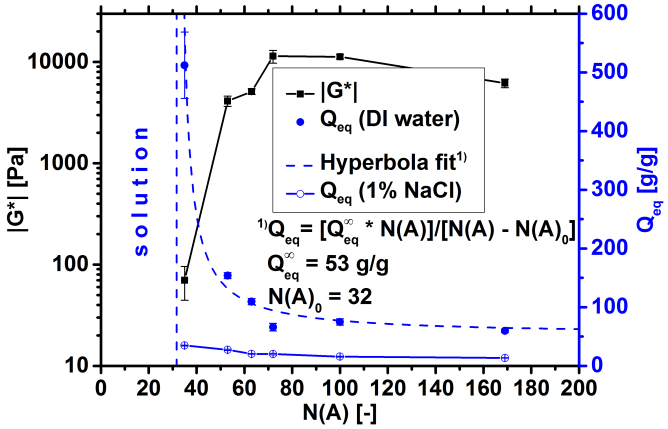


**Figure 5.22:** The water absorbency in deionized (DI) water and in a 1 wt% NaCl solution, as well as the complex modulus $G^*$ are plotted against the number of MMA units per endblock $N$(A) for triblock copolymers with a midblock size of ca. 410 SMA units.

Comparable results have been reported by Wegner *et al.*, who analyzed the exchange rates of PMMA-*b*-PSMA diblock copolymers in water. They found at room temperature no chain ex-

change within weeks when the PMMA block was comprised of 70 units, but a large dissociation with 40 and 20 MMA units [Rager97].

As described in Section 4.3.3, the stability of the hydrogels depends on the formation of frozen micelles. Once the PMMA micelles are not kinetically frozen anymore, a dynamic but macroscopically unstable system is obtained. On the other hand, if the polymer chains are kinetically trapped at room temperature, no large differences can be expected. Thus, above a number of 60 monomer units, the absorbency and the mechanical properties are almost independent of the block length and stay constant.

The data of the absorbency in deionized water was fitted quite well with the empirical, hyperbola function in Equation 5.23. It should be noted that this monotonically decreasing function needs two free parameters: A singularity at a small number $N(\mathrm{A})$, where no stable hydrogels are formed anymore, and a limit for higher endblock lengths, when stable hydrogels are obtained, where the PMMA chains are kinetically trapped.

$$Q_{\mathrm{eq}} = \frac{Q_{\mathrm{eq}}^{\infty} * N(\mathrm{A})}{N(\mathrm{A}) - N(\mathrm{A})_0}\,, \tag{5.23}$$

where the parameter $Q_{\mathrm{eq}}^{\infty}$ (=53 g/g) corresponds to the degree of swelling in deionized water with an infinitely large number of MMA in the endblock and $N(\mathrm{A})_0$ (=32) gives the number of MMA units at which the first stable hydrogels are obtained at room temperature. If the polymer endblock A consists of less than 32 MMA monomers, the $T_{\mathrm{g}}$ of PMMA in water will be exceeded, resulting in too fast chain exchange kinetics to form stable hydrogels.

The $T_{\mathrm{g}}$ for a PMMA with 30 monomer units is indeed about 70 °C [O'Driscoll91], but PMMA can also absorb a few percent of water. The water acts as a plasticizer and lowers the $T_{\mathrm{g}}$ by about $\Delta T_{\mathrm{g}} = 10\,^{\circ}\mathrm{C}$ per percent of water [Hancock94].[4]

When the hydrogels were not swollen in deionized water, but in a 1 wt% NaCl solution instead, no sharp increase in the water absorbency with sample 38-505-31 was measured, since the polymer association of PMMA blocks is more promoted, in good agreement with the observations by Wegner *et al.* [Rager97]. The lower water absorbency in salt solutions leads to more densely packed PSMA chains around the physical crosslinking points. Hence, the PMMA blocks have less space to diffuse through the corona and their self-assembly is more pronounced.

[4] The $T_{\mathrm{g}}$ of PMMA was, even in the dried samples, not detectable by DSC measurements. The aggregation size ($r \approx 5$ nm) might be not large enough.

### Variation of the number of SMA units in the midblock B

In this section, the number of hydrophilic SMA units in the midblock $N$(B) was varied in the range of 80 to 374, while the endblock length was kept constant at ca. 67 MMA units. The number of monomers in the midblock defines the elastic chain length between two crosslinking points ($N$(M) = $N$(B)). Larger elastic chains reduce the crosslinking density, which was expressed in the FRP samples by the $DC$. Thus, the trends for $N$(B) and $1/DC$ are qualitatively the same. An increase of the midblock length results in larger pores of the network, the water absorbency becomes larger and the $G$-moduli of the hydrogels are decreasing, as displayed in Figure 5.23, left. The dependency of the water absorbency on $N$(B) was fitted with a linear function. The slope is considerably smaller in a 1 wt% NaCl solution (0.07) than in deionized water (0.46), which is in good agreement with the results of the reference hydrogels made by FRP in Section 5.2.

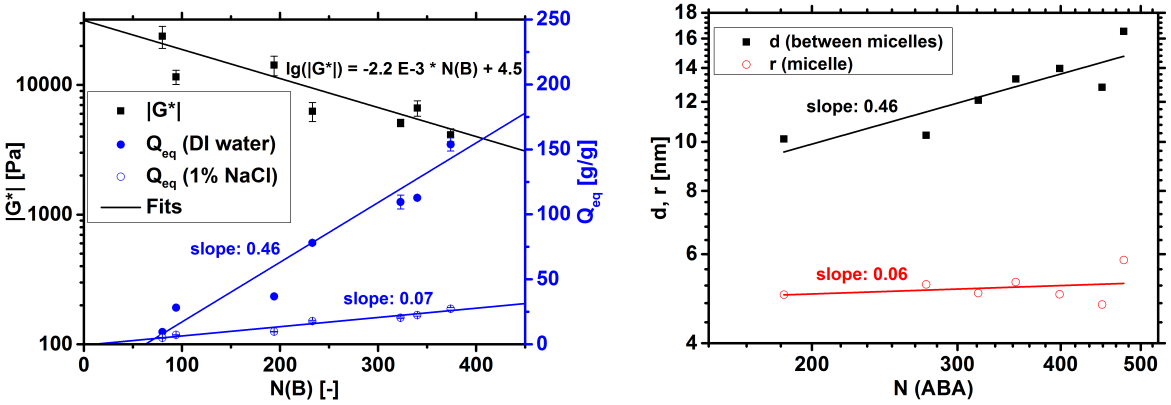


**Figure 5.23:** Left) The complex modulus $|G^*|$ and the water absorbency in deionized (DI) water, respectively in a 1 wt% NaCl solution, are plotted against the number of SMA units in the elastic midblock chain $N$(B). Right) The micelle radius $r$ and the distance $d$ between the PMMA aggregates are plotted against the overall number of monomer units in the triblock copolymer $N$(ABA).

The structural analysis of the dried samples by SAXS demonstrates that the micelle size stays almost constant, while the distance between the aggregates increases with the midblock length $N$(B). This indicates that the crosslinking functionality $f$ is unchanged, while the elastic chain length increases, as expected. The micelle radius $r$ and the distance $d$ between the PMMA aggregates are plotted against the overall number of monomer units in the triblock copolymer $N$(ABA) in a double logarithmic plot in Figure 5.23, right. Theoretical calculations of *bcc*-ordered block copolymer melts would suggest a dependency of $d \propto N(\mathrm{ABA})^{2/3}$ and $r \propto N(\mathrm{ABA})^{2/3}$, if the volume fraction of both polymers is unchanged [Semenov85]. These values were also found in this thesis, when the ratio of PSMA and PMMA was kept constant

(see next section). However, only $N$(B) was changed in the present case, while $N$(A) was fixed. Thus, not only the polymer length is increasing with more SMA units, but also the PMMA fraction changes from 71 to 25 mol%. Hence, the slope of the micelle (or crosslinking) distance is considerably smaller with $d \propto N(\mathrm{ABA})^{0.46}$ in the present system. This can be expected, but it is not observable in polymer melts, where such a large change in the polymer block ratio also alters the morphology from spheres to hexagonal or lamellar structures [Semenov85, Matsen96].

#### Varation of the overall number of monomer units with a constant ratio of PSMA to PMMA

In the previous sections, either the number of MMA units in the endblock A or the number of SMA units in the midblock B was varied, while the counterpart was kept constant. This inevitably results in a changing ratio between hydrophobic PMMA and hydrophilic PSMA. In this section, the molar ratio of PMMA:PSMA was kept constant at ca. 38:62 mol%, while the overall number of monomer units $N$(ABA) was varied.

The structural analysis of the dried samples by SAXS shows that the PMMA micelle size and the distance between these aggregates are both monotonically increasing with $N$(ABA), as expected. In Figure 5.24, right, these quantities are plotted against $N$(ABA) and fitted with a power law function. The dependency of $d \propto N(\mathrm{ABA})^{0.64}$ and $r \propto N(\mathrm{ABA})^{0.63}$ are close to calculated values in *bcc*-ordered block copolymer melts ($d \propto N(\mathrm{ABA})^{2/3}$) [Semenov85].

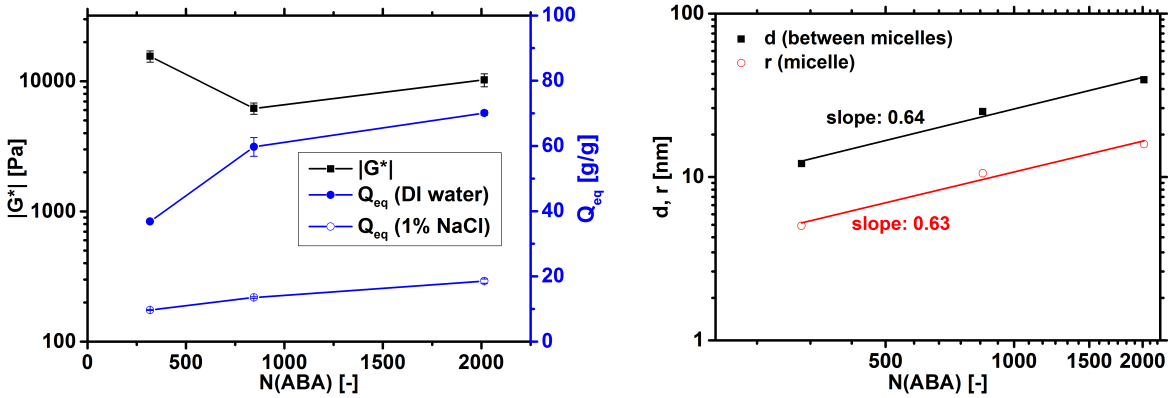


**Figure 5.24:** Left) The degree of swelling $Q_{\mathrm{eq}}$ and the complex modulus $|G^*|$ of the fully swollen hydrogels as a function of the overall number of monomer units $N$(ABA). Right) The distance $d$ between the aggregates measured by SAXS and the resulting PMMA micelle radius $r$.

The formed networks with the larger polymers have longer elastic chains, but also larger PMMA aggregation sizes. The number of PMMA blocks per micelle was found to increase, resulting in more elastic chains among the crosslinks. Thus, the differences of the swelling and rheological properties in the samples, which are plotted in Figure 5.24, left, might be less

pronounced than expected. The absorbency increases with $N$(ABA), while the mechanical moduli are decreasing. Furthermore, it should also be considered that larger elastic chains will have more network entanglements among the meshes, which act as additional non-fixed crosslinking points.

Part of the physically crosslinked hydrogels were also studied by NMR-relaxometry to obtain more information about the polymer mobility in the network. The $T_2$-relaxation curves for five different samples and the corresponding distributions of the relaxation rates are shown in Figure 5.25. The relaxation behavior depends mainly on the rigid PMMA content of the sample, since the hydrophobic block relaxes very fast in water below its $T_g$. Therefore, the initial decay in the MSE part increases with an increasing amount of PMMA. The loss of signal after 0.1 ms scales almost linear with the PMMA content (not shown). Sample 90-80-105, which has with 71 mol% the highest PMMA content, relaxes to almost 90% within 0.1 ms.

The Laplace inversion results show a pronounced peak in between 10 and 200 kHz for every hydrogel, which can be assigned to the hydrophobic endblocks. This peak is increasing with the PMMA content and no such high relaxation rates were present in the PSMA samples synthesized via FRP. The rest of the distribution seems to be underrepresented in the hydrogels with a very high PMMA content, but shows similar features as the reference hydrogels with a comparable width.

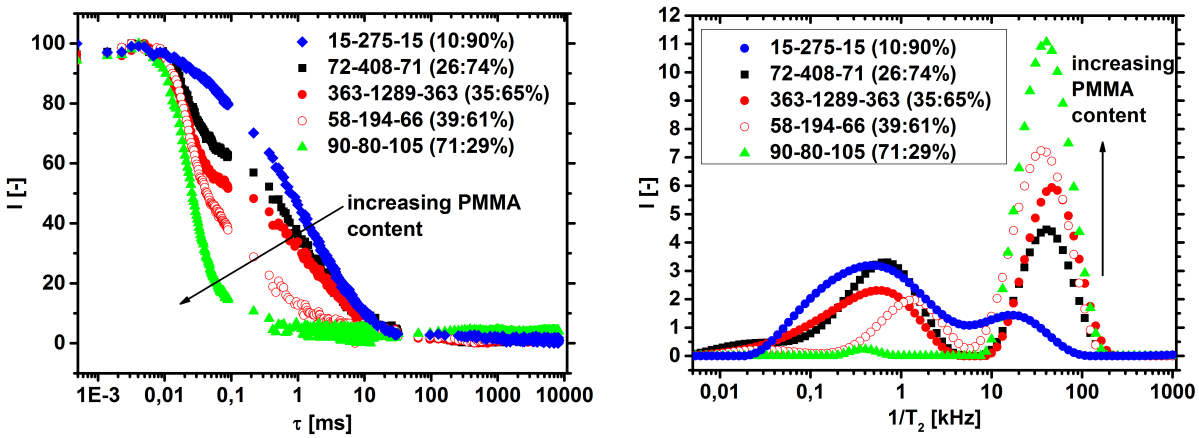


**Figure 5.25:** Left) The $T_2$-relaxation curves for different self-assembled triblock copolymers are shown. The PMMA to PSMA ratio is given in brackets after the sample name and determines the relaxation behavior. Right) The corresponding distributions of relaxation rates obtained by the ILT.

The results of the DQ-measurements for the same samples are plotted in Figure 5.26. The build-up curves are faster with a higher PMMA content, since the hydrophobic aggregates are highly dipolar coupled. In sample 90-80-105, the first measurable data point has therefore

already reached over 60 % of its final signal. The $D_{res}$ distributions are shifted to higher coupling constants with a higher PMMA fraction and a pronounced shoulder is present in all samples at 10 kHz.

The distributions of $D_{res}$ are in good agreement with the $T_2$-relaxation rates and also comparable to the results of the reference PSMA hydrogels. One interesting feature is seen with sample 15-275-15, which had no observable DQ signal. As discussed before, this sample does not form stable hydrogels, since the PMMA chain exchange kinetics are too fast and no stable self-assembled aggregates are formed. Hence, the triblock copolymers are rather dissolved in water, resulting in no residual dipolar coupling.

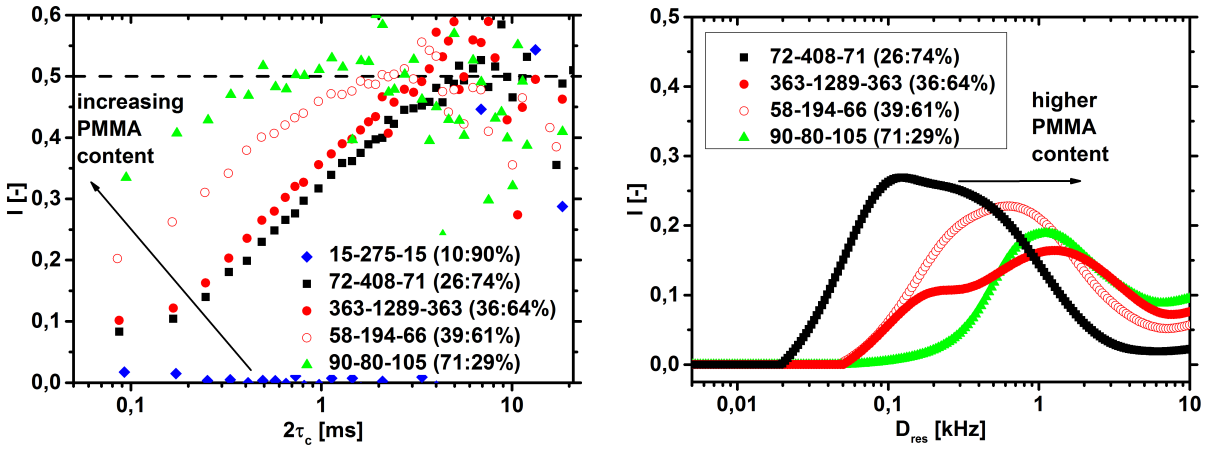


**Figure 5.26:** Left) The DQ build-up curves for various self-assembled PMMA-*b*-PSMA-*b*-PMMA triblock copolymers are shown. Right) The corresponding distributions of the residual dipolar coupling constants $D_{res}$, obtained by the Tikhonov regularization.

#### Variation of the AB content in the ABA system in order to increase the amount of dangling ends

As discussed in Section 4.3, the decoupling of mechanical strength and charge density could be beneficial for the desalination efficiency. As one attempt to achieve this, the triblock copolymer 72-408-71 with two PMMA endblocks was mixed with a varying amount of the diblock copolymer 80-187 with only one PMMA endblock. The diblock copolymer can only be part of one PMMA micelle, which means that the chain is only physically connected to the network at one point, resulting in a non-elastic dangling end.

An increasing amount of diblock copolymer, *i. e.* more dangling ends, results in mechanically weaker hydrogels, as displayed in Figure 5.27. This can be explained by the replacement of bridging elastic chains with dangling ends, as already schematically shown in Figure 4.14. This argument is also supported by SAXS experiments, since no significant change in neither the

distance nor the size of the PMMA aggregates was measured (see red dashed lines in Figure 5.27).

Furthermore, the triblock copolymer 72-408-71 was also mixed with the diblock copolymer 80-587, where the PSMA-block is not half of the length of the mesh, but longer.[5] In this case, a small structural change can be observed by SAXS (see open symbols in Figure 5.27). The micelle distance increased, since the longer dangling ends had probably not enough space during the hydrogel formation (with the same polymer concentration of 2 wt%) to form a network with identical dimensions. The larger distance between the crosslinking points leads to an increased water absorbency (not shown), resulting in mechanically weaker hydrogels.

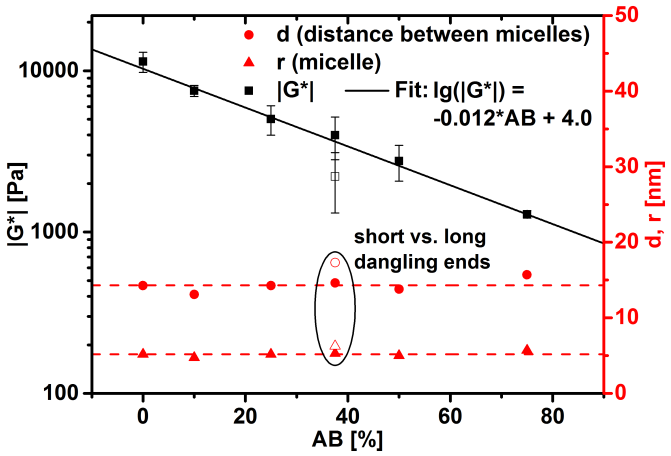


**Figure 5.27:** The complex modulus $|G^*|$ is shown for mixtures of the triblock copolymer 72-408-71 with an increasing amount of the diblock copolymer 80-187. In the same graph also the distance $d$ and the radius $r$ of the PMMA aggregates are plotted. An increase in the micelle size is only observed by incorporating longer dangling ends (sample 80-587, open symbols).

The polymer mobility in the various ABA/AB mixtures was analyzed by TD-NMR experiments. In Figure 5.28, left, the Laplace inversion results are displayed. Two distinctive peaks are observable, the one at higher relaxation rates (10 – 200 kHz) is related to PMMA and the one at smaller rates (0.02 – 5 kHz) corresponds to the PSMA chains of the network. The $T_2$-distribution indicates that the relaxation behavior between dangling ends and bridging, elastic chains is similar. The distributions have the same shape and width and merely the ratio of the peak height between higher and lower relaxation rates is changing, as shown in the inset in Figure 5.28, left. However, this originates from the fact that the length of the dangling ends is about 8% smaller than half of the elastic chains, resulting in an increasing PMMA content with an increasing amount of AB. When the triblock copolymer 72-408-71 was mixed with

[5] The diblock copolymer 80-587 was only mixed at one concentration of 37.5% with the triblock copolymer due to the limited amount of sample 72-408-71.

the diblock copolymer 80-587, where the dangling ends are longer than the mesh length, the $T_2$-relaxation rate distribution is shifted to lower rates, indicating a higher polymer mobility.

The $D_{res}$ distributions in Figure 5.28, right, show differences among the hydrogels in a more pronounced way than the $T_2$-relaxation rate distributions. An increasing spike at around 0.09 kHz is observed with either longer or more dangling ends, which is not present in the distributions of the pure triblock copolymers: The dangling ends are more mobile, but their motion is not fully anisotropic near the crosslinking point. Therefore, they still have a RDC, where the related $D_{res}$ constants are rather small.

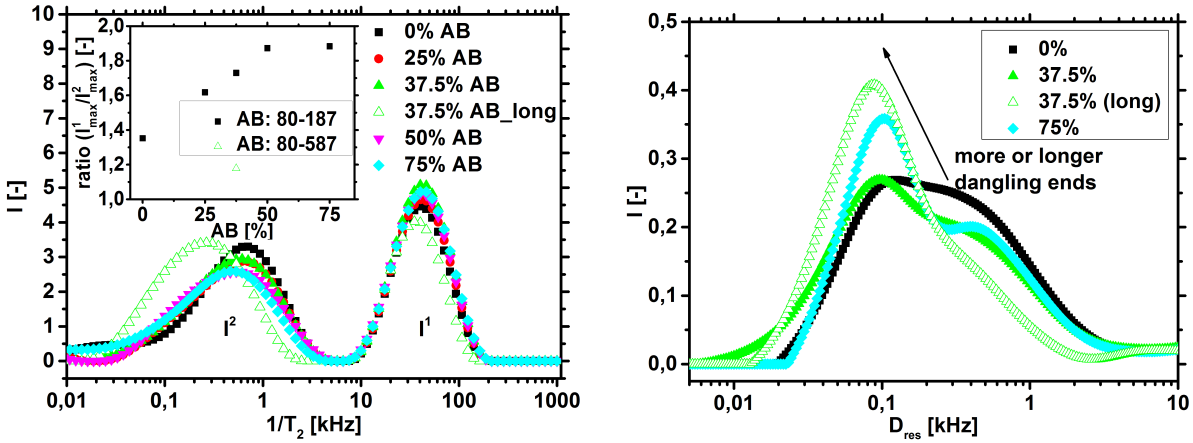


**Figure 5.28:** Left) The distributions of the $T_2$ relaxation rates are shown for different ABA/AB mixtures. The inset displays the peak ratio between higher relaxation rates and smaller ones, which is only related to the PMMA content. Right) The $D_{res}$ distributions show a pronounced spike at around 0.08 kHz with more or longer dangling ends. This peak corresponds to the weaker dipolar coupling of dangling ends compared to elastic chains.

### 5.4.2 Chemically end-linked PSMA-EGDMA hydrogels

The trends in the macroscopic properties of the chemically end-linked quasi-model systems (see Section 4.3.4) are similar compared to the other hydrogel systems. Longer elastic chains lead to a larger distance between the crosslinking junctions, as observed by SAXS measurements (see Figure 5.29, right). From this data, the diameter of the EGDMA junctions was estimated to approximately 3 – 4 nm, which is smaller than the PMMA aggregates in the ABA hydrogels, but much larger than the crosslinking points in the reference samples made by FRP. The hydrogels with an increasing number of monomer units per elastic chain $N$(M) have larger pores and thus, they absorb more water and have lower mechanical moduli (see Figure 5.29, left), as already explained in Section 5.2.

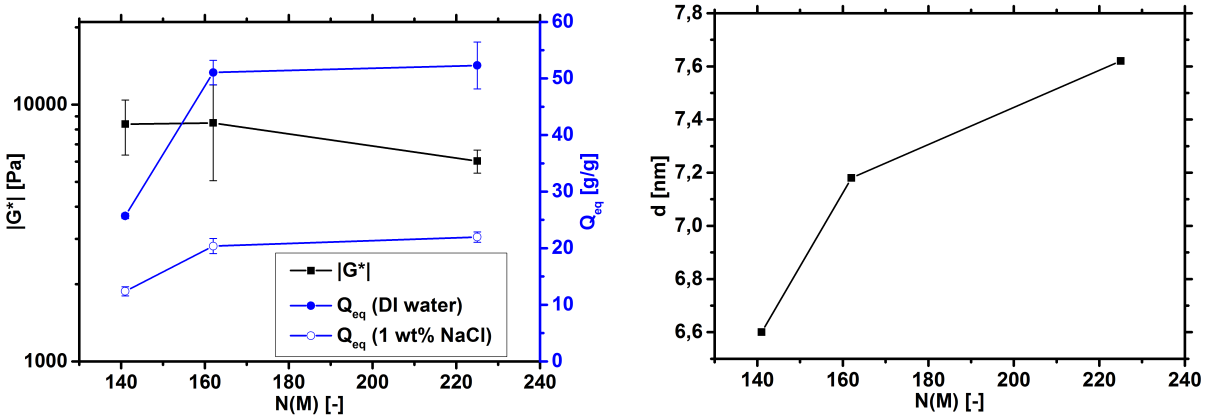


**Figure 5.29:** Left) The degree of swelling and the mechanical moduli of fully swollen chemically end-linked PSMA-EGDMA hydrogels. Right) The distance between the crosslinking junctions as a function of the number of monomers per mesh $N$(M), measured by SAXS.

The analysis of the TD-NMR measurements is summarized in Figure 5.30. The Laplace inversion results show similar to the ABA hydrogels a pronounced peak in the range from 10 to 200 kHz. This is related to the very immobile EGDMA crosslinking junctions. Consequently, this peak is increasing with a higher amount of EGDMA in the hydrogel. The rest of the $T_2$-relaxation rate distribution has no distinctive features and the width is comparable with the distributions of the reference hydrogels. The same statements are also valid for the $D_{\text{res}}$ data.

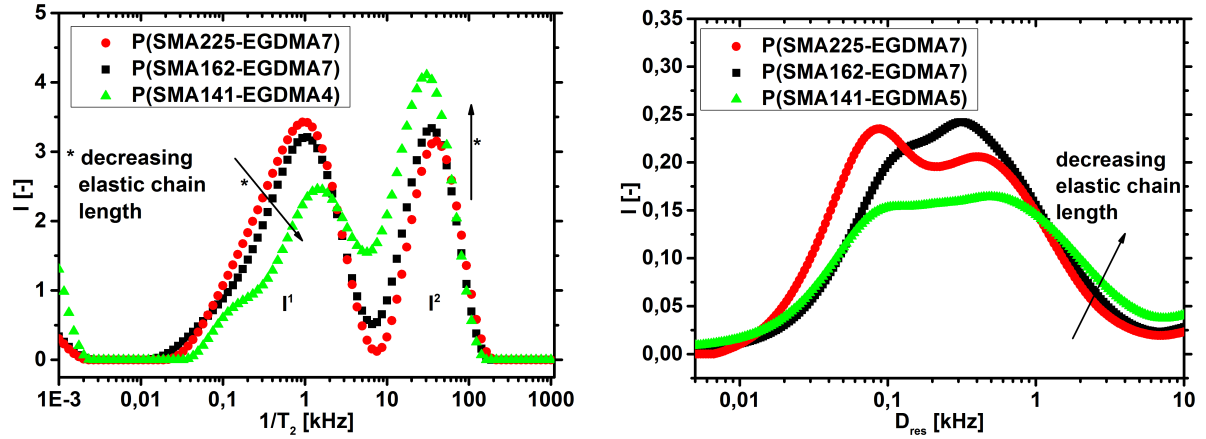


**Figure 5.30:** Left) The Laplace inversion results of the $T_2$-relaxation rates for three chemically end-linked quasi-model systems. Right) The corresponding distributions of the residual dipolar coupling constants $D_{\text{res}}$.

### 5.4.3 Comparison with randomly crosslinked hydrogels

In this section, the different PSMA networks, made by either the chemically end-linking of living polymer chains, the self-assembly of amphiphilic triblock copolymers ABA or FRP, shall be compared. The question arises, how a meaningful comparison can be made, although the synthetic parameters and procedures are fundamentally different? To do so, the degree of crosslinking (*DC*), which is the main synthetic parameter in the reference hydrogels made by FRP has to be translated into the average number of monomer units per elastic chain $N(\mathrm{M})$, which was directly obtainable in the quasi-model systems by measuring the linear precursor polymer chains in SEC.

As already discussed in Section 5.2, $N(\mathrm{M})$ is inverse proportional to the *DC*, but the exact correlation depends on the crosslinker efficiency $k$ of the present system (see Equation 5.22). Unfortunately, it is not straightforward to predict $k$ or obtain it experimentally. Additionally, typical values for $k$ can differ over a broad range, *e. g.* 15 – 78% in the present systems [Wack06].

A method often used to estimate the crosslinker efficiency $k$ from rheological data is based on the phantom model (see Section 3.1). Using this model, $N(\mathrm{M})$ is calculated from the $G'$-modulus of the fully swollen sample by

$$N(M) = \frac{M_\mathrm{c}}{M_\mathrm{m}} = \frac{RT\rho}{G'} \left(1 - \frac{2}{f}\right) Q_\mathrm{syn}^{-2/3} \, Q_\mathrm{eq}^{-1/3}, \tag{5.24}$$

where $M_\mathrm{m}$ is the molar mass of SMA (= 108 g/mol) and $\rho$ is the density of PSMA (= 1.285 g/mL). The other parameters are for the FRP samples $f = 4$ and $Q_\mathrm{syn} = 4$, for the chemically end-linked systems $f = 5$ and $Q_\mathrm{syn} = 5$, and for the physically crosslinked hydrogels $f = 8$ and $Q_\mathrm{syn} = 50$. The calculated and the theoretical number of monomer units between two crosslinking points $N(\mathrm{M})$ are compared in Figure 5.31. Under the phantom network assumption, the crosslinker efficiency $k$ (see Equation 5.25) is in the range from 13 to 27% for the free radical polymerized reference systems.

$$k = \frac{N(\mathrm{M})(\text{phantom network})}{N(\mathrm{M})(\text{theory})} \tag{5.25}$$

The calculated values for the chemically end-linked P(SMA-EGDMA) networks are close to the $N(\mathrm{M})$ measured by SEC, whereas the values for the ABA triblock copolymers would suggest a much higher crosslinking density. This could be explained by additional network entanglements, since the SAXS measurements indicated that this system has several elastic chains between the same crosslinking points. However, another reason for this strong deviation

is probably caused by the much larger value of $Q_{syn}$ in the physically crosslinked hydrogels, which might underestimate the true elastic chain length.[6]

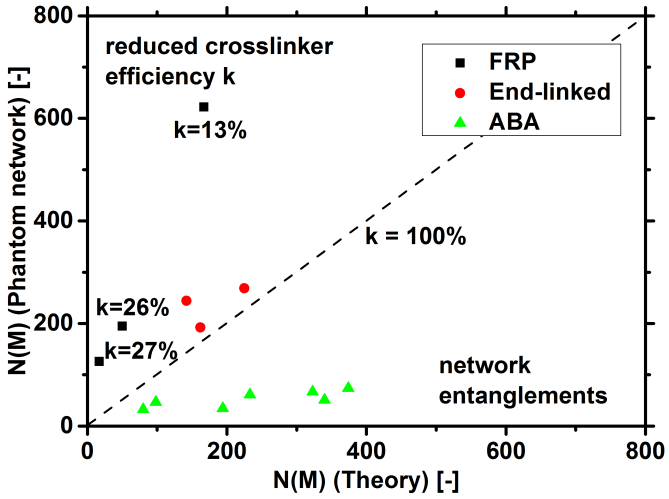


**Figure 5.31:** The theoretical number of monomer units per elastic chain $N(\mathrm{M})$, obtained by the weighed portions and by SEC, respectively, is compared to the calculated values from the rheological moduli using the phantom model (Equation 5.24).

In Figure 5.32, left, $Q_{eq}$ in deionized water is plotted against $N(\mathrm{M})$ for the different hydrogel systems. In the FRP reference samples, $N(\mathrm{M})$ is calculated by Equation 5.22 for different $k$ values (100%, 50% and the values obtained from the phantom model). In this graph, no significant differences among the various systems seem to be present, if the crosslinker efficiency was calculated by the phantom model. However, it should also be considered that the three systems have a different crosslinker functionality $f$. In Section 3.1, where Flory's network theory was introduced, it was shown that the macroscopic properties of polymer networks depend on the cycle rank $\xi$ (Equation 3.4), which is proportional to $\left(1-\frac{2}{f}\right) * \frac{1}{N(\mathrm{M})}$. Therefore, the swelling data is also plotted as a function of $\left(1-\frac{2}{f}\right) * \frac{1}{N(\mathrm{M})}$ in Figure 5.32, right, to eliminate the effect of $f$.

Both graphs in Figure 5.32 show that a comparison among the different network types is not straightforward, since the crosslinker efficiency in the FRP samples drastically influences the average elastic chain length. Further assumptions are necessary, like the applicability of the phantom model. Even though, this model describes swollen rubbers quite good and is often used to describe swollen hydrogels [Wack06, Mark07], its validity for polyelectrolyte hydrogels with their very high absorbency is critical (see also Section 3.2).

[6] The $Q_{syn}$ of 50 was chosen to ensure that the crosslinking points will be formed by spherical PMMA aggregates and not by hexagonal, lammelar or other micellar structures, which are principally possible at higher polymer concentrations [Mortensen96, Swann10].

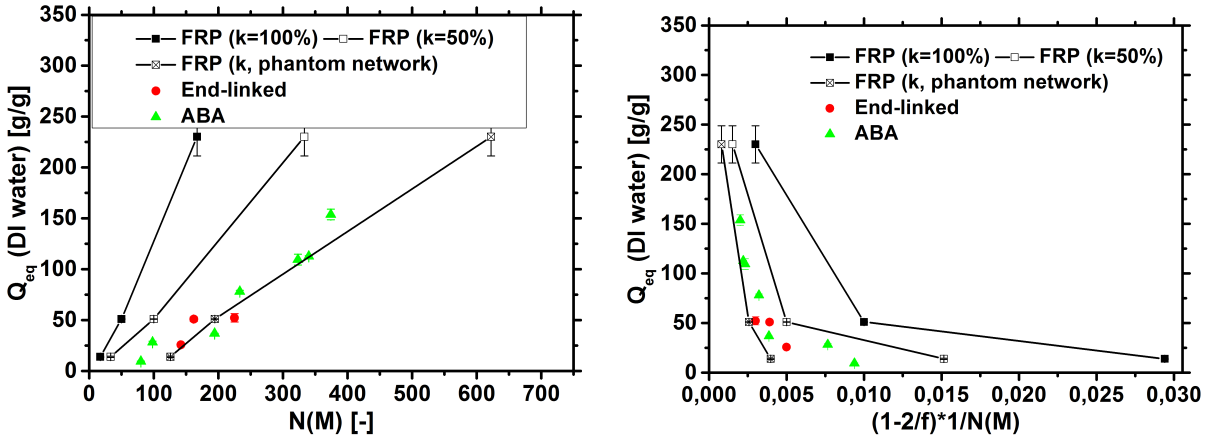


**Figure 5.32:** Left) The degree of swelling $Q_{\mathrm{eq}}$ is plotted against the elastic chain length. Right) $Q_{\mathrm{eq}}$ is shown as a function of $\left(1-\frac{2}{f}\right) * \frac{1}{N(\mathrm{M})}$ to also consider the different crosslinking functionality $f$. The lines for the FRP samples, using different $k$ values, are only a guide to the eye.

To compare the different systems independent of the elastic chain length, the hydrogel properties can be plotted as a function of their absorbency. The driving question behind the quasi-model network types is, whether the charge distribution in the network influences the salt rejection and the desalination efficiency. Therefore, a comparison of the network types with respect to their degree of swelling $Q_{\mathrm{eq}}$ seems to be legitimate. An identical $Q_{\mathrm{eq}}$ will result in the same polymer concentration per volume and hence, in the same average charge density in the swollen networks. Differences in the salt rejection and the desalination efficiency could be therefore related to the network topology, under the assumption that the absorbency is independent of the pore size distribution.

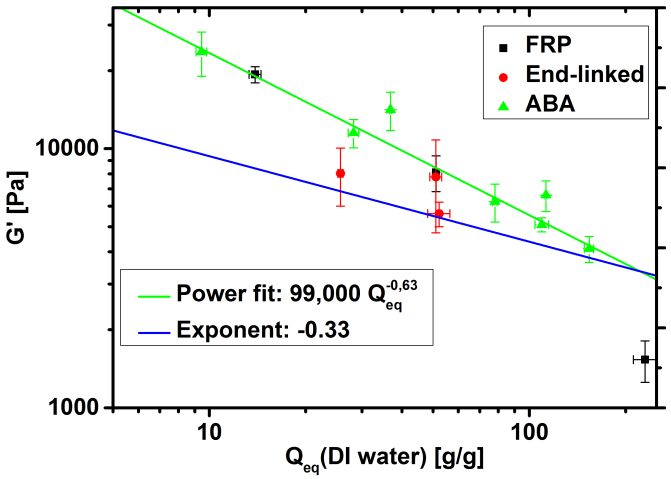


**Figure 5.33:** The storage moduli $G'$ of the fully swollen hydrogels are plotted as a function of the degree of swelling $Q_{\mathrm{eq}}$.

The mechanical moduli of the fully swollen samples are plotted as a function of the degree of swelling in Figure 5.33. All moduli are in a similar range except for sample PSMA-DC03, the slightly crosslinked sample made by FRP. The physically crosslinked samples were fitted with a power law, whereas the other network types were not fitted due to the rather small amount of data points. The ABA hydrogels have a dependency of $G' \propto Q_{eq}^{-0.63}$. This demonstrates that the elastic chain length not only changes the degree of swelling (in this case the exponent would be -0.33, as seen in Equation 5.24), but also directly influences the elastic moduli.

In Figure 5.34, the distributions of the $T_2$-relaxation rates (left) and the $D_{res}$ constants (right) are plotted for one sample of each network type. As already described above, the distributions were found to be rather broad in all network types. A direct comparison reveals that the PSMA-EGDMA networks, and especially the ABA hydrogels have more restricted polymer segments, which originate from the larger crosslinking junctions in these systems. A direct correlation to the distribution in the elastic chain length could not be found.

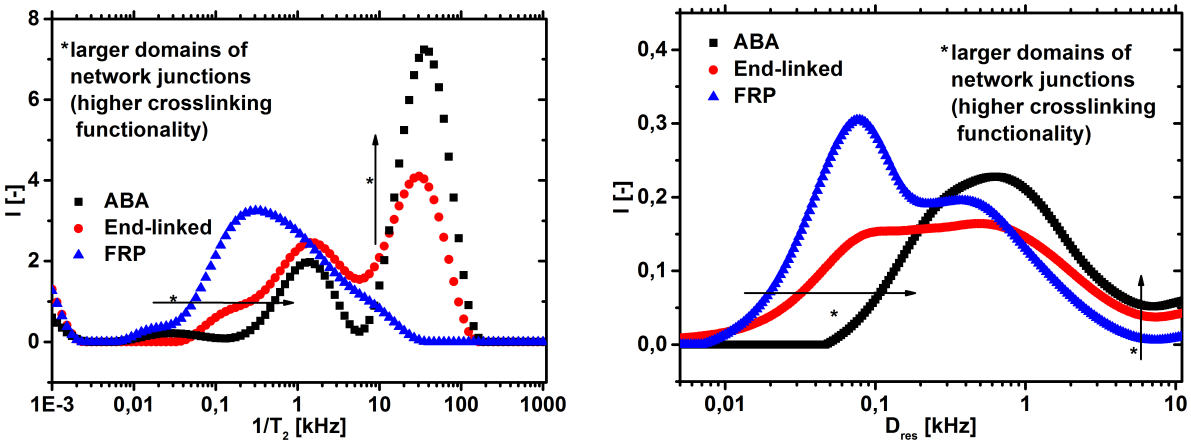


**Figure 5.34:** Left) $T_2$-relaxation rate distributions obtained by the ILT for the different hydrogel systems. Right) The corresponding DQ-results.

## 5.5 Interpenetrating PSA-*i*-PSA double networks

The interpenetrating networks (IPNs) were synthesized by polymerizing a second monomer solution within a single hydrogel network, as described in Section 4.4. Therefore, it is useful to compare the double networks with respect to the single precursor networks.

The water absorbency in a 1 wt% NaCl solution is shown for the various samples in Figure 5.35. In general, the water uptake decreases in the IPNs compared to the single network (SN), since the incorporation of the second polymer causes more constraints of the elastic chains due to

additional network entanglements. In the more restricted double networks, the mechanical moduli are therefore also increasing (not shown).

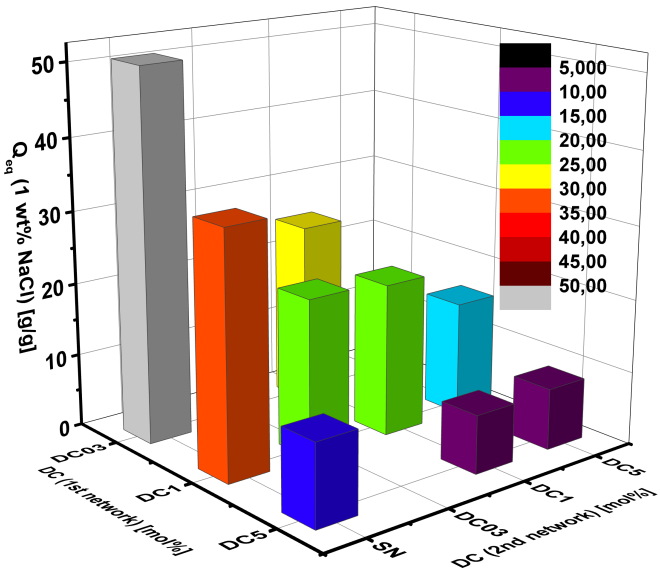


**Figure 5.35:** The degree of swelling in a 1 wt% NaCl solution for various interpenetrating networks, together with the precursor single networks (SN).

The differences between SN and IPN are more pronounced when the *DC* of the second network is larger than the *DC* of the first network. Furthermore, the amount of the second polymer network depends on the solution uptake of the precursor hydrogel, as already explained in Section 4.4. Hence, a lower crosslinked SN has a higher amount of the second polymer incorporated. Consequently, the changes in the absorbencies between IPN and SN are less pronounced, when the first network was already highly crosslinked. Additionally, the order of the synthesis is crucial for the macroscopic properties, *i. e.* sample PSA-DC1-*i*-PSA-DC5 differs from sample PSA-DC5-*i*-PSA-DC1.

The macroscopic properties, like swelling and mechanical strength, reveal the more constrained structure of the double networks, compared to the reference hydrogels, due to more network entanglements. TD-NMR was used to also investigate the heterogeneity in the network mobility. The results of the inverse Laplace transform and the Tikhonov regularization, in order to get the $T_2^{-1}$ and $D_{\text{res}}$ distributions, are plotted in Figure 5.36 for samples, where the SN was made of PSA-DC1. All double networks have an increased heterogeneity in their distributions compared to the single networks, while the results of the $T_2$-relaxation and the DQ measurements are similar.

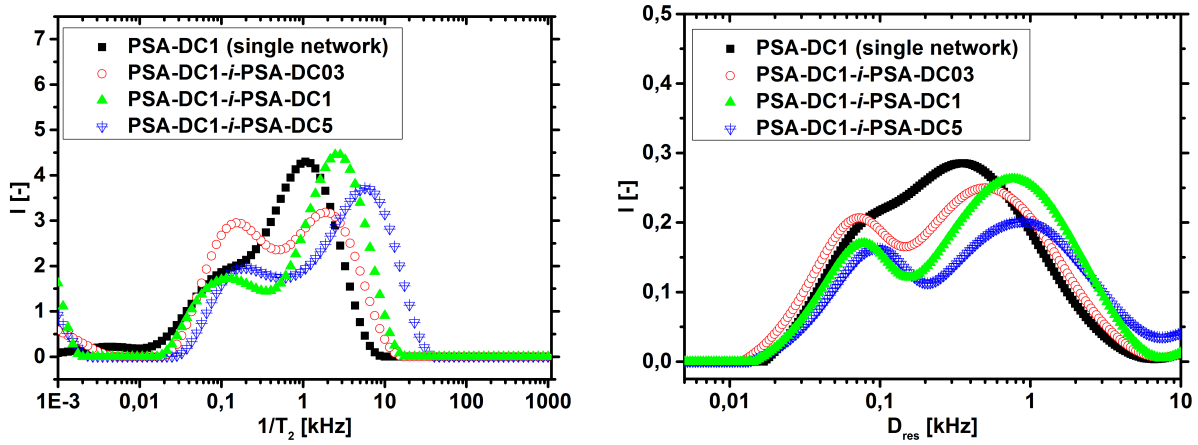


**Figure 5.36:** Interpenetrating networks, in which the *DC* of the second network is varied, are compared with the precursor single network PSA-DC1. Left) The inverse Laplace results. Right) The $D_{res}$ distributions obtained by the Tikhonov regularization.

When the *DC* of the second network was smaller than the *DC* of the first network, a higher amount of smaller $T_2$-rates was observable, whereas an increased peak at higher rates was obtained, when the second network had a higher *DC*. In all IPN samples, also higher relaxation rates than in the single networks were present, even if the second network had a smaller *DC*. This can be related to the additional entanglements between the networks.

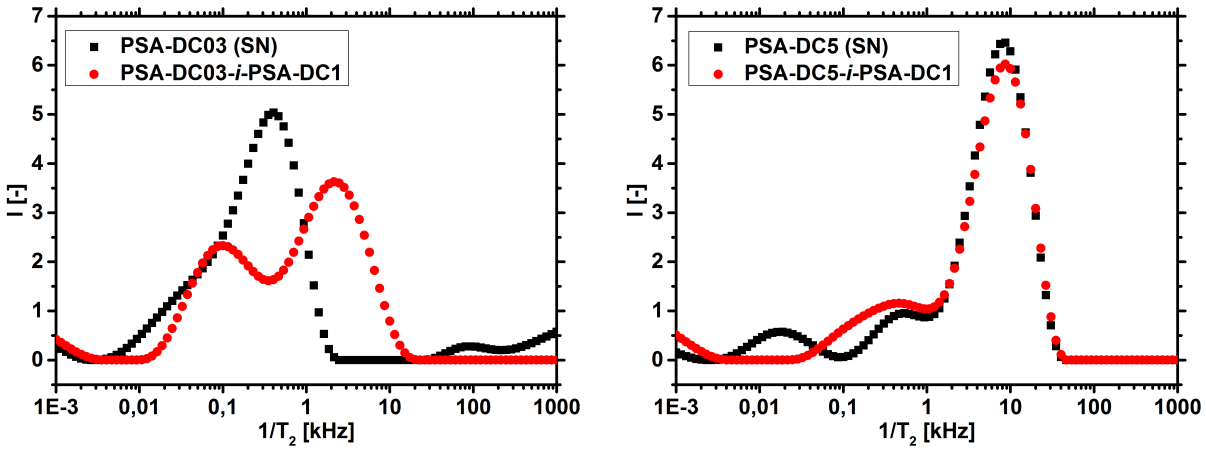


**Figure 5.37:** The $T_2$-relaxation rate distributions of two double networks are compared with the respective precursor single network.

The LF-NMR results are able to reveal the increased heterogeneity in the network mobility, which can be related to the interpenetrating double network structure. The increased heterogeneity is more pronounced in samples, where the first network is lower crosslinked (see Figure 5.37), since more of the second network gets incorporated.

## 5.6 Thermally responsive hydrogels based on PNIPAAm

In contrast to the other network types, the elastic chains in this section were not exclusively made by (meth-)acrylic monomers, but consisted also of NIPAAm monomers to obtain thermally responsive hydrogels. Before the temperature dependency is characterized in more detail, the trends for the degree of swelling at room temperature shall be described for the various samples first.

In Figure 5.38, left, the degree of swelling $Q_{eq}$ in deionized water is plotted as a function of the NIPAAm content for three different degrees of crosslinking. As expected, a larger *DC* results in smaller pores and therefore in a smaller absorbency. Furthermore, the water uptake decreases with a higher NIPAAm content in the networks, in good agreement with previous work [Yu93, Chen04], since NIPAAm is less hydrophilic than the charged acrylic acid.

On the right side in Figure 5.38, the degree of swelling in aqueous NaCl solutions with different salinities is plotted for a 1 mol% crosslinked network. A higher salinity results in a larger osmotic pressure and thus, the water uptake decreases. However, the dependency of $Q_{eq}$ from the salinity is larger in the samples with a higher sodium acrylate fraction, since the charges interact more with the dissolved salt ions, which was also reported by Hsieh *et al.* [Chen04]. In the pure PNIPAAm network, the difference is negligible and $Q_{eq}$ is almost independent of the salt concentration.

The rheological properties of the hydrogels are mainly influenced by the degree of crosslinking of the network and less by the polymer composition, where no trend was observable (not shown).

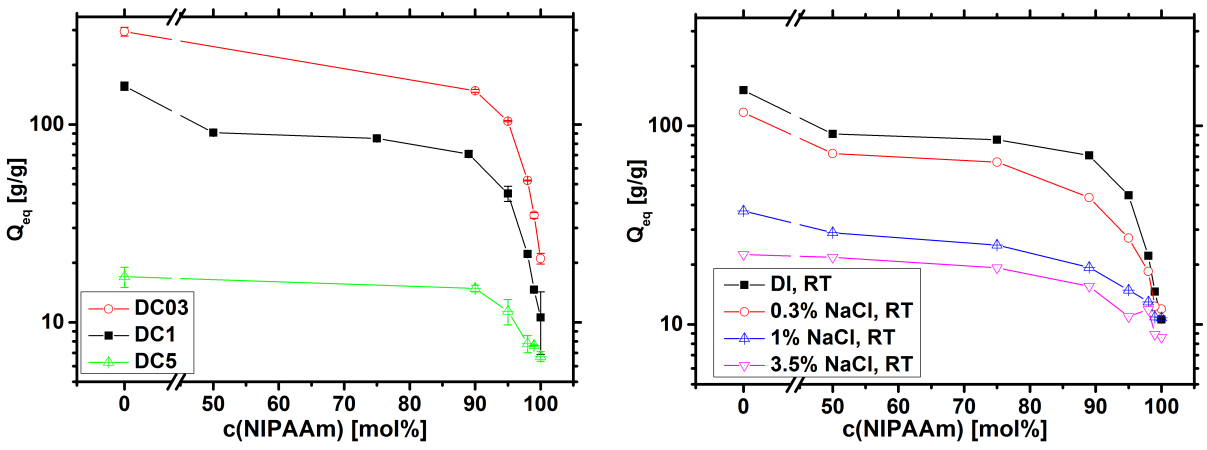


**Figure 5.38:** Left) The degree of swelling $Q_{eq}$ in deionized water for P(NIPAAm-*co*-SA) hydrogels with a varying *DC* and NIPAAm fraction. Right) $Q_{eq}$ is shown for a 1 mol% crosslinked network with a varying NIPAAm fraction in different NaCl solutions.

The material shall be employed in the desalination process using temperature instead of pressure as an external stimulus. Hence, the thermal response and the behavior at the LCST should be characterized as well. The most important and due to the simplicity also most studied quantity that changes upon a temperature increase is the water absorbency of the hydrogels. The temperature dependent degree of swelling in deionized water is shown for some selected samples in Figure 5.39. The general trend is that the changes in the absorbency are less pronounced in higher crosslinked samples. Furthermore, even introducing only small amounts of sodium acrylate causes a vanishing of a distinct LCST, although the hydrogels still have a thermal dependency. Several publications demonstrated that the incorporation of small amounts of hydrophilic groups such as sodium acrylate increases the LCST [Chen04], leads to a broader transition [Yu93] and finally causes a loss of the thermal response at higher SA contents (around 10 – 18 mol%) [Hirotsu87, Brazel95]. This is related to a weakened hydrophobic aggregation force, as already explained in Section 4.5 [Zhang08].

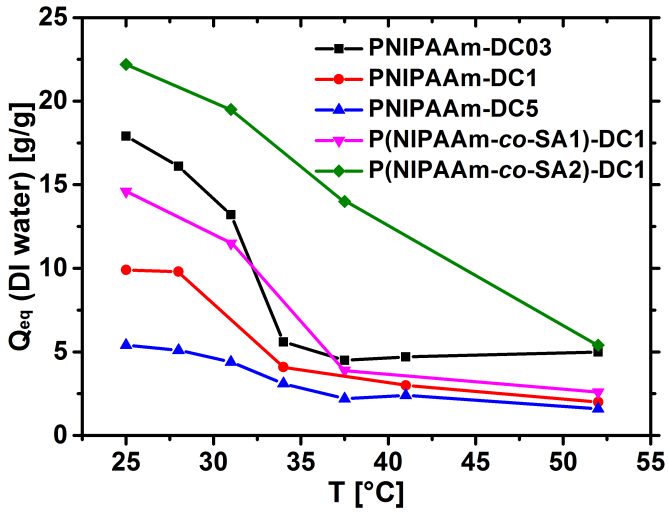


**Figure 5.39:** The degree of swelling in deionized water as a function of temperature for different hydrogel samples.

The differential scanning calorimetry (DSC) is another method often used to determine the LCST in thermally responsive systems [Liu04, Pei04]. The fully swollen hydrogels show an endothermic peak at their LCST upon heating, as displayed in Figure 5.40, left. The peak minimum for the pure PNIPAAm was found to be at about 35 °C (independent of *DC*), when the samples were prior swollen in deionized water, which is in good agreement with previous work [Adrus12]. While this specific temperature is not affected by the *DC*, the peak becomes broader in the higher crosslinked samples. For the copolymer networks, even introducing only a small amount of 1 mol% SA lead to a vanishing of a distinctive LCST and only an endothermic decrease in the heat flow was measured (not shown).

On the right side in Figure 5.40, the LCST values, obtained by the peak minimum in the DSC measurements, are shown for the sample PNIPAAm-DC1, which was prior swollen in different NaCl solutions. The LCST decreases in higher concentrated solutions in good agreement with previous work on linear PNIPAAm polymers [Zhang05]. The data could be fitted quite well with the linear function $LCST = 35.1 - 2.5 * c(NaCl)[^{\circ}C]$. Qualitatively, the same behavior in PNIPAAm hydrogels was also reported by He *et al.*, who observed that the addition of NaCl increases the hydrogen bonding among water molecules and thus, decreases that among water and hydrophilic chains [Liu04].

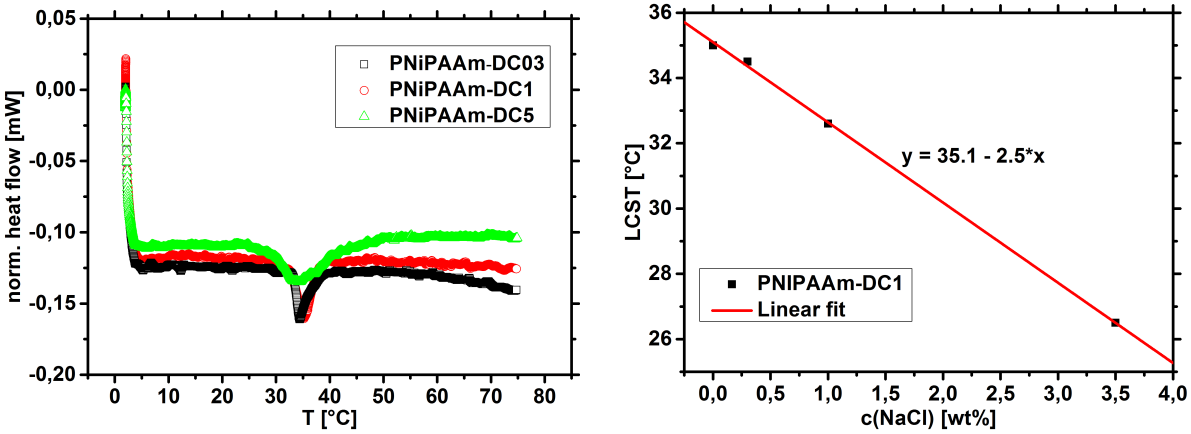


**Figure 5.40:** Left) DSC profiles for the different crosslinked PNIPAAm hydrogels, fully swollen in deionized water. Right) The peak minimum from the DSC measurements as a function of the NaCl concentration, in which sample PNIPAAm-DC1 was prior swollen.

The absorbency and the DSC measurements show that the thermal behavior is quite complex in the present systems, since the LCST is determined by the combination of the PNIPAAm segment length and the amount of sodium acrylate in the copolymer networks, as well as the salinity of the aqueous solutions.

For a better understanding how the hydrogels change other properties above the LCST, the mechanical moduli and the polymer mobility upon heating is shown for sample PNIPAAm-DC1 as an example in Figure 5.41. The elastic modulus $E'$ increases by a factor of $4 - 5$ above the LCST,[7] while the decreasing polymer mobility lead to a two decades faster $T_2$-relaxation. This demonstrates again the strong changes in the hydrogel network at the LCST.

[7] This value is rather a lower assumption since the shrinking diameter upon heating was not considered.

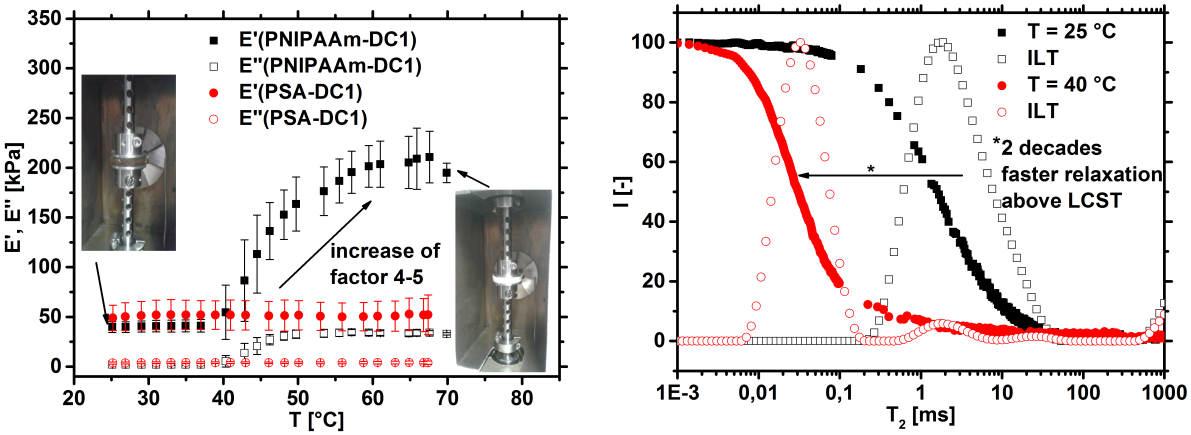


**Figure 5.41:** Left) Temperature sweeps during oscillatory compression with a controlled relative humidity of 90%. Right) $T_2$-relaxation measurements with the results obtained by the inverse Laplace transformation (ILT) for sample PNIPAAm-DC1 above and below the LCST.

## Interpenetrating PSA-*i*-PNIPAAm double networks

Interpenetrating double networks made of one PSA and one PNIPAAm network were synthesized in order to increase the fraction of sodium acrylate in the hydrogel without losing the thermal response, as described in Section 4.5 and in previous work by Hsieh *et al.* [Chen04].

The results of the rheological measurements are summarized in Table 5.2 and are comparable to the homo-IPNs (PSA-*i*-PSA). The incorporation of the second polymer network causes more constraints to the elastic chains due to additional network entanglements, and thus, higher mechanical moduli are observed.

| Sample | $G'$ [Pa] | $G''$ [Pa] |
|---|---|---|
| PSA-DC03 | 4,600 ± 1,100 | 60 ± 10 |
| PSA-DC03-*i*-PNIPAAm-DC1 | 11,700 ± 2,000 | 200 ± 100 |
| PSA-DC1 | 18,400 ± 4,500 | 250 ± 80 |
| PSA-DC1-*i*-PNIPAAm-DC03 | 33,300 ± 6,900 | 1,200 ± 780 |
| PSA-DC1-*i*-PNIPAAm-DC1 | 32,400 ± 7,400 | 1,060 ± 340 |
| PSA-DC1-*i*-PNIPAAm-DC5 | 54,000 ± 5,900 | 2,900 ± 1,300 |
| PSA-DC5 | 48,800 ± 7,900 | 5,300 ± 600 |
| PSA-DC5-*i*-PNIPAAm-DC1 | 53,000 ± 20,000 | 4,300 ± 2,700 |
| PSA-DC5-*i*-PNIPAAm-DC5 | 46,000 ± 15,000 | 6,000 ± 4,300 |

**Table 5.2:** The storage and loss moduli at room temperature for different interpenetrating double networks and the respective PSA precursors.

The degree of swelling in a 1 wt% NaCl solution at room temperature is plotted for the different hydrogels in Figure 5.42. The trends are qualitatively the same as for the PSA-*i*-PSA double networks. The water uptake decreases in the IPNs compared to the single network (SN), whereas the degree of swelling of PSA-*i*-PNIPAAm hydrogels are in general lower than PSA-*i*-PSA, due to the more hydrophobic NIPAAm monomer.

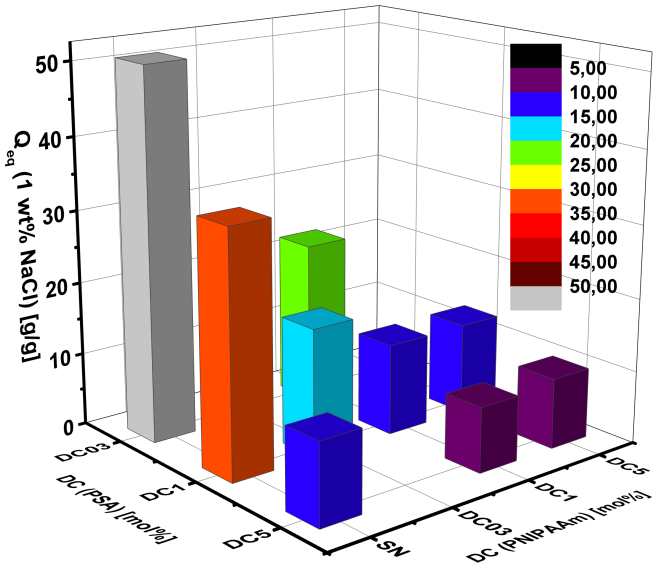


**Figure 5.42:** The degree of swelling in a 1 wt% NaCl solution at room temperature for various PSA-*i*-PNIPAAm double networks and the corresponding precursor single PSA networks (SN).

The increased thermal response of the PSA-*i*-PNIPAAm double networks compared to the P(NIPAAm-*co*-SA) single (co-)networks will be described in Section 6.4 by means of the increased water recovery during the desalination experiments. Here, the $T_2$-relaxation rate distributions at two different temperatures for the samples P(NIPAAm-*co*-SA50)-DC1 and PSA-DC1-*i*-PNIPAAm-DC1, which have both about 50 mol% SA groups in their network, shall be briefly discussed (see Figure 5.43). A temperature increase from 25 °*C* to 40 °*C* does not change the relaxation behavior in the single co-network, whereas the double network shows a marked transition. At 40 °*C*, the distribution becomes broader and a peak at larger relaxation rates appears. This peak can be related to the collapsed PNIPAAm network, while the peak at lower relaxation rates can be assigned to the unchanged PSA network. This clearly demonstrates that the double network has a thermal response, which is not the case in the single (co-)network.

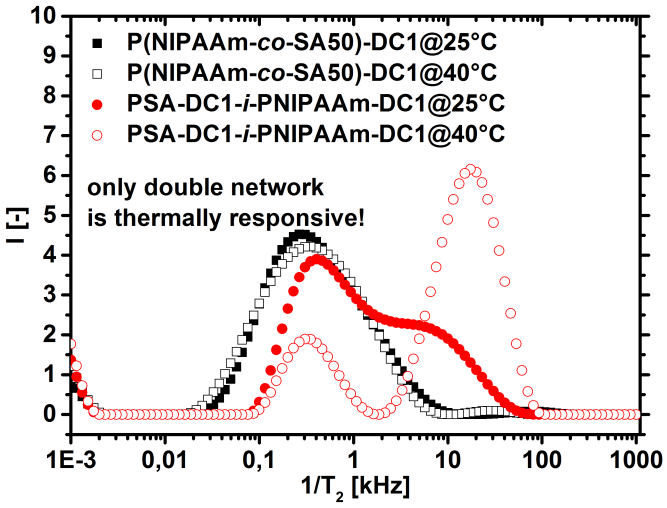


**Figure 5.43:** The $T_2$-relaxation rate distributions at two different temperatures for a single co-network and an interpenetrating double network, where the total SA content is about 50 mol% in both systems.

## 5.7 Summary

Several characterization techniques were employed in this thesis to study the various self-synthesized hydrogel systems and establish basic trends for their properties.

Swelling and mechanical measurements were used as the main methods, since they give access to the fundamental hydrogel properties, which are used in the desalination experiments (see Chapter 6) and the osmotic engine (see Chapter 7). In general, more constraints in the network, *e. g.* introduced by an increasing *DC*, the additional crosslinking of the surface or a second network (IPN), led to higher mechanical moduli and a lower water absorbency in all studied polymer samples (see Figure 5.15, 5.18 and 5.35). Typical numbers spanned over a wide range from $80 < G' < 54{,}000$ Pa and $6 < Q_{\text{eq}}$ (DI water) $< 600$, as the structures of the produced samples were very diverse and many synthetic parameters were studied.

SAXS measurements suggested a periodical distribution of the crosslinking junctions in the anionically synthesized systems (see Figure 5.7), where the elastic chain length was narrowly distributed ($PDI = 1.04 - 1.17$). Hence, these hydrogels can be regarded as more defined with a narrower pore size distribution. The distance between the crosslinking points could be calculated from the correlation peak in the SAXS patterns. Typical values for dried PMMA-*b*-PSMA-*b*-PMMA triblock copolymers were in between 10 and 40 nm. This distance increased with longer PSMA blocks and, upon swelling, which caused a 3D expansion of the crosslinking points, as shown in Figure 5.20.

The physically crosslinked hydrogels, which were made by self-assembled amphiphilic ABA triblock copolymers, were studied intensively as a function of several synthetic parameters:

A systematic variation of the hydrophobic block length A demonstrated that about 50 MMA units are necessary to obtain stable hydrogels at room temperature (see Figure 5.22). Increasing the midblock B resulted qualitatively in the same results than reducing the crosslinking density in the reference hydrogels made by FRP (see Figure 5.23). By mixing the ABA triblock copolymers with AB diblock copolymers, the amount of dangling ends in the hydrogels could be varied. In these systems, no additional polymer chains were introduced, but bridging chains were rather exchanged by dangling ends, since the aggregate size did not change. Consequently, the mechanical moduli could be drastically reduced with the AB content (more than a factor of 2 at 50% AB, as shown in Figure 5.27).

A quantitative comparison between the two quasi-model systems and the reference hydrogels made by FRP was found to be difficult to accomplish, since the average elastic chain length was not straightforward to calculate or to predict in the reference systems without further assumptions, like the validity of the phantom model. Therefore, the conclusion was drawn to compare the different hydrogels with respect to their absorbency to get the most meaningful informations. While the mechanical moduli showed in this case no large changes (see Figure 5.33), the influence on the salt rejection and desalination performance will be discussed in the next chapter.

NMR relaxometry was used to study the local polymer dynamics in the swollen hydrogels, to gain insights into the network structure. The relaxation time $T_1$ depended only on the monomer type (PSMA: 24 ms, PSA: 41 ms and PNIPAAm: 58 ms), but not on the network topology, as shown in Figure 5.11. In contrast, by measuring $T_2$-relaxation or DQ coherences, the mobility of local chain segments could be studied. The hydrogels revealed a large heterogeneity, having $T_2^{-1}$ and $D_{\text{res}}$ distributions over several decades (typical range: 0.01 – 200 kHz). More constraints in the polymer network led to a lower mobility and thus, higher $D_{\text{res}}$ constants and $T_2^{-1}$ rates were found. A direct comparison of the NMR relaxometry results between the reference hydrogels made by FRP and the anionically polymerized quasi-model systems was not straightforward. The networks with a narrowly distributed mesh length had quite large crosslinking junctions, leading to immobile parts with fast relaxation rates. This very inflexible parts caused thus a even broader distribution in the $D_{\text{res}}$ constants and $T_2^{-1}$ rates. TD-NMR was therefore not suitable to approve the narrower pore size distribution in the quasi-model systems (see Figure 5.34).

However, the measurement of $T_2$-relaxation and DQ-NMR was suitable to characterize an increased heterogeneity of the polymer mobility in other network structures. The surface crosslinking and the incorporation of a second network in the IPNs lead to bimodal distributions of the respective constants, as shown in Figure 5.19 and 5.36. Thus, the desired topology could be confirmed with this method, which is of great interest since other techniques cannot directly

study the network structure but rather investigate the improved properties of these network types.

In addition to the PSA and PSMA hydrogels, thermally responsive hydrogels with PNIPAAm segments were studied. The PNIPAAm homo-networks showed a distinctive LCST at around 35 $^{\circ}C$ (see Figure 5.40), where a strong change in many properties was measured. For example in sample PNIPAAm-DC1, the water absorbency decreased by a factor of $2-3$, while $E'$ increased by a factor of $4-5$ and the polymer relaxed much faster (the $T_2$-distribution shifted by a factor of 2 to smaller relaxation times, as shown in Figure 5.41). A distinct LCST value could solely be detected in the pure PNIPAAm networks by DSC measurements, but not in the P(NIPAAm-*co*-SA) hydrogels, where the thermal transition was broader. The interpenetrating PNIPAAm-*i*-PSA double networks showed an increased thermal response compared to the single co-networks with the same SA content: When the samples were heated to 40 °C, a marked transition in the $T_2$-relaxation behavior was probed with the IPN, which was not present in the single co-network, as shown in Figure 5.43.

In the present chapter, the basic properties of the hydrogels were described and their macroscopic quantities were correlated to their network structure. The following two chapters focus on the application of these hydrogels in the membrane-free saltwater desalination (Chapter 6) and the osmotic engine (Chapter 7).

# 6 Desalination

In the present chapter, the fully characterized hydrogels are used for the desalination of saltwater. It is discussed, how the PSA and PSMA hydrogels response to an externally applied pressure. Typical desalination curves during compression are explicitly explained for the reference hydrogels synthesized via free radical polymerization, and an efficiency criterion is introduced.

A standard protocol for the desalination experiment is defined and different self-synthesized hydrogels are studied to investigate the influence of the network topology on the desalination performance. The various network architectures are first individually compared. This allows to examine the influence of synthetic parameters. Afterward, the differences among the polymer systems are discussed, where the hydrogels are compared with respect to their degree of swelling. In this context, the salt separation is also compared with theoretical predictions from the Donnan theory.

In addition to the pressure driven desalination, thermally responsive hydrogels based on PNIPAAm are deswollen using temperature as an external stimulus. Various synthetic parameters are investigated and the effect on the salt separation as well as the desalination performance is discussed.

In the last section, the influence of different process parameters on the desalination efficiency is evaluated using the commercial polymer LB1110 as the separation agent, as this sample is available in larger quantities. The membrane-free desalination via polyelectrolyte hydrogels is compared to other commercially established methods. The criteria for a successful commercialization of the proposed method are discussed. Some criteria are already met and some questions still remain to be investigated in the next steps, as explained in an outlook.

## 6.1 Typical desalination results during the compression by an external force

The desalination experiments were conducted on an in-house built press setup with a volume of about 400 mL (see Appendix A.3.1), where the construction and the data acquisition is described more detailed in previous work [Höpfner13a, Höpfner13b, Arens17a].

In a standard experiment, the dried hydrogel beads are mixed with a 1 wt% NaCl model solution at a defined swelling ratio $Q_{rel} = 2$, which means that half of the brine volume is in the swollen polymer network and half of it is left in the supernatant phase. The mixture is stirred overnight to reach equilibrium conditions, if not otherwise noted, and eventually transferred into the press chamber. The typical trend of the salt concentration during a desalination cycle is displayed in Figure 6.1 for sample PSA-DC1.

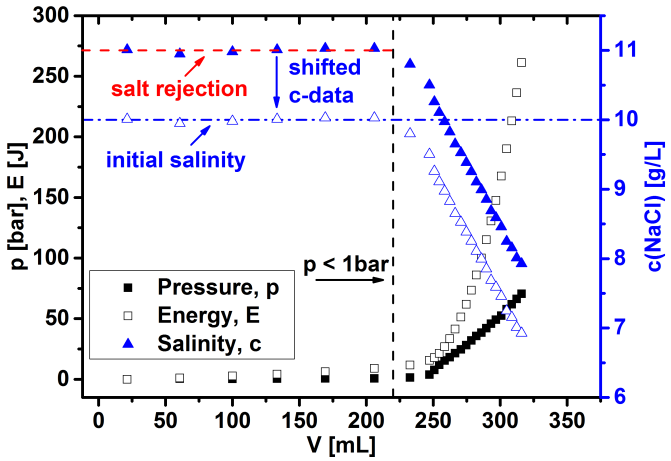


**Figure 6.1:** Typical trend of the salt concentration in the collected fractions (blue solid triangles) during a desalination cycle of sample PSA-DC1. After the supernatant is completely removed, the pressure on the gel (black solid squares) is linearly increased by 60 bar/h, consequently, also the expended energy (black open circles) increases. The higher pressure leads to a compression of the hydrogel and water with a decreasing salinity is recovered.

At the beginning of each desalination experiment, the supernatant is removed first by applying a low pressure below 1 bar. This phase has an enriched salt concentration compared to the initial NaCl solution, since the mobile salt ions are partially shielded by the fixed charges of the polyelectrolyte network, as already described in Section 2.2.4. Hence, the salt concentration of this solution directly quantifies how strong the different networks reject salt. The average salt concentration of the first fractions (see the red dashed line in Figure 6.1) is used to determine

the salt rejection

$$SR = \frac{\frac{1}{n} * \sum_i^n (c_i - c_0)}{c_0}, \tag{6.1}$$

where $c_0$ is the initial salt concentration (usually 10 g/L NaCl) and $c_i$ is the salt concentration of fraction $i$. For the calculation of $SR$ only fractions were taken into account before the pressure was increased above 1 bar (black, vertical line in Figure 6.1). After the supernatant is completely removed, the pressure on the gel is linearly increased to compress the hydrogel and water with a decreasing salinity is obtained — an effective desalination is achieved.

In the next section, a criterion is introduced to quantify the desalination efficiency of a certain experiment. This allows to keep the amount of data manageable and to compare different chemical or process parameter in a straightforward way. Section 6.3 describes the influence of the various network structures on the salt rejection and the desalination properties. The trends of the $p$, $V$ and $c$ data during the compression are shown for the PSA reference hydrogels in more detail.

## 6.2 Efficiency criterion — Assumption of the specific energy

The desalination efficiency is determined from the expended energy and the removed amount of salt. The energy $E$ used in the experiments is calculated by the numerical integration of the volume work (open black squares in Figure 6.1):

$$E = \int -p dV, \tag{6.2}$$

while the potential extracted salt mass is given by

$$\Delta m(\text{NaCl}) = m(\text{NaCl, initial}) - m(\text{NaCl, fractions}) = c_0 * \sum_i V_i - \sum_i (c_i * V_i), \tag{6.3}$$

where $c_0$ is the initial salt concentration and $c_i$ is the salt concentration of fraction $i$ with the volume $V_i$. The shifted concentration data (open blue triangles in Figure 6.1) was used to calculate $\Delta m$(NaCl). The original $c$ data was shifted (by subtraction) to the initial salt concentration, since in a real process the hydrogel would be swollen (at least in the first step) in an infinite large external salt bath (*e. g.* the sea) resulting in no apparent salinity change of the supernatant, as shown in preliminary results [Arens17a]. In further steps, the supernatant phase could be easily removed without spending much energy leading to a similar starting point. For the calculation of $\Delta m$(NaCl), only fractions after the pressure was increased above 1 bar (vertical, black dotted line in Figure 6.1) were taken into account in Equation 6.3. Below

1 bar, no desalination is achieved and the obtained values for $\Delta m$(NaCl) scatter only around 0, depending on the noise of the data.

The efficiency increases in one desalination cycle, if either the energy demand is lower or more salt can be removed. The ratio of expended energy $E$ to removed salt mass $\Delta m$(NaCl), expressed in Equation 6.4 by the parameter $\kappa$ (kWs/g), is therefore a criterion to quantify the desalination efficiency [Albrecht13].

$$\kappa = \frac{E}{\Delta m(\mathrm{NaCl})} \tag{6.4}$$

Alternatively, the specific energy, calculated from the perspective energy to remove 35 kg of salt in one cubic meter water as a mimic for seawater, can be estimated by

$$E_{\mathrm{m^3}} = \kappa * \frac{35,000}{3,600\ \mathrm{s/h}} \approx 10 * \kappa\,. \tag{6.5}$$

While $\kappa$ and $E_{\mathrm{m^3}}$ can be both used to describe the energy efficiency of the different hydrogels, the latter parameter also allows a comparison with data from the literature.

In order to compare different hydrogel samples, it has to be considered that the energy efficiency is also a function of the applied pressure, as displayed in Figure 6.2.

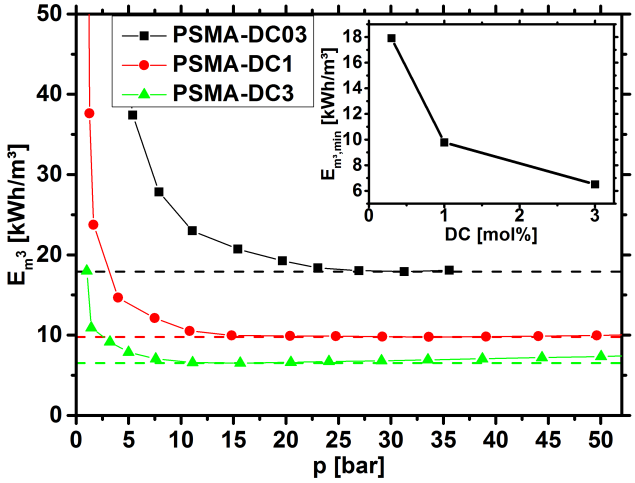


**Figure 6.2:** The specific energy $E_{\mathrm{m^3}}$ is plotted as a function of the applied pressure for a 0.3, 1 and 3 mol% crosslinked PSMA hydrogel. The minimum is reached within 10 – 30 bar and afterward, only minor changes are observed. The inset additionally displays the energy minimum $E_{\mathrm{m^3,min}}$ (dashed lines) as a function of the degree of crosslinking ($DC$).

At low pressure, the desalination is inefficient. With increasing pressure to 10 – 30 bar, depending on the sample, the specific energy becomes almost constant. This can be explained

since the slope for the $c - p$ data is almost constant, as discussed in the next section. In the following considerations, the minimum $E_{m^3,min}$ is used as the efficiency value to quantify different samples.

## 6.3 Influence of the network topology on the desalination efficiency

### 6.3.1 Degree of crosslinking and monomer type

The desalination results of the PSA and PSMA hydrogels with a varying *DC*, synthesized via FRP (see Section 4.1 and Appendix A.1.2), shall be discussed first. PSA networks have been used in the proof of principle [Höpfner10] and shall serve as a reference system in the present thesis. In previous work, it was found that the *DC*, which defines the pore size of the network, is one of the crucial parameters to influence the desalination properties [Höpfner10, Höpfner13a, Arens17a]. As described in Chapter 5, a denser network has a lower solution capacity and a higher mechanical strength. Hence, a higher pressure is needed to squeeze water out of the hydrogel. On the other hand, higher crosslinked hydrogels have a higher charge density and thus, a larger salt rejection, which is beneficial for the desalination process.

Typical results for three PSA hydrogels with a varying *DC* of 0.3, 1 and 5 mol% are displayed in Figure 6.3. The probed $c$, $p$ and $V$ data is correlated into a 3D plot. However, only the projections are shown, as the trends of the curves are quite complex. This depiction is clearer, while the $c-p-d$-data can be still easily correlated by eye. At the beginning of each experiment, the mobile ions from the brine are partially rejected by the polyelectrolyte and the salt concentration increases in the supernatant phase. The salt rejection *SR* increases with a higher degree of crosslinking, since these gels have more charges per volume in the swollen state. The actual desalination experiment starts by applying a low pressure of about 1 bar to remove the supernatant phase and loosely bound water with a high volume flux (independent of *DC*) and a constant salt concentration. After this water is removed, a linear decrease in the volume flux ($\frac{dV}{dt}$) can be observed. It is necessary to apply a higher pressure to further compress the hydrogels. The decrease in the salt concentration $c$(NaCl) as a function of time $t$ and pressure $p$ is almost linear. This linear relationship between $c$ and $p$ can be expected as the osmotic pressure scales linearly with the salt concentration, as explained in Section 2.2.2 (Equation 2.1). The slope for the $c - p$ data is steeper for a higher *DC*, since more pressure is needed to deform the hydrogels with a lower capacity and a higher mechanical modulus. The flux within this region increases with a lower *DC* due to the higher water content in the lower crosslinked samples and the slope in the $c - V$ diagram becomes also smaller.

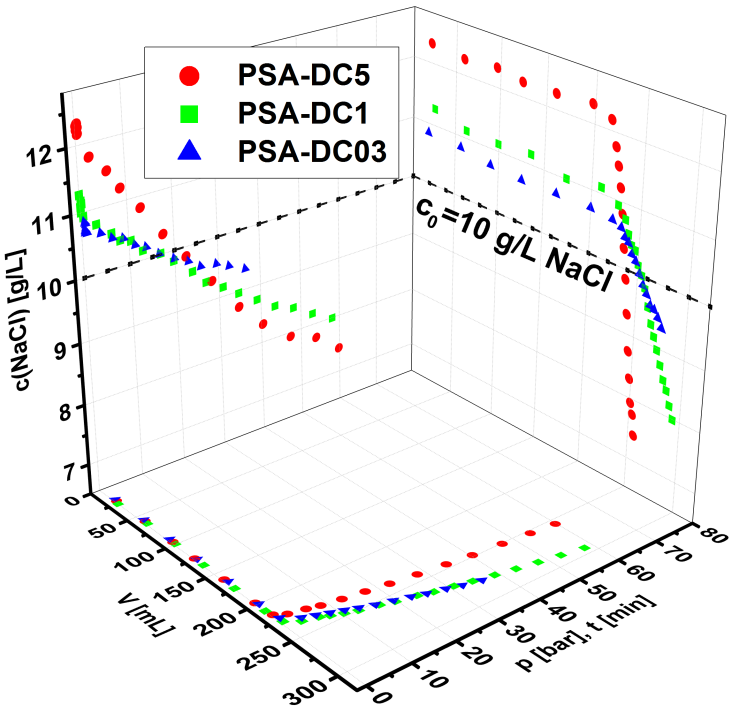


**Figure 6.3:** Typical results of the desalination experiments for PSA with three different degrees of crosslinking ($DC$ = 0.3, 1 and 5 mol%). For the sake of clarity, only the respective projections of the three-dimensional $c - p - V$ curves are shown.

The values for the salt rejection $SR$ and the specific energy $E_{m^3,min}$ are summarized in Table 6.1 for different hydrogels synthesized via FRP. Several conclusions can be drawn from this data:

The salt separation increases in higher crosslinked samples, which is to be expected due to the higher charge density. Furthermore, the energy efficiency is increasing with a higher $DC$. In general, $E_{m^3,min}$ can be optimized by either lowering the expended energy $E$ or by increasing the amount of removed salt $\Delta m$(NaCl). The latter quantity depends on the volume of collected water and the corresponding salt concentration. Hydrogels with a higher $DC$ have larger mechanical moduli, which means that more energy is needed to compress the hydrogels ($E$ increases). Additionally, the degree of swelling is lower and thus, also the water productivity. On the other hand, the salt rejection increases with a higher $DC$. The $E_{m^3,min}$ values demonstrate that the increased salt rejection is the essential quantity and the desalination becomes therefore more efficient with higher crosslinked hydrogels. It should be however noted that more (dried) material is used for the higher crosslinked samples with the lower absorbencies (see Appendix A.3.1), since the desalination experiments are conducted at a fixed gel volume of about 200 mL (due to the fixed size of the press setup).

A qualitatively similar behavior has been described in coarse-grained hydrogel simulations by the group of Christian Holm [Richter17a, Richter17b]. In that work, it was observed that

either highly charged hydrogels or soft hydrogels with a low *DC* and *DN* will perform best (with specific energies between 1.5 and 3 kWH/m³). Very soft samples cannot be experimentally investigated since they are mechanically too weak and are pushed through the filter units. Therefore, it is better to use the highly charged hydrogels with a high *DC* and *DN* due to practical reasons.

| Sample | *SR* [wt%] | $E_{m^3,min}$ [kWh/m³] | $Q_{eq}$ (1 wt% NaCl) [g/g] |
|---|---|---|---|
| PSA-DC03 | 6.6 | 18.4 | 50.8 ± 0.7 |
| PSA-DC1 | 11.0 | 14.7 | 33.5 ± 1.5 |
| PSA-DC1 (microfluidic) | 10.4 | 11.7 | 33.1 ± 0.3 |
| PSA-DC5 | 22.7 | 9.1 | 11.8 ± 0.1 |
| PSA-DC5 (microfluidic) | 22.7 | 8.1 | 10.6 ± 0.3 |
| PSMA-DC03 | 12.7 | 17.9 | 22.5 ± 0.6 |
| PSMA-DC1 | 18.1 | 9.8 | 11.7 ± 0.1 |
| PSMA-DC3 | 29.7 | 6.5 | 7.7 ± 0.3 |
| PSA-DC1-TEGDA | 7.0 | 18.1 | 33.6 ± 0.3 |
| PSA-DC5-TEGDA | 18.7 | 9.2 | 15.9 ± 1.2 |
| PSA-DC10-TEGDA | 23.4 | 7.9 | 10.4 ± 0.9 |
| PSA-DC20-TEGDA | 23.0 | 7.1 | 10.3 ± 0.0 |
| PSA-DC30-TEGDA | 19.5 | 7.9 | 8.8 ± 0.0 |

**Table 6.1:** Salt rejection *SR*, specific energy $E_{m^3,min}$ and degree of swelling $Q_{eq}$ (1 wt% NaCl) for various free radical polymerized PSA and PSMA hydrogels.

Highly crosslinked hydrogels have been synthesized, using the more soluble crosslinker TEGDA instead of MBA, to further increase the accessible *DC*. Compared at the same degree of crosslinking (*e. g.* DC1 and DC5), the TEGDA crosslinked hydrogels are slightly less energy efficient and have a lower salt rejection. This could be related to a reduced crosslinker efficiency in case of the long TEGDA molecule, which can easily form rings instead of effective crosslinks. Yet, with TEGDA much higher values of *DC* are accessible. In good agreement with previous results, a higher *DC* leads to a higher salt rejection and an increased desalination efficiency. However, as already discussed in Section 5.2, the crosslinker is quite long and above approximately 13 mol%, the crosslinker itself becomes longer than the actual elastic PSA mesh. Hence, neither the charge density nor the pore size increases further and the desalination performance is about the same for the three samples with a *DC* of 10, 20 and 30 mol%.

Furthermore, hydrogels were fabricated by the droplet-based microfluidic technique to generate monodisperse particles (see Appendix A.1.3). This polymers show a better desalination efficiency (about 11 – 20% lower $E_{m^3,min}$), whereas the salt rejection is unaffected. As the chemical structure is the same as in the other PSA hydrogels, no change in the salt rejection can be

expected and the lower $E_{m^3,min}$ values can be explained by a reduced gel-blocking. Gel-blocking most probably increases the force required to press the water out of the gel as there is less space among the particles for the water molecules to flow freely. Therefore, the bound water from the polymer beads in the sample chamber must be pressed via a higher pressure through a blocking gel layer, resulting in a less energy efficient process. The microfluidic technique allows fabricating monodisperse particles of sub-millimeter-sized spheres, which results in more inter-particle voids and thus, less gel-blocking.

In some samples, the monomer sodium acrylate has been substituted by sodium methacrylate. In the desalination experiments, PSMA hydrogels show a higher salt rejection and a higher efficiency compared to PSA hydrogels with the same *DC*. PSMA is a more hydrophobic polymer and hence, the degree of swelling is lower in these systems. Similar to the already mentioned argumentation, the lower water uptake causes a higher charge density per volume in the swollen network. Hence, *SR* increases, while $E_{m^3,min}$ decreases.

### 6.3.2 Surface crosslinked PSA hydrogels

In the previous section, it has been discussed that a higher *DC* is more energy efficient due to the increased salt separation, although higher crosslinked samples need more energy for the compression of the gel. Here, the desalination results of the PSA hydrogels, which were additionally crosslinked on their surface (see Section 4.2 and Appendix A.1.4), are discussed. The surface crosslinked hydrogels have been synthesized with the intention to combine the advantages of a high *DC*, such as a high *SR* with the advantages of a low *DC*, such as a lower mechanical modulus and a higher water capacity.

As seen in Section 5.3, the degree of swelling is decreasing with the thickness of the shell in the surface crosslinked samples. At the same time, the number of charges in the hydrogel particles is reduced as the crosslinker EGDE has reacted with the carboxyl groups of the network. However, the salt rejection is still enhanced in all the surface crosslinked samples with the shell thickness, except sample PSA-DC5-P1 (see Table 6.2).

The desalination efficiency is improving in all samples where a thin part of the surface was additionally crosslinked (P1), but it is worsened when the shell was thicker (P10). However, this is rather related to the lower water absorbency than to the core-shell structure, as discussed in Section 6.3.5. Furthermore, the changes of the specific energies between the untreated and surface crosslinked networks were found to be small and do not exceed the uncertainty of the experiment.

| Sample | *SR* [wt%] | $E_{m^3,min}$ [kWh/m³] | $Q_{eq}$ (1 wt% NaCl) [g/g] |
|---|---|---|---|
| PSA-DC03 | 6.6 | 18.4 | 50.8 ± 0.7 |
| PSA-DC03-P1 | 7.5 | 15.8 | 40.2 ± 2.0 |
| PSA-DC03-P10 | 14.0 | 16.6 | 30.1 ± 1.5 |
| PSA-DC1 | 11.0 | 14.7 | 33.5 ± 1.5 |
| PSA-DC1-P1 | 12.8 | 13.3 | 23.1 ± 1.2 |
| PSA-DC1-P10 | 20.0 | 14.3 | 14.6 ± 0.7 |
| PSA-DC5 | 22.7 | 9.1 | 11.8 ± 0.1 |
| PSA-DC5-P1 | 17.2 | 8.1 | 10.1 ± 0.5 |

**Table 6.2:** Salt rejection *SR*, specific energy $E_{m^3,min}$ and degree of swelling $Q_{eq}$ (1 wt% NaCl) for various self-synthesized surface crosslinked PSA hydrogels.

### 6.3.3 Quasi-model systems with a defined elastic chain length

In this section, the typical trends of the different quasi-model systems are briefly explained, while a more detailed comparison with the reference hydrogels made by FRP will follow in Section 6.3.5. Hydrogels with a defined mesh length were synthesized via anionic polymerization to study whether the pore size distribution influences the salt separation and desalination efficiency, as a narrow distribution is crucial in any 2D membrane process.

#### Chemically end-linked PSMA-EGDMA hydrogels

The chemically end-linked PSMA-EGDMA networks have been synthesized (see Section 4.3.4 and Appendix A.1.6) as an alternative to the physically crosslinked hydrogels and their number of monomers per elastic chain was not varied over a large range. Therefore, no systematic trend in their desalination behavior can be observed and *SR* was found to be in the range of 13 – 14 wt%, while the energy efficiency is about 12.5 kWh/m³ (see Table 6.3).

| Sample | *SR* [wt%] | $E_{m^3,min}$ [kWh/m³] | $Q_{eq}$ (1 wt% NaCl) [g/g] |
|---|---|---|---|
| PSMA225-EGDMA5 | 12.7 | 12.3 | 22.0 ± 0.9 |
| PSMA162-EGDMA7 | 14.3 | 12.8 | 20.4 ± 1.3 |

**Table 6.3:** Salt rejection *SR*, specific energy $E_{m^3,min}$ and degree of swelling $Q_{eq}$ (1 wt% NaCl) for two chemically end-linked PSMA-EGDMA hydrogels.

#### Physically crosslinked hydrogels made by self-assembled ABA triblock copolymers

A broader spectrum of synthetic parameters was varied in the physically crosslinked hydrogels, made by the self-assembly of amphiphilic ABA triblock copolymers (see Section 4.3.3 and

Appendix A.1.5). The number of MMA units $N$(A) per endblock, the number of SMA units $N$(B) in the midblock and the total number of monomers $N$(ABA) using a constant ratio of A to B was systematically varied (see Table 6.4). Furthermore, the PMMA-*b*-PSMA-*b*-PMMA triblock copolymers were mixed with PMMA-*b*-PSMA diblock copolymers to decouple mechanical strength and charge density (see Table 6.5).

| Sample | $SR$ [wt%] | $E_{m^3,min}$ [kWh/m³] | $Q_{eq}$ (1 wt% NaCl) [g/g] |
|---|---|---|---|
| 178-507-160 | 12.5 | 13.5 | 13.5 ± 0.2 |
| 87-371-113 | 16.2 | 13.8 | 15.8 ± 0.7 |
| 56-374-47 | 13.7 | 15.5 | 27.3 ± 0.2 |
| 38-505-31 | no water recovery possible | no desalination | 34.7 ± 0.8 |
| 15-275-15 | no water recovery possible | no desalination | soluble |
| 90-80-105 | 23.7 | no data collected* | 4.9 ± 0.3 |
| 60-98-81 | 21.8 | no data collected* | 7.3 ± 0.1 |
| 58-194-66 | 20.7 | 10.4 | 9.7 ± 0.2 |
| 63-323-63 | 15.7 | no data collected* | 20.4 ± 0.6 |
| 60-340-53 | 16.4 | 17.7 | 22.4 ± 0.8 |
| 56-374-47 | 13.4 | 15.5 | 27.3 ± 1.0 |
| 363-1289-363 | 12.5 | 12.2 | 18.6 ± 0.7 |
| 178-507-160 | 12.5 | 13.5 | 13.5 ± 0.2 |
| 87-371-113 | 16.2 | 13.8 | 15.8 ± 0.7 |
| 58-194-66 | 20.7 | 10.4 | 9.7 ± 0.2 |

**Table 6.4:** Salt rejection $SR$, specific energy $E_{m^3,min}$ and degree of swelling $Q_{eq}$ (1 wt% NaCl) for various physically crosslinked PMMA-*b*-PSMA-*b*-PMMA hydrogels. Note: It was not enough material for all samples available to conduct the desalination experiments (samples marked with an asterisk (*)).

As already discussed in the previous chapter, the number of MMA monomers $N$(A) in the endblock was found to be crucial for the hydrogel stability. Therefore, the desalination experiments are only possible to conduct with samples that have at least 50 MMA units in their endblock. Otherwise, the samples cannot sustain the high pressures needed and are pushed through the filter units of the apparatus. The maximum applied pressure without destroying the hydrogel was 38 bar for $N(A) = 52$, and over 70 bar for samples with a larger endblock. The salt rejection (13 – 16 wt%) shows no systematic change and the differences in the energy efficiency of the desalination process (between 13.5 – 15.5 kWh/m³) did not exceed the uncertainty of the experiment, when $N$(B) was fixed, while varying $N$(A). This can be explained as the variation of $N$(A) leads to no large changes in the network charge density.

In the samples, where the size of the endblock is fixed at about 67 MMA units, but the midblock length is varied in the range of 80 to 374, the trends are similar to the reference

hydrogels. Fewer monomer units in the midblock, resulting in smaller elastic chains, lead to a higher salt rejection and a better desalination efficiency caused by the higher charge density of the network. The salt rejection increases for example from 13 to 21 wt%, reducing the elastic chain length from $N(\mathrm{B}) = 374$ to $N(\mathrm{B}) = 194$ units, while the desalination efficiency improves from 15.5 to 10.4 kWh/m³ for these samples.

The following trends can be observed, when the ratio of PMMA to PSMA is fixed, but the overall polymer length is increased. The smaller polymers have a shorter elastic chain length and therefore a higher salt rejection and a higher desalination efficiency, although this effect becomes less pronounced in the very large molecules. For example, the samples 58-194-66 and 363-1289-363 have a salt rejection of 21 wt% and 13 wt%, respectively.

Furthermore, the ABA triblock copolymer 72-408-71 was mixed with a varying amount of the AB diblock copolymer 80-187 in order to pointedly increase the fraction of dangling ends. Samples with more dangling ends need less energy $E$ to recover the desalinated water but also have a lower salt separation, as seen in Table 6.5.

| AB diblock copolymer [wt%] | $SR$ [wt%] | $E_{\mathrm{m^3,min}}$ [kWh/m³] | $Q_{\mathrm{eq}}$ (1 wt% NaCl) [g/g] |
|---|---|---|---|
| 0 | 15.8 | 16.6 | 20.1 ± 2.0 |
| 25 | 13.6 | 17.2 | 23.8 ± 0.4 |
| 37.5 | 11.0 | 15.5 | 24.8 ± 0.4 |
| 37.5 (long) | 9.2 | 34.6 | 33.0 ± 0.5 |
| 50 | no water recovery possible | no desalination | 22.7 ± 1.1 |
| 75 | no water recovery possible | no desalination | 21.5 ± 0.5 |

**Table 6.5:** Salt rejection $SR$, specific energy $E_{\mathrm{m^3,min}}$ and degree of swelling $Q_{\mathrm{eq}}$ (1 wt% NaCl) for physically crosslinked hydrogels with a varying amount of dangling ends. The networks were prepared by mixing the sample 72-408-71 with different amounts of the diblock 80-187 and sample 80-587 (long), respectively.

The lower salt rejection can be explained by two reasons: First, the water absorbency is slightly higher in the ABA/AB mixtures and second, the PSMA block is about 8% smaller than half of the PSMA block in the triblock copolymers. Both arguments result in a slightly reduced charge density. As a consequence of the reduced charge density and mechanical modulus, the desalination efficiency is about the same for the different samples, as given in Table 6.5. Qualitatively the same results were also found in simulations of coarse-grained hydrogels: Increasing the number of dangling ends led to a higher water absorbency, to a slightly worse salt rejection, but also to a reduced value of the bulk modulus [Richter17a]. Experimentally, hydrogels with a high amount of diblock copolymers (≥ 50%) were found to be mechanically

too weak to achieve an effective desalination and were pushed through the filter units during the compression.

Mixing the triblock copolymer 72-408-71 with the diblock copolymer 80-587, in which the PSMA-block, *i. e.* the dangling ends are larger than the elastic chains, causes a significant structural change, as discussed already in Section 5.4.1. The larger distance between the crosslinking points in this network results in mechanically weaker hydrogels with an increased absorbency. Hence, the charge density in this system is even smaller in the swollen state, which causes a decreased salt separation and a strong increase of $E_{m^3,min}$.

### 6.3.4 Interpenetrating PSA-*i*-PSA double networks

Interpenetrating PSA-*i*-PSA double networks were synthesized to increase and homogenize the charge density, as discussed in Section 4.4. The values of the salt rejection and the specific energies of the interpenetrating PSA-*i*-PSA double networks are summarized in Table 6.6. Both, the salt rejection and the desalination efficiency are increasing in all double networks compared to their single precursor networks. This is simply explained by the increased charge density in the IPNs. Especially in the already highly crosslinked sample PSA-DC5, adding a second network did not change the mechanical properties much but added additional charges to the hydrogel. Hence, the salt separation is improved without the need to apply a higher pressure to compress the gel. Consequently, the double network PSA-DC5-*i*-PSA-DC1 was found to be the most energy efficient sample in this thesis, with a potential specific energy of only 5.6 kWh/m³.

| Sample | *SR* [wt%] | $E_{m^3,min}$ [kWh/m³] | $Q_{eq}$ (1 wt% NaCl) [g/g] |
|---|---|---|---|
| PSA-DC03 (SN) | 6.6 | 18.4 | 50.8 ± 0.7 |
| PSA-DC03-*i*-PSA-DC1 | 13.0 | 12.4 | 25.1 ± 1.3 |
| PSA-DC1 (SN) | 11.0 | 14.7 | 33.5 ± 1.5 |
| PSA-DC1-*i*-PSA-DC03 | 16.0 | 12.3 | 21.7 ± 1.1 |
| PSA-DC1-*i*-PSA-DC1 | 14.6 | 12.7 | 21.0 ± 1.1 |
| PSA-DC1-*i*-PSA-DC5 | 18.2 | 8.5 | 15.7 ± 0.8 |
| PSA-DC5 (SN) | 22.7 | 9.1 | 11.8 ± 0.1 |
| PSA-DC5-*i*-PSA-DC1 | 23.8 | 5.6 | 8.0 ± 0.4 |
| PSA-DC5-*i*-PSA-DC5 | 24.3 | 5.9 | 8.4 ± 0.4 |

**Table 6.6:** Salt rejection *SR*, specific energy $E_{m^3,min}$ and degree of swelling $Q_{eq}$ (1 wt% NaCl) for various self-synthesized PSA-*i*-PSA interpenetrating double networks and the corresponding precursor hydrogels.

### 6.3.5 Comparison of the different network topologies

In this section, the different polymer network architectures are compared in their ability to reject salt and in the corresponding desalination efficiency. As already discussed in Section 5.4.3, plotting the salt rejection $SR$ and specific energy $E_{m^3,min}$ as a function of the degree of swelling in the respective NaCl solutions is the most straightforward way to compare the various hydrogels.

#### Monomer type and particle shape

In Figure 6.4, the influence of the monomer type (SA or SMA) and the particle shape (microfluidic samples) is shown. The salt rejection in the PSA hydrogels is independent of the particle size (not shown) and shape as expected, since only the amount of charges in the swollen state influences this quantity. In contrast, the specific energy is lower for the monodisperse particles with a uniform, spherical shape produced by the droplet-based microfluidic technique. Hence, the increased desalination efficiency can be referred to the reduced gel-blocking, which reduces the energy needed to compress the hydrogels. While gel-blocking is reduced with the spherical beads, the particle size of the ground particles with no regular shape had no influence on the gel-blocking and thus, also no change in the specific energy was observed (not shown). However, gel-blocking is a more pronounced problem in mechanical weaker hydrogels and thus, the particle shape leads to less improvement for higher crosslinked samples.

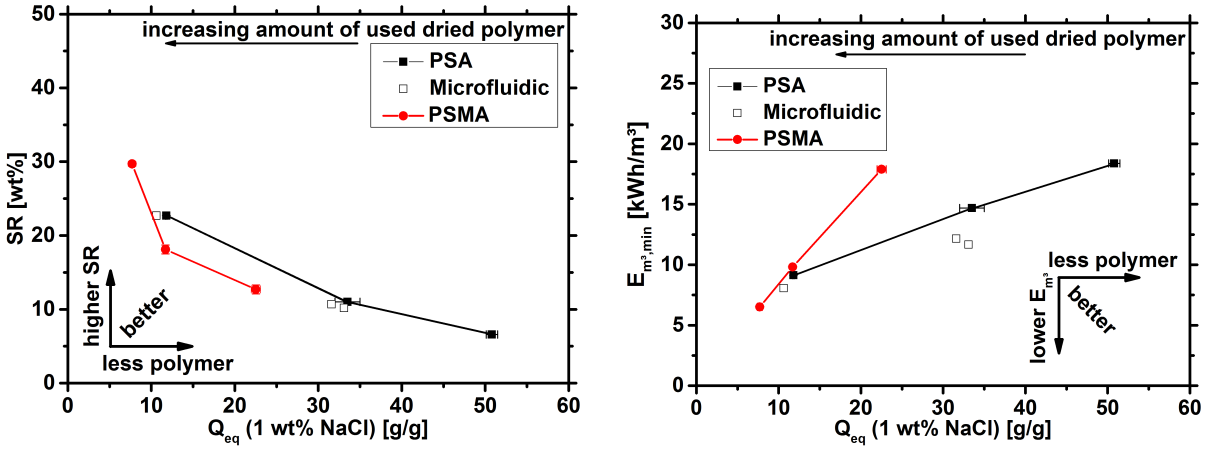


**Figure 6.4:** Left) Salt rejection $SR$ at a fixed $Q_{rel} = 2$. Right) The specific energy $E_{m^3,min}$ as a function of the water absorbency for PSA, PSMA and uniform PSA beads (microfluidic). The lines are only a guide to the eye.

PSMA has a lower salt rejection than PSA, when the samples are compared with respect to their degree of swelling. At the same $Q_{eq}$, PSMA has the lower charge density and can consequently reject less ions. However, in the samples with the highest $DC$, the degree of

swelling is considerably smaller in the PSMA samples and therefore, the charge density, the salt rejection and the desalination efficiency is higher.

It should be noted that this is a general statement: A lower water absorbency leads to more charges per volume in the swollen state. Consequently, the salt rejection is increasing from the right to the left in Figure 6.4, left, while the specific energy is decreasing in the same direction (Figure 6.4, right). However, with a lower $Q_{eq}$ also more dried raw material is needed, since around 200 g of swollen hydrogel were always used in the experiments due to the fixed volume of the press setup. If either a higher water productivity (high $Q_{eq}$) or the lowest energy consumption (low $E_{m^3,min}$) is more desirable would dependent in the end on the application. A direct improvement of the desalination efficiency can be seen anyway, if $E_{m^3,min}$ is reduced at the same $Q_{eq}$ or, if $Q_{eq}$ is increasing at the same $E_{m^3,min}$ (as indicated by the arrows in Figure 6.4).

#### Quasi-model systems

The reference PSMA hydrogels synthesized via FRP and the quasi-model systems with a defined elastic chain length are compared in Figure 6.5. On the left graph, the salt rejection is shown for the different hydrogels and the data is compared with theoretical calculations from the Donnan theory (see Equation 6.6, 6.7 and 6.8) [Donnan32, Höpfner13b]:

The salt concentration of mobile anions in the gel phase $c_-$ is given under the assumption of an infinite salt bath by:

$$c_- = \sqrt{\left(\frac{DN * c_p}{2}\right)^2 + c_0^2} - \frac{DN * c_p}{2}, \tag{6.6}$$

where $c_p = \frac{1}{Q_{eq}}$ is the polymer concentration in the swollen hydrogel and $c_0$ is the initial salt concentration of the bath (here: 10 g/L = 0.17 mol/L [NaCl]).

From the mass balance of added NaCl, the salt concentration in the supernatant phase $c_{out}$ is calculated, using

$$c_{out} = \frac{(Q_{rel} * c_0 - c_-)}{(Q_{rel} - 1)}, \tag{6.7}$$

where the relative degree of swelling $Q_{rel} = 2$.

The salt rejection $SR$ is then given relatively to the initial salt concentration by

$$SR_{Donnan} = \left(\frac{c_{out} - c_0}{c_0}\right) * 100\, wt\%\,. \tag{6.8}$$

In Figure 6.5, left, the salt rejection is plotted with respect to the degree of swelling for the quasi-model systems and the reference hydrogels. The different network types show similar behavior having $SR$ values in the same order of magnitude. The salt rejection is admittedly slightly higher for the quasi-model systems at larger $Q_{eq}$ values, though the differences to the

hydrogels made by FRP are rather insignificant. In contrast, the salt rejection is smaller in the self-assembled ABA systems at lower absorbencies $Q_{eq} < 10$ g/g. The relative amount of PMMA in these systems is rising with a decreasing $Q_{eq}$ from 24 to 71 mol%. Hence, at lower degrees of swelling, the relative amount of charged SMA groups is smaller than in the FRP samples, since the PMMA is only non-active mass that does not contribute to the salt separation, but reduces $Q_{eq}$.

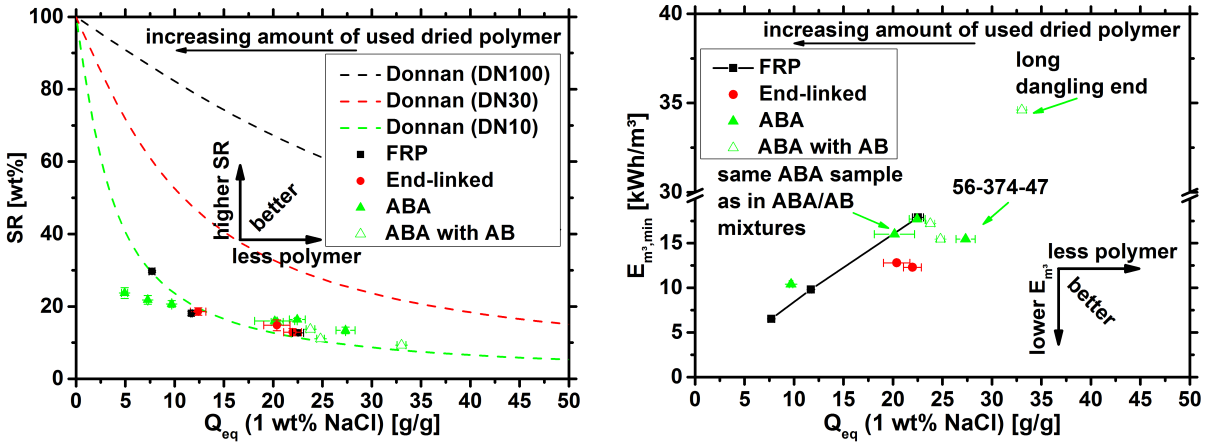


**Figure 6.5:** Salt rejection $SR$ (left) and specific energy $E_{m^3,min}$ (right) as a function of the degree of swelling for the quasi-model systems and the reference hydrogels (both PSMA). In the left graph, the theoretical salt rejections are additionally displayed, using the Donnan equilibrium with various charge densities (see Equation 6.8).

The experimental data demonstrates that the Donnan theory strongly overestimates the salt rejection, which was also found in previous work [Höpfner13b]. In that publication, the author showed that the deviations are increasing at higher $DN$. The Donnan theory is expected to fail at higher ionic strength, since in Equation 6.6, concentrations are used instead of activities. Furthermore, the in Chapter 3 introduced counterion condensation leads to a reduced effective charge concentration along the polymer backbone. Typically, Manning condensation starts once the $DN$ exceeds 30 mol%. However, even with this value, the Donnan prediction still strongly overestimates the experimental data, and only assuming a very small $DN$ of ca. 10 mol% would result in a good agreement between theory and experiment, as shown in Figure 6.5, left.

In the right graph of Figure 6.5, the specific energies of the different hydrogels are compared.[1] Except sample 56-374-47, the self-assembled pure ABA triblock copolymers and the FRP hydrogels showed basically no differences. Mixing sample 72-408-71 with the diblock copolymer 80-187 in order to increase the amount of dangling ends did not reduce the specific energy but resulted in larger degrees of swelling without increasing $E_{m^3,min}$. Therefore, dangling

[1] Only a smaller number of quasi-model systems could be experimentally studied in the desalination process due to the limited quantities, which were accessible via the anionic polymerization.

ends are beneficial for the desalination efficiency. The same behavior was found for sample 56-374-47. This triblock copolymer has just long enough endblocks to form stable hydrogels (see Figure 5.22 in Chapter 5). However, slow chain exchange kinetics are probably also present at room temperature in this specific sample, which lead to reversible dangling ends. The introduction of longer dangling ends by mixing the samples 72-408-71 and 80-587 causes a much higher degree of swelling, but also a drastically increased specific energy.

The chemically end-linked PSMA-EGDMA networks show a higher efficiency with respect to the degree of swelling compared to the free radical polymerized reference hydrogels. However, if this is related to the more defined elastic chain length or just to the rather high uncertainty of the experiment (see Figure 6.6), could not be finally answered in this thesis due to the low amount of data points. Furthermore, also a higher amount of dangling ends in the chemically end-linked PSMA-EGDMA systems compared to the FRP hydrogels could be possible, since the amount of unreacted precursor molecules in the PSMA-EGDMA star polymer synthesis was also found to be in the range of 12 to 17 mol% (see Table 4.1 in Section 4.3.4). More experiments are still needed to finally answer the influence of the pore size distribution on the desalination properties.

#### PSA network architecture

In Figure 6.6, the desalination results are compared for the different PSA network architectures. The basic trends in the curves are similar for all samples: A lower absorbency results in a higher salt rejection and a lower specific energy.

In the left graph, it is seen that the salt rejection can be qualitatively, but not quantitatively described by the Donnan theory. Except for a few samples, a smaller $Q_{eq}$ always leads to a higher salt rejection. However, in some samples higher amounts of non-charged components, such as the longer TEGDA crosslinker or the surface crosslinking agent EGDE, were incorporated into the polymer network. Hence, $Q_{eq}$ is reduced in these hydrogels without increasing the number of charges and thus, the salt rejection decreases. The distribution of the fixed charges inside the polymer network does not significantly influence the salt partitioning. The differences among the interpenetrating PSA-*i*-PSA networks, the surface crosslinked and the randomly crosslinked PSA hydrogels are rather negligible. Thus, not the distribution of charges, but only the total number of charges throughout the whole network influences *SR*, as qualitatively predicted by the Donnan theory. The core-shell particles particularly demonstrate that the hydrogels may not be regarded as a 2D membrane, having only one interface between solution and gel phase. The sum of all charges, inside and outside the hydrogel, must always be considered.

The specific energies are compared in Figure 6.6, right. The uncertainty of the specific energy is shown for sample PSA-DC1 ($\Delta E_{m^3,min} = 6.3\%$), for which the desalination experiment was

repeated three times using each time a new sample. The larger error bar of the commercial sample LB1110 ($\Delta E_{m^3,min}$ = 21.5%) originates from the recycling experiment (see Section 6.5), where the same hydrogel particles were used in 20 successive desalination cycles (without a systematic change in $E_{m^3,min}$) [Arens17a].

The differences in the desalination efficiency at the same degree of swelling among the various samples did not exceed the uncertainty in most experiments. As shown in the previous chapter, the hydrogel properties, like the water absorbency, the mechanical moduli or the polymer segment mobility could be widely changed. However, comparing the salt separation and the desalination efficiency in the various samples, the network architecture plays only a minor role.

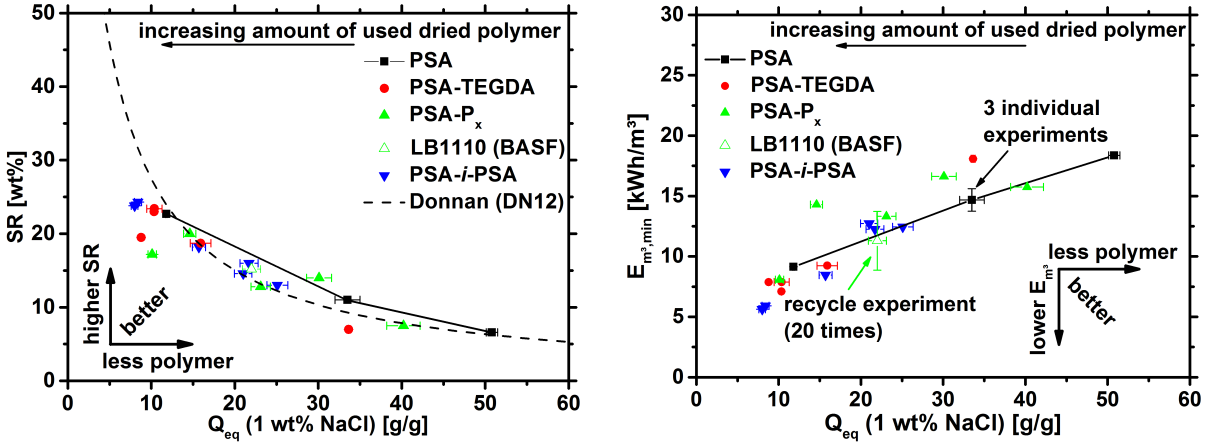


**Figure 6.6:** Salt rejection *SR* (left) and specific energy $E_{m^3,min}$ (right) as a function of the degree of swelling for PSA samples with different network architectures. The y-error bars show the standard deviation of three individual desalination experiments (PSA) or 20 repeating experiments, reusing the same hydrogel (LB1110).

## 6.4 Desalination using temperature as external stimulus

In this section, the hydrogels are deswollen by temperature instead of pressure as an external stimulus. Thermally responsive NIPAAm groups were incorporated into the networks either by the simultaneous copolymerization of SA and NIPAAm or in the form of interpenetrating double networks (see Section 4.5 and Appendix A.1.8). The PNIPAAm segments cause a temperature dependent water uptake as described in Section 5.6 and eventually lead to a network collapse above the LCST. Fundamentally different experiments are needed to investigate the temperature induced desalination. Hence, the experiments are desrcibed first and the measured quantities are introduced. Then, the influence of the different network parameters on these quantities will be described.

### 6.4.1 Thermal desalination experiments and characteristic quantities

The thermal desalination experiments contain three steps, as displayed in Figure 6.7, which are described in more detail in Appendix 6.9:

1) Swelling of the dried hydrogel until equilibrium in an excess of an external salt bath (usually a 1 wt% NaCl solution, if not otherwise noted).
2) Filtration of the swollen hydrogel particles and transfer in a sealed tube. Approximately 20 g fully swollen hydrogel were obtained by adapting the amount of dried polymer.
3) Heating the particles to 50 °C for 1 h by placing the tube in a water bath. The supernatant phase is then taken off by a syringe and its salinity is analyzed by conductivity.

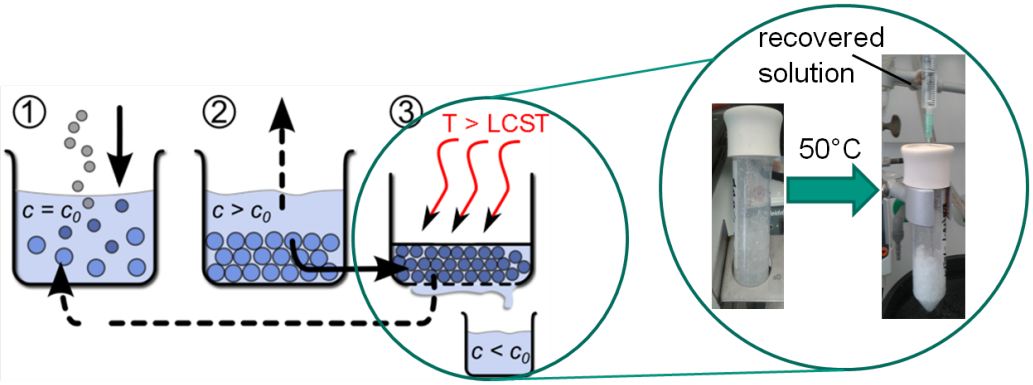


**Figure 6.7:** Schematic drawing of the thermal desalination experiment.

The following properties are compared to quantify the desalination experiments: The recovered water *RW*, given by Equation 6.9, is a measure for the water productivity per desalination cycle and is related to the thermal response of the network. A higher *RW* is beneficial, as less working material is needed to gain a certain amount of water.

$$RW = \left( \frac{m_{\mathrm{rw}}}{m_{\mathrm{h}} - m_{\mathrm{p}}} \right) * 100\,\mathrm{wt\%}\,, \tag{6.9}$$

where $m_{\mathrm{rw}}$ is the mass of recovered water, $m_{\mathrm{h}}$ is the mass of swollen hydrogel and $m_{\mathrm{p}}$ is the mass of dry polymer in the hydrogel.

The reduced salinity *RS* in the recovered solution is defined by Equation 6.10. A high salt reduction indicates a better separation mechanism.

$$RS = \left( 1 - \frac{c_{\mathrm{rw}}}{c_0} \right) * 100\,\mathrm{wt\%}\,, \tag{6.10}$$

where $c_{rw}$ is the salt concentration in the recovered solution and $c_0$ is the initial salt concentration.

The product of *RW* and *RS* (Equation 6.11) is a direct measure for the amount of NaCl ions that can be removed per desalination cycle.

$$\Delta m_{NaCl}[\text{wt\%}] = \frac{RW * RS}{100\,\text{wt\%}} \tag{6.11}$$

Some general remarks on the thermal desalination experiments shall be noted, before the results are presented in the next sections. In the pressure driven desalination cycles, the monotonically decreasing salinity was measured fraction by fraction, whereas only one fraction is obtained by the thermally induced collapse of the hydrogel. In this one fraction, the measured quantities *RS*, *RW* and $\Delta m_{NaCl}$ are not independent from each other. The standard deviations of these quantities, which are indicated as error bars in the respective graphs, were usually quite high. The experiments were therefore more often repeated (usually at least five times per data point). Another issue is related to the bound water on the surface of the hydrogels, which cannot be completely removed by a simple filtration. Hence, the salinity in the recovered solution is additionally increased by this influence. The amount of surface water depends on the sample itself. A softer hydrogel with a lower *DC* and more hydrophilic SA groups holds more surface water. Therefore, the salinity in the recovered water of these samples might be additionally increased rather due to the experiment than only due to the hydrogel structure itself.

### 6.4.2 P(NIPAAm-*co*-SA) copolymer networks

As already shown in Chapter 5, the thermal response of P(NIPAAm-*co*-SA) hydrogels is quite complex, since it depends on many parameters, such as *DC*, the ratio of NIPAAm to SA and the salinity of the external salt bath.

The amount of recovered water *RW* of the desalination experiments is shown for various P(NIPAAm-*co*-SA) hydrogels in Figure 6.8, left. The absolute degree of swelling is decreasing with the PNIPAAm content, while the thermal response increases. As a consequence, the highest water recovery of over 80 wt% is found, when 1 – 2 mol% SA groups are present in the network. At higher concentrations of the polyelectrolyte, the thermal dependency of the water absorbency becomes less pronounced and thus, no water recovery at all is seen for samples, where the SA content is $\geq$ 25 mol%.

The degree of crosslinking has only a minor influence on the amount of recovered water. A lower *DC* shows a slightly higher *RW*, except for sample PNIPAAm-DC1. This is in good

agreement with data from Yu *et al.*, who observed that a higher *DC* reduces the water recovery, but much less pronounced than changing the acrylic acid content [Yu93].

On the right graph in Figure 6.8, the reduced salinity *RS* in the recovered solution is shown for the same samples. As expected, a higher *DC* leads to a stronger salt rejection similar to the results of the previous desalination experiments with the pure polyelectrolytes. Sample PNIPAAm-DC5 has with about 11 wt% the highest salt reduction, whereas the separation of the 0.3 mol% crosslinked samples is almost negligible.

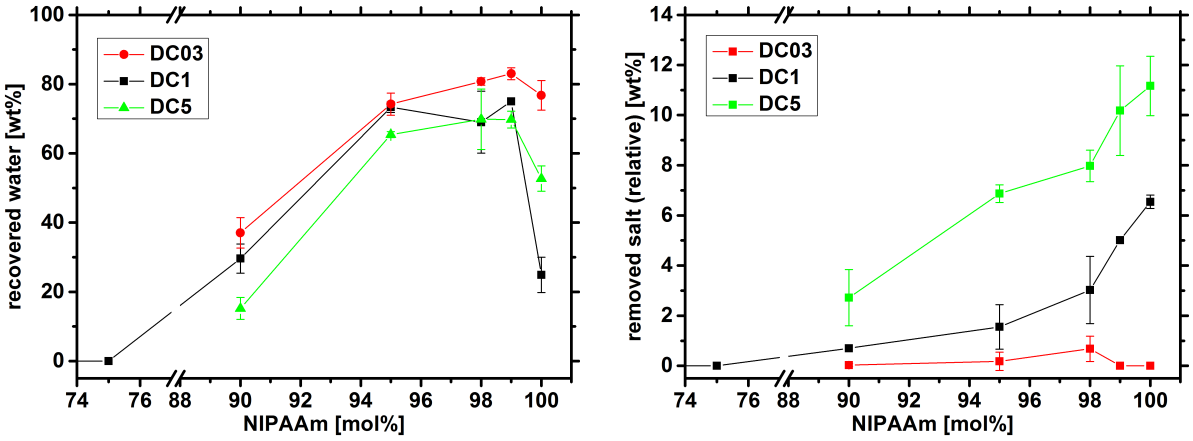


**Figure 6.8:** Left) Recovered water *RW* as a function of NIPAAm fraction in P(NIPAAm-*co*-SA) hydrogels for three different degrees of crosslinking. Right) Removed salt *RS* in the recovered solution for the same samples.

Surprisingly, the salt reduction increases monotonically with the NIPAAm fraction, where the pure PNIPAAm hydrogels have the highest reduced salinity *RS*. This is counter-intuitive, because the charges of the polyelectrolyte were thought to be responsible for the salt rejection. Charges might be introduced into the network by the initiator sodium persulfate, but only in small amounts (about 0.1% assuming an initiator efficiency of 50%). Even tough the degree of swelling is considerably smaller in the pure PNIPAAm, the charges from initiator cannot solely explain the increased salt rejection and other effects may be responsible.

The amount of NaCl ions, which is removed per desalination cycle, is shown for the copolymer hydrogels in Figure 6.9, left. The highest value of about 7 wt% was found with sample P(NIPAAm-*co*-SA1)-DC5. In this hydrogel, the high *DC* combined with the large NIPAAm fraction results in a high salt separation with a good thermal response, while the small amount of SA increases the fraction of recovered water.

In Figure 6.9, right, the thermal desalination behavior of the 1 mol% crosslinked hydrogels was additionally studied with different salinities of the external salt bath. A lower initial salinity resulted in a slightly increase of $\Delta m_{\mathrm{NaCl}}$. However, the effect of the different salt concentration

was less pronounced for the temperature induced desalination than for the pressure driven desalination of the pure PSA hydrogels [Arens17a].

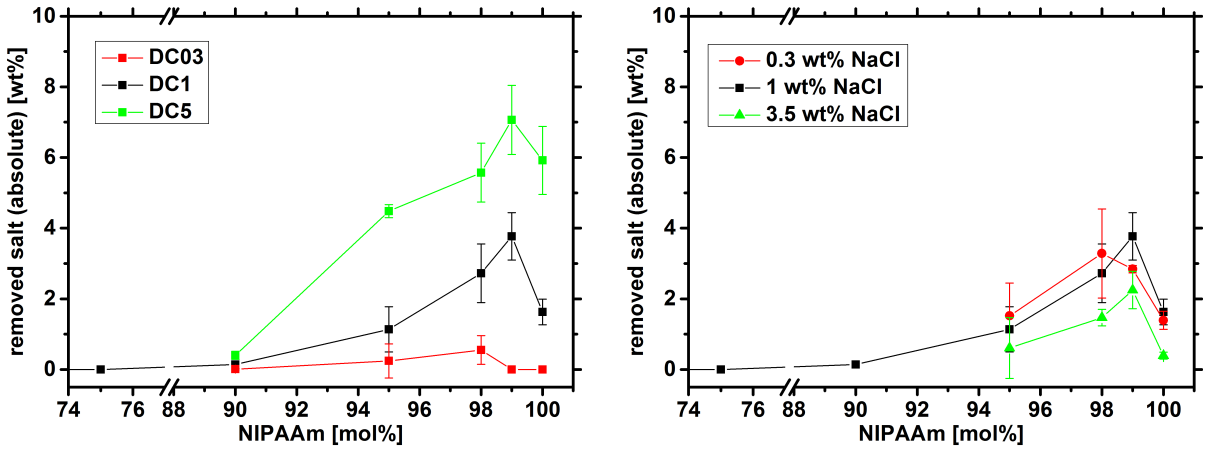


**Figure 6.9:** Left) Absolute amount of removed salt $\Delta m_{\mathrm{NaCl}}$ as a function of NIPAAm fraction in the P(NIPAAm-*co*-SA) hydrogels for three different degrees of crosslinking. Right) $\Delta m_{\mathrm{NaCl}}$ as a function of NIPAAm fraction in a 1 mol% crosslinked hydrogel at three different initial salinities $c_0$.

### 6.4.3 Interpenetrating PSA-*i*-PNIPAAm double networks

The PSA-*i*-PNIPAAm double networks were synthesized in order to increase the SA content in the network without losing the thermal response. In this manner, the PNIPAAm network induces the phase transition, while the PSA network can reject the salt ions.

As shown in Figure 6.8, left, the thermal response of the copolymer hydrogels was lost, when the SA content was 25 mol% or higher. In contrast, the interpenetrating PSA-*i*-PNIPAAm networks, where the PSA content was even higher, have indeed an increased thermal response compared to the P(NIPAAm-*co*-SA) co-networks, as shown in Table 6.7. Among the IPN samples, the amount of recovered water (*RW*) is increasing with the PNIPAAm fraction, as expected. As explained in Section 4.5, the percentage of the second network (PNIPAAm) depends on the absorbency of the first network (PSA). Hence, the lower crosslinked PSA samples with the higher absorbencies have a larger PNIPAAm fraction and thus, a higher *RW*.

Surprisingly, the removed salt $\Delta m_{\mathrm{NaCl}}$ was found to be negligibly small ($\ll$ 1 wt%) in all PSA-*i*-PNIPAAm networks and hence, much lower than in the pure PNIPAAm hydrogels. This might be related to the increased amount of bound surface water, as discussed above. This argument is supported by the actual salt repulsion *SR* in the supernatant phase at $Q_{\mathrm{rel}} = 2$, which is higher in the IPNs compared to the pure PNIPAAm hydrogels (see most right column in Table 6.7).

| Sample | *RW* [wt%] | SA fraction [mol%] (by mass) \ (by FT-IR) | SR [wt%] ($Q_{rel}$) |
|---|---|---|---|
| PNIPAAm-DC03 | 77±5 | 0 | 2.6±0.3 |
| PNIPAAm-DC1 | 25±5 | 0 | 3.4±1.5 |
| PNIPAAm-DC5 | 47±4 | 0 | 6.4±0.8 |
| P(NIPAAm-*co*-SA25)-DC1 | 0 | 25 | 5.4± 1.6 |
| PSA-DC03-*i*-PNIPAAm-DC1 | 28±5 | 25 \ 22 | 4.6±2.7 |
| PSA-DC1-*i*-PNIPAAm-DC03 | 12±6 | 67 \ 59 | 3.4±0.7 |
| PSA-DC1-*i*-PNIPAAm-DC1 | 22±5 | 50 \ 59 | 3.6±2.7 |
| PSA-DC1-*i*-PNIPAAm-DC5 | 17±7 | 50 \ 39 | 5.8±2.2 |
| PSA-DC5-*i*-PNIPAAm-DC1 | 14±3 | 80 \ 77 | 10.7±3.6 |
| PSA-DC5-*i*-PNIPAAm-DC5 | 6±3 | 75 \ 84 | 11.2±2.4 |

**Table 6.7:** The recovered water *RW* in the interpenetrating PSA-*i*-PNIPAAm networks compared to single networks. The SA fraction in the double networks was measured by FT-IR and mass, respectively (see Section 4.5). The most right column shows the salt rejection *SR* in the supernatant phase (analogous to Equation 6.1).

These first experiments demonstrate that the thermal response can be improved using interpenetrating networks without lowering the PSA fraction in the hydrogel to keep the enhanced salt rejection. However, this advantage could not yet been used to successfully increase the salt reduction and further experiments are necessary to answer, which role the bound surface water plays in the desalination experiments.

## 6.5 Technical aspects and current state of desalination by pressure

Besides changing the chemical structure of the working material, the process parameters of the desalination experiments can be adapted. These process parameters are at least equally important to the chemical parameters, since they show the feasibility of the proposed technique in a real process and on a larger scale. Furthermore, the desalination efficiency itself can be also optimized in this way. Most of these experiments were already performed on the commercial sample LB1110 (BASF) in previous work [Albrecht13, Höpfner13a]. However, in the present thesis some missing data was completed and the specific energy was recalculated, as described in Section 6.2. In previous work, the specific energies of the different parameters were calculated at the maximum applied pressure and without considering an infinite salt bath. In that case, the energy efficiency is highly pressure dependent [Arens17a]. However, the maximum applied pressure was not always the same in the experiments and therefore, the

obtained energy values are more difficult to interpret. For the sake of completeness, the main results shall be briefly summarized at this point.

#### Applied pressure profile to compress the hydrogels

In previous work, the pressure increase as a function of time $p(t)$ to compress the hydrogels was varied [Höpfner13a]. Linear pressure increases with a constant slope $dp/dt$ in the range of 6 – 120 bar/h were applied. Additionally, two non-linear $p$-profiles were performed, specifically a step increase to 50 bar and a quadratic increase ($p = t^2 * 3.5\,\text{bar/h}^2$). While the specific energy showed no significant change in the linear and quadratic profiles, the step experiment resulted in a lower energy efficiency, because the water was removed in the beginning at a high pressure even though a much lower pressure would have been sufficient.

The results indicate that a fast pressure increase can be used without considerably decreasing the energy efficiency. This is for a potential application of immense importance, since the pressure profile controls the volume flux of the water and thus, also the potential water productivity per time.

#### Salt concentration of the external salt bath

The standard desalination experiments were all performed with a 1 wt% NaCl solution. This value was chosen in previous work, as a logarithmic mean between the NaCl concentration in potable water and typical seawater [Höpfner13a]. To be comparable with previous data, this value was also used in the present thesis.[2]

In previous work, the influence of the salt concentration of the external salt bath was varied from 0.1 to 35 g/L NaCl, as a typical range from seawater to potable water [Albrecht13]. The relative salt separation normalized to the initial NaCl concentration is much higher at lower salinities in qualitatively good agreement with the prediction from the Donnan theory [Donnan32, Arens17a]. Furthermore, the lower salinity results also in a higher water absorbency (compare Figure 5.1, right), which leads to lower mechanical moduli of the hydrogels, as described in Chapter 5. Therefore, a higher water productivity is obtainable, while less working material and less energy is needed to compress the hydrogels at lower salt concentrations.

The compression tests demonstrated that desalination is possible over the whole range of interest. The absolute energy to remove 1 g NaCl of the solution logically increased at lower salinities, but the relative energy to remove 1 wt% of the present NaCl ions became smaller with

[2] The chosen concentration is also close to the physiological concentration of 0.9 wt% NaCl, which is typically used as a model solution for baby urine. Hence, the water absorbencies for superabsorbent hydrogels are usually reported in the literature for this particular salt concentration.

a lower initial salt concentration [Arens17a]. Therefore, the proposed method via hydrogels might be more suitable for the desalination of brackish water.

#### Swelling time of dried particles in the salt bath

The standard experiments were all performed after a long swelling time of at least 12 hours to ensure that the system reached its equilibrium state. To increase the water productivity, a much higher turnover number of desalination cycles would be necessary in a potential plant. Hence, a fast swelling and deswelling of the hydrogel is crucial.

Applying a shorter swelling time of only 3 minutes resulted in both, an increase of the desalination efficiency per cycle and a reduction of the cycling time [Albrecht13, Höpfner13a]. This demonstrates that shorter swelling times are possible and even beneficial for the desalination process. This finding can be explained by the results from Section 6.3. A shorter swelling time leads to a lower degree of swelling. Hence, the charge density in the swollen state is higher and less mobile ions can enter the network. The salt separation increases, while the specific energy decreases. This means that the smaller degree of swelling $Q$, which is related to a better performance (compare Figure 6.6), cannot solely adapted by changing the hydrogel structure, but also by adjusting the contact time between polymer and saline feedwater.

#### Reusability

The potential use of the polyelectrolyte hydrogels for saltwater desalination can obviously only be economical if the material can be used for many (*e. g.* 1,000 or even better 10,000) cycles without losing its desalination efficiency [Albrecht13]. However, with the current, non-automated press setup, the desalination experiments are quite time consuming with 2 – 3 hours per cycle (including preparation time) and hence, a steady efficiency is difficult to prove.

While in previous work the material was reused up to five times [Höpfner13a], in the present thesis the commercial hydrogel LB1110 was tested in 20 successive desalination cycles, where no sign of material degradation was determined. The desalination efficiency showed no systematic trend and scattered around the same value with an uncertainty of 21.5% [Arens17a]. This demonstrates that the material is principally reusable, but also that a new continuous press setup is needed to confirm this statement.

#### Effect of multivalent ions

All the presented desalination experiments in this thesis were conducted with pure NaCl model solutions. Even though, NaCl corresponds to almost 90% of the ion composition in seawater, real seawater is a more complex system that also contains multivalent cations, dominantly

$Mg^{2+}$ and $Ca^{2+}$ [ASTM13]. These multivalent cations can penetrate the hydrogel to replace the $Na^{+}$ counterions [Horkay00, Horkay01].

First experiments, where model solutions that contained besides NaCl also $MgCl_2$ and $CaCl_2$ were used in five successive desalination cycles, revealed indeed a partial replacement of the sodium counterions by the multivalent ions. As a consequence, the salt rejection was almost unaffected, but the water capacity in the hydrogel and thus, also the amount of recovered water was stepwise reduced due to the additional crosslinking points [Heinze14]. Those experiments showed that the desalination efficiency is gradually decreasing over the five cycles, when multivalent ions are present. Hence, these ions have to be removed in advance. As already described in Chapter 2, this can be easily realized by ion exchangers or via nanofiltration, which is usually also employed as a pretreatment in the RO process.

### 6.5.1 Comparison with established methods and further challenges

In this section, the presented desalination process with polyelectrolyte hydrogels as separation agent shall be compared with the commercially established methods, which were introduced in Chapter 2. In this manner, the potential and the further development needs for the proposed technique can be discussed.

The costs and energy demands for commercially established desalination methods are summarized in Table 6.8. Both values depend on the plant size with larger plants being more efficient. The calculated specific energies of about 6 to 20 kWh/m³ for the proposed desalination technique with polyelectrolyte hydrogels are already in the same range as the established techniques. This is a very promising result, considering the early stage of this new method.

| Technique | Energy demand [kWh/m³] | Cost/m³ [€] |
|---|---|---|
| Multi-stage flash distillation (MSF) | 10 – 58 | 0.42 – 1.40 |
| Multiple-effect distillation (MED) | 5 – 58 | 0.42 – 8 |
| Reverse Osmosis (RO) | 3 – 6 | 0.36 – 15 |
| Theoretical limit | 0.7 – 1 | |

**Table 6.8:** Energy consumption and costs per cubic meter freshwater for commercially established desalination methods [Wade01, Karagiannis08].

However, it should be also noted that the calculated specific energy in the present thesis cannot be exactly compared to the values in Table 6.8, as several assumptions were made:

First, only smaller quantities of water (< 200 mL) with a reduced salinity were recovered due to the limited size of the press setup. The calculation to the perspective energy needed to desalinate one cubic meter freshwater includes therefore a large extrapolation.

Second, the salinity was not reduced from seawater-like NaCl concentrations to potable water. The specific energy $E_{m^3,min}$ was calculated under the assumption that the required energy to remove 1 g NaCl from the brine is independent from the initial salt concentration over the total range from 0.1 to 35 g/L NaCl, although this is not the case [Arens17a]. However, the standard experiments were conducted with a 10 g/L NaCl solution and thus, the salinity as well as the energy efficiency is somewhere in the logarithmic mean of the range of interest. Therefore, the calculation of the specific energies should still provide meaningful values.

Third, for the evaluation of the expended energy, the pressure was recorded online directly at the hydrogel inside the press chamber. However, the actual pressure applied by the apparatus is about 10% higher, as seen by an external force gauge. The deviation is probably due to friction at the sealings.

Furthermore, any energetic costs for pumping, handling, pre- or posttreatments were not considered at all. As already explained, pretreatments might be necessary to remove the multivalent ions, which reduce the desalination performance over time. Additionally, previous work analyzed which material can be extracted from a commerical hydrogel (sample LB1110), when it is washed with deionized water [Gaine14]. Besides calcium, which is harmless, only the ions sodium and sulfate were found above the detection limit. The latter ones are probably from unreacted initiator molecules (sodium persulfate) and the concentration were always far below the limit of the German drinking water ordinance (0.2 g/L for $Na^+$, 0.25 g/L for $SO_4^{2-}$). Furthermore, organic content was measured as dissolved organic carbon (DOC) that is released in considerable concentrations. The DOC originates from extractable polymer (sol) caused by an incomplete polymerization. To be precise, the sol content was 7 – 8 wt% (normalized to the polymer) in the commercial sample and polyelectrolytes with a $DC \geq 1\,mol\%$. This resulted in a DOC concentration within the first desalination cycle in the range of 500 mg/L, if a new unwashed hydrogel was used. Even though, poly(acrylic acid) is not a hazardous, a reduction of DOC is desirable. First results showed that this concentration was already reduced by a factor of 100 after the 4th cycle, when the same hydrogel is used in repeating cycles (which is a key idea of this process). A similar reduction was also realized by simply washing the hydrogel prior to use. To summarize, the sol of the hydrogel seems to be the only critical substance that reduced the produced water quality, which however can be removed by the introduction of a few cleaning cycles in the start-up phase.

Apart from the mentioned challenges of the proposed method, several conceptional advantages are also conceivable for the desalination technique with polyelectrolyte hydrogels towards membrane processes, which have not yet been examined.

As introduced in Chapter 2, RO has problems with membrane deterioration, clogging and other blocking phenomena like biofouling and scaling, which cannot be totally avoided, even if an effective pretreatment of feedwater is conducted [Flemming97]. A regular cleaning of the membranes is necessary that includes chemical cleaning and mechanical forces, which leads to additional stress for the material. Failure in one point of the membrane will make the desalination module unusable and thus, a regular replacement of the expensive high-tech semi-permeable membranes is necessary.

In contrast, the here proposed desalination technique uses hydrogels, which are much less expensive with only circa 2 – 3 €/kg and have an already high annual production of over 3 million tons [Yu15]. Hence, the hydrogels are inexpensive to replace in case of pollution (*e. g.* by seaweed). Furthermore, during the desalination process, water molecules enter and leave the polyelectrolyte network in each compression cycle. Therefore, a back-washing and cleaning procedure is included in each step, which could result in a substantial reduction of the various blocking phenomena.

### 6.5.2 Outlook and further steps

The presented desalination technique via polyelectrolyte hydrogels meets already a couple of necessary criteria:

- The method is feasible in the entire range of interest (*e. g.* 0.1 – 35 g/L NaCl).
- The first estimate for the perspective specific energy is comparable to commercially established methods.
- The material is in principle reusable without decreasing the performance, when multivalent ions are removed by pretreatment.
- A high water throughput seems accessible, since short swelling times of the hydrogel are possible.

While some essential issues of the desalination process are already covered, further questions still remain and the following points should be investigated in the next steps:

- Increase of the salt separation efficiency
- Longer reusability tests
- Upscaling of the process
- Transition from a discontinuous to a continuous, automated process
- Desalination tests with real seawater

The presumably biggest disadvantage of the proposed desalination method is the limited salt separation per cycle, which was found to be considerably below the Donnan equilibrium. This means that a cascade of desalination steps (*e. g.* by multiple stages) is necessary to decrease the salinity to a potable concentration. To reduce the number of levels in a potential plant, the working material could be further improved. However, this seems to be limited as shown in the present thesis, and might be even not necessary, since a further improvement of the salt separation can also be realized using shorter swelling times, where the charge density in the network is higher. A high *DC* is still to be preferably used due to practical reasons. These samples have a lower sol content, have a lower tendency to gel-blocking and will probably show less degradation in long-time experiments. A further increase of the charge density seems possible using maelic acid instead of acrylic acid as the monomer, whereas an effective increase of charges is questionable, if Manning condensation is considered. Moreover, samples with dangling ends were found to increase the water absorbency without increasing the specific energy, which is beneficial for the desalination performance. While the dangling ends in this thesis were only attached to the crosslinking points, other synthetic strategies could be used to incorporate such dangling ends also along the elastic chains. This could be realized by the copolymerization of sodium acrylate with short PSA macromonomers.

Another issue is the implementation of the desalination process in a new setup. The current apparatus allowed studying basic synthetic parameters and answering fundamental questions, but it cannot be used as a model for a larger scale. A new, larger setup is needed with an intermediate size of 10 – 100 L. In this manner, more reliable data for the energy estimate can be gathered. Furthermore, the new system should include a continuous process that can be automated to allow longer reusability tests, as this is a further key issue of the proposed method. In order to realize these demands, two possible apparatus could serve as a model: An electrically driven filter chamber press or a roll to roll setup, which are both shown in Figure 6.10.

The filter chamber press can be seen as an accordion type apparatus, having several chambers per module, which would be filled with the hydrogel. By applying pressure, the volume of the chambers will be reduced. The hydrogel compresses and desalinated water is recovered, whereas a pressure release results in an extension of the chambers, while new feed solution can enter the module.

The roll to roll setup is usually used in the paper and metal industry. If the hydrogel would be embedded into a kind of woven fabric, it could be pulled through the saline feedwater bath to swell and be eventually compressed by the rolls, while the desalinated water would flow in the next bath. In this manner, it would be also easy to control $Q(t)$ by adjusting the velocity of

circulation. An automation of this continuous process seems easy to realize and also a larger water productivity per time could be so accessible.

**Figure 6.10:** Potential setups that could serve as a model for a continuous process: Filter chamber press (left) and roll to roll process (right). Figures are taken from [Murúg07, Limited13].

After the installation of the automated and continuous process, the reusability tests of the working material should be extended until failure or a degradation of the efficiency is observed. Furthermore, real seawater should be tested in the subsequent experiments, maybe after an ion-exchanger as pretreatment, to see how biofouling will affect the process and the material in the long term. After this intermediate sized apparatus, it can be seen if a further upscaling to a pilot plant with over 1,000 L per day will make sense.

## 6.6 Summary

The desalination experiments under an externally applied pressure to compress the hydrogels were introduced in this chapter. The typical course of the volume flux, the salt concentration and the pressure increase evolving in one cycle was shown. In general, higher crosslinked samples have a higher salt rejection (*SR*), but a lower water recovery (*RW*).

A criterion for the energy efficiency was introduced in form of the specific energy $E_{m^3,min}$ that allows easily to compare different hydrogels and process parameters. Typical values for $E_{m^3,min}$ were found to be within 6 – 20 kWh/m³, which is in a similar range than commercially established methods. Hydrogels with a higher charge density were more efficient, though more material was needed. The following conclusions could be drawn by comparing the different polyelectrolytes with respect to their absorbency:

i) PSA has a higher salt rejection than PSMA hydrogels (about 20%) and thus, a better desalination performance (about 8% lower $E_{m^3,min}$), as shown in Figure 6.4.

ii) Spherical shaped (microfluidic) hydrogel beads reduce gel-blocking, resulting in higher desalination efficiencies (11 – 20% lower $E_{m^3,min}$), especially with lower crosslinked samples (see Figure 6.4).

iii) The polymer architecture has only a minor influence on the salt rejection and the specific energy. However, introducing dangling ends results in higher water absorbencies without increasing $E_{m^3,min}$ (see Figure 6.5).

iv) The salt rejection can be qualitatively described by the Donnan theory, but the values found in the experiment are quantitatively much lower, even if a counterion condensation above a $DN$ of 30 mol% is considered. A good agreement between Donnan-theory and experiment can be only found, assuming lower values of $DN = 12$ mol% and $DN = 10$ mol% for PSA and PSMA, respectively (see Figure 6.5 and 6.6).

Furthermore, analyzing different process parameter revealed that several technical aspects, which would be necessary for a commercial use, are already met [Arens17a]:

i) The desalination technique works in the whole range of interest (0.1 – 35 g/L).

ii) Improving the water productivity can be realized by higher pressure increases and by shorter swelling times of the hydrogel, which was found to be even beneficial due to a stronger salt rejection.

iii) The material is principally reusable, since the commercial sample LB1110 showed no sign of degradation over 20 successive desalination cycles.

Additional to the achieved progress, it was discussed which issues should be investigated in the next steps. These steps include an upscaling and a new continuous, automated process in order to obtain more reliable data for the energy estimation and the long-time stability of the material.

Besides the desalination experiments under externally applied pressure, a temperature increase to 50 °C was used as an external stimulus to collapse hydrogels based on PNIPAAm. The best desalination performance was achieved on samples with the highest $DC$ of 5 mol% and only a small amount of 1 – 2 wt% sodium acrylate (SA) in the copolymer networks. Sample P(NIPAAm-*co*-SA1)-DC5 removed about 7 wt% of salt ions in one desalination cycle. The thermal response could be further improved in the interpenetrating PSA-*i*-PNIPAAm networks, compared to copolymers with the same SA content. However, further experiments are still necessary since almost no effective salt separation was yet realized with these samples.

# 7 Osmotic engine

In the previous chapter, the synthesized polyelectrolyte hydrogels were employed for the salt-water desalination. In the present chapter, the desalination process is reversed (see Figure 7.1). Instead of applying a pressure to change the salt concentration in a solution, it is possible to recover energy from salt gradients using superabsorbent polymers in an osmotic engine.

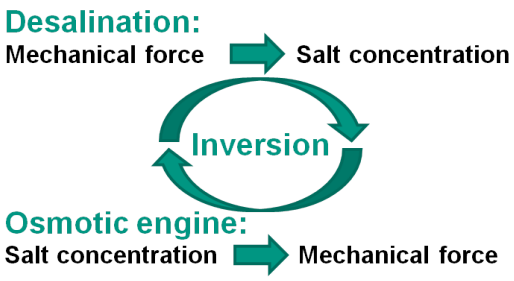


**Figure 7.1:** Inversion of the desalination process: Instead of applying mechanical force to desalinate water, salt gradients can be used to generate power.

As already shown in Chapter 5.1.1, polyelectrolyte hydrogels can swell up to several hundred times their own weight in deionized water, while the absorbency in saline solutions is about a factor of 2 – 12 lower (see Figure 5.1, right). These changes in the absorbency are caused by a different osmotic pressure, as explained in Section 2.2.2. Hence, a cyclic swelling in dilute salt concentrations followed by shrinking in highly concentrated salt solutions can be used to move a piston in a potential osmotic engine (see Figure 7.2).

The concept to recover energy from salt gradients *e. g.* at deltas, where river water enters the sea, is highly interesting. Especially in times of climate change, the increasing demand for clean, emission-free energy is of high importance. The most frequently applied regenerative alternatives to fossil fuels are based on photovoltaics and wind energy. Unfortunately, both methods depend on the weather as well as the time of day and year, resulting in a highly fluctuating energy output. In contrast, the use of salt gradients between river and seawater could allow a continuous production of energy. Worldwide, the potential power production, generated by osmosis, is estimated to about 2 TW, which is comparable to the global energy demand [Ramon11].

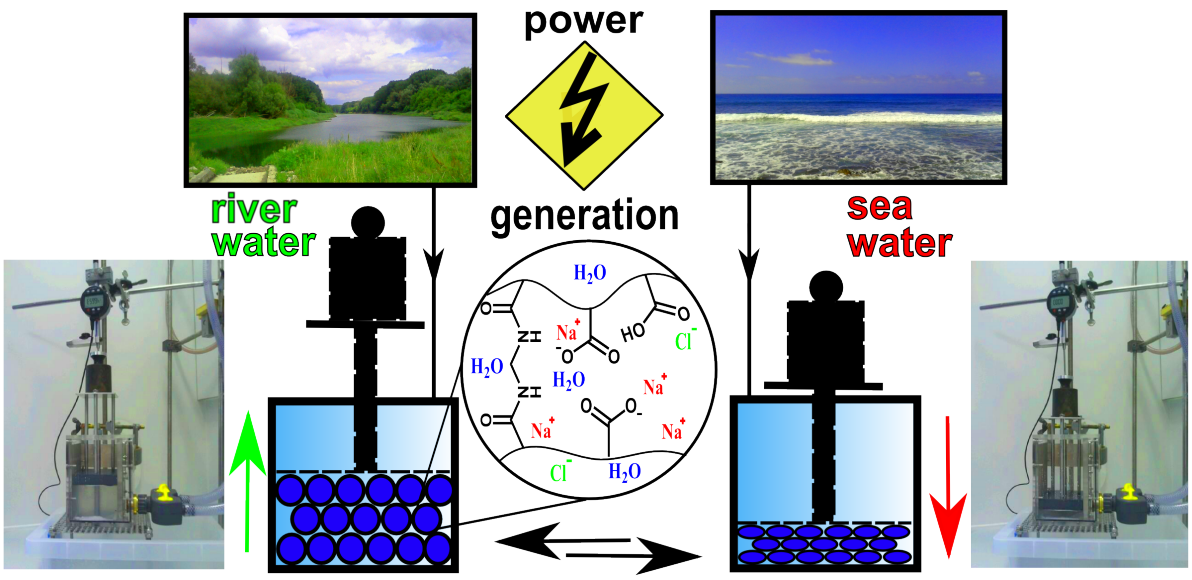


**Figure 7.2:** Principle to recover energy from salt gradients using polyelectrolyte hydrogels in an osmotic engine [Arens17b].

In the next section, different concepts are discussed how these salt gradients can be used to generate energy. The main results from two previous theses [Schlag14, Weißenfeld16], where polyelectrolyte hydrogels were used in an osmotic engine, are briefly summarized in Section 7.2. In Section 7.3, the most representative synthesized samples from the present thesis are compared, in order to understand how the network architecture influences the performance in the osmotic engine. Finally, it is discussed how the energy output can be further improved.

## 7.1 Energy recovery from controlled mixing of salt- and freshwater

The concept of using differences in chemical potential and entropy, to translate chemical energy into macroscopic mechanical energy, is not new. In 1962, Werner Kuhn introduced the idea of a pH-muscle, where a polyelectrolyte filament is pulled through two basins filled with either HCl or NaOH. The filament shrinks in the acid bath and expands in the basic bath, which has been used to pull a weight [Kuhn62].

In 1966, Katchalsky *et al.* published the idea to use solutions with different salinities to generate mechanical energy. They developed a mechanochemical engine, where collagen strings were used in differently concentrated LiCl solutions to generate a torque that moved a weight upwards [Steinberg66].

The most advanced method on a large scale, to convert chemical energy into mechanical energy via salt gradients, is based on the idea of Sydney Loeb, who used membranes and the principle of osmosis [Loeb75]. In 2009, the Norwegian company Statkraft built a first prototype of an osmotic power plant with an energy output between 2 and 4 kW in Tofte, Norway [Williams13]. The heart of the plant consists of two chambers, which are separated by a semi-permeable membrane. One chamber contains river water with a low salt concentration, while the other chamber contains seawater with a high salinity. River water flows into the chamber with the seawater caused by the osmotic pressure difference. The pressure increases, which drives a turbine to produce electrical energy [Gerstandt08]. However, the project was canceled at the end of 2013, since the investments cost were too high and the osmotic power plant was not regarded to be competitive with other power plants in the near future [Steen13].

The proof of principle, to recover energy from salt gradients by inexpensive polyelectrolyte hydrogels instead of the high-performance membranes was demonstrated by Logan *et al.* in 2014. They generated 0.1 W/kg (dry) poly(acrylic acid) with a *DC* of 2 mol% and a *DN* of 60 mol% by a cyclic shrinking and swelling of the hydrogel [Zhu14].

## 7.2 Preliminary results using an osmotic engine

The experiments were conducted in a 50 mL syringe, as a simple model for an osmotic engine, which works well with 0.25 g dried polymer. The polymer was first swollen to equilibrium in a 4.3 wt% NaCl solution as a model for seawater having the same ionic strength of 0.729 mol/kg [ASTM13]. The hydrogel was further transferred into the syringe and exposed to deionized water for 15 minutes. The height $h_1$ was measured with a simple ruler. Next, the hydrogel was exposed to the salt solution and after 5 minutes the height $h_0$ was again measured. The experiments were repeated with an increasing external load until no or only little expansion was observed.

The obtained mean power output $\bar{P}$ over one swelling/shrinking cycle was calculated by Equation 7.1 and normalized to 1 kg dry polymer mass. The experimental details are summarized in Appendix A.4.

$$\bar{P} = \frac{\Delta W}{\Delta t} = m * g * \frac{\Delta h}{\Delta t}\,, \tag{7.1}$$

where $\Delta W$ is the work, $\Delta t$ it the cycle time, $m$ is the moved mass, $g = 9.81\,\mathrm{m^2/s}$ is the gravitational constant and $\Delta h = h_1 - h_0$ is the lifting height.

### Influence of the degree of neutralization

As explained in Chapter 3 and experimentally shown in section 5.1.1, the charges inside the polymer network are responsible for the high absorbencies typically found in superabsorbers. Hence, the absorbency increases with a higher *DN* (without an external pressure). However, the ratio between the degree of swelling in deionized water over saltwater decreases by increasing *DN* [Arens17b].

The effect of *DN* for a 1.7 mol% crosslinked PSA on the mean power output is shown as a function of the external load in Figure 7.3, left. The power is independent of *DN* at a small external load, whereas fewer charges along the polymer chain are advantageous at higher external loads. One possible explanation is that the more charged hydrogels have a higher degree of swelling and thus, the hydrogels are mechanically weaker, tend to more gel-blocking and are less able to move heavier weights [Elliott04].

### Influence of the degree of crosslinking

As already extensively described in the previous chapters, the *DC* determines the pore size of the network and influences essentially the absorbency and mechanical properties (see Chapter 5). A denser network has a lower water uptake, but forms mechanically more stable hydrogels. The results on the mean power for different external loads and a varying *DC*, where the *DN* is kept constant at 75 mol%, are shown in Figure 7.3, right. Each *DC* has a specific pressure, where the maximum power is reached. This specific pressure increases with an increasing *DC* since the higher crosslinked polymers have larger *E*-modulus and are therefore able to move heavier weights, but mainly over a shorter distance. As a compromise, the *DC* with the highest mean power was found to be 2.5 mol%.

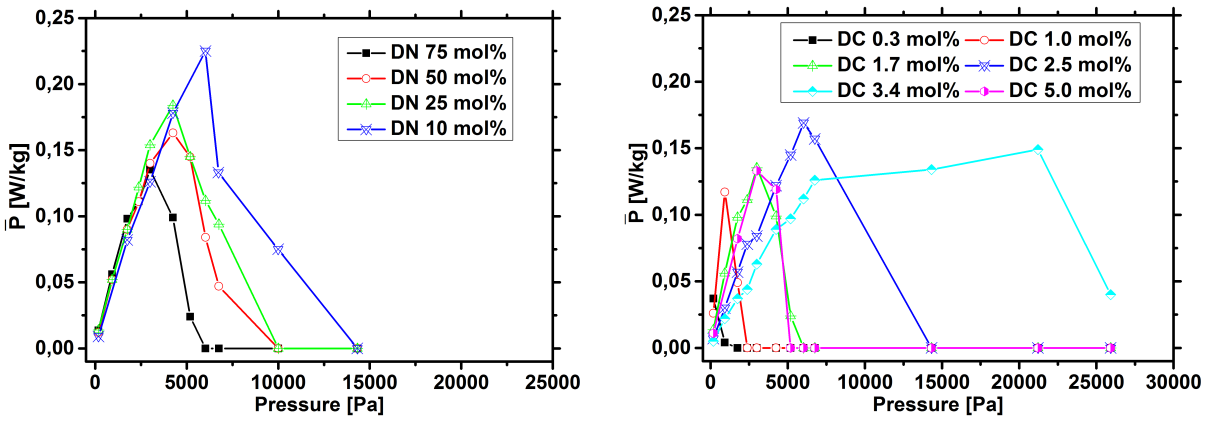


**Figure 7.3:** Left) Mean power output for a varying *DN* with a 1.7 mol% crosslinked PSA. Right) Mean power output for a varying *DC* with a 75 mol% neutralized PSA. Figures are adapted from [Arens17b].

#### Influence of other parameters

The influence of several other factors on the power output was studied in previous work [Schlag14, Zhu14, Weißenfeld16], which are summarized elsewhere [Arens17b]. The main results are briefly explained here:

The best particle size with respect to the swelling kinetics and the power output was found to be within 370 – 670 µm [Wack07]. While smaller particles lead to more gel-blocking, the larger particles expand rather radially to fill the inter voids before expanding primarily axially to move the weight [Arens17b].

One method to increase the swelling kinetics, the cycling rate as well as the energy output, is the use of drainage materials, such as molecular sieves, silicone tubes, clay granulates, polyurethane foam or diaper fleece. In this manner, gel-blocking can be reduced and the penetration of the inner hydrogel particles can be accelerated. The largest increase in the swelling rate was found with diaper fleece (polypropylene), where the mean power output could be improved by 150% [Schlag14].

Furthermore, several setups for the osmotic engine were tested, but no significant changes in the accumulated power production over one cycle were found [Weißenfeld16]. A required demand is the reuse of the hydrogel over many swelling and shrinking cycles without damaging the material. In the first experiments, the superabsorbers were reused between 5 – 9 times, since the setup was not automated. The results suggested that the hydrogel is not damaged during the cycles and that the power output can be increased within the first cycles before it levels off to a steady lifting height. This was found to be related to the amount of sol in the hydrogels. The extraction of the linear polymer chains from the network lead to a higher lifting height and a faster swelling and thus, to a larger power production. Therefore, the power output increases over the number of cycles (up to a factor of 3.5), when sol is extracted during the experiment. However, if the sol content was extracted beforehand or was already negligibly small (< 2 wt%), no changes in the energy output were observed [Arens17b].

## 7.3 State of the art

The results presented in the previous section showed that the power output depends on several parameters, such as $DC$, $DN$ and particle size. A prediction, which hydrogel structure will perform best, is not straightforward because the energy production depends on a complex interaction between the water absorbency in salt- and freshwater, the mechanical strength and the swelling kinetics. In the present thesis, different hydrogel samples with various network architectures were synthesized for their use in saltwater desalination. The polyelectrolytes are

not optimized for the osmotic engine, but distinct polymers are tested to observe the general trends how the energy output can be further improved.

The interpenetrating PSA-*i*-PSA networks are able to lift larger weights compared to the single precursor networks due to their higher mechanical strength. However, the many entanglements between both networks suppress a larger swelling and the overall mean power does not increase, as displayed in Figure 7.4, left.

Comparable results are also seen in the highly crosslinked PSA networks, which were polymerized with TEGDA instead of MBA as the crosslinker. The hydrogels with a higher *DC* can support large external loads of up to 21 kPa. This means that 250 mg polymer are able to lift over 1.5 kg mass (area: ca. 7 $cm^2$), but only over a small distance. The resulting maximum mean power is therefore not enhanced above a *DC* of 5 mol%, as seen in Figure 7.4, right.

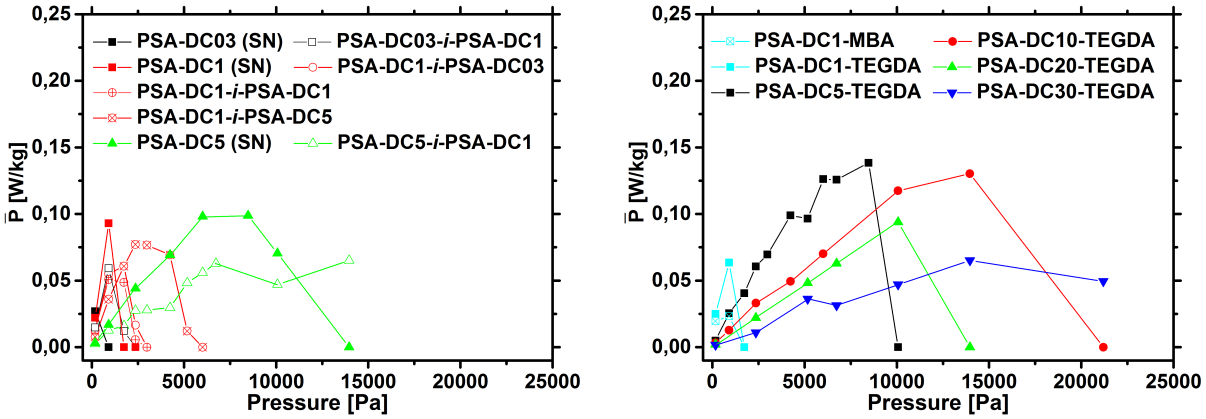


**Figure 7.4:** Mean power output in the osmotic engine as a function of the external load (pressure). Left) Interpenetrating PSA-*i*-PSA double networks. Right) Highly crosslinked PSA hydrogels using TEGDA as the crosslinker.

The quasi-model systems, either made by the chemically end-linked PSMA-EGDMA networks or the self-assembled PMMA-*b*-PSMA-*b*-PMMA triblock copolymers, exhibit no improvement in the osmotic engine compared to the free radical polymerized samples (not shown).

Networks with an increased amount of dangling ends (ABA/AB mixtures) have a lower performance. The dangling ends lead to mechanically softer hydrogels (see Figure 5.27), where gel-blocking is much more pronounced. Hence, even small external loads of 1,000 Pa cannot be lifted within 15 minutes. This means that in contrast to the desalination application, an increasing amount of dangling ends is disadvantageous for the osmotic engine and it is better to use defect-free hydrogels. Furthermore, these results indicate the importance to reduce gel-blocking, as it seems to be the limiting factor for the obtained mean power.

In order to minimize gel-blocking, the spherical hydrogel beads made by the droplet-based microfluidic technique and the surface crosslinked hydrogels were tested in the osmotic engine

(see Figure 7.5). As expected, both structures lead to a strong reduction of gel-blocking and much higher flow rates of the salt- and freshwater are accessible, which are related to a faster penetration of the hydrogel particles. These hydrogels can lift heavier weights at short times due to their larger absorbency under load. Hence, the mean power output in the osmotic engine increases by a factor of 2, using microfluidic particles or surface crosslinked samples, compared to the reference hydrogels.

The effect of the monomer type is additionally shown in Figure 7.5, left. The PSMA chains in the network are less flexible compared to the PSA segments, though the swelling ratio between fresh- and saltwater is smaller. Hence, the PSMA hydrogel forms mechanically more stable hydrogels that can lift heavier weights, but only over a shorter distance.

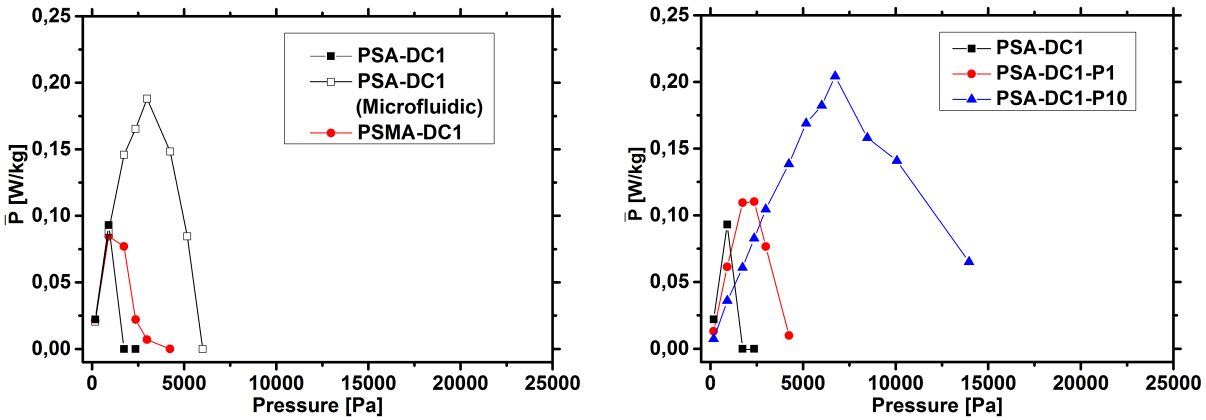


**Figure 7.5:** Mean power output in the osmotic engine for different network types. Left) The influence of the monomer type and particle shape (microfluidics). Right) The influence of surface crosslinking.

## 7.4 Summary

The polyelectrolyte hydrogels can be applied for the saltwater desalination and they can also be used to translate chemical energy into mechanical energy via the osmotic pressure difference of salt gradients. In this manner, the cyclic swelling and shrinking of the hydrogels can be used to generate power.

The current maximum mean power produced was 0.23 W/kg dry polymer using a 1.7 mol% crosslinked and 10 mol% neutralized PAA with an external load of 6,000 Pa. However, it was also demonstrated that this value can be further increased by the reduction of gel-blocking, which was found to be an essential limitation of the power output. To reduce the tendency towards gel-blocking, spherical particles produced by the microfluidic technique or an additional surface crosslinking of the polymers were found to offer a solution. Further improvements are possible

using drainage material or a new prototype of the osmotic engine, where the cycling times are additionally optimized.

Furthermore, the synthesized hydrogels should be not too soft, as these samples cannot support higher external loads. Hence, networks with less flexible polymer chains are beneficial and the hydrogels should be defect-free. Changing sodium acrylate to sodium methacrylate or even bulkier monomers could be advantageous, as the elastic chains are more rigid and the resulting hydrogels have higher mechanical moduli.

However, it should be also noted that the mean power output depends not exclusively on only one parameter, but always on the interplay of several parameters, such as degree of crosslinking (*DC*), degree of neutralization (*DN*), number of dangling ends, particle shape, bead size and external load. As these quantities influence each other, their optimal combination cannot be easily found, if only one parameter is varied, while the others are fixed. For example, a high *DN* results in softer hydrogels and thus, a lower *DN* of 10 mol% was found to be the best, if the *DC* was fixed at 1.7 mol% (see Figure 7.3, left). However, the mechanical strength of the hydrogel could be also optimized by a higher *DC*, keeping a high *DN*, as displayed in Figure 7.3, right. In future, the design of experiments (DOE) should be used as a concept instead of the one-factor-at-a-time (OFAT) experiments. In the DOE, several factors are varied simultaneously, which allows to find an optimum for the power output with fewer experiments [Czitrom99].

These early results show promise to imagine these types of osmotic engines present in river deltas as a steady source of renewable energy. However, even though this method is from a scientific point of view highly interesting, several challenges should be considered and solved in the next steps:

First, the experiments were performed with NaCl model solutions. As already explained in Chapter 6, seawater contains also multivalent cations, like $Mg^{2+}$ and $Ca^{2+}$, which reduce the water capacity of the hydrogels over time. An ion-exchanger for the water pretreatment might be necessary, which however reduces the energy efficiency.

Second, an upscaling of the osmotic engine is necessary, since the first prototypes were limited to a maximum of 10 g dried hydrogel particles [Arens17b]. In order to get more reliable data for the power output, an upscaling to a 1 kg motor design should be realized in a next step. The upscaling of the osmotic engine might be not so straightforward, since the hydrogel has always to support also its own weight. Therefore, thin hydrogel sheets would be necessary in a larger setup, which is however related to a larger area.

Third, the new motor design has to be automated and the switching between fresh- and saltwater computerized. This allows longer reusability tests and more profound statements for

the long-term performance of the material. Furthermore, the cycling times could be optimized with this setup in order to improve the mean power output.

# 8 Conclusion and outlook

Polyelectrolyte hydrogels are an important material, which are used in many industrial applications due to their superabsorbent properties (see Chapter 1). The polymers are usually based on sodium acrylate and are synthesized via free radical polymerization. This process allows for variation of the average mesh length in the network structure, but the control over the architecture is poor.

Several concepts exist, which usually originate from Flory's network theory, to qualitatively describe important characteristics of hydrogels, such as the water uptake and mechanical strength. However, a satisfying theory to quantitatively predict how the network topology influences the macroscopic properties, which derives only from molecular parameters, does not exist. The polyelectrolyte character of the polymer, leading to its substantive absorption and highly expanded networks, makes even a description of an ideal, defect-free network very complex and further fit parameters are necessary (see Chapter 3).

In this thesis, a large variety of different network architectures was synthesized (see Chapter 4). The influence of the polyelectrolyte architecture on macroscopic properties, such as the mechanical moduli and the absorbency of water or aqueous NaCl solutions, was studied. Furthermore, techniques like SAXS and NMR-relaxometry were used to map the network structure in a more sophisticated way (see Chapter 5). The synthesized polymers were employed in two different potential applications, where the proof of principle for both methods was presented in recent years [Höpfner10, Zhu14]. The hydrogels were first tested in a membrane-free desalination process (Chapter 6) and then in an osmotic engine to recover energy from salt gradients (Chapter 7). In both applications, only randomly crosslinked hydrogels synthesized via free radical polymerization (FRP) were previously studied and therefore, it was unknown how the different network architectures influence the desalination performance and the energy production in the osmotic engine.

## Synthesis and standard characterization

Different synthetic methods and strategies were used to accomplish the various network topologies. Poly(sodium acrylate) (PSA) and poly(sodium methacrylate) (PSMA) hydrogels with a varying degree of crosslinking (*DC*) were synthesized via free radical polymerization.

This method is often found in industry and such PSA hydrogels were also used in the proof of principle of the new desalination method and the osmotic engine. While in previous work, the degree of crosslinking was varied in the range of 0.05 – 5 mol%, in the present thesis samples with a *DC* of up to 30 mol% were fabricated by using MBA and the more soluble crosslinker TEGDA. Furthermore, the droplet-based microfluidic technique was employed to generate monodisperse particles of sub-millimeter-sized spheres.

The mechanical moduli and the water absorbency of the PSA and PSMA hydrogels were studied as they are the most important macroscopic quantities. An increasing *DC* led to more network constraints and higher mechanical moduli were measured, while the water absorbency decreased. The fully swollen hydrogels were measured via oscillatory shear rheology. The storage modulus $G'$ was always about a factor of 10 – 100 larger than the loss modulus $G''$. Typical values of $G'$ were found to be in the range of 1,000 – 50,000 kPa. The water absorbency showed a strong dependency on *DN*, *DC* and the salt concentration of the solution (studied from 0 – 35 g/L NaCl). A higher degree of neutralization resulted in a larger water uptake, while a higher salinity reduced the absorbency. Typical degrees of swelling in deionized water for the fully neutralized PSA hydrogels were in the range of 15 to 300 g/g, when *DC* was varied between 0.3 and 5 mol%.

Apart from the randomly crosslinked polymers, several other polymer architectures were realized in this thesis. Core-shell particles were synthesized via an additional crosslinking of the particle surface (esterification with a diepoxide). In these PSA hydrogels, the degree of crosslinking of the core was varied in the range of 0.3 to 5 mol%, while the thickness of the highly crosslinked shell was adjusted from 0 to 10 vol%.

Interpenetrating PSA-*i*-PSA double networks were synthesized as another network type, where these double networks consist of two individual PSA polymer networks. This structure was accomplished by polymerizing a second monomer solution within the first network. As synthetic parameters, the degree of crosslinking of both networks was varied individually over the range of 0.3 to 5 mol%. The incorporation of the second network led to more constraints in the form of intermolecular network entanglements. Therefore, the mechanical moduli increased, while the water absorbency decreased compared to the single precursor networks. The differences were more pronounced when the *DC* of the second network was larger than the *DC* of the first network. Furthermore, the order of polymerization had a large influence, as the fraction of the second network increased with the absorbency of the first network.

Two approaches were used to produce quasi-model networks with a defined elastic chain length ($PDI = 1.04 - 1.17$) via anionic polymerization of poly(*tert*-butyl methacrylate) (P*t*BMA), followed by hydrolysis and neutralization to PSMA. The meshes were crosslinked either by the chemical end-linking of the living polymer chains with ethylene glycol dimethacrylate

(EGDMA) or by the self-assembly of PMMA-*b*-PSMA-*b*-PMMA (ABA) triblock copolymers, as the hydrophobic poly(methyl methacrylate) (PMMA) endblocks phase separate into aggregates to obtain physically crosslinked hydrogels. SAXS measurements suggested a periodical distribution of the crosslinking junctions in these systems. The distance between the crosslinking points was calculated from the correlation peak in the SAXS patterns. Typical values for dried amphiphilic ABA triblock copolymers were between 10 and 40 nm. This distance increased with longer PSMA blocks and, upon swelling, which caused a three-dimensional expansion of the crosslinking points. The physically crosslinked hydrogels were studied intensively as a function of several synthetic parameters:
The polymer concentration during the hydrogel formation determined the ratio between bridging and looping chains leading to a factor of 4 change in the mechanical and absorbent properties. A temperature increase to a value above the $T_g$ of PMMA in water was necessary to enable this transition, as the PMMA blocks formed frozen micelles at room temperature. A systematic variation of the hydrophobic block length A showed that about 50 MMA units are necessary to obtain stable hydrogels at room temperature. Increasing the midblock B resulted in larger pores of the hydrogel and led to higher absorbencies and lower mechanical moduli. The fraction of dangling ends in the physically crosslinked hydrogels was varied by mixing the ABA triblock copolymers with AB diblock copolymers, where only one end is aggregated in a PMMA micelle. In these systems, no additional polymer chains were introduced, but bridging chains were exchanged by dangling ends, since the aggregate size did not change. Consequently, the mechanical moduli drastically decreased with an increase in the AB content (more than a factor of 2 at 50% AB).

In addition to the pure polyelectrolyte hydrogels, thermally responsive PNIPAAm segments were incorporated into the polymer networks, either by copolymerization of the respective monomers or in form of interpenetrating PSA-*i*-PNIPAAm double networks. The degree of crosslinking of the networks was varied in the range of 0.3 to 5 mol%, while the SA fraction was systematically increased from 0 to 100 mol%.

The swollen PNIPAAm homo-networks showed a distinctive lower critical solution temperature (LCST) at around 35 °*C* (independent of *DC*), which decreased linearly with the increasing salinity of the solution. At the LCST, a strong change in several properties was observed: The water absorbency decreased by a factor of 2 to 3, while $E'$ increased by a factor of 4 to 5 for a 1 mol% crosslinked PNIPAAm hydrogel. At room temperature, the degree of swelling $Q_{eq}$ of PNIPAAm with a varying *DC* was in the range of 6 to 20 and was almost independent of the salinity. The degree of swelling and the dependency on the salt concentration increased with higher SA contents in the network. However, even with a SA fraction of only 1 mol% in the

P(NIPAAm-*co*-SA) hydrogels, no distinct LCST was detectable via DSC, whereas the thermal response vanished completely above 10 mol% SA.

The fraction of SA could be increased further without losing thermal response with the use of interpenetrating PSA-*i*-PNIPAAm networks. Similar to the PSA-*i*-PSA double networks, the mechanical moduli increased and the water absorbency decreased in these systems compared to their single precursor networks.

## NMR relaxometry

NMR relaxometry was used to study the local polymer dynamics in the swollen hydrogels to gain insight into the network structure. The longitudinal relaxation time $T_1$ depended on the monomer type (PSMA: 24 ms, PSA: 41 ms and PNIPAAm: 58 ms), but not on the network topology. In contrast, by measuring the transverse $T_2$-relaxation or double quantum (DQ) coherences, the mobility of the local chain segments could be studied. These experiments revealed a large heterogeneity in the polymer mobility with $T_2^{-1}$ and $D_{\mathrm{res}}$ distributions over several decades (typical range: 0.01 – 200 kHz). More constraints in the polymer network led to a lower mobility and thus, to higher $D_{\mathrm{res}}$ constants and $T_2^{-1}$ rates, which is in good agreement with previous work [Höpfner14]. In that work, only randomly crosslinked polyelectrolyte hydrogels and commercial samples were studied with TD-NMR and therefore, it was previously unknown whether the different topologies can be determined with this technique.

The quasi-model systems with a fixed elastic chain length did not show a narrower distribution of $D_{\mathrm{res}}$ or $T_2^{-1}$. In contrast, the larger crosslinking junctions in these hydrogels were immobile leading to very short relaxation rates (10 – 200 kHz) and the distributions were even broader.

However, TD-NMR was found to be a powerful tool to characterize the increased dynamic heterogeneity in other network structures. The surface crosslinking or the incorporation of a second network in the interpenetrating networks (IPNs) led to bimodal distributions in the respective constants. Thus, the creation of the desired topology could be confirmed with this method. This is of great interest as other techniques cannot directly study the network architecture, but only measure macroscopic properties resulting from their average structure.

The $T_2$-relaxation measurements of PNIPAAm hydrogels at different temperatures showed some interesting features. Above the LCST, the mobility of PNIPAAm was reduced by a factor of 2 due to the collapse of the polymer network. Furthermore, it was possible to clearly distinguish between an interpenetrating network and a hydrogel made by the simultaneous copolymerization of the respective monomers for samples with the same SA content. The co-network showed no change in the polymer mobility between 25 and 40 °C, since the thermal

response was lost. In contrast, the distribution in the $T_2$-relaxation rates of the IPN became bimodal at 40 °C, where one peak could be assigned to PSA and the other to the collapsed PNIPAAm network.

These results show that TD-NMR is a suitable technique to map the network structure of hydrogels and to validate *i. a.* synthetic procedures that increase the network heterogeneity.

## Membrane-free desalination

The synthesized hydrogels were used for the desalination of NaCl model solutions. This rather new desalination technique may be described as a membrane-free forward osmosis process using superabsorbent polymers as the drawing and separation agent simultaneously (see Chapter 2): Upon swelling in salt water, the mobile ions are partially rejected by the fixed charges of the network and remain mainly in the supernatant. The water with its reduced salinity inside the hydrogel can be recovered by applying an external force.

The different hydrogel networks were compared in their ability to reject salt and their desalination efficiency. In general, hydrogels with a lower degree of swelling had a higher salt rejection and better efficiency, which is related to their higher charge density in the swollen state. The following conclusions could be drawn:

i) PSA shows a higher salt rejection and a better desalination efficiency than PSMA hydrogels.

ii) The microfluidic particles have a lower tendency towards gel-blocking and have therefore a higher desalination efficiency.

iii) The polymer architecture has only a minor influence on the salt rejection and the specific energy.

The distribution of the fixed charges inside the polymer did not significantly affect the salt partitioning and only the total number of charges throughout the whole network influenced this property. The salt rejection could therefore be qualitatively described by the simple Donnan theory, which only considers the amount of charges in the network. However, values for the salt rejection from this theory were much higher than those found experimentally. While the salt rejection was not affected by the polymer architecture, the introduction of dangling ends resulted in higher accessible water absorbencies without increasing the specific energy. This is beneficial for this potential process as less polymer material is needed.

First estimations for the specific energy, using NaCl model solutions, were found to be within 6 – 20 kWh/m³, which is approximately similar to the values in the commercially established

methods. In general, samples with a higher charge density were found to be more efficient, although more material was needed.

The analysis of different process parameters showed that several criteria for the feasibility of the desalination method were already met:

i) The desalination technique works in the whole range of interest (0.1 – 35 g/L NaCl).

ii) Increasing the water productivity seems possible, since short swelling times of the hydrogel are possible.

iii) The material is principally reusable (no sign of degradation over 20 successive desalination cycles).

Thermally responsive hydrogels were used to induce the water recovery by temperature instead of pressure as an external stimulus. The principle of proof of this different concept was just recently shown [Ali15] and therefore, it was unknown how the *DC* or the PSA to PNIPAAm ratio in the hydrogel will affect the desalination behavior. In general, a high *DC* and only a small fraction of 1 – 2 mol% SA in the network were found to be beneficial. The best desalination performance was achieved with sample P(NIPAAm-*co*-SA1)-DC5 that removed about 7 wt% of salt ions in one desalination cycle. The salt rejection was further improved, without losing the thermal response, using interpenetrating PSA-*i*-PNIPAAm networks. However, an effective desalination was not achieved with these hydrogels and further experiments will be necessary to answer for example the effect of bound water on the particle surface.

Table 8.1 summarizes the optimum parameters for the membrane-free desalination process.

| Influence | Best parameter | Explanation |
|---|---|---|
| Monomer | Sodium acrylate | Highest charge density |
| Degree of crosslinking | High *DC* (MBA: 5 mol% or TEGDA: 10 mol%) | Lowest sol content & highest charge density |
| Network architecture (I) | Interpenetrating networks (PSA-DC5-*i*-PSA-DC1) | Highest charge density (lowest $E_{m^3,min}$ at swelling equlibirum $Q_{eq}$) |
| Network architecture (II) | Dangling ends | Higher $Q_{eq}$ without increased $E_{m^3,min}$ (less polymer needed) |
| Particle shape | Microfluidic particles | Reduced gel-blocking |
| Swelling time *t* | Short *t* (swollen to non-equilibrium) | Higher charge density |
| Desalination via temperature | P(NIPAAm-*co*-SA1)-DC5 | high *DC* → largest salt rejection<br>high NIPAAm fraction → thermal response<br>low SA fraction → more recovered water |

**Table 8.1:** The influence of various parameters on the desalination efficiency.

### Osmotic engine

The polyelectrolyte hydrogels were also studied in another potential application: The cyclic swelling in dilute salt concentrations followed by shrinking in highly concentrated salt solutions was used to translate chemical energy into mechanical energy in an osmotic engine. Such osmotic engines offer the possibility for a steady source of renewable energy from salt gradients present in river deltas.

The current maximum mean power produced was 0.23 W/kg dry polymer using a 1.7 mol% crosslinked PAA with a $DN$ of 10 mol% and an external load of 6,000 Pa. However, different possibilities were demonstrated that can lead to further improvements. Gel-blocking was seen as the main challenge of the method. A reduction of this phenomenon was possible using spherical particles (fabricated via microfluidic technique) or surface crosslinked hydrogels. The energy output could be doubled in this manner.

Table 8.2 summarizes the optimum parameters in the osmotic engine, which should be combined in future work.

| Influence | Best parameter | Explanation |
|---|---|---|
| *DC* & *DN* | $DC = 1.7$ mol% and $DN = 10$ mol% (**combination**) | Good compromise between high $Q_{eq}$ and $E$ moduli |
| Dangling ends | No dangling ends (defect-free hydrogels) | Dangling ends reduce $E$ moduli |
| Particle shape | Uniform microgel spheres (microfluidic) | Reduced gel-blocking |
| Network topology | Surface crosslinked hydrogels | Reduced gel-blocking |
| Drainage material | Diaper fleece | Fastest penetration of particles |

**Table 8.2:** Important parameters to improve the mean power output in the osmotic engine.

## Outlook

A wide range of polyelectrolyte network structures were compared in this thesis. However, the influence of the pore size distribution was particularly difficult to study, since the investigated quasi-model systems and the randomly crosslinked hydrogels had different crosslinking junctions and crosslinking functionalities. Ongoing research focuses on model systems, where not only the elastic chain length, but also the crosslinker functionality is defined. In that approach,

the elastic chains are synthesized first with a defined endgroup via anionic polymerization, followed by the network formation via click-chemistry. This allows for the production of defined, but more heterogeneous, network structures by coupling pointedly linear precursor chains with different lengths. With this approach, it is possible to avoid the difficulties that emerged in this work with respect to comparing the different systems leading to more conclusive results.

In the present thesis, dangling ends were found to be beneficial for the desalination performance. While the dangling ends were here only attached to the crosslinking points, other synthetic strategies could be used to attach non-elastic chains along the network meshes as well. This could be realized by the copolymerization of sodium acrylate with short PSA macromonomers.

Patrickios *et al.* synthesized a large variety of poly(alkyl (meth-)acrylate) network architectures via group transfer polymerization resulting in crosslinked star polymers [Vamvakaki01, Georgiou06] or shell-crosslinked polymer networks [Triftaridou07, Kafouris09a, Kafouris09b]. If the networks are polymerized with *tert*-butyl (meth-)acrylate, subsequent hydrolysis offers the possibility to obtain polyelectrolytes. These network structures would be interesting to study for their desalination performance, as a decoupling of charge density and mechanical moduli might then be possible.

Table 8.3 summarizes some ideas that could be investigated in the next steps to further improve the desalination process.

| Parameter | Desired | Idea |
|---|---|---|
| Monomer | Highest charge density without lowering $Q_{eq}$ | Copolymerization of sodium acrylate with maelic acid |
| Crosslinker | Lowest sol content | Higher crosslinking functionality (*e. g.* pentaerythritol tetraacrylate) |
| Dangling ends | High $Q_{eq}$ and low $E_{m^3,min}$ | Dangling ends attached along the elastic chains |
| Setup | Automated & continuous process | Filter chamber press or roll to roll setup |

**Table 8.3:** Several ideas to further improve the desalination process, which could be investigated in the future.

The hydrogels synthesized here were investigated for their use in saltwater desalination and in an osmotic engine. However, the prototypes used for the experiments were operating only at a small scale and were not automated, which made reusability tests of the hydrogel difficult. In the future, a new continuous, automated process should be installed on a larger scale, allowing for the study of for example up to 1 kg of polymeric material. More reliable data for the energy estimation in the desalination process and the energy output in the osmotic

engine could then be gathered. This would provide data for making more conclusive statements about the long-term stability of the material.

All the experiments in this thesis were performed with NaCl model solutions. However, as already explained in Chapter 6, seawater also contains multivalent cations, like $Mg^{2+}$ and $Ca^{2+}$, which reduce the water capacity of the hydrogels over time. An ion-exchanger for water pretreatment might be necessary, which would however reduce the energy efficiency. On the other hand, these results also demonstrated the potential to use polyelectrolyte hydrogels to selectively remove toxic multivalent ions, such as $Cd^{2+}$, $Pb^{2+}$ and $Cr^{3+}$ [Fu11, Singh14, Wagner17]. These ions are present at too high concentrations near tanneries in India and cause multiple diseases [Gowd08]. A cheap and simple method to remove these ions could be achieved using PSA hydrogels.

# Bibliography


[Abragam61] A. Abragam, *The principles of nuclear magnetism*, 1st ed., Clarendon Press, Oxford, **1961**.

[Adrus12] N. B. Adrus, *Stimuli-Responsive Hydrogels and Hydrogel Pore-Filled Composite Membranes*, Ph.D. thesis, Universität Essen-Duisburg, **2012**.

[Albrecht13] J. Albrecht, *Experimentelle Untersuchung zum Energiebedarf bei Entsalzungsprozessen mit Hilfe von polymeren Hydrogelen*, Student thesis, Karlsruhe Institute of Technology, **2013**.

[Ali15] W. Ali, B. Gebert, T. Hennecke, K. Graf, M. Ulbricht, J. Gutmann, *Appl. Mater. Interfaces* **2015**, *7*, 15696.

[Anderson72] W. A. Anderson, R. Freeman, H. Hill, *Pure Appl. Chem.* **1972**, *32*, 27.

[Annable93] T. Annable, R. Buscall, R. Ettelaie, D. Whittlestone, *J. Rheol.* **1993**, *37*, 695.

[Arens14] L. Arens, *Synthese von physikalisch-vernetzten Hydrogelen basierend auf Blockcopolymeren aus Polystyrol und Polymethacrylsäure*, Diploma thesis, Karlsruhe Institute of Technology, **2014**.

[Arens17a] L. Arens, J. B. Albrecht, J. Höpfner, K. Schlag, A. Habicht, S. Seiffert, M. Wilhelm, *Macromol. Chem. Phys.* **2017**, *218*, 1700237.

[Arens17b] L. Arens, F. Weißenfeld, C. O. Klein, K. Schlag, M. Wilhelm, *Adv. Sci.* **2017**, *4*, 1700112.

[Aristotle52] Aristotle, H. D. P. Lee, *Meteorologica*, Harvard University Press, **1952**.

[ASTM13] ASTM, *Standard Practice for the Preparation of Substitute Ocean Water*, ASTM International, West Conshohocken, PA, **2013**.

[Avlonitis02] S. A. Avlonitis, *Desalination* **2002**, *142*, 295.

[Avlonitis03] S. A. Avlonitis, K. Kouroumbas, N. Vlachakis, *Desalination* **2003**, *157*, 151.

[Barther16] D. Barther, *Synthese und Charakterisierung von oberflächenvernetzten Polyacrylsäure-Partikeln und deren Verwendung in der Wasserentsalzung*, Bachelor thesis, Karlsruhe Institute of Technology, **2016**.

[Baselga87] J. Baselga, I. Hernández-Fuentes, I. F. Piérola, M. A. Llorente, *Macromolecules* **1987**, *20*, 3060.

[Baselga89] J. Baselga, M. A. Llorente, I. Hernándes-Fuentes, I. F. Piérola, *Eur. Polym. J.* **1989**, *25*, 471.

[Baskaran07] D. Baskaran, A. H. E. Müller, *Prog. Polym. Sci.* **2007**, *32*, 173.

[Bastide88] J. Bastide, L. Leibler, *Macromolecules* **1988**, *21*, 2647.

[Baum86] J. Baum, A. Pines, *JACS* **1986**, *108*, 7447.

[Beinert75] G. Beinert, A. Belkebir-Mrani, J. Herz, G. Hild, P. Rempp, *Faraday Discussions* **1975**, *577*, 27.

[Beltran90] S. Beltran, H. H. Hooper, H. W. Blanch, J. M. Prausnitz, *J. Chem. Phys.* **1990**, *9*, 2061.

[Billmeyer84] F. W. Billmeyer, *Textbook of Polymer Science*, John Wiley & Sons, New York, **1984**.

[Bloch46] F. Bloch, W. W. Hansen, M. Packard, *Phys. Rev.* **1946**, *127*.

[Bovey88] F. A. Bovey, *Nuclear Magnetic Resonance Spectroscopy*, 2nd ed., Academic Press, San Diego, **1988**.

[Brannon-Peppas90] L. Brannon-Peppas, R. S. Harland, *Absorbent Polymer Technology*, Studies in Polymer Science, Elsevier, Amsterdam, **1990**.

[Brazel95] C. S. Brazel, N. A. Peppas, *Macromolecules* **1995**, *28*, 8016.

[Brendel99] U. Brendel, *Quellungsverhalten und mechanische Eigenschaften von Polyelektrolytnetzwerken und technischen Superabsorbern*, Ph.D. thesis, Johannes Gutenberg-Universität Mainz, **1999**.

[Buchholz98] F. L. Buchholz, A. T. Graham, *Modern Superabsorbent Polymer Technology*, 1st ed., Wiley-VCH, New York, **1998**.

[Cadova08] E. Cadova, J. Dybal, J. Kriz, P. Vlcek, M. Janata, L. Toman, *Macromol. Chem. Phys.* **2008**, *209*, 1657.

[Cai13] Y. Cai, W. Shen, S. L. Loo, W. B. Krantz, R. Wang, A. G. Fane, X. Hu, *Water Res.* **2013**, *47*, 3773.

[Cai16] Y. Cai, X. Hu, *Desalination* **2016**, *391*, 16.

[Carr54] H. Y. Carr, E. M. Purcell, *Phys. Rev.* **1954**, *94*, 630.

[Cath06] T. Y. Cath, A. E. Childress, M. Elimelech, *J. Membr. Sci.* **2006**, *281*, 70.

[Charbonneau11] C. Charbonneau, C. Chassenieux, O. Colombani, T. Nicolai, *Macromolecules* **2011**, *44*, 4487.

[Chassé11] W. Chassé, J. L. Valentín, G. D. Genesky, C. Cohen, K. Saalwächter, *J. Chem. Phys.* **2011**, *134*, 044907.

[Chen04] H. Chen, Y.-L. Hsieh, *J. Polym. Sci. Part A: Polym. Chem.* **2004**, *42*, 3293.

[Chen15] Q. Chen, H. Chen, L. Zhua, J. Zheng, *J. Mater. Chem. B* **2015**, *3*, 3654.

[Cohen91] A. Cohen, *Rheol. Acta* **1991**, *30*, 270.

[Czitrom99] V. Czitrom, *Am. Stat.* **1999**, *53*, 126.

[Derome87] A. E. Derome, *Modern NMR Techniques for Chemistry Research*, Pergamon Press, Oxford, **1987**.

[Donnan32] F. G. Donnan, E. A. Guggenheim, *Z. phys. Chem.* **1932**, *A162*, 346.

[Dragan14] E. S. Dragan, *Chem. Eng. J.* **2014**, *243*, 572.

[Drzal03] P. L. Drzal, K. R. Shull, *Macromolecules* **2003**, *36*, 2000.

[Ebara14] M. Ebara, Y. Kotsuchibashi, R. Narain, N. Idota, Y.-J. Kim, J. M. Hoffman, K. Uto, T. Aoyagi, *Smart Biomaterials*, Springer Japan, Tokio, **2014**.

[Edwards86] S. Edwards, T. Vilgis, *Polymer* **1986**, *27*, 483.

[Efstratiadis94] V. Efstratiadis, G. Tselikas, N. Hadjichristidis, *Polym. Int.* **1994**, *33*, 171.

[Elimelech11] M. Elimelech, W. A. Philiip, *Science* **2011**, *333*, 712.

[Elliott04] M. Elliott, *Superabsorbent Polymers*, BASF, Ludwigshafen, **2004**.

[Fayt87] R. Fayt, R. Forte, C. Jacobs, R. Jerome, T. Ouhadi, P. Teyssie, S. K. Varshney, *Macromolecules* **1987**, *20*, 1442.

[Flemming97] H.-C. Flemming, *Exp. Therm. Fluid Sci.* **1997**, *14*, 382.

[Flohr07] A. Flohr, T. Lindner, Y. Mitsukami, *Method of surface cross-linking superabsorbent polymer particles using ultraviolet radiation*, EU Patent 1917280A1, **2007**.

[Flory43] P. J. Flory, J. Rehner, *J. Chem. Phys.* **1943**, *11*, 512.

[Flory53] P. J. Flory, *Principles of Polymer Chemistry*, 1st ed., Cornell University Press, Ithaca, New York, **1953**.

[Flory76] P. J. Flory, *J. Proc. R. Soc. London Ser. A* **1976**, *A351*, 351.

[Flory77] P. J. Flory, *J. Chem. Phys.* **1977**, *66*, 5720.

[Freeman71] R. Freeman, H. D. W. Hill, *J. Chem. Phys.* **1971**, *54*, 3367.

[Fu11] R. Fu, Q. Wang, *J. Environ. Manag.* **2011**, *92*, 407.

[Gaine14] M. Gaine, *Untersuchung der Freisetzung von Chemikalien und Adsorption von natürlichen organischen Molekülen (NOM) bei der Anwendung von wiederverwendbaren Hydrogelen in der Wasseraufbereitung*, Bachelor thesis, Karlsruhe Institute of Technology, **2014**.

[Ganta08] S. Ganta, H. Devalapally, A. Shahiwala, M. Amiji, *J. Control. Release* **2008**, *126*, 187.

[Gaylord90] R. Gaylord, J. Douglas, *Polym. Bull.* **1990**, *23*, 529.

[Georgiou06] T. K. Georgiou, C. S. Patrickios, *Macromolecules* **2006**, *39*, 1560.

[Gerstandt08] K. Gerstandt, K.-V. Peinemann, S. E. Skilhagen, T. Thorsen, T. Holt, *Desalination* **2008**, *224*, 64.

[Glatter82] O. Glatter, O. Kratky, *Small Angle X-ray Scattering*, Academic Press, London, **1982**.

[Gong03] J. P. Gong, Y. Katsuyama, T. Kurokawa, Y. Osada, *Adv. Mater.* **2003**, *15*, 1155.

[Gong10] J. P. Gong, *Soft Matter* **2010**, *6*, 2583.

[Gowd08] S. S. Gowd, P. K. Govil, *Environ. Monit. Assess.* **2008**, *136*, 197.

[Graessley75] W. Graessley, *Macromolecules* **1975**, *8*, 186.

[Gullion90] T. Gullion, D. B. Baker, M. S. Conradi, *J. Magn. Reson.* **1990**, *89*, 479.

[Gulrez11] S. K. H. Gulrez, S. Al-Assaf, G. O. Phillips, *Progress in Molecular and Environmental Bioengineering - From Analysis and Modeling to Technology Applications*, chap. Hydrogels: Methods of Preparation, Characterisation and Applications, IntechOpen, Rijeka, **2011**, pp. 117–150.

[Guthausen98] A. Guthausen, G. Zimmer, P. Blümler, B. Blümich, *J. Magn. Reson.* **1998**, *130*, 1.

[Guvendiren07] M. Guvendiren, K. R. Shull, *Soft Matter* **2007**, *3*, 619.

[Habicht14] A. Habicht, W. Schmolke, F. Lange, K. Saalwächter, S. Seiffert, *Macromol. Chem. Phys.* **2014**, *215*, 1116.

[Hadjichristidis00] N. Hadjichristidis, H. Iatrou, S. Pispas, M. Pitsikalis, *J. Polym. Sci. A: Polym. Chem.* **2000**, *38*, 3211.

[Hahn50] E. L. Hahn, *Phys. Rev.* **1950**, *80*, 580.

[Halperin89] A. Halperin, *Macromolecules* **1989**, *22*, 2403.

[Halperin15] A. Halperin, M. Kröger, F. M. Winnik, *Angew. Chem. Int. Ed.* **2015**, *54*, 15342.

[Hancock94] B. C. Hancock, G. Zografi, *Pharm. Res.* **1994**, *11*, 471.

[Hasa75] J. Hasa, M. Ilavský, K. Dušek, *J. Polym. Sci. B: Polym. Phys.* **1975**, *13*, 253.

[Heinze14] F. P. Heinze, *Application of reusable hydrogels in water desalination: Influence of the water matrix*, Student thesis, Karlsruhe Institute of Technology, **2014**.

[Held00] D. Held, A. E. Müller, *Macromol. Symp.* **2000**, *157*, 225.

[Henderson10] K. J. Henderson, T. C. Zhou, K. J. Otim, K. R. Shull, *Macromolecules* **2010**, *43*, 6193.

[Hild98] G. Hild, *Prog. Polym. Sci* **1998**, *23*, 1019.

[Hirotsu87] S. Hirotsu, Y. Hirokawa, T. Tanaka, *J. Chem. Phys.* **1987**, *87 (2)*, 1392.

[Hoff87] J. H. van't Hoff, *Z. Phys. Chem.* **1887**, *1*, 481.

[Hooper90] H. H. Hooper, J. P. Bakerand, H. W. Blanch, J. M. Prausnitz, *Macromolecules* **1990**, *23*, 1096.

[Horkay00] F. Horkay, I. Tasaki, P. J. Basser, *Biomacromolecules* **2000**, *1*, 84.

[Horkay01] F. Horkay, I. Tasaki, P. J. Basser, *Biomacromolecules* **2001**, *2*, 195.

[Howse06] J. R. Howse, P. Topham, C. J. Crook, A. J. Gleeson, W. Bras, R. A. L. Jones, A. J. Ryan, *Nano Lett.* **2006**, *6*, 73.

[Höpfner10] J. Höpfner, C. Klein, M. Wilhelm, *Macromol. Rapid Commun.* **2010**, *31*, 1337.

[Höpfner13a] J. Höpfner, *A new method of seawater desalination via acrylic acid based hydrogels: Synthesis, characterisation, and experimental realisation*, Ph.D. thesis, Karlsruhe Institute of Technology, **2013**.

[Höpfner13b] J. Höpfner, T. Richter, P. Košovan, C. Holm, M. Wilhelm, *Prog. Coll. Polym. Sci.* **2013**, *140*, 247.

[Höpfner14] J. Höpfner, G. Guthausen, K. Saalwächter, M. Wilhelm, *Macromolecules* **2014**, *47*, 4251.

[Hsieh96] H. Hsieh, R. P. Quirk, *Anionic Polymerization: Principles and Practical Applications*, Taylor & Francis, New York, Basel, **1996**.

[IDA15] IDA, *Annual Report 2015*, International Desalination Association, **2015**.

[James47] H. James, E. Guth, *J. Chem. Phys.* **1947**, *15*, 651.

[Jedynak15] R. Jedynak, *Rheol. Acta* **2015**, *54*, 29.

[Jockusch09] S. Jockusch, N. J. Turro, Y. Mitsukami, M. Matsumoto, T. Iwamura, T. Lindner, A. Flohr, G. di Massimo, *J. Appl. Polym. Sci.* **2009**, *111*, 2163.

[Kadam11] V. Kadam, T. Nicolai, E. Nicol, L. Benyahia, *Macromolecules* **2011**, *44*, 8225.

[Kafouris09a] D. Kafouris, M. Gradzielski, C. S. Patrickios, *Macromol. Chem. Phys.* **2009**, *210*, 367.

[Kafouris09b] D. Kafouris, C. S. Patrickios, *Eur. Polym. J.* **2009**, *45*, 10.

[Kali06] G. Kali, T. K. Georgiou, B. Iván, C. S. Patrickios, E. Loizou, Y. Thomann, J. C. Tiller, *Macromolecules* **2006**, *39*, 1560.

[Karagiannis08] I. C. Karagiannis, P. G. Soldatos, *Desalination* **2008**, *223*, 448.

[Katchalsky55] A. Katchalsky, I. Michaeli, *J. Polym. Sci.* **1955**, *15*, 69.

[Khawaji08] A. D. Khawaji, I. K. Kutubkhanah, J.-M. Wie, *Desalination* **2008**, *221*, 47.

[Kim10] J. K. Kim, C. D. Han, *Adv. Polmy. Sci.* **2010**, *231*, 77.

[Kitano77] T. Kitano, T. Fujimoto, M. Nagasawa, *Polym. J.* **1977**, *9*, 153.

[Konak89] C. Konak, R. Bansil, *Polymer* **1989**, *30*, 677.

[Kucera14] J. Kucera, *Desalination: water from water*, Wiley Online Library, Scrivener Publishing, Salem, Massachusetts, **2014**.

[Kuhn62] W. Kuhn, *Kolloid Z. Z. Polym.* **1962**, *182*, 40.

[Laftah11] W. A. Laftah, S. Hashim, A. N. Ibrahim, *Polym.-Plast. Technol. Eng.* **2011**, *50*, 1475.

[Lange11] F. Lange, K. Schwenke, M. Kurakazu, Y. Akagi, U. i. Chung, M. Lang, J.-U. Sommer, T. Sakai, K. Saalwächter, *Macromolecules* **2011**, *44*, 9666.

[Langela01] M. Langela, *Struktur und rheologische Eigenschaften von PS-PI und PS-PB Blockcopolymeren*, Ph.D. thesis, Johannes-Gutenberg-Universität Mainz, **2001**.

[Leon94] A. Leon, B. Vincent, N. Cawdery, *Colloid Polym. Sci.* **1994**, *272*, 427.

[Li11] D. Li, X. Zhang, J. Yao, G. P. Simon, H. Wang, *Chem. Commun.* **2011**, *47*, 1710.

[Li13a] D. Li, H. Wang, *J. Mater. Chem. A* **2013**, *1*, 14049.

[Li13b] D. Li, X. Zhang, G. P. Simon, H. Wang, *Water Res.* **2013**, *47*, 209.

[Limited13] R. H. Limited, *Pakistan Textile Journal* **2013**, *4*, 42.

[Liu04] X.-M. Liu, L.-S. Wang, L. Wang, J. Huang, C. He, *Biomaterials* **2004**, *25*, 5659.

[Loeb64] S. Loeb, S. Srinivasa, *High flow porous membranes for separating water from saline solutions*, US Patent 3133132A, **1964**.

[Loeb75] S. Loeb, *Method and apparatus for generating power utilizing pressure-retarded-osmosis*, US Patent 3906250A, **1975**.

[Lorenzo13] F. D. Lorenzo, S. Seiffert, *Macromolecules* **2013**, *46*, 1962.

[Malkoch06] M. Malkoch, R. Vestberg, N. Gupta, L. Mespouille, P. Dubois, A. F. Mason, J. L. Hedrick, Q. Liao, C. W. Frank, K. Kingsbury, C. J. Hawker, *Chem. Commun.* **2006**, *26*, 2774.

[Mann05] B. A. F. Mann, *The Swelling Behavior of Polyelectrolyte Networks*, Ph.D. thesis, Johannes Gutenberg-Universität Mainz, **2005**.

[Manning69] G. S. Manning, *J. Chem. Phys.* **1969**, *51*, 924.

[Manning78] G. S. Manning, *Biophys. Chem.* **1978**, *9*, 65.

[Marino07] I.-G. Marino, *Regularized Inverse Laplace Transform*, https://de.mathworks.com/matlabcentral/fileexchange/6523-rilt (accessed: June 22, 2016), **2007**.

[Mark07] J. E. Mark (ed.), *Physical Properties of Polymers Handbook*, 2nd ed., Springer-Verlag, New York, **2007**.

[Matsen96] M. W. Matsen, F. S. Bates, *Macromolecules* **1996**, *29*, 1091.

[Matsuo13] Y. Matsuo, R. Konno, T. Ishizone, R. Goseki, A. Hirao, *Polymers* **2013**, *5*, 1012.

[Maus06] A. Maus, C. Hertlein, K. Saalwächter, *Macromol. Chem. Phys.* **2006**, *207*, 1150.

[Mengel01] C. Mengel, W. H. Meyer, G. Wegner, *Macromol. Chem. Phys.* **2001**, *202*, 1138.

[Mezger06] T. G. Mezger, *The Rheology Handbook*, vol. 2, Vincentz Network, Hannover, **2006**.

[Mezher11] T. Mezher, H. Fath, Z. Abbas, A. Khaled, *Desalination* **2011**, *266*, 263.

[Mori03] H. Mori, A. H. E. Müller, *Prog. Polym. Sci.* **2003**, *28*, 1403.

[Mortensen96] K. Mortensen, *J. Phys.: Condens. Matter* **1996**, *8*, 103.

[Murúg07] Murúg, *Filter press*, https://en.wikipedia.org/wiki/Filter_press#/media/File:Kalolis.jpg (accessed: March 8, 2018), **2007**.

[Nicolai10] T. Nicolai, O. Colombani, C. Chassenieux, *Soft Matter* **2010**, *6*, 3111.

[Obayashi82] S. Obayashi, M. Nakamura, K. Fujiki, T. Yamamoto, *Alkali Metal Acrylate or Ammonium Acrylate Polymer Excellent in Salt Solution-Absorbency and Process for Producing Same*, US Patent 4340706A, **1982**.

[O'Driscoll91] K. O'Driscoll, R. Sanayei, *Macromolecules* **1991**, *24*, 4479.

[Oppermann92] W. Oppermann, *Polyelectrolyte Gels — Properties, Preparation, and Applications*, chap. Swelling Behavior and Elastic Properties of Ionic Hydrogels, American Chemical Society, Washington DC, **1992**, pp. 159–170.

[Pei04] Y. Pei, J. Chen, L. Yang, L. Shi, Q. Tao, B. Hui, J. Li, *J. Biomater. Sci.* **2004**, *15*, 585.

[Pitsikalis99] M. Pitsikalis, S. Sioula, S. Pispas, N. Hadjichristidis, D. C. Cook, J. Li, J. W. Mays, *J. Polym. Sci. A: Polym. Chem.* **1999**, *37*, 4337.

[Powles63] J. G. Powles, J. H. Strange, *Proc. Phys. Soc.* **1963**, *82*, 6.

[Prange89] M. M. Prange, H. H. Hooper, J. M. Prausnitz, *AIChE J.* **1989**, *35*, 803.

[Provencher79] S. W. Provencher, *Makromol. Chem.* **1979**, *180*, 201.

[Provencher82a] S. W. Provencher, *Comput. Phys. Commun.* **1982**, *27*, 213.

[Provencher82b] S. W. Provencher, *Comput. Phys. Commun.* **1982**, *27*, 229.

[Purcell46] E. M. Purcell, H. C. Torrey, R. V. Pound, *Phys. Rev.* **1946**, *69*, 37.

[Rager97] T. Rager, W. H. Meyer, G. Wegner, *Macromolecules* **1997**, *30*, 4911.

[Ramazani-Harandi06] M. Ramazani-Harandi, M. Zohuriaan-Mehr, A. Yousefi, A. Ershad-Langroudi, K. Kabiri, *Polym. Test.* **2006**, *25*, 470.

[Ramon11] G. Z. Ramon, B. J. Feinberg, E. M. V. Hoek, *Energy Environ. Sci.* **2011**, *4*, 4423.

[Razmjou13] A. Razmjou, G. P. Simon, H. Wang, *Chem. Eng. J.* **2013**, *215–216*, 913.

[Rempp79] P. Rempp, J. E. Herz, *Angew. Makromol. Chem.* **1979**, *76/77*, 373.

[Richter17a] T. Richter, *Coarse grained Hydrogels*, Ph.D. thesis, Universität Stuttgart, **2017**.

[Richter17b] T. Richter, J. Landsgesell, P. Košovan, C. Holm, *Desalination* **2017**, *414*, 28.

[Ricka84] J. Ricka, T. Tanaka, *Macromolecules* **1984**, *17*, 2916.

[Ronca75] G. Ronca, G. Allegra, *J. Chem. Phys.* **1975**, *63*, 4990.

[Ruttscheid04] A. Ruttscheid, *Synthese und Charakterisierung von superabsorbierenden Polymeren mit Kern/Schale-Struktur*, Ph.D. thesis, Universität Duisburg, **2004**.

[Ryan05] A. J. Ryan, C. J. Crook, J. R. Howse, P. Topham, R. A. L. Jones, M. Geoghegan, A. J. Parnell, L. Ruiz-Pérez, S. J. Martin, A. Cadby, A. Menelle, J. R. P. Webster, A. J. Gleeson, W. Bras, *Faraday Discuss.* **2005**, *128*, 55.

[Saalwächter04] K. Saalwächter, F. Kleinschmidt, *Macromolecules* **2004**, *37*, 8556.

[Saalwächter07a] K. Saalwächter, *Prog. Nucl. Magn. Reson. Spectrosc.* **2007**, *51*, 1.

[Saalwächter07b] K. Saalwächter, J.-U. Sommer, *Macromol. Rapid Commun.* **2007**, *28*, 1455.

[Saalwächter12] K. Saalwächter, *Rubber Chem. Technol.* **2012**, *85*, 350.

[Safronov15] A. P. Safronov, L. V. Adamova, A. S. Blokhina, I. A. Kamalov, P. A. Shabadrov, *J. Polym. Sci. A* **2015**, *57*, 33.

[Schlag14] K. Schlag, *Optimierung von vernetzten Polyelektrolyten für einen Osmosemotor*, Diploma thesis, Karlsruhe Institute of Technology, **2014**.

[Schmidt-Rohr94] K. Schmidt-Rohr, H. W. Spiess, *Multidimensional Solid-State NMR and Polymers*, 1st ed., Academic Press, London, **1994**.

[Schmidt04] M. Schmidt, *Polyelectrolytes with Defined Molecular Architecture II*, Springer Verlag, Berlin/Heidelberg, **2004**.

[Schnablegger13] H. Schnablegger, Y. Singh, *The SAXS Guide - Getting acquainted with the principles*, Anton Paar GmbH, Graz, 3rd ed., **2013**.

[Schröder96] U. P. Schröder, W. Oppermann, *Physical Properties of Polyelectrolyte Gels*, chap. Properties of Polyelectrolyte Gels, John Wiley & Sons, New York, **1996**, pp. 19–38.

[Seiffert11] S. Seiffert, *Macromol. Rapid Commun.* **2011**, *32*, 1600.

[Semenov85] A. N. Semenov, *Sov. Phys. JETP* **1985**, *61*, 733.

[Shapiro11] Y. E. Shapiro, *Prog. Polym. Sci.* **2011**, *36*, 1184.

[Shefer93] A. Shefer, A. J. Grodzinsky, K. L. Prime, J.-P. Busnel, *Macromolecules* **1993**, *26*, 5009.

[Singh14] T. Singh, R. Singhal, *Desalin. Water Treat.* **2014**, *52*, 28.

[Skolnick77] J. Skolnick, M. Fixman, *Macromolecules* **1977**, *10*, 944.

[Steen13] T. Steen, *Statkraft halts osmotic power investments*, Statkraft News, **2013**.

[Steinberg66] I. Z. Steinberg, A. Oplatka, A. Katchalsky, *Nature* **1966**, *210*, 568.

[Swann10] J. M. G. Swann, P. D. Topham, *Polymers* **2010**, *2*, 454.

[Szwarc56] M. Szwarc, *Nature* **1956**, *178*, 1168.

[Tae05] G. Tae, J. A. Kornfield, J. A. Hubbell, *Biomaterials* **2005**, *26*, 5259.

[Tam98] K. C. Tam, R. D. Jenkins, M. A. Winnik, D. R. Bassett, *Macromolecules* **1998**, *31*, 4149.

[Tanaka79] T. Tanaka, D. J. Fillmore, *J. Chem. Phys.* **1979**, *70*, 1214.

[Treloar75] L. R. G. Treloar, *The physics of rubber elasticity*, 3rd ed., Clarendon Press, Oxford, **1975**.

[Triftaridou07] A. Triftaridou, D. Kafouris, M. Vamvakaki, T. K. Georgiou, T. C. Krasia, E. Themistou, N. Hadjiantoniou, C. S. Patrickios, *Polymer Bulletin* **2007**, *58*, 185.

[Tsitsilianis00] C. Tsitsilianis, I. Iliopoulos, G. Ducouret, *Macromolecules* **2000**, *33*, 2936.

[Tsitsilianis02] C. Tsitsilianis, I. Iliopoulos, *Macromolecules* **2002**, *35*, 3662.

[Tsitsilianis18] C. Tsitsilianis, *Hydrogels Recent Advances*, chap. Self-assembling Hydrogels from pH-Responsive Ionic Block Copolymers, Springer Nature, Singapure, **2018**, pp. 259–295.

[Umendra99] D. Umendra, S. K. Metha, M. S. Choudhary, R. Jain, *Rev. Macromol. Chem. Phys.* **1999**, *C39*, 507.

[Valentín09] J. L. Valentín, D. López, R. Hernández, C. Mijangos, K. Saalwächter, *Macromolecules* **2009**, *42*, 263.

[Vamvakaki01] M. Vamvakaki, S. C. Hadjiyannakou, E. Loizidou, C. S. Patrickios, *Chem. Mater.* **2001**, *13*, 4738.

[Varshney90] S. . K. Varshney, J. P. Hautekeer, R. Fayt, R. Jerome, P. Teyssie, *Macromolecules* **1990**, *23*, 2618.

[Varshney91] S. K. Varshney, C. Jacobs, J.-P. Hautekeer, P. Bayard, R. Jerome, R. Fayt, P. Teyssie, *Macromolecules* **1991**, *24*, 4997.

[Varshney98] S. K. Varshney, P. Kesani, N. Agarwal, J. X. Zhang, M. Rafailovich, *Macromolecules* **1998**, *32*, 235.

[Wack06] H. Wack, *Zum Quellungsdruck von polymeren Hydrogelen*, Ph.D. thesis, Universität Duisburg-Essen, **2006**.

[Wack07] H. Wack, M. Ulbricht, *Ind. Eng. Chem. Res.* **2007**, *46*, 359.

[Wade01] N. M. Wade, *Desalination* **2001**, *136*, 3.

[Wagner17] I. Wagner, *Wechselwirkung mehrwertiger Metallionen mit definiert vernetzten Polyacrylsäuren*, Bachelor thesis, Karlsruhe Institute of Technology, **2017**.

[Wang78] H. C. Wang, G. Levin, M. Szwarc, *JACS* **1978**.

[Waters10] D. J. Waters, K. Engberg, R. Parke-Houben, L. Hartmann, C. N. Ta, M. F. Toney, C. W. Frank, *Macromolecules* **2010**, *43*, 6861.

[Weese92] J. Weese, *Comput. Phys. Commun.* **1992**, *69*, 99.

[Weißenfeld16] F. Weißenfeld, *Neukonstruktion und Optimierung eines durch Hydrogele angetriebenen Osmosemotors*, Master's thesis, Master thesis, Karlsruhe Institute of Technology, **2016**.

[Weiss71] P. Weiss, J. Herz, P. Rempp, *Makromol. Chem.* **1971**, *141*, 145.

[Williams13] A. Williams, *Water & Wastewater International* **2013**, *28*, 2.

[Xu05] S. Xu, Z. Nie, M. Seo, P. Lewis, E. Kumacheva, H. A. Stone, P. Garstecki, D. B. Weibel, I. Gitlin, G. M. Whitesides, *Angew. Chem. Int. Ed.* **2005**, *44*, 724.

[Yin92] Y.-L. Yin, R. K. Prud'homme, F. Stanley, *Polyelectrolyte Gels — Properties, Preparation, and Applications*, chap. Relationship Between Poly(acrylic acid) Gel Structure and Synthesis, American Chemical Society, Washington DC, **1992**, pp. 91–113.

[Yu93] H. Yu, D. W. Craincer, *J. Appl. Polym. Sci.* **1993**, *49*, 1553.

[Yu15] J. Yu, *Global and China Superabsorbent Polymers (SAP) Industry Report, 2014–2018*, Research in China, Beijing, **2015**.

[Yu16] C. Yu, Y. Wang, X. Lang, S. Fan, *Environ. Sci. Technol.* **2016**, *50*, 13024.

[Zhang05] Y. Zhang, S. Furyk, D. E. Bergbreiter, P. S. Cremer, *JACS* **2005**, *127*, 14505.

[Zhang08] X.-Z. Zhang, X.-D. Xu, S.-X. Cheng, R.-X. Zhuo, *Soft Matter* **2008**, *4*, 385.

[Zhang11] R. Zhang, T. Shi, H. Li, L. An, *J. Chem. Phys.* **2011**, *134*, 035903.

[Zhu14] X. Zhu, W. Yang, M. Hatzell, B. Logan, *Environ. Sci. Technol.* **2014**, *48*, 7157.

[Zohuriaan-Mehr10] M. J. Zohuriaan-Mehr, H. Omidian, S. Doroudiani, K. Kabiri, *J. Mater. Sci.* **2010**, *45*, 5711.

# Appendix

## A.1 Polymer samples and synthetic procedures

### A.1.1 Materials and purification

In the free radical polymerization and the other organic reactions, most of the chemicals could be used as received and only the monomers had to be distilled to remove the inhibitor. In contrast, the anionic polymerization is very sensitive to impurities such as water, oxygen and carbon dioxide. Small traces of these components will terminate the reaction and make a *living* polymerization impossible. Therefore, the anionic polymerization was carried out under an argon atmosphere and the chemicals were carefully purified in advance. All glassware was dried at 600 °C under vacuum and purged with the inert gas in three successive cycles prior to the synthesis.

The chemicals used in this work, were purified by the following procedures:
Methyl methacrylate (MMA, 99%, Acros Organics), *tert*-butyl methacrylate (*t*BMA, 98%, Sigma-Aldrich) and ethylene glycol dimethacrylate (EGDMA, 97.5%+, Merck) were purified by distillation at reduced pressure after drying over calcium hydride ($CaH_2$, 92%, Alfa Aesar) overnight, and degassed by three successive freeze-pump-thaw cycles. The monomers were then stored under an argon atmosphere at -20 °C in a freezer and used within one week.

1,1-diphenylethylene (DPE, 98%, Alfa Aesar) was titrated with *n*-butyllithium (*n*-BuLi, 1.6 M in hexane, Acros Organics) until the formation of a persistently red color, followed by the distillation at reduced pressure.

Tetrahydrofuran (THF, 99.5%+, Carl Roth) was distilled first from $CaH_2$ and then from sodium benzophenone (99%, Acros Organics) directly into the reaction flask.

Lithium chloride (LiCl, 98%+, Alfa Aesar) was dried at 120 °C for one week and heated with the reaction flask to 600 °C under reduced pressure prior to the synthesis.

Acrylic acid (AA, 99%+, Merck), methacrylic acid (MAA, 99%+, Merck) and tetra(ethylene glycol) diacrylate (TEGDA, technical grade, Sigma-Aldrich) were freshly distilled prior to the synthesis at reduced pressure.

Methanol (MeOH, 99.5%+, Carl Roth), lithium (Li, 98.5%+, Acros Organics), *sec*-butyllithium (*s*-BuLi, 1.4 M in cyclohexane, Sigma-Aldrich), sodium hydroxide (NaOH, 33 wt% in water, AnalaR Normapur), hydrochloric acid (HCl, 4 M in water, AVS Titrinorm), 1,4-dioxane (99.5%+, Carl Roth), *n*-heptane (99%+, Carl Roth), isopropanol (99.5%+, Carl Roth), N,N,N',N'-tetramethylethylenediamine (TEMED, 99.5%, Sigma-Aldrich), sodium persulfate (SPS, 98%+, Sigma-Aldrich), sodium chloride (NaCl, 99%+, Acros Organics), 2,2'-azobis(amidinopropane) dihydrochloride (V50, 98%, Acros Organics), ABIL EM90 (Evonik Industries), sorbitan monolaurate (technical grade, Alfa Aesar), N-isopropylacrylamide (NIPAAm, 99%, Acros Organics), ethylene glycol diglycidyl ether (technical grade, TCI Chemicals), N,N'-methylenebis(acrylamide) (MBA, 99%, Sigma-Aldrich), deuterium oxide ($D_2O$, 99.9%+ D, Sigma-Aldrich), deuterated chloroform ($CDCl_3$, 99.8% D, Sigma-Aldrich) and deuterated dimethyl sulfoxide (DMSO-d6, 98.8% D, Deutero) were all used as received.

### A.1.2 PSA and PSMA reference hydrogels made by free radical (co)polymerization

The PSA and PSMA hydrogels were synthesized by the free radical copolymerization of partially neutralized (meth)acrylic acid with N,N'-methylenebis(acrylamide) (MBA) as a 25 wt% solution in water. The degree of neutralization during the polymerization was always 75 mol%, while some samples were fully neutralized after the complete reaction. The degree of crosslinking was varied in the range of 0.3 to 5 mol%, when MBA was used as the crosslinker. To achieve a higher DC of up to 30 mol%, the more soluble tetra(ethylene gylcol) diacrylate (TEGDA) was used instead. A complete list of the synthesized reference hydrogels is given in Table A.1.

The synthetic procedure was adapted from previous work [Oppermann92, Höpfner13a] and a detailed instruction to polymerize the fully neutralized poly(sodium acrylate) hydrogel PSA-DC1 with a degree of crosslinking of 1 mol% is here given as an example:
First, 0.01 eq (0.01 mol, 1.54 g) MBA were dissolved in a three-neck flask by adding 230 g of deionized water under constant stirring. Then, 1.00 eq (1.00 mol, 72.06 g) of freshly distilled acrylic acid were added. Next, the acrylic acid was partially neutralized to 75 mol% by adding 0.75 eq (0.75 mol, 30.00 g) of NaOH as a 33 wt% solution in water drop-by-drop, while the reaction mixture was cooled to 5 °C with an ice bath, to avoid a premature thermal initiation by neutralizing heat. After the neutralization, the solution was still cooled by the ice bath and 0.002 eq (0.002 mol, 0.476 g) of the initiator sodium persulfate, dissolved in 4 g deionized water were added. Next, the reaction mixture was purged with $N_2$ for 30 minutes and 0.02 eq (0.02 mol, 2.324 g) of the accelerator N,N,N',N'-tetramethylethylenediamine were subsequently added. After the ice bath was removed, the reaction usually started within 30 minutes, which was indicated by a temperature increase to about 50 °C and the rise of the viscosity. The reaction

was allowed to complete and after 16 h, the resulting hydrogel was cut into small pieces. The hydrogel was eventually fully neutralized by adding 36 g of the 33 wt% NaOH solution and stirring the mixture in an excess of water for at least 16 h. The PSA was washed several times with deionized water until the filtrate was neutral and free of any unbound polymer. Finally, the hydrogel was dried at 70 °C under reduced pressure.

| Sample | *DC* [mol%] | Crosslinker |
|---|---|---|
| PSA-DC03 | 0.3 | MBA |
| PSA-DC1 | 1 | MBA |
| PSA-DC5 | 5 | MBA |
| PSMA-DC03 | 0.3 | MBA |
| PSMA-DC1 | 1 | MBA |
| PSMA-DC3 | 3 | MBA |
| PSA-DC1-TEGDA | 1 | TEGDA |
| PSA-DC5-TEGDA | 5 | TEGDA |
| PSA-DC10-TEGDA | 10 | TEGDA |
| PSA-DC20-TEGDA | 20 | TEGDA |
| PSA-DC30-TEGDA | 30 | TEGDA |

**Table A.1:** Overview of the synthesized reference hydrogels made by FRP in this work.

### A.1.3 Microfluidic emulsification and microgel fabrication

The construction of the flow-focusing glass capillary microfluidic device with an inner channel diameter of 1.4 mm, to get uniform and monodisperse spheres, is described elsewhere in detail [Habicht14]. As the continuous phase, a low viscous paraffin oil with 10 wt% of the silicone based surfactant ABIL EM90 was used. The composition of the SA/MBA monomer solutions for the dispersed phase was already described in detail in section A.1.2, but instead of the redox initiating system, 2.75 g/L of the photoinitiator 2,2'-azobis(amidinopropane) dihydrochloride (V50) was used to trigger the polymerization. The flow rates were adjusted by syringe pumps (Havard Apparatus, PhD Ultra) to 17 mL/h for the aqueous monomer solution and 60 mL/h for the oil phase, resulting in a native particle diameter of 650 – 800 µm. The droplets were collected in a vial and exposed for 2 h to UV light (Blak-Ray UV source, $\lambda$ = 365 nm) to trigger the polymerization. After the gelation, the microgel particels were first washed several times with isopropanol to remove the oil phase, and subsequently with deionized water.

### A.1.4 Surface crosslinking

First, PSA hydrogels with a varying *DC* were synthesized, as described in Section A.1.2. Second, these samples were dried and sieved into three different fractions. Then, particles of the middle fraction with a dried size in between 350 and 650 µm were used to additionally crosslink the surface. Here, the surface crosslinking for 5 g of sample PSA-DC1-P10 is described in detail. The nomenclature from section A.1.2 is extended by P10, which means that 10 vol% of the initial hydrogel network is penetrated with the second crosslinker and will be additionally (fully) crosslinked. 200 mL *n*-heptane, 0.1 g of the emulsifier sorbitan monolaurate and 5 g of the 75 mol% neutralized polymer PSA-DC1 were mixed in a 500 mL three-necked flask. Then, 0.6 g (0.05 eq., 3.47 mmol) EGDE were dissolved in 55.5 mL deionized water and added to the mixture. Next, the reaction mixture was heated to 65 °C for 4 h and stirred at 250 rpm with a sealed precision glass (KPG) stirrer. Afterward, the particles were washed with deionized water and dried at 70 °C under reduced pressure.

| Sample | *DC* [mol%] | *P* [vol%] | Crosslinker |
|---|---|---|---|
| PSA-DC03 | 0.3 | 0 | MBA |
| PSA-DC03-P1 | 0.3 | 1 | MBA/EGDE |
| PSA-DC03-P10 | 0.3 | 10 | MBA/EGDE |
| PSA-DC1 | 1 | 0 | MBA |
| PSA-DC1-P1 | 1 | 1 | MBA/EGDE |
| PSA-DC1-P10 | 1 | 10 | MBA/EGDE |
| PSA-DC5 | 5 | 0 | MBA |
| PSA-DC5-P1 | 5 | 1 | MBA/EGDE |
| PSA-DC5-P10 | 5 | 10 | MBA/EGDE |

**Table A.2:** Overview of the synthesized surface crosslinked hydrogels in this work.

### A.1.5 Physically crosslinked hydrogels based on self-assembled ABA triblock copolymers

The physically crosslinked hydrogels were prepared in three steps:
i) Synthesis of the protected block copolymers by anionic polymerization.
ii) Conversion of the P*t*BMA block to PSMA by hydrolysis and neutralization.
iii) Formation of the hydrogel by self-assembly of the amphiphilic block copolymers.
An overview of the synthesized physically crosslinked hydrogels with their block length and *PDI* is provided in Table A.3.

### AB block copolymers

The PMMA-*b*-P*t*BMA diblock copolymers were synthesized via the sequential monomer addition of MMA and *t*BMA. In principle, this polymerization can be started with both blocks, since both living polymers are able to initiate the other monomer type. However, in this thesis the PMMA block was synthesized first. The molecular weight was determined after the synthesis of each block by SEC against PMMA standards and thus, more precise values are so accessible.

In a typical synthesis (here: sample 80-187), LiCl (50 mg, 1.18 mmol) was added to a glass flask, which was dried at 600 °C under vacuum and purged with argon in three successive cycles. Then, about 150 mL THF were condensed directly into the flask. Next, the initiator 1,1-diphenyl-3-methylpentyllithium (DPHLi) was prepared *in situ* by adding a 0.077 mol/L *s*-BuLi solution in THF (3.25 mL, 0.25 mmol) and a 0.814 mol/L DPE solution in THF (0.92 mL, 0.75 mmol) to the flask. The dark red solution was cooled to -80 °C with an acetone/liquid nitrogen cooling bath and MMA (6.1 mL, 0.33 g/L, 20 mmol) diluted in THF was added. After stirring for 30 minutes at -80 °C, the polymerization of the first block was completed and 2 mL of the solution were taken out to analyze the molecular weight by SEC. Next, the second monomer *t*BMA (14.3 mL, 88.0 mmol) was added via a syringe and the reaction mixture was stirred for another 2 h without further cooling, while the temperature reached approximately 0 °C. Finally, the polymerization was terminated by the addition of about 2 mL MeOH. The polymer was precipitated in an excess of a MeOH/water mixture (80/20 vol%) and dried at 70 °C under reduced pressure in a vacuum oven.

### ABA block copolymers

The synthesis of the triblock copolymers was done either by the sequential monomer addition or by using a difunctional initiator.

### Sequential monomer addition

Here, the detailed description for the preparation of sample 90-80-105 is given as a typical example. First, LiCl (50 mg, 1.18 mmol) was added to a glass flask, which was dried at 600 °C under vacuum and purged with argon in three successive cycles. Next, the initiator DPHLi was prepared *in situ* in about 200 mL THF by mixing *s*-BuLi dissolved in cyclohexane (0.54 mL, 1.4 M, 0.75 mmol) with DPE dissolved in THF (2.03 mL, 1.1 M, 2.25 mmol). The dark red solution was cooled to -80 °C. Next, MMA dissolved in THF (31.5 mL, 0.15 g/L, 60 mmol) was added and allowed to polymerize for 30 minutes. Then, *t*BMA (7 mL, 42 mmol) was given to the living polymer via a syringe, and polymerized for about 2 h without further cooling, until the temperature reached approximately 0 °C. Next, the solution was cooled to -80 °C and MMA

dissolved in THF (31.5 mL, 0.15 g/L, 60 mmol) was added. The polymerization was carried out for 30 minutes and was eventually terminated by the addition of 2 mL MeOH. After the polymerization of each block, 2 mL of the reaction mixture were taken out to analyze the polymer by SEC and $^1$H-NMR. The final triblock copolymer was precipitated in an excess of a MeOH/water mixture (80/20 vol%) and dried at 70 °C under reduced pressure in a vacuum oven.

#### Use of a difunctional initiator

In a typical reaction (sample 306-718-306), the difunctional initiator 1,1,4,4-tetraphenyl-1,4-dilithiobutane was prepared *in situ*. Therefore, an excess of freshly cut Li (18 mg, 2.59 mmol) and LiCl (50 mg, 1.18 mmol) was added to a glass flask, dried at 600 °C under vacuum and purged with argon in three successive cycles. After the distillation of about 200 mL THF into the flask, a 1.8 mol/L DPE solution in THF (0.06 mL, 0.1 mmol) was added via a syringe and the mixture was stirred overnight at room temperature, whereupon the color changed to a dark red. Then, the solution was cooled to -80 °C, the monomer *t*BMA (11.5 mL, 70 mmol) was added and allowed to polymerize without further cooling for 2 h, while the temperature reached ca. 0 °C. Next, the solution was again cooled to -80 °C, MMA in THF (14 mL, 0.43 g/mL, 60 mmol) was added via a syringe and polymerized within 30 minutes. The polymerization was terminated by the addition of 2 mL MeOH. The triblock copolymer was precipitated in an excess of a MeOH/water mixture (80/20 vol%) and finally dried at 70 °C under reduced pressure.

#### Hydrolysis

About 10 g polymer were dissolved in 100 mL dioxane and 10 mL of a 4 M aqueous HCl were added to hydrolyze the P*t*BMA block. The reaction mixture was heated for 6-8 h to 85 °C. Afterward, the solvent was removed by a rotary evaporator and the polymer was dried at 70 °C under reduced pressure. The polymer was then neutralized by stirring it in a diluted NaOH solution in water. Typically, 1.5 mL of a 33 wt% aqueous NaOH and 100 mL deionized per gram of dry polymer were used. The resulting amphiphilic block copolymer was washed with deionized water until the filtrate was neutral and finally dried at 70 °C under reduced pressure.

#### Hydrogel formation

Typically, about 10 g of polymer were stirred as a 2 wt% solution in deionized water for 6 h under reflux conditions (100 °C) to increase the exchange kinetics of the PMMA block in the amphiphilic block copolymers. The resulting hydrogel was then washed with deionized water and finally dried at 60 °C under reduced pressure.

| Sample | $M_w$ (SEC) | *PDI* (SEC) | Ratio of PMMA to P*t*BMA (NMR) | Synthetic approach |
|---|---|---|---|---|
| 15-275-15 | 1kDa-39kDa-1kDa | 1.10 | 10%:90% | difunctional |
| 38-505-31 | 4kDa-77kDa-4kDa | 1.06 | 12%:88% | sequential |
| 56-374-47 | 5kDa-70kDa-8kDa | 1.07 | 24%:76% | sequential |
| 58-194-66 | 6kDa-26kDa-8kDa | 1.09 | 39%:61% | sequential |
| 60-340-53 | 6kDa-59kDa-6kDa | 1.04 | 25%:75% | sequential |
| 60-98-81 | 6kDa-14kDa-7kDa | 1.07 | 65%:45% | sequential |
| 62-233-58 | 6kDa-36kDa-10kDa | 1.15 | 34%:66% | sequential |
| 63-323-63 | 6kDa-46kDa-6kDa | 1.10 | 28%:72% | difunctional |
| 72-408-71 | 7kDa-64kDa-8kDa | 1.07 | 26%:74% | sequential |
| 87-371-113 | 9kDa-49kDa-9kDa | 1.05 | 35%:65% | sequential |
| 90-80-105 | 9kDa-9kDa-8kDa | 1.10 | 71%:29% | sequential |
| 178-507-160 | 18kDa-115kDa-18kDa | 1.06 | 40%:60% | sequential |
| 306-718-306 | 19kDa-102kDa-19kDa | 1.12 | 46%:54% | difunctional |
| 363-1289-363 | 27kDa-183kDa-27kDa | 1.17 | 36%:64% | difunctional |
| 80-187 | 8kDa-26kDa | 1.06 | 30%:70% | sequential |
| 80-587 | 8kDa-142kDa | 1.07 | 12%:88% | sequential |

**Table A.3:** Overview of the synthesized PMMA-*b*-PSMA(-*b*-PMMA) block copolymers in this thesis. The sample names are derived from the monomer units in each block, as calculated by the combined use of $^1$H-NMR with SEC. Additionally, $M_w$ for each block measured by SEC, the *PDI* of the final polymer and the ratio of PMMA to P*t*BMA in the block copolymer, obtained by integrating the respective peaks of the NMR spectra, are given in column two, three and four, respectively.

### A.1.6 Chemically end-linked PSMA-EGDMA polymers

#### Star polymers

The P*t*BMA-star polymers were synthesized first by anionic polymerization, followed by hydrolysis and neutralization to the PSMA-star polymers. The synthetic procedure for the P*t*BMA-star polymers was adapted from Hadjichristidis *et al.*, who synthesized PMMA-star polymers in a similar way [Efstratiadis94]. In a typical reaction, to get a five star polymer with an arm length of 120 monomer units, LiCl (50 mg, 1.18 mmol) was added to a glass flask, which was dried at 600 °C under vacuum and purged with argon in three successive cycles. Then, about 150 mL of dehydrated THF were directly distilled into the flask to dissolve the salt. Next, the initiator 1,1-diphenyl-3-methylpentyllithium (DPHLi) was prepared in situ by adding a 1.4 mol/L *s*-BuLi solution in cylcohexane (0.18 mL, 0.25 mmol) and a 1.8 mol/L DPE solution in THF (0.68 mL, 1.25 mmol) to the flask, leading to a dark red color. The reaction mixture was cooled to -80 °C with an acetone/liquid nitrogen bath and *t*BMA (5 g, 35.2 mmol) was added via a syringe. The reaction mixture was stirred for about 2 h without further cooling until the temperature reached approximately 0 °C. About 2 mL of the mixture were taken out via a syringe to analyze the length of the arms-to-be by SEC. Next, the solution was cooled to -80 °C and a 2.5 molar solution of EGDMA in THF (0.41 mL, 1 mmol) was added. After keeping the temperature for another hour at -80 °C, the reaction mixture was stirred for another 16 h without further cooling, while room temperature was reached. Then, the polymerization was terminated by addition of about 5 mL degassed MeOH. Afterward, the polymer was precipitated in a MeOH/water mixture (80/20 vol%) and dried at 70 °C under reduced pressure. The hydrolysis and neutralization was preformed, as already described in section A.1.5, to convert the P*t*BMA-star polymer into the PSMA-star polymers.

#### Networks

The synthesis of the PSMA-EGDMA networks was similar to the PSMA-star polymer synthesis. But instead of the monofunctional, the difunctional initiator 1,1,4,4-tetraphenyl-1,4-dilithiobutane was used, which was prepared *in situ*, as already described in Section A.1.5. In a typical reaction, an excess of freshly cut Li (135 mg, 19.4 mmol) and LiCl (50 mg, 1.18 mmol) was added to a glass flask, which was dried at 600 °C under vacuum and purged with argon in three successive cycles. Then, about 100 g of THF were distilled into the reaction flask. Next, a 1.8 mol/L DPE solution in THF (1.1 mL, 1.98 mmol) was added and the solution was stirred overnight to form the dark red difunctional initiator 1,1,4,4-tetraphenyl-1,4-dilithiobutane. Then, the initiator solution was cooled to -80 °C and the monomer *t*BMA (20 g, 140.8 mmol) was added. The reaction mixture was stirred for 2 h without further cooling, until the temperature

reached 0 °C. Next, about 2 mL of the mixture were taken via a syringe to analyze the length of the meshes-to-be by SEC. In the next step, the solution was cooled to -80 °C and a 2.5 molar solution of EGDMA in THF (5.6 mL, 14 mmol) was added. After about 15 minutes, a strong increase in viscosity was observed, leading to the formation of a transparent organogel. The mixture was stirred for additional 16 h without further cooling to allow the reaction to complete. Finally, the polymerized hydrogel was washed in several steps with THF and the sol content $w_{sol}$ was determined by

$$w_{sol} = \frac{m_{sol}}{m_{gel}} = \frac{m_{monomer} - m_{gel}}{m_{gel}}, \tag{A.1}$$

where $m_{gel}$, $m_{sol}$ and $m_{monomer}$ are the respective masses of the dried gel, sol and monomer, respectively.

The organogel was hydrolyzed and neutralized to a hydrogel (see section A.1.5), which was subsequently washed with deionized water until the filtrate was neutral. Three different networks were synthesized by this approach and are listed in Table A.4. The names PSMA$x$-EGDMA$y$ are derived from the number of monomers in the mesh $x$ and the ratio of EGDMA to initiator $y$.

| Sample | $[EGDMA]/[I]$ [–] | $M_w$ (mesh) [kDa] | $PDI$ (mesh) [–] | $N$(M) (mesh) [–] | $w_{sol}$ [wt%] |
|---|---|---|---|---|---|
| PSMA225-EGDMA5 | 5 | 32 | 1.10 | 225 | 10 |
| PSMA162-EGMDA7 | 7 | 23 | 1.10 | 162 | 2 |
| PSMA141-EGDMA7 | 7 | 20 | 1.18 | 141 | 5 |

**Table A.4:** Overview of the synthesized networks made by the chemical end-linking approach.

### A.1.7 Interpenetrating PSA-*i*-PSA double networks

The synthesis of the first poly(acrylic acid) network, which has been neutralized to 75 mol% prior to the polymerization, was already described in detail in Section A.1.2. However, the monomer was directly polymerized in a cylindrical mold (usually about 4 mL solution per mold with a diameter of approximately 30 mm) to get a disk-shaped hydrogel. This disk was then placed in an excess of the second monomer solution, which had about 20 times the mass of the first network. The second monomer solution had the same polymer concentration as the first network, but was totally uncharged to ensure the highest soaking into the first network. The degree of crosslinking of the second monomer solution was varied in the range of 0.3 to 5 mol% and the photoinitiator 2,2'-azobis(amidinopropane) dihydrochloride (V50) was used

(2 wt% with respect to the acrylic acid) instead of the redox initiator. The disk was allowed to swell in the second monomer solution for 3 days under the exclusion of light at 8 °C. Next, the disk was separated from the monomer solution and traces thereof were gently removed with a paper towel. The fully swollen gel was then radiated by UV light ($\lambda$ = 366 nm) for 2 h to trigger the polymerization. The double network was fully neutralized by a 33 wt% NaOH solution and extensively washed with deionized water to remove all unreacted chemicals and sol. To keep the number of samples manageable, only the *DC* of the first and the second network was varied, while all other synthetic parameters were kept constant (see Table A.5).

| Sample | *DC* [mol%] 1st network | *DC* [mol%] 2nd network |
|---|---|---|
| PSA-DC03-*i*-PSA-DC1 | 0.3 | 1 |
| PSA-DC1-*i*-PSA-DC03 | 1 | 0.3 |
| PSA-DC1-*i*-PSA-DC1 | 1 | 1 |
| PSA-DC1-*i*-PSA-DC5 | 1 | 5 |
| PSA-DC5-*i*-PSA-DC1 | 5 | 1 |
| PSA-DC5-*i*-PSA-DC5 | 5 | 5 |

**Table A.5:** Overview of the synthesized PSA-*i*-PSA double networks.

### A.1.8 Thermally responsive hydrogels based on PNIPAAm

#### P(NIPAAm-*co*-SA) copolymer networks

The hydrogels were synthesized by free radical copolymerization of acrylic acid (AA), which was neutralized to 75 mol% with NaOH, N-isopropylacrylamide (NIPAAm) and the difunctional crosslinker N,N'-methylenbis(acrylamide) (MBA) as a 20 wt% solution in water at about 10 °C. Sodium persulfate (SPS) and TEMED were used as the radical redox-initiator agent. An overview of the samples synthesized in this study and their respective composition is given in Table A.6.

The preparation of sample P(NIPAAm-co-SA5)-DC03, a hydrogel with a 0.3 mol% degree of crosslinking and a ratio of 95:5 mol% of NIPAAm to SA, is given in detail as an example: First, MBA (24.3 mg, 0.16 mmol) was dissolved in 24.4 mL of deionized water. Second, freshly distilled AA (190 mg, 2.6 mmol) was added and partly neutralized by NaOH as a 33 wt% solution in water (239 mg, 20 mmol). NIPAAm (6.66 g, 50.0 mmol) was then completely dissolved in the reaction mixture. The clear solution was cooled to 10 °C and SPS (23.8 mg, 0.10 mmol) dissolved in 5 mL of deionized water was given to the monomer solution. Afterward, nitrogen gas was bubbled through the (still cooled) mixture over a period of 30 min to remove oxygen. Next,

TEMED (10 µL, 0.05 mmol) was added and the polymerization was carried out at about 10 °C.[1] The reaction mixture was stirred for 12 h while the gelation usually set in within a few minutes. The remaining hydrogel was cut into small pieces and placed in a large excess of water to remove traces of unreacted material and sol. The washed hydrogel was finally dried overnight at 70 °C in a vacuum oven. The homopolymers were synthesized the same way without adding a second monomer (NIPAAm or SA, respectively).

| Sample | SA content [mol%] | *DC* [mol%] |
|---|---|---|
| PNIPAAm-DC03 | 0 | 0.3 |
| P(NIPAAm-*co*-SA1)-DC03 | 1 | 0.3 |
| P(NIPAAm-*co*-SA2)-DC03 | 2 | 0.3 |
| P(NIPAAm-*co*-SA5)-DC03 | 5 | 0.3 |
| P(NIPAAm-*co*-SA10)-DC03 | 10 | 0.3 |
| PSA-DC03 | 100 | 0.3 |
| PNIPAAm-DC1 | 0 | 1 |
| P(NIPAAm-*co*-SA1)-DC1 | 1 | 1 |
| P(NIPAAm-*co*-SA2)-DC1 | 2 | 1 |
| P(NIPAAm-*co*-SA5)-DC1 | 5 | 1 |
| P(NIPAAm-*co*-SA11)-DC1 | 11 | 1 |
| P(NIPAAm-*co*-SA25)-DC1 | 25 | 1 |
| P(NIPAAm-*co*-SA50)-DC1 | 50 | 1 |
| PSA-DC1 | 100 | 1 |
| PNIPAAm-DC5 | 0 | 5 |
| P(NIPAAm-*co*-SA1)-DC5 | 1 | 5 |
| P(NIPAAm-*co*-SA2)-DC5 | 2 | 5 |
| P(NIPAAm-*co*-SA5)-DC5 | 5 | 5 |
| P(NIPAAm-*co*-SA10)-DC5 | 10 | 5 |
| PSA-DC5 | 100 | 5 |

**Table A.6:** Overview of the P(NIPAAm-*co*-SA) hydrogels, which were synthesized in this thesis.

#### Interpenetrating PSA-*i*-PNIPAAm double networks

The synthesis of the interpenetrating double networks was similar to the approach in Section A.1.7: PSA hydrogels were synthesized as the first network in a disk shape (diameter: ≈ 30 mm) with a volume of about 4 mL. The obtained disks were then placed in 80 mL of a NIPAAm solution prepared in the same way as in the previous section, but without adding any

[1] The synthesis was done in smaller batches below 10 g to keep the polymerization heat under control. In this manner, the temperature could be kept below the LCST of NIPAAm throughout the reaction.

SA and using the photoinitiator 2,2'-azobis(amidinopropane) dihydrochloride (V50) instead of the thermal redox-initiator system. The disks were allowed swelling in the second monomer solution for 3 days at 8 °C in the dark. Afterward, the disks were separated from this solution and traces thereof were gently removed with a paper towel. The fully soaked hydrogels were exposed to UV light ($\lambda$ = 366 nm) for 3 h at about 10 °C to trigger the polymerization, as seen in Figure A.1. Finally, the double networks were extensively washed with deionized water to remove all unreacted chemicals and sol. An overview of the synthesized PSA-*i*-PNIPAAm double networks is given in Table A.7.

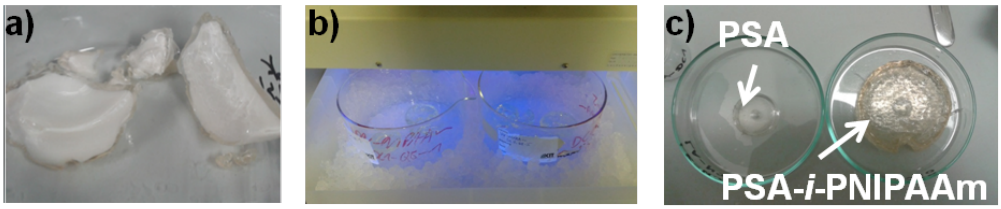


**Figure A.1:** Synthesis of the interpenetrating PSA-*i*-PNIPAAm double networks. a) Polymerization using a thermal initiator at 70 °C above the LCST of NIPAAm, which leads to white, mechanically weak hydrogels. b) The use of an UV initiator allows to keep the temperature below the LCST during the polymerization. c) The result of the polymerization triggered by UV light: PSA disk (left) and PSA-*i*-PNIPAAm double network (right).

| Sample | *DC* [mol%] 1st network | *DC* [mol%] 2nd network |
|---|---|---|
| PSA-DC03-*i*-PNIPAAm-DC1 | 0.3 | 1 |
| PSA-DC1-*i*-PNIPAAm-DC03 | 1 | 0.3 |
| PSA-DC1-*i*-PNIPAAm-DC1 | 1 | 1 |
| PSA-DC1-*i*-PNIPAAm-DC5 | 1 | 5 |
| PSA-DC5-*i*-PNIPAAm-DC1 | 5 | 1 |
| PSA-DC5-*i*-PNIPAAm-DC5 | 5 | 5 |

**Table A.7:** Overview of the PSA-*i*-PNIPAAm double networks, which were synthesized in this thesis.

## A.2 Experimental characterization procedures

### A.2.1 Size exclusion chromatography (SEC)

The molecular weight and the molecular weight distribution were determined using an Agilent 1100 pump with an Agilent 1200 differential refractive index (DRI) detector (Agilent, Santa Clara, US) with two SDV Lux 300 mm x 8 mm i.d. columns (1,000 and 10,000 Å pore size, PSS, Mainz, Germany). The polymers were measured in SEC-grade THF with a concentration of about 2 g/L at 25 °C with a flow rate of 1 mL/min. PMMA standards from PSS were used for the calibration.

### A.2.2 Water absorbency

The time dependent degree of swelling $Q(t)$ was gravimetrically determined by bringing the dry polymer particles with a particle size in between 350 and 650 µm in contact with deionized water or an aqueous NaCl solution for a time $t$ (see Figure A.2).

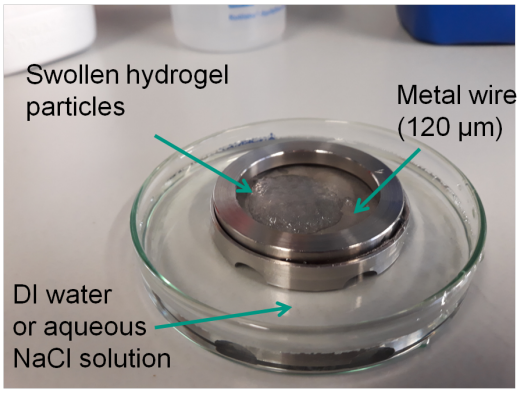


**Figure A.2:** Absorbency experiment to determine the degree of swelling.

This procedure has been adapted from previous work [Buchholz98, Brendel99, Höpfner13a]. In detail, the dried polymer with a mass $m_p$ of about 10 – 50 mg, depending on the degree of swelling, was placed on a metal sieve (120 µm mesh size) with the mass $m_{sieve}$. The sieve was then put in an excess of the solution to allow the particles to swell for a time $t$, where the polymer was wetted only through the sieve. Then, the sieve with the swollen hydrogel was removed, gently pressed onto a paper towel to remove excess solution and weighed ($m_{wet}$). The swelling degree was determined by

$$Q(t) = \frac{m_s(t)}{m_p} = \frac{m_{wet}(t) - m_{sieve} - m_p}{m_p} \, [\mathrm{g/g}] \, . \tag{A.2}$$

The degree of swelling at equilibrium $Q_{eq}$ was determined by swelling the polymer overnight ($t > 12$ hours). The swelling measurements were typically conducted in deionized water and a 1 wt% NaCl solution. They were repeated three times and the mean value is used, while the standard deviation is indicated as error bars in the respective graphs.

### A.2.3 Rheology and sample preparation

For the rheological measurements, disk-shaped specimens are desirable, which can be prepared by polymerizing the monomer solution in a cylindrical mold (see [Höpfner13a], p.32). However, as most of the hydrogels synthesized in this thesis needed an additional chemical treatment (like hydrolysis, surface crosslinking, etc.), this was only possible for some samples (*e. g.* P(NIPAAm-*co*-SA) copolymers). Therefore, the hydrogel specimens were prepared in two different ways (see Figure A.3), but were always measured in their fully swollen state:

i) The interpenetrating double networks and the P(NIPAAm-*co*-SA) copolymers were directly polymerized in a cylindrical mold to get a disk-shaped hydrogel. These disks were then allowed swelling to their full extension by placing them for at least 16 hours in deionized water. Next, the actual specimen was punched out to get a disk with a diameter of either 13 or 25 mm (see Figure A.3, left). Before the measurement, the surface was carefully dewatered by placing them on a paper towel until the unbound water was removed. These samples were then measured by oscillatory shear and partially also by oscillatory compression.

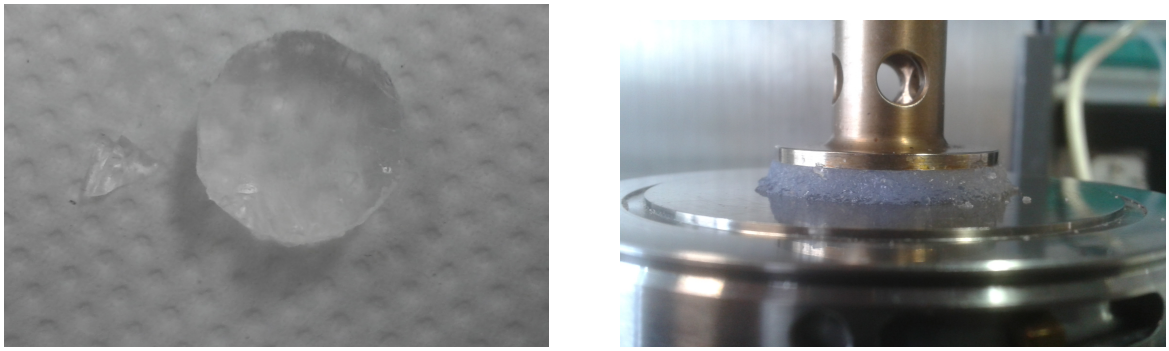

**Figure A.3:** Rheological specimen: Left) Samples that were punched from swollen hydrogel disks (diameter: 13 mm). Right) Filtered hydrogel particles.

ii) The other polymer samples were prepared by the following way, where the procedure was previously described elsewhere in more detail [Ramazani-Harandi06]. The dried polymer samples were ground and then swollen to equilibrium in deionized water overnight. Next, the swollen hydrogel particles were filtered through a 120 µm wire gauze and carefully dewatered by squeezing gently the gauze bottom on a paper towel until the unbound water was removed. The hydrogel was eventually placed on the geometry of the rheometer (see Figure A.3, right)

and the rheological properties were measured with a fixed gap of 3 mm (axial force ca. 0.5 N). These samples could be only measured via oscillatory shear, as the necessary static strain in the compression tests would directly change the shape of the hydrogels.

Both specimen types led to similar rheological results with no significant difference in their complex modulus $G^*$ in the LVE regime, which might be related to the small amplitudes used.

The oscillatory shear measurements were carried out on the strain controlled rotational rheometer Ares G2 (TA Instruments, Eschborn, Germany). Plate-plate geometries made from aluminum with a diameter of either 13 or 25 mm were used. The temperature was controlled to 25 ± 0.1 °C by a Peltier element (Advanced Peltier System, TA Instruments). First, an amplitude sweep was carried out by varying the strain from $\gamma_0 = 2 * 10^{-5} - 10$ with a constant frequency of $\omega = 1$ rad/s to find the LVE regime for every new sample. Then, frequency sweeps for three different specimens from the same hydrogel sample were employed: The frequency was changed from 0.1 to 100 rad/s, while the strain was kept constant at 0.1%. From these measurements the mean value of the complex modulus $G^*$ at 1 rad/s was taken to be representative for the sample. The error bars in the respective graphs indicate the standard deviation around this mean value.

The oscillatory compression measurements were carried out with an Eplexor 150N equipped with the humidity generator Hygromator (Gabo Qualimeter, Ahlden, Germany). Plate-plate geometries with a diameter of 25 mm made from aluminum were used. Frequency sweeps were carried out with a static strain of 6% and a dynamic strain of 2% in the range from 0.3 to 100 Hz. The temperature was controlled to 25 ± 1 °C and the relative humidity was kept at 90 ± 2%. The temperature sweeps were measured with the same parameters for static strain, dynamic strain and relative humidity. In these experiments, the frequency was kept constant at 5 Hz and the temperature was varied in the range from 25 to 75 °C. Three specimens were measured from the same hydrogel and the error bars in the respective graphs show the standard deviation around the mean value.

### A.2.4 Fourier-transform infrared spectroscopy (FT-IR)

FT-IR spectra of the dried and ground hydrogel particles were recorded in attenuated total reflection (ATR) mode using a Vertex 70 spectrometer with a DTGS detector (Bruker, Ettlingen, Germany). 64 scans were employed over a range of 600 – 4,000 $cm^{-1}$ with a resolution of 4 $cm^{-1}$. Three samples were measured from each hydrogel and evaluated as described in Section 4.5.

### A.2.5 Differential scanning calorimetry (DSC)

DSC was used to investigate the LCST of the fully swollen, thermally responsive hydrogels. The dried and ground polymer particles were swollen in deionized water or an aqueous NaCl

solution until equilibrium. The particles were then gently pressed onto a paper towel to remove excess solution and about 15 mg of the sample were weighed in an aluminum pan. The DSC measurements were performed with a DSC30 (Mettler Toledo, Gießen, Germany). The sample was cooled to 2 °C and kept constant for 5 minutes before the temperature was increased to 75 °C at a heating rate of 2 °C/min.

### A.2.6 Small angle X-ray scattering (SAXS)

The 2D-SAXS measurements were conducted at room temperature with a S3-Micro Hecus X-ray system using a two-dimensional CCD detector from Photonic Science (Saint-Étienne de Saint-Geoirs, France). The ground samples were measured either in the dried state or swollen in aqueous solutions in a sample holder capped with Kapton sheets (100 HN, 25 µm) to prevent evaporation.

The raw data was analyzed using the *FIT2D* software, where the 2D scattering patterns were radially averaged into a 1D plot. The maximum of the first peak was taken to calculate the further quantities, as described in Section 5.1.3.

### A.2.7 Scanning electron microscopy (SEM)

The dried triblock copolymers were ground to a fine powder. Afterward, the samples were coated with platinum and the SEM images were recorded with a LEO Gemini 1530 microscope from Zeiss (Oberkochen, Germany).

### A.2.8 Nuclear magnetic resonance (NMR)

#### NMR spectroscopy at high-field

The $^{1}$H-NMR spectra were measured with an Avance III Microbay 400 MHz spectrometer (Bruker, Karlsruhe, Germany) using 256 scans. The samples were prepared by dissolving about 10 – 20 mg in 1 mL of $CDCl_3$, DMSO-$D_6$ or $D_2O$.

#### NMR relaxometry at low-field

The NMR relaxometry measurements were recorded with the benchtop spectrometer minispec mq20 (Bruker, Karlsruhe, Germany) at low-field (19.95 MHz). The sample temperature was controlled by a BVT3000 unit (Bruker) and kept constant at 32 °C, unless otherwise stated. For all hydrogels, the magnetic field was matched and the pulse lengths were determined prior to the start of the actual experiment.

The hydrogel samples were prepared by the following procedure: The polymer particles were swollen in $D_2O$ and subsequently dried in vacuo at 70 °C to reduce residual $H_2O$. About 60 mg of the water-free particles were again mixed with $D_2O$ in a ratio of 1:9 and transferred to the bottom of a 10 mm glass tube. The tube was sealed with parafilm and the hydrogel was allowed to equilibrate for at least 16 hours before the measurement.

### $T_1$-relaxation measurement

The longitudinal relaxation was probed with the saturation recovery (SR) experiment. The pulse sequence is displayed in Figure A.4 and is implemented in the Bruker application *t1_sat_mb.app*. The whole magnetization of the sample is saturated ($M_z = 0$) by a sequence of 90° pulses with non-uniform pulse spacings. After the variable time delay $\tau$, a 90° pulse is used to convert $M$ into an observable transverse magnetization.

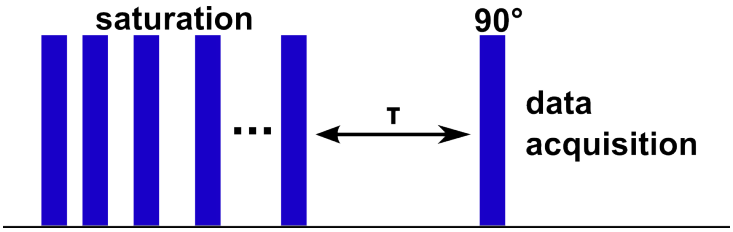


**Figure A.4:** Schematic representation of the saturation recovery (SR) sequence to measure $T_1$-relaxation.

The following parameters were used for the SR experiments:
Number of scans *ns*: 32.
Number of dummy echoes *de*: 4.
Recycle delay *rd*: 100 ms.
Delay time $\tau$: 1 – 20,000 ms.
Number of data points: 44.
Delay sampling window: 50 µs.
Sampling window: 20 µs.
The saturation time was individually adjusted for each sample to reach a minimum intensity of the first point below 5%.

### $T_2$-relaxation measurement

The transverse relaxation was measured by the combination of a magic sandwich echo (MSE, see Figure A.5, top) and the advanced CPMG/XY16 pulse train. A simple CPMG experiment with its phase $(y)^n$, which is displayed in Figure A.5, bottom, leads to spin-locking effects

[Höpfner14]. Hence, the advanced XY16 cycling scheme (phase: $(y\bar{x}y\bar{x}\ \bar{x}y\bar{x}y\ \bar{y}x\bar{y}x\ x\bar{y}x\bar{y})^n$) was used instead.

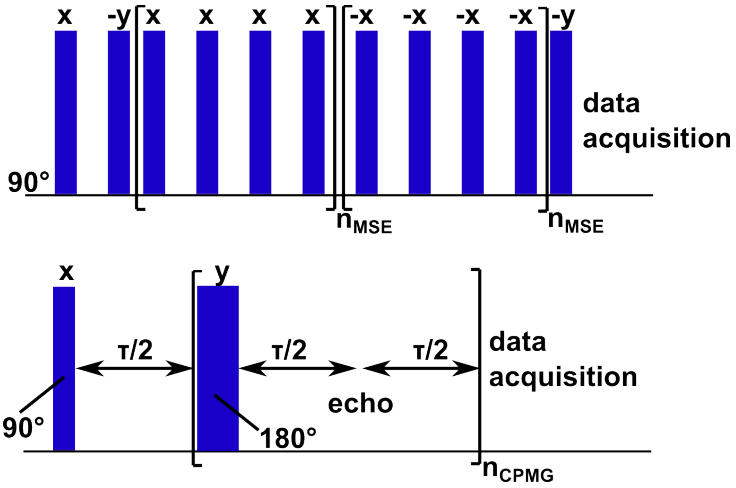


**Figure A.5:** Schematic representation of the pulse sequences for measuring the $T_2$-relaxation times: MSE-sequence at the top and CPMG-sequence at the bottom.

The whole relaxation curve could be measured by four individual experiments — one MSE and three CPMG/XY16 experiments with varying delay times $\tau$. The parameters are listed in Table A.8 and were taken from previous work [Höpfner14]. The four individual experiments can be also combined in one application (*mse-cp-3tauechoes.app*) to save measuring time.[2] Even though this led to a reduced data density, the further data treatment, *e. g.* the inverse Laplace transform was not significantly affected.

| Parameter | xy16_short | xy16_middle | xy16_long | MSE | DQ |
|---|---|---|---|---|---|
| *ns* [–] | 256 | 128 | 128 | 128 | 1024 |
| *ds* [–] | 4 | 4 | 4 | 4 | 16 |
| $\tau_E$ [ms] | 0.04 | 1 | 1 | – | – |
| *de* [–] | 0 | 0 | 15 | – | – |
| *rd* [–] | 20 | 20 | 20 | 20 | 0.1 |
| *ne* [–] | 256 | 256 | 256 | – | – |

**Table A.8:** Parameters used for measuring $T_2$-relaxation and DQ-coherences: The number of acquired scans (*ns*), the number of dummy scans *ds*, the echo time $\tau_E$, the number of dummy echoes *de*, the recycle delay *rd* and the number of acquired echoes *ne*.

[2]The combination was kindly implemented in one pulse program by Volker Räntzsch.

### Residual dipolar coupling measurements

The DQ coherences were measured with the advanced Baum-Pines pulse sequence in Figure A.6, which was implemented by Saalwächter *et al.* for the minispec in the pulse program *ksbaum_ldi2cfit_korr.app*. The first 12 pulses stimulate the DQ-coherences, while the second 12 pulses reconvert them to an observable magnetization. The last pulse discriminates between the DQ signal $I_{DQ}$ and the reference signal $I_{ref}$, which are alternately recorded for the increasing cycle time $\tau_c$.

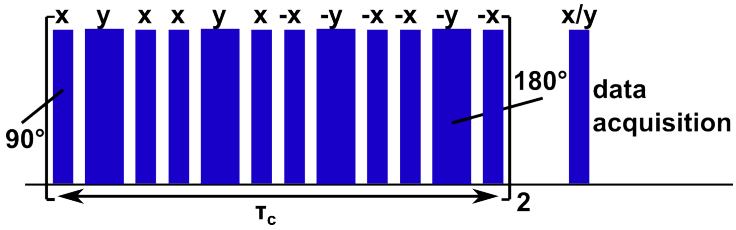


**Figure A.6:** Schematic representation of the modified Baum-Pines pulse sequence for measuring the double quantum coherence build-up.

The experimental parameters were taken from previous work [Höpfner14] and are listed in Table A.8. The initial cycle time $\tau_c$ was 0 ms and was increased by 0.04 ms per point. In total 70 points were measured and the cycle time increment was doubled after every 10 points. The two curves $I_{DQ}$ and $I_{ref}$ in Figure A.7, left, were obtained by recording the FID for 0.1 ms, followed by a linear extrapolation to its initial signal. Thereby, both signals were already normalized with respect to the initial value of $I_{ref}$.

As a next step, a normalization procedure was applied to recover the true build-up curve undistorted by relaxation effects. The raw data was plotted in a lin-log plot (see Figure A.7, left), which simplifies the identification of the long-time tail, which is related to solvent [Valentín09]. The long-time tail was fitted after 40 ms with a simple exponential function and was subtracted from $I_{ref}$, to obtain the reduced data

$$I_{red} = I_{ref} - I_{DQ} - A * \exp\left(-\frac{2\tau_c}{\tau_A}\right) . \tag{A.3}$$

In the reduced data $I_{red}$ (see brown triangles in Figure A.7, left), another long-time tail, which is related to non-coupled, *i. e.* elastically non-active defects [Valentín09], was fitted by a second exponential function and was finally subtracted to obtain the real build-up curve (Equation A.4). The identification of suitable fitting boundaries for the second long-time tail was even in the lin-log plot not straightforward, as the tail in hydrogels is much less pronounced than in elastomers. Unfortunately, the fitting boundaries strongly influence the further data treatment and the normalized build-up curves. Therefore, the second fit was performed in the range of 5 –

15 ms for all samples to keep the data treatment consistent. In this way, it could be guaranteed that the normalized build-up curve (blue triangles in Figure A.7, left) reached always its plateau value of 0.5, which is the theoretical long-time prediction, before the data started to scatter.

$$I_{\mathrm{nDQ}} = \frac{I_{\mathrm{DQ}}}{I_{\mathrm{ref}} + I_{\mathrm{DQ}} - A * \exp\left(-\frac{2\tau_{\mathrm{c}}}{\tau_{\mathrm{A}}}\right) - B * \exp\left(-\frac{2\tau_{\mathrm{c}}}{\tau_{\mathrm{A}}}\right)} \tag{A.4}$$

The normalized DQ build-up curves were analyzed by the numerical Tikhonov regularization to calculate the distribution in $D_{\mathrm{res}}$ constants. The inversion procedure was performed with the *FTIKREG* program, which is freely accessible online [Chassé11]. As input, only data points were used before the normalized DQ build-up curve started to scatter. The distributions were calculated with the "Abragam-like" kernel function [Lange11] for different error parameters $\epsilon$, where the range of $\epsilon$ was adapted to the noise level of the recorded data.

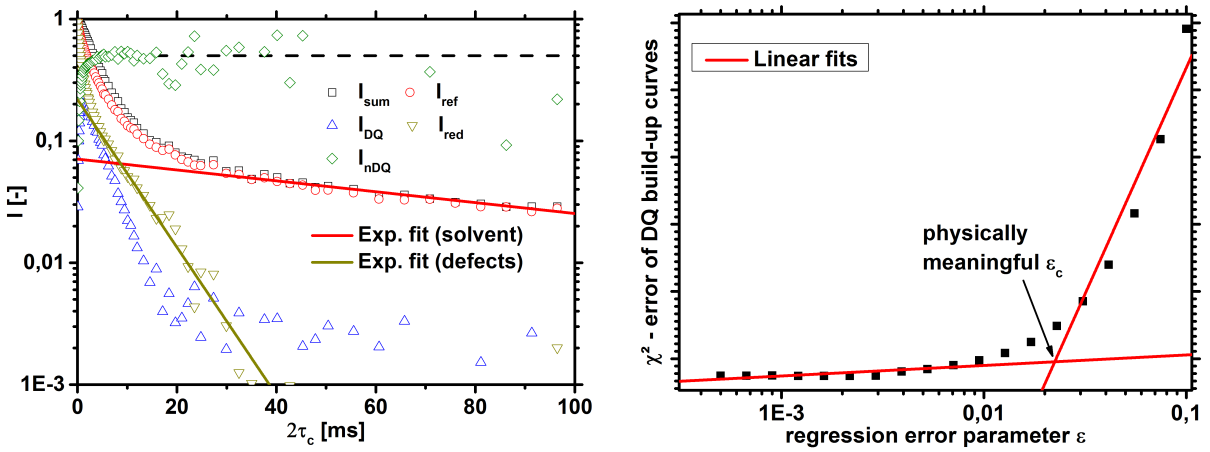


**Figure A.7:** Data treatment of the DQ measurements. Left) Calculation of the true build-up curve by subtracting the two long-time tails. Right) Calculated $\chi^2$ for a series of error parameters $\epsilon$ from the Tikhonov regularization.

The regularization results highly depend on the used error parameter $\epsilon$. In order to obtain the most reliable distribution in coupling constants, $\epsilon$ was plotted against the $\chi^2$-error of the DQ build-up curves in a log-log plot, as shown in Figure A.7, right. The $\chi^2$-error calculates the mean square deviation between the experimental and the fitted build-up curves. The most reliable distribution curve is found at a certain $\epsilon_{\mathrm{c}}$ value. At this point, a further reduction of $\epsilon$ does not bring a significant improvement of the accuracy of the calculated distribution. The accuracy is rather overestimated and the resulting data is physically meaningless showing multiple peaks [Chassé11].

## A.3 Desalination experiments

### A.3.1 Press setup and standard desalination experiments using pressure as external stimulus

The desalination experiments were conducted on an in-house built press setup (see Figure A.8). The construction is described in more detail in previous work [Höpfner13a, Höpfner13b]. The heart of the apparatus is a sample chamber of about 400 mL volume for the gel and the supernatant phase. On top and below this chamber are two sieve units of cellulose filter paper (3 – 5 µm pore size) and two supporting metal wire layers.

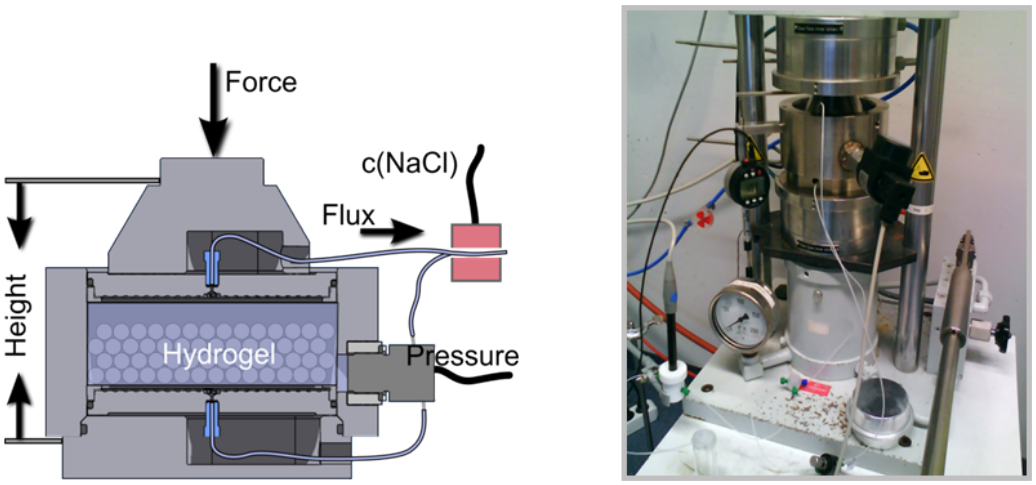


**Figure A.8:** Left) Schematic drawing of the press setup. Right) In-house constructed press to conduct the desalination experiments. Figures are taken from [Höpfner13a].

During an experiment, the upper sieve unit was moved by a hand driven oil hydraulic piston to compress the gel. Meanwhile, the pressure on the gel inside the chamber and the volume flux were measured by a pressure sensor (SD-40, Suchy Messtechnik, Lichtenau, Germany) and a distance gauge (MarCator 1086, Mahr, Göttingen, Germany), respectively.

Prior to the desalination experiments, the dried polymer was mixed with a NaCl aqueous solution at a defined swelling ratio $Q_{\mathrm{rel}} = \frac{m_{\mathrm{s}}}{m_{\mathrm{max.\ solution\ uptake}}}$. In a standard experiment, if nothing else is noted, a 1 wt% NaCl solution was used and $Q_{\mathrm{rel}}$ was chosen to be two, so that half of the brine volume is in the swollen polymer network and half of it is left in the supernatant phase. The constant volume of the swollen gel and the supernatant phase was chosen due to the fixed size of the press chamber (ca. 400 mL). Consequently, the mass of dry polymer $m_{\mathrm{p}}$ and salt solution $m_{\mathrm{s}}$ depend on the maximum degree of swelling $Q_{\mathrm{eq}}$ in the respective brine

solution and were calculated by Equation A.5 and A.6.

$$m_{\mathrm{p}} = \frac{m_{\mathrm{ges}}}{Q_{\mathrm{rel}} * (Q_{\mathrm{eq}} + 1)} \tag{A.5}$$

$$m_{\mathrm{s}} = m_{\mathrm{ges}} - m_{\mathrm{p}} \tag{A.6}$$

The mixture with the mass $m_{\mathrm{ges}} = 400\,\mathrm{g}$ was usually stirred overnight at room temperature to reach equilibrium conditions and was eventually transferred into the press chamber. The actual desalination experiment was started by lowering the piston to apply a small pressure below 1 bar on the mixture to first remove excess solution until the flux decreased noticeably within 20 minutes.

Then, a linear pressure increase of 60 bar/h to a maximum of 80 bar or until failure of the experiment (*e. g.* by pushing the hydrogel through the sieve elements), was applied. At the same time, 3 – 10 mL fractions of the eluate were collected and their salt content was analyzed by conductivity measurements (SevenMulti, Mettler Toledo, Gießen, Germany) and appropriate calibration [Höpfner13a].

### A.3.2 Desalination experiments using temperature as external stimulus

A typical thermal desalination experiment included the following steps: The dried hydrogel particles were placed in an excess of a 1 wt% NaCl solution and allowed to swell to equilibrium overnight. The mass of the dried particles $m_{\mathrm{p}}$ was calculated with respect to the degree of swelling $Q_{\mathrm{eq}}$ in the respective salt solution, in order to obtain a constant mass of the fully swollen hydrogel $m_{\mathrm{h}}$ of about 20 g, by

$$m_{\mathrm{p}} = \frac{m_{\mathrm{h}}}{Q_{\mathrm{eq}} + 1}\,. \tag{A.7}$$

The swollen hydrogel particles were then filtrated and washed so often (usually twice) with the same salt solution (salt concentration $c_0$, usually 1 wt% NaCl unless otherwise noted) until the salinity of the filtrate $c$ was the same as $c_0$. In this manner, an infinite large salt reservoir like the sea was simulated. The filtrated hydrogel with a mass of about 20 g was transferred into a plastic tube (centrifuge tube, 40 mL volume) and sealed with a septum. Next, the tube was placed in a 50 °C water bath. After 60 minutes, the exposed water with the mass $m_{\mathrm{rw}}$ was collected via a syringe and the salinity $c_{\mathrm{rw}}$ was measured by conductivity (SevenMulti, Mettler Toledo, Gießen, Germany) at room temperature.

The desalination experiments were typically repeated five times. The mean values and standard deviation as error bars are shown for the observed quantities in the respective graphs.

## A.4 Osmotic engine

The experiments were conducted in the following way, if not otherwise noted. Dried polymer particles with a size of 350 – 650 µm were swollen overnight in a 4.3 wt% NaCl solution to reach the degree of swelling at equilibrium. The swollen hydrogel was transferred in a 50 mL syringe (see Figure A.9), where the particles were placed in between two sheets of cellulose filter paper (3 – 5 µm pore size) and a metal wire (120 µm pore size).

The polyelectrolyte was then exposed to deionized water for 15 minutes and the expansion was measured by a simple ruler (height $h_1$). Next, the feedwater was changed to a 4.3 wt% NaCl solution and the height $h_0$ was noted after 5 minutes. The mean power $\bar{P}$ was calculated using the difference in the height by Equation 7.1 and renormalized to 1 kg dry polymer.

The experiments were performed with different external loads using always the same sample, where the lifted weight was increased step by step until no or only little expansion was observed.

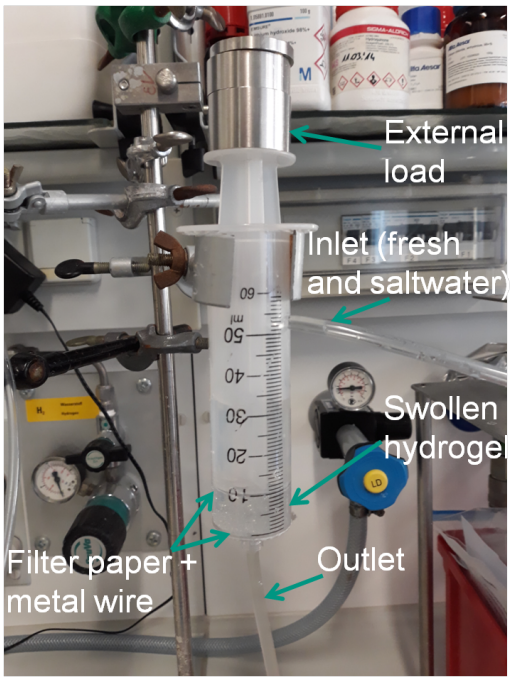


**Figure A.9:** Simple osmotic engine in form of a syringe during operation.

# Acknowledgements

At this point, I would like to thank all the people who helped and supported me during this thesis. I want to highlight:

- **Prof. Dr. Manfred Wilhelm**
  for the possibility to work in his group, for all the freedom during my thesis to explore my own ideas and for the opportunities to present my work at various conferences.
- **Prof. Dr. Christian Holm, Dr. Tobias Richter, Jonas Landsgesell and Dr. Peter Košovan**
  for the interesting discussions about polyelectrolytes and for providing also a different point of view on this topic.
- **Prof. Dr. Sebastian Seiffert and Axel Habicht**
  for the kind introduction into microfluidics and for the possibility to conduct some synthesis in Berlin.
- **Dr. Johannes Höpfner and Julius Albrecht**
  for the helpful discussions about the desalination process.
- **Karin Schlag and Felix Weißenfeld**
  for introducing me to the osmotic engine and for discussing ongoing challenges.
- **Dennis Barther, Raphael Geissinger and Ilona Wagner**
  worked as students under my supervision on different parts of the project and helped me a lot in the lab.
- **Dr. Nico Dingenouts**
  for helping me in all aspects related to SAXS.
- **Dr. Karl Ratzsch and Volker Räntzsch**
  for their support during the NMR measurements.
- **Sabine Weiland, Daniel Zimmermann, Wolfgang Arbogast and Helena Hörig**
  for helping with administrative or technical problems and making life easier.

- **The whole group**
  for the nice discussions about science and life besides work, all the help with different instruments, for the nice activities, the BBQs, the great X-mas movies, …
  Special thanks to Dr. Jennifer Kübel, Begüm Özen, Dr. Mahdi Abbasi, Jonas Keller, Lorenz Faust, Dr. Nico Dingenouts, Dr. Karl Ratzsch, Dr. Christopher Klein, Britta Mayerhöfer, Dr. Johannes Höpfner and Dr. Roxana Figuli for commenting on different parts of my thesis.

- **German Research Foundation (DFG)**
  for the financial support of this work (WI 1911/24-1).

- **AKK & team**
  for all the great concerts and letting me stay late at campus.

- **My family and all my friends**
  for their support and all the nice time besides work.